STRUCTURAL ANALYSIS OF SYNTHETIC FERRIHYDRITE NANOPARTICLES AND ITS REDUCTION IN A HYDROGEN ATMOSPHERE

by

COLANI JOHN MASINA

Thesis submitted in fulfilment of the requirements for the degree

PHILOSOPHIAE DOCTOR

in

PHYSICS

in the faculty of science of the

NELSON MANDELA METROPOLITAN UNIVERSITY

Promoter: Prof. J.H. Neethling (NMMU)

Co-promoter: Dr. L Lodya (Sasol Technology R&D)

2014

"To those whose tracks I have followed

and those who will follow mine"

ACKNOWLEDGEMENTS

The author wishes to express sincere gratitude to the following people:

- My promoter Prof. J.H Neethling for his support, help, and encouragement throughout this work. I appreciate all his time and effort in guiding me.
- My former co-promoter Dr B.G Anderson for his guidance, support and brilliant ideas during the research project.
- My current co-promoter Dr L. Lodya for taking over from Dr Anderson and guiding me through the last few months of my PhD tenure. Thank you for your help with running Mössbauer and magnetic measurements. I also thank you for your brilliant ideas during the manuscript writing.
- Dr E.J Olivier for his help with all microscopy related experiments and helpful discussions. Thank you for taking your time teaching me how to use the JEM-2100 TEM
- A special thanks to Dr S.S Manzini who worked overtime helping with Mössbauer reduction experiments.
- I thank Dr M.W Ngobeni for assisting me with the running and interpretation of TPR experiments. Thank you for your friendship and encouragement during my visits at Sasol.
- Dr A. Ferreira for teaching me how to prepare ferrihydrite samples and thank you for the fruitful discussions we had at the beginning of the project.
- Dr E. du Plessis and Dr R. Forbes for their help and support with XRD experiments and teaching me how to run XRD experiments and how to use some of the XRD software.
- Dr W. Barnard for helping with Raman spectroscopy work.
- Everyone from Sasol Technology R&D group who directly or indirectly helped in this project.
- Prof P.A van Aken and Dr Vesna Srot for assistance with EELS experiments and helpful discussions.
- Dr A. Brown and Dr G. Vaughan for teaching me the NLLS fitting procedure using the IGOR software.

- Staff and friends inside and outside the department of physics at NMMU especially the microscopy group.
- Many thanks are due my fiancée for her patience, encouragement, moral support and mostly for her love. Thank you for typing the references cited in this thesis.
- A special thanks to my parents LaVilane and Elphas Masina, brothers (Joey, SiphoSethu, and Kwazi), and the family’s female child (Sharon) for their continuous support through the years.
- Last but not least, I fully acknowledge Sasol Technology R&D for the financial support of this PhD project.

DECLARATION

In accordance with Rule G4.6.3,

4.6.3 A treatise/dissertation/thesis must be accompanied by a written declaration on the part of the candidate to the effect that it is his/her own work and that it has not previously been submitted for assessment to another University or for another qualification. However, material from publications by the candidate may be embodied in a treatise/dissertation/thesis.

I, Colani John Masina, student number 210248939, hereby declare that this thesis for "***PHILOSOPHIAE DOCTOR***" is my own original work and that I have not previously in its entirety or in part submitted it at any university for a degree.

Signature: ……………………………………………………………

Date: ………………………………………………………………

SUMMARY

Ferrihydrite (FHYD), a nanocrystalline material has long been described as a poorly crystalline disordered mineral mainly due to its small crystal size which is typically $2 - 6\,nm$. The three-dimensional structure of the mineral has long been described by a multi-phase structural model that consists of Fe^{3+} only in octahedral (O_h) coordination. In this model ferrihydrite is described as a mixture of two major phases (akaganeite/goethite-like f-phase and feroxyhite-like d-phase) and a minor ultradispersed nanohematite phase. This model has been recently challenged and a new, single-phase model was proposed, having a basic structural motif closely related to the Baker-Figgs δ-Keggin cluster and is isostructural with the mineral akdalaite, $\mathrm{Al_{10}O_{14}(OH)_2}$. In its ideal form, the proposed new structure of FHYD consist of 80 % O_h and 20 % tetrahedral (T_d) Fe^{3+} polyhedra which can be adequately described by a single-domain model with the hexagonal spacegroup $P6_3mc$ and unit cell dimensions $a = 5.95$ Å and $c = 9.06$ Å.

In this study, nanoparticles of 2-line FHYD (FHYD2), 2-line FHYD deposited onto SiO_2 ($FHYD2/SiO_2$) and 6-line FHYD (FHYD6) synthesised using rapid hydrolysis of $Fe(NO_3)_3.9H_2O$ solutions were characterized using X-ray diffraction (XRD), Raman spectroscopy, transmission electron microscopy (TEM), Mössbauer spectroscopy (MS) as well as magnetization and magnetic susceptibility measurements. The coordination environment of iron atoms in the structure of FHYD was investigated using TEM and MS. The thermal transformation of FHYD nanoparticles was monitored through changes in the magnetization as a function of temperature and the reduction behaviour in hydrogen environment was studied using temperature programmed reduction (TPR), *in-situ* XRD and MS. Electron diffraction, TEM/ scanning TEM (STEM) imaging, and electron energy loss (EELS) measurements were carried out on three different microscopes *viz*. JEOL JEM-2100 LaB6 TEM, aberration corrected Schottky-FEG JEOL JEM-ARM200F HRTEM and cold-FEG Zeiss SESAM TEM. EELS studies were concentrated mainly on the iron L-edge of FHYD and iron oxides reference spectra with well known crystal structures. The iron oxide Fe L-edge is usually characterized by two intense sharp peaks termed “white lines”. The fine structures introduced by the crystal field effect on the L- edge contain information that is highly specific to the Fe^{3+} site symmetry.

FHYD2 and FHYD2/SiO_2 presented two broad XRD peaks indicative of the poor crystallinity while FHYD6 featured 6 peaks suggesting a relatively better crystallinity. The average crystallite sizes were estimated to 3.5, 4.0 and 6.0 nm for FHYD2, FHYD2/SiO_2 and FHYD6, respectively. However the structural arrangements for Fe atoms remained the same in all three samples. The temperature dependence of the magnetisation featured typical superparamagnetic (SPM) behaviour above a blocking temperature (T_B) in the range 36 – 50 K giving large anisotropy constants of $K = 5.5 \times 10^5$ J/m^3 for FHYD2/SiO_2, $K = 4.5 \times 10^5$ J/m^3 for FHYD2, $K = 1.5 \times 10^5$ J/m^3 for FHYD6. The Arrhenius plots of the frequency dependence of the magnetic susceptibility gave K = 4.04 x 10^5 J/m^3 for FHYD2 and K = 1.73 x 10^5 J/m^3 for FHYD6. These values are consistent with $K = 0.4 - 6.1 \ \times 10^5$ J/m^3 reported for bulk FHYD. The fits of the Curie-Weiss model to the temperature dependence of the magnetic susceptibility gave the effective magnetic moment per atom of μ_{eff} = 5.78 μ_B for FHYD2 and μ_{eff} = 5.20 μ_B for FHYD6, consistent with previously reported values μ_{eff} = 5.75 μ_B for FHYD2 and μ_{eff} = 5.17 μ_B for FHYD6 as well as with the experimental value μ_{eff} = 5.85 μ_B and the theoretical value μ_{eff} = 5.92 μ_B expected Fe^{3+}.

High resolution EELS data provided evidence of the presence of Fe^{3+} on O_h sites Fe1 and Fe2 as well as on T_d sites Fe3 for both FHYD2 and FHYD6, compatible with a basic structural motif closely related to the Baker-Figgs δ-Keggin cluster and isostructural $\mathrm{Al_{10}O_{14}(OH)_2}$. The experimental Fe L-edge of FHYD2 and FHYD6 was modeled using the Fe L-edge of the iron oxides reference spectra and the percentage of O_h and T_d Fe^{3+} was estimated from the weighting coefficients of non-linear least squares (NLLS) fitting procedure. Based on the NLLS fitting procedure, a significant amount of 20±5 % and 15±5 % T_d Fe^{3+} was estimated for FHYD2 and FHYD6, respectively. The MS spectra recorded at 4.2 K in zero-field and at 4.2 K in an applied magnetic field of 10 T were successfully fitted with three set of sextets representing the octahedral sites Fe1 and Fe2, and the tetrahedral sites Fe3.

The thermal transformation of FHYD nanoparticles appeared to proceed through the loss of the lattice water and sintering accompanied by improved crystallinity and structural changes. Such a transformation is initiated at relatively low temperature (i.e. T ~ 580 K) for FHYD2 and

FHYD6 and at a relatively higher temperature (i.e. T ~ 660 K) for FHYD2/ SiO_2 implying that the presence of SiO_2 inhibits the transformation and prevents sintering.

FHYD2, FHYD2/SiO_2 and FHYD6 showed different reduction pathways when exposed to H_2 stream. The reduction mechanism of FHYD2 involved two steps ($\mathrm{FHYD2} \rightarrow \mathrm{Fe_3O_4} \rightarrow \mathrm{Fe}$). The kinetic activation energies obtained using the Kissinger and Ozawa model-free isoconversion method amounted to E_a = 74 kJ/mol for the first step (FHYD2 → Fe_3O_4) and E_a = 54 kJ/mol for the second step (i.e. Fe_3O_4 → Fe). The reduction mechanism of FHYD2/SiO_2 comprised three well separated steps ($\mathrm{FHYD2/SiO_2} \rightarrow \mathrm{Fe_3O_4} \rightarrow \mathrm{FeO} \rightarrow \mathrm{Fe}$) of the activation energy $E_a = 73, 56,$ and $100\ \mathrm{kJ/mol}$, respectively. For FHYD6, the reduction proceeded via the thermal transformation of FHYD6 to hematite (Fe_2O_3) followed by a two-step reduction of Fe_2O_3, i.e. $\mathrm{Fe_2O_3} \rightarrow \mathrm{Fe_3O_4} \rightarrow \mathrm{Fe}$, with activation energies E_a = $77\ \mathrm{kJ/mol}$ for the first step and E_a = $66\ \mathrm{kJ/mol}$ for the second step.

LIST OF FIGURES

LIST OF TABLES

LIST OF ACRONYMS AND ABBREVIATIONS

Acronym or Abbreviation	Definition
ADF	Annular Dark Field
AFM	Antiferromagnetic
BF	Bright Field
DF	Dark Field
DP	Diffraction Pattern
DSC	Differential Scanning Calorimetric
EELS	Electron Energy Loss Spectroscopy
FEG	Field Emission Gun
FHYD	Ferrihydrite
FHYD2	2-line Ferrihydrite
FHYD2/SiO_2	SiO_2 co-precipitated 2-line Ferrihydrite
FHYD6	6-line Ferrihydrite
FiM	Ferrimagnetic
FM	Ferromagnetic
FT	Fischer-Tropsch
HAADF	High Angle Annular Dark Field
HRTEM	High Resolution Transmission Electron Microscopy
IFMS	In-field Mössbauer Spectroscopy
MS	Mössbauer Spectroscopy
NLLS	Non-Linear Least Squares
O_h	Octahedral symmetry
PDF	Pair Distribution Function
SPM	Superparamagnetic
STEM	Scanning Transmission Electron Microscopy
T_d	Tetrahedral symmetry
TDA	Differential Thermal analysis
TEM	Transmission Electron Microscopy
TG	Thermogravimetric
TPR	Temperature Programmed Reduction
XRD	X-ray Diffraction
ZFMS	Zero-field Mössbauer Spectroscopy

TABLE OF CONTENTS

Chapter 1

Introduction

This chapter states the aims, objectives, scope and structure of the work presented in this thesis. The materials under investigation in the entire work are nanoparticles of iron oxyhydroxide known as ferrihydrite.

1.1 Background

Due to their unique physical and chemical properties, there has been considerable research interest in nanomaterials in recent years. These unique properties relate to their size, shape, composition and atomic structure (Michel, 2007a). One of the nanomaterials which has attracted widespread interest in recent years is the nanocrystalline iron oxyhydroxide referred to as ferrihydrite (FHYD). While detailed investigations of the structure of this ferric oxyhydroxide mineral have been carried out, its atomic structure is still a matter of intense debate. The lack of knowledge of the crystal structure of the mineral is a stumbling block in the understanding of its composition and role in various processes e.g. geological (adsorbent), biological (iron storage) and catalytic processes.

FHYD, of chemical formula $5Fe_2O_3{\cdot}9H_2O$ or $FeOOH{\cdot}0.4H_2O$, is one of the 16 known iron oxides and oxyhydroxides (Cornell and Schwertmann, 2003). It is customary to collectively refer to all the iron oxides, hydroxides and oxide hydroxides as iron oxides and, for this reason, throughout the thesis they will all be referred to as iron oxides. These include $Fe(OH)_3$, Fe(OH), FeO, Fe_3O_4, FeOOH polymorphs (α, β, γ, δ), four Fe_2O_3 polymorphs (α, β, γ, ε), Schwertmannite ($Fe_8O_8(OH)_6(SO_4){\bullet}nH_2O$), and green rust (Schwertmann and Cornell, 2000; Cornell and Schwertmann, 2003). FHYD and Schwertmannite are the only two iron oxides that crystallize in a poorly defined state, showing only a maximum of six and eight broad X-ray reflections, respectively (Cornell and Schwertmann, 2003).

FHYD's unique characteristic among the other iron oxides is that it only exists in nanocrystalline form, with crystallite size in the range 2-6 nm (Jambor and Dutrizac, 1998; Janney *et al.*, 2000a; Janney *et al.*, 2000b; Janney *et al.*, 2001; Cornell and Schwertmann, 2003). As a result it possesses a large surface-to-volume ratio, high surface reactivity and exhibits a superparamagnetic (SPM) behavior. These properties are being exploited in many fields including geological, biological, and industrial processes. FHYD is appealing for its good catalytic properties resulting from its extremely high surface area and reactivity. Indeed, as a useful requirement for catalytic materials to have a high surface area, FHYD is preferred in the catalytic industry because of its reactivity and large specific surface area of 100-700 m^2/g (Schwertmann and Cornell, 2000). Under reducing conditions, FHYD can transform to the elemental or catalytically active form.

Figure 1.1 shows the multidisciplinary nature of iron oxides in general as reported by Cornell and Schwertmann, 2003. It is interesting to note that FHYD alone finds applications in almost all the disciplines depicted in Figure 1.1. Of interest to the current project are the catalytic properties of FHYD.

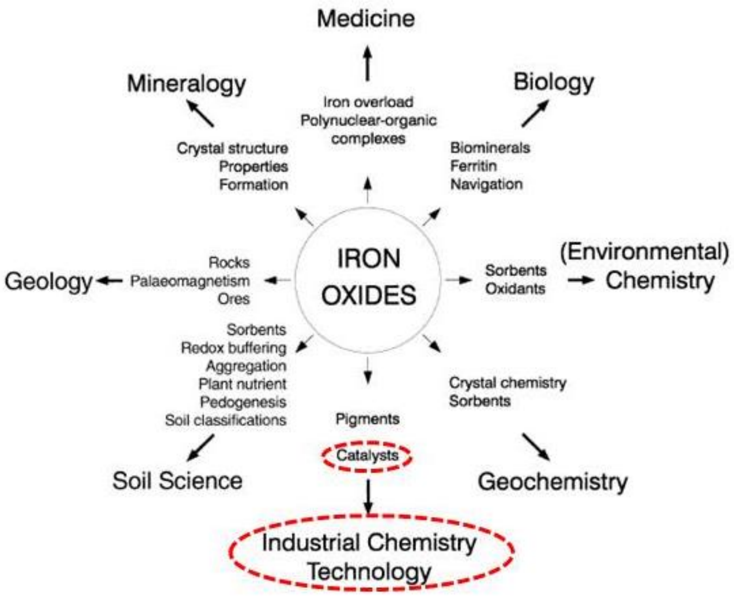

Figure 1.1: **Iron oxides research in multidisciplinary fields (from Cornell and Schwertmann, 2003).**

The crystal structure of FHYD is a topic of interest for mineralogists and in many other disciplines. In biological systems the structure of FHYD is thought to resemble to that of the core material of the iron storage protein known as ferritin (Kilicoyne *et al.*, 1992; Kilicoyne and Cywinski, 1995). The structure of ferritin consists of a spherical shell (apoferritin) of external diameter ~12 nm, which surrounds an antiferromagnetic iron oxyhydroxide core (7 nm in diameter) that can carry a total number of ~ 4500 Fe ions in its full capacity (Kilicoyne *et al.*, 1992; Kilicoyne and Cywinski, 1995; Makhlouf and Parker, 1997). In biological research fields, the interest is to establish the iron storage mechanism of ferritin in living organisms. But in order to do that the first problem is to solve the structure of the mineral core. The structure of the core material is however subject to controversy. Based on the similarities of X-ray diffraction and selected area electron diffraction, Cowley *et al.*, 2000, concluded that the structure of the core of ferritin is based on a hexagonal structure similar to the mineral FHYD.

Nanoparticles of iron oxides find applications in the biomedical field, particularly in magnetic resonance imaging (MRI) as contrast agents in diagnostics applications (Vatta *et al.*, 2006). The requirements for a material to be used in medical applications are (1) small enough to interact in the region of interest, (2) exhibit superparamagnetic behavior, and (3) high saturation magnetization (Vatta *et al.*, 2006). Nanocrystalline FHYD fulfills these requirements.

1.2 Aims, objectives and scope of the investigation

Presented in this thesis is a comprehensive study aimed at understanding the structural and magnetic properties of 2- and 6-line FHYD as well as the thermal transformation and the reduction mechanisms of FHYD. The role of SiO_2 on the thermal transformation and the reduction behavior is also investigated. The thesis deals with the structure of two forms of synthetic FHYD, i.e. 2- and 6-line FHYD, referred to as FHYD2 and FHYD6, respectively, throughout the thesis. Also included in the study is a sample of FHYD2 deposited into SiO_2 and referred to as FHYD2/SiO_2.

One of the obvious disagreements between the two models by Drits *et al.*, 1993 and Michel *et al.*, 2007c describing the structure of FHYD is the presence (Michel's model) and absence (Drits's model) of tetrahedrally (T_d) coordinated Fe^{3+}. Knowledge of the Fe^{3+} coordination environment is significant in determining which model best describes the structure of the mineral FHYD. In this thesis the presence or absence of tetrahedral Fe^{3+} coordination (T_d Fe^{3+}) in the structure of FHYD is investigated using techniques that are sensitive to the local environment of Fe^{3+}. These include high spectral energy resolution electron energy loss spectroscopy (EELS) and applied magnetic field Mössbauer spectroscopy (MS). It is envisioned that these techniques will provide the insight needed for an understanding of the coordination sites of iron atoms.

As mentioned, the magnetic properties of iron oxide nanoparticles are also of great industrial importance. It has been previously pointed out that as the particle size decreases the spins are affected by thermal fluctuations (Vatta *et al.*, 2006) and that they exhibit a superparamagnetic (SPM) behavior below a certain threshold size, when their spin flip directions due to thermal energy such that the overall magnetization average to zero as expected for paramagnetic materials (Murad, 1996). The magnetic properties of synthetic FHYD2, FHYD6 and $FHYD_2$/SiO2 are also investigated in this study in relation with the nature of the structural disorder exhibited by the nanoparticles.

The Fischer-Tropsch synthesis (FTS), a process that converts syngas into whole range hydrocarbons, has received great attention because it offers a clean option for the production of transportation fuels and chemicals. Catalysts usually have to undergo reduction prior to FTS to produce catalytically active phases. There are few available examples of FHYD reduction under H_2 in the literature, e.g. (Jozwiak *et al.*, 2007; Schneeweiss *et al.*, 2008; Schneeweiss *et al.*, 2010; Schneeweiss *et al.*, 2011). However, there is no work that has explicitly studied and compared the reduction behavior of FHYD2 and FHYD6. In addition, the role of SiO_2 on the reduction behavior of FHYD has not been given attention. These shortcomings are addressed in this study which aims at providing an insight into the mechanisms of the reduction of FHYD2 and FHYD6 and $FHYD_2$/SiO_2.

It is usually believed that the role of a structural promoter such as SiO_2 in catalysis is to stabilize the catalyst and prevent particle sintering (Li *et al.*, 2002; Lohitharn *et al.*, 2008). Some studies have also pointed to strong interactions between the catalysts and the promoters which influence the reducibility and activity of the catalysts (Lund and Dumesic, 1981; Dlamini *et al.*, 2002). The role of silica in the reduction behavior of FHYD2 is also investigated.

Iron oxides and oxyhydroxides usually undergo thermal transformation to a more stable form, hematite (α-Fe_2O_3) (Cornell and Schwertmann, 2003). Experimental results suggest that α-Fe_2O_3 nucleates and grows within FHYD aggregates (Cornell *et al.*, 1989). This solid-state transformation is thought to be facilitated by the similar sharing of hexagonal close-packed anion sublattice between FHYD and α-Fe_2O_3. Stanjek and Weidler, 1992, proposed a transformation mechanism of FHYD to α-Fe_2O_3 that involves continual removal of structural OH from FHYD structure and reduces the average coordination number of oxygens and OH around iron and thus creating charge imbalance. When the concentration of defects reaches a critical value, structural rearrangements (e.g. face sharing) to α-Fe_2O_3 is initiated (Cornell *et al.*, 1989; Stanjek and Weidler, 1992; Cornell and Schwertmann, 2003). Notwithstanding, the mechanism of FHYD transformation to hematite is still not fully understood as yet. Thermal transformations of FHYD2, FHYD2/SiO_2 and FHYD6 under vacuum are investigated in this study by monitoring changes in the magnetization as a function of temperature.

1.3 Structure of the thesis

This study is structured as follows. Chapter 2 gives a literature review of different models used to describe the structure of FHYD and the reduction mechanisms of iron oxides. Also reviewed are the experimental results on FHYD obtained using X-ray and neutron diffraction, XANES/EXAFS, Mössbauer spectroscopy, HRTEM, Raman as well as PDF analysis of neutron and synchrotron X-rays. The experimental techniques and the investigation methods used in this study are described in chapter 3.

Chapter 4 discusses the synthesis and the results of the characterization of FHYD nanoparticles with emphasis on their magnetic properties. The coordination environments of iron atoms in FHYD are discussed in chapter 5 with particular focus on the critical question of the presence or absence of tetrahedral (T_d) coordinated iron cations in the structure of FHYD. The thermal transformation of FHYD under vacuum are discussed in chapter 6 together with the mechanisms of the reduction of FHYD upon exposure to H_2 and the effect of SiO_2 on the thermal transformation and the reducibility of FHYD nanoparticles. The study ends with conclusions and recommendations presented in chapter 7.

Chapter 2

Literature review

2.1 Introduction

Ferrihydrite (FHYD), which is known as an “amorphous ferric oxide” is a poorly nanocrystalline oxyhydroxide that forms mainly in low temperature surface environments such as aquatic sediments, mine wastes and water wells (Jambor and Dutrizac, 1998; Schwertmann and Cornell, 2000; Janney *et al.*, 2000a; Janney *et al.*, 2000b; Janney *et al.*, 2001; Cornell and Schwertmann, 2003). It can also be synthesized in the laboratory by rapid hydrolysis of Fe (III) solutions or oxidation of Fe(II) compounds. It is a metastable compound which can easily transform to hematite (α-Fe_2O_3), akaganeite (β-FeOOH), and goethite (α-FeOOH), hence it is an important soil mineral in a sense that it is a necessary precursor in the formation of soil α-Fe_2O_3 (Jambor and Dutrizac, 1998; Cornell and Schwertmann, 2003).

As mentioned, FHYD is a short range ordered material with crystal size around 2-6 nm (Jambor and Dutrizac, 1998; Janney *et al.*, 2000a; Janney *et al.*, 2000b; Janney *et al.*, 2001; Cornell and Schwertmann, 2003). The small size of the nanoparticles and its high surface area (> 200 m^2/g) make FHYD appropriate as a precursor for iron-based catalysts (Jambor and Dutrizac, 1998; Hausner *et al.*, 2009; Bali *et al.*, 2011; Bali *et al.*, 2012). Due to the poor crystallinity and uncertainty of the composition (e.g. variability in water content) researchers are still unable to fully establish its exact atomic structure. Its crystallinity is indicated by the number of X-ray reflections, and usually two types are recognized i.e. 2-line (FHYD2) and 6-line (FHYD6) as shown in Figure 2.1.

The relationship between the FHYD2 and FHYD6 is another topic of debate with many reports suggesting that they have the same atomic arrangement and the only main difference is their coherent scattering domain which is smaller for the FHYD2 (~2 nm) than for FHYD6 (~6 nm) (Drits *et al.*, 1993; Michel *et al.*, 2007c). However, electron nanodiffraction work on the structure of FHYD2 and FHYD6 has shown that the FHYD6 is not just a more crystalline form of FHYD2 (Janney *et al.*, 2001). The FHYD2 has shown a high fraction of disordered material compared to FHYD6 and the double chain and maghemite-like structure observed on the FHYD2 were not observed in FHYD6 (Janney *et al.*, 2000b; Janney *et al.*, 2001). This observation refutes the suggestions that the only difference in the FHYD2 and FHYD6 is the size of their coherent scattering domain.

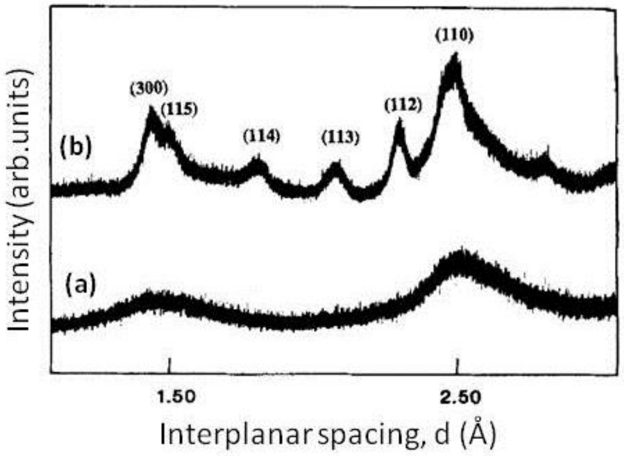

Figure 2.1: Classical XRD patterns for (a) 2-line and (b) 6-line FHYD (from Manceau *et al.*, 1990).

It is difficult to describe FHYD with one chemical formula as it is associated with many chemical formulas due to variable water content, the most widely reported being $5Fe_2O_3 \cdot 9H_2O$, $Fe_5HO_8 \cdot 4H_2O$, $2FeOOH \cdot 26H_2O$, and $Fe(OH)_3$ (Jambor and Dutrizac, 1998). In a study of the solubility of synthetic schwertmannite and FHYD, Yu *et al.*, 2002, proposed a revised chemical formula $Fe_2O_{3-0.5y}(OH)_y \cdot nH_2O$ for FHYD. Based on PDF analysis of high energy X-rays by Michel *et al.*, 2007c, FHYD was given a new chemical formula $Fe_{10}O_{14}(OH)_2$. This new chemical formula was criticized for being anomalously H-poor, it was later revised and approximately three structural waters were added to yield a chemical formula $Fe_{8.2}O_{8.5}(OH)_{7.4} + 3H_2O$ for disordered FHYD and $Fe_{10}O_{14}(OH)_2 + \sim H_2O$ for ordered ferrimagnetic FHYD (ferrifh) phase (Michel *et al.*, 2010). The disagreement with regard to the chemical formula of FHYD arises from the amount of structural OH and water present in the mineral.

This chapter is dedicated to a literature review of the different models used to describe the structure of FHYD and its reduction mechanisms upon exposure to H_2. It starts with a review of the structures of iron oxides in section 2.2. Section 2.3 outlines the two competing structural models for FHYD, i.e. Drits and Michel's models, with emphasis on the obvious disagreements that exist between them. The surface structural models for FHYD are reviewed in section 2.4 followed by experimental observations in section 2.5. The chapter ends with a review of the mechanisms of the reduction of iron oxides in H_2 atmosphere in section 2.6.

2.2 Structures of iron oxides

2.2.1 General overview

It is recalled that FHYD is a metastable phase that can thermally transform to thermodynamically more stable crystalline iron oxides including goethite and hematite. In addition, it can be fully reduced to metallic iron (α-Fe) magnetite (Fe_3O_4) and wüstite (FeO) intermediates. The structures of the iron oxides that can possibly form during FHYD thermal transformation and reduction in H_2 atmosphere are briefly discussed in this section. The crystal and magnetic structures of these iron oxides, namely Fe_3O_4, FeO, hematite (α-Fe_2O_3), maghemite (γ-Fe_2O_3), and goethite (α-FeOOH), are also briefly summarized. Only the iron oxides that are somehow related to FHYD are covered in this thesis. Interested readers are encouraged to explore the following references (Schwertmann and Cornell, 2000; Cornell and Schwertmann, 2003; Wang *et al.*, 2009) for a full discussion of the other iron oxides structures.

The structures of iron oxides have been established by means of X-ray, neutron and electron diffraction methods. Supplementary structural information has also been obtained using spectroscopic techniques such as EXAFS/XANES, Infrared (IR), Raman and MS. The structures of all the iron oxides are based on stacking of closed-packed arrays of oxygen/hydroxyl sheets in which iron cations occupying the octahedral (O_h) or tetrahedral (T_d) interstices (Bernal *et al.*, 1959; Cornell and Schwertmann, 2003). The most common valence states of Fe in the iron oxides are the trivalent (Fe^{3+}) and divalent (Fe^{2+}) states. Because of their smaller ionic radii (Fe^{3+} = 0.065 and Fe^{2+} = 0.082 nm), these cations fit in the O_h and T_d interstices created by the anion layers with large ionic radii (e.g. O^{2-} radius is 0.14 nm) (Cornell and Schwertmann, 2003). In three dimensions, the anions sheets in the oxides arrange themselves in a closed-packed hexagonal stacking (ABAB…) and cubic closest packing (ABCABC…) (Schwertmann and Cornell, 2000; Cornell and Schwertmann, 2003).

The basic structural unit in iron oxide compounds is the most common FeO_6 or $FeO_3(OH)_3$ octahedron and the FeO_4 tetrahedron, in some cases (Cornell and Schwertmann, 2003). The structural arrays of the compounds are formed by the linkages of these polyhedra. The iron oxides take different structural forms based on the type of linkages and how these entities connect in their structures during formation. Figure 2.2 shows three geometrical possible types of linkages (corner, edge, and face) observed in iron oxides (Cornell and Schwertmann, 2003).

The Fe-Fe distances between two polyhedra depend on the type of linkage that exists in that particular arrangement. For example, the cations are kept further apart in a corner-sharing arrangement for an octahedral linkage. They are drawn a bit closer in an edge-sharing and closest in face-sharing arrangement (compare Fe-Fe distances in Figure 2.2). The different iron oxides structures and their structural relationships can be visualized using the linkage representation (Cornell and Schwertmann, 2003).

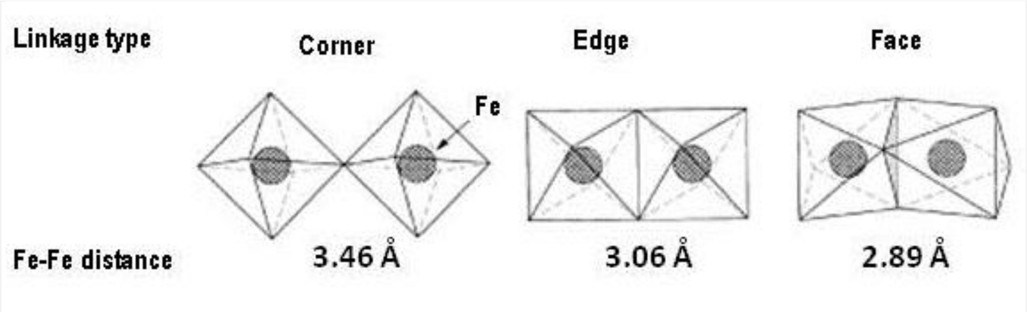

Figure 2.2: Octahedra linkage types and their Fe-Fe distances in iron oxides (from Cornell and Schwertmann, 2003).

In terms of magnetic behavior of iron compounds, the dominant type of magnetic interaction that exists between the iron ions in the adjacent sites is the exchange interaction. This tends to cause the spins to align parallel or antiparallel to each other. Most of the iron oxides have two interpenetrating magnetic sublattices in which the spins have antiparallel orientation (see Figure 2.3). In this arrangement, the magnetic order is termed antiferromagnetic (AFM) and the net magnetization is zero as a result of the spins cancelling each other because they are of equal magnitudes but opposite directions. The magnetic order is ferromagnetic (FM) if spins of equal magnitude are exactly parallel to each other. None of the iron oxides show genuine FM ordering (Murad, 1996).

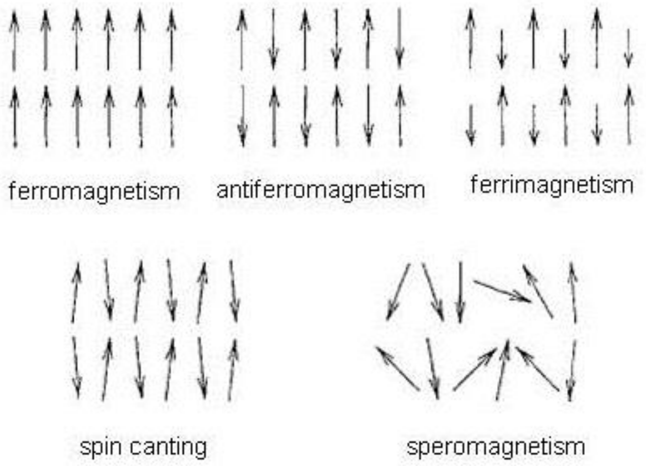

Figure 2.3: Types of magnetic ordering and disorder in crystalline materials (from Murad, 1996).

Another type of magnetic ordering which is common amongst the spinels (Fe_3O_4 and γ-Fe_2O_3) is ferrimagnetism (FiM). In this arrangement, the magnetic moments align themselves antiparallel to each other similarly to AFM ordering but the magnitudes of the spins of the two sublattices differ, a net magnetization appears which is however smaller than in a FM ordering. In some other cases there are deviations from the normal parallel/antiparallel spin orientations. This happens when the spins are not exactly antiparallel (canted) or when the spins are randomly oriented (speromagnetism). Spin canting results in a weak net magnetic moment.

Magnetic ordering are observed at temperatures below the magnetic transition temperatures known as Curie temperature (T_C) for FM and FiM materials and Néel temperature (T_N) for AFM materials. Above T_C and T_N the thermal energy causes a random alignment of the spins and the net magnetization cancel out; materials become paramagnetic (PM).

2.2.2 Crystal structures and magnetic properties

Hematite (α-Fe_2O_3) is the most stable of the four Fe_2O_3 polymorphs. It is an iron (III) oxide with all the trivalent iron occupying O_h sites, i.e. the Fe^{3+} ions are surrounded by six oxygen atoms (Cornell and Schwertmann, 2003; Hill *et al.*, 2008; Wang *et al.*, 2009) as shown in Figure 2.4 (d). The structure of α-Fe_2O_3 consists of hcp arrays of oxygen ions stacked along the [001] direction. These planes of anions are stacked parallel to the (001) planes. The Fe^{3+} ions occupy two thirds of O_h interstices which are arranged regularly in the (001) plane; with every two filled sites followed by a vacant site and forming six fold rings in that way. The oxide possesses a rhombohedral corundum structure with space group $R\overline{3}c$ (N° 167) and lattice constants of a = 5.035 Å and c = 13.75 Å (Cornell and Schwertmann, 2003; Mohapatra and Anand, 2010). α-Fe_2O_3 presents a weak FM ordering below $T_C \sim 950$ K and an AFM ordering below the Morin transition temperature at $T_M = 260$ K with the spins orientated along the electric field gradient axis (Zboril *et al.*, 2002; Cornell and Schwertmann, 2003).

Maghemite (γ-Fe_2O_3) is one of the four Fe_2O_3 polymorphs (α, β, γ and ε). It is isostructural with inverse spinel magnetite and only differs from magnetite in that it contains only Fe in trivalent state (Da Casta *et al.*, 1994; Grau-Crespo *et al.*, 2010). The cubic unit cell of maghemite can be represented by that of magnetite with the introduction of cation vacancies in the structure to ensure charge neutrality. The cation vacancies are reported to be confined in the octahedral sites giving γ-Fe_2O_3 a unit cell formula of $[Fe^{3+}]_8(Fe^{3+}_{5/6}\square_{1/6})_{16}O_{32}$, where $\square$ = vacant sites (Da Casta *et al.*, 1994; Grau-Crespo *et al.*, 2010). Depending on vacancy ordering, the structure of γ-Fe_2O_3 (Figure 2.4(c)) usually crystallizes in a cubic form with the space group $P4_332$ (212) and lattice parameter a $= 8.3474$ Å and tetragonal system with space group $P4_12_12$ with $a = 8.33$ Å and $c = 25.01$ Å. The Fe^{3+} ions in γ-Fe_2O_3 occupy 37.5 % T_d interstices coordination and the rest of Fe^{3+} ions occupying O_h sites (Da Casta *et al.*, 1994). γ-Fe_2O_3 presents an FiM ordering at all temperatures below $T_C \sim 820 - 986$ K (Da Casta *et al.*, 1994; Cornell and Schwertmann, 2003; Grau-Crespo *et al.*, 2010). The transformation of γ-Fe_2O_3 to α-Fe_2O_3 at the temperature range $700 - 800$ K makes it difficult to accurately measure its T_C value (Cornell and Schwertmann, 2003). Although the atomic moments in each sublattice are parallel, the spins in the octahedral sublattice are antiparallel to the spins in the tetrahedral sublattice. The net magnetic moment in γ-Fe_2O_3 results from uncompensated spins in the octahedral sublattice.

Magnetite (Fe_3O_4) is the only iron oxide with mixed Fe^{2+} and Fe^{3+} valence states among the 16 know iron oxides. It crystallizes in the simple cubic inverse spinel structure with the space group Fd3m (N° 227) and lattice constant a = 8.3941 Å (Jeng and Guo, 2002; Wright *et al.*, 2002; Cornell and Schwertmann, 2003; Wang *et al.*, 2009). Figure 2.4(b) represents a structural unit cell of Fe_3O_4 with the all the Fe^{2+} ions in octahedral sites and Fe^{3+} in both octahedral and tetrahedral sites (Wang *et al.*, 2009). Fe_3O_4 is made of eight formula units per unit cell containing a total of 24 Fe atoms and 32 O atoms packed in a regular cubic stacking along the [111]. Its unit formula can be written as $[Fe^{3+}](Fe^{2+},Fe^{3+})O_4$ or generally $[B](AB)O_4$, where the [] and () brackets represents the tetrahedral and octahedral sites, respectively. One third of the Fe^{3+} is distributed among the eight tetrahedral sites and 2/3 of the iron occupy tetrahedral coordination (Jeng and Guo, 2002; Wright *et al.*, 2002; Cornell and Schwertmann, 2003). Fe_3O_4 presents also an FiM ordering at all temperatures below $T_C = 850$ K. (Cornell and Schwertmann, 2003). Similar to γ-Fe_2O_3, the spins of the Fe ions in the tetrahedral A-sites are antiparallel to those at octahedral B-sites. The net magnetic moment in Fe_3O_4 originates from the Fe^{2+} ions with effective magnetic moment $4\mu_B$ per ion (where μ_B is the Bohr magneton) since the magnetic moment of the Fe^{3+} ions is compensated by the antiparallel alignment between the two sublattices (Cornell and Schwertmann, 2003).

Wüstite (FeO) is an iron (II) oxide with all the divalent iron (Fe^{2+}) in octahedral coordination environment. Each Fe^{2+} ion is surrounded by six O^{2-} ions (Figure 2.4(a)) (Cornell and Schwertmann, 2003; Wang *et al.*, 2009). It crystallizes in the rock salt (NaCl) structure with space group *Fm3m* (N° 225) and lattice constant of a = 4. 3088 Å (Cornell and Schwertmann, 2003; Wang *et al.*, 2009). FeO exists in a nonstoichiometric form (cation deficiency) and it is thermodynamically metastable below 843 K (Cornell and Schwertmann, 2003). This is because it decomposes to Fe and Fe_3O_4 during a slow cooling at low temperatures in a disproportionation reaction ($4\mathrm{FeO} \rightleftharpoons \mathrm{Fe_3O_4} + \mathrm{Fe}$) (Jozwiak *et al.*, 2007). FeO presents an AFM ordering at all temperatures below $\mathrm{T_N} = 203 - 211$ K, depending on the concentration of defects that commonly exist in the structure of the oxide (Cornell and Schwertmann, 2003).

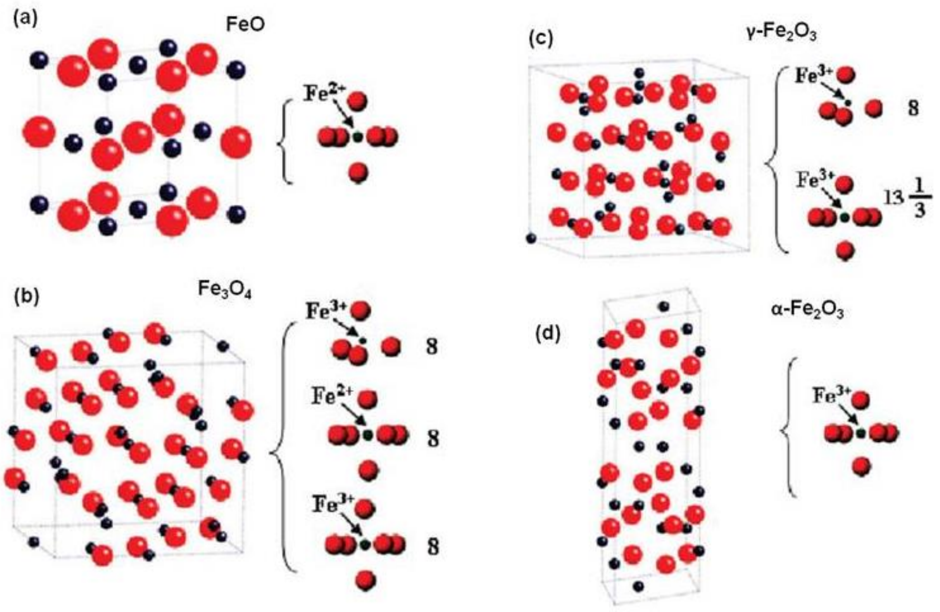

Figure 2.4: Crystallographic unit cells of (a) FeO, (b) Fe_3O_4, (c) γ-Fe_2O_3, and (d) α- Fe_2O_3. Red spheres represents oxygen and dark spheres represents iron (from Wang *et al.*, 2009).

Goethite (α-FeOOH) is an iron (III) oxide hydroxide that crystallizes in the orthorhombic crystal system (Cornell and Schwertmann, 2003; Christensen *et al.*, 2007). The oxide hydroxide mineral has a crystal structure isostructural to diaspore, AlO(OH) with its space group being moved from *pbnm* to *pnma* (N° 62) and lattice constants of a = 9.9510 Å, b = 3.0178 Å and c = 4.5979 Å (Cornell and Schwertmann, 2003; Christensen *et al.*, 2007). In the crystal structure of α-FeOOH each Fe^{3+} ion is surrounded by three O^{2-} ions and three OH^- ions which gives $FeO_3(OH)_3$ octahedra. α-FeOOH presents an AFM ordering at all temperatures below $T_N = 400$ K, in its AFM state the spins are oriented along the b-axis with up and down spins in alternate chains of octahedra and the strongest exchange interaction existing between corner sharing octahedral in continuous chains (Cornell and Schwertmann, 2003). The lower bond angle involved between the edge sharing octahedra (within the double chains) results in weak super-exchange interactions (Cornell and Schwertmann, 2003).

2.3 Ferrihydrite structural models

2.3.1 Drits model

The crystal structure of FHYD has long been described by various models, one being known as the standard model which was developed by Drits *et al.*, 1993. The Drits model, based on trial-and-error method of fitting laboratory XRD data, proposes a multiphase model which consists of three components: (i) defect-free FHYD (*f*-phase), (ii) defective FHYD (*d*-phase), and (iii) ultradispersed hematite (Figure 2.5). In this multiple domain octahedral Fe structural model the *f*-phase has an akaganeite/goethite-like structure while the *d*-phase is based on feroxyhyte-like structure (Drits *et al.*, 1993). The Drits model suggests that in the *f*-phase the oxygens and hydroxyls are closed-packed according to the AcBcAbCbA pattern with space group $P\bar{3}1c$ (Drits *et al.*, 1993; Jansen *et al.*, 2002; Manceau, 2009; Manceau, 2011). The Fe cations in the f-phase are randomly distributed in octahedral sites with 50% probability of occupancy and displaced in the direction of the B and C planes.

Prior study by Manceau and Drits, 1993, using EXAFS suggested that FHYD consists of only Fe octahedra linked by corners, edges and faces. The model is shown in Figure 2.5 with the anions in A sites forming continuous 2D planes while anions in B and C positions occupy only 85% of the sites due to the presence of cavities/channels inside the ABA and ACA fragments in the defect-free *f*-phase. The cavities between successive A plans is occupied by water molecules which account for the remaining 15% of space. The second component is the defective *d*-phase with a feroxyhyte-like (δ-FeOOH) structure (Drits *et al.*, 1993; Manceau, 2009; Manceau, 2011).

The third component consists of subordinate ultradisperse amount of nanohematite which can coexist with a spinel-type phase (Fe_3O_4 or γ-Fe_2O_3). According to Drits *et al.*, 1993, the *f*-phase is twice as abundant as the d-phase and the third phase is three times less abundant than the f-phase giving a 6:3:1 ratio of *f*-phase, d-phase and third phase, respectively. Jansen *et al.*, 2002, based on neutron diffraction, confirmed the presence of the *f*- and *d*-phase. HR-TEM observations confirmed the presence of all three components (Janney *et al.*, 2000a; Janney *et al.*, 2000b; Janney *et al.*, 2001).

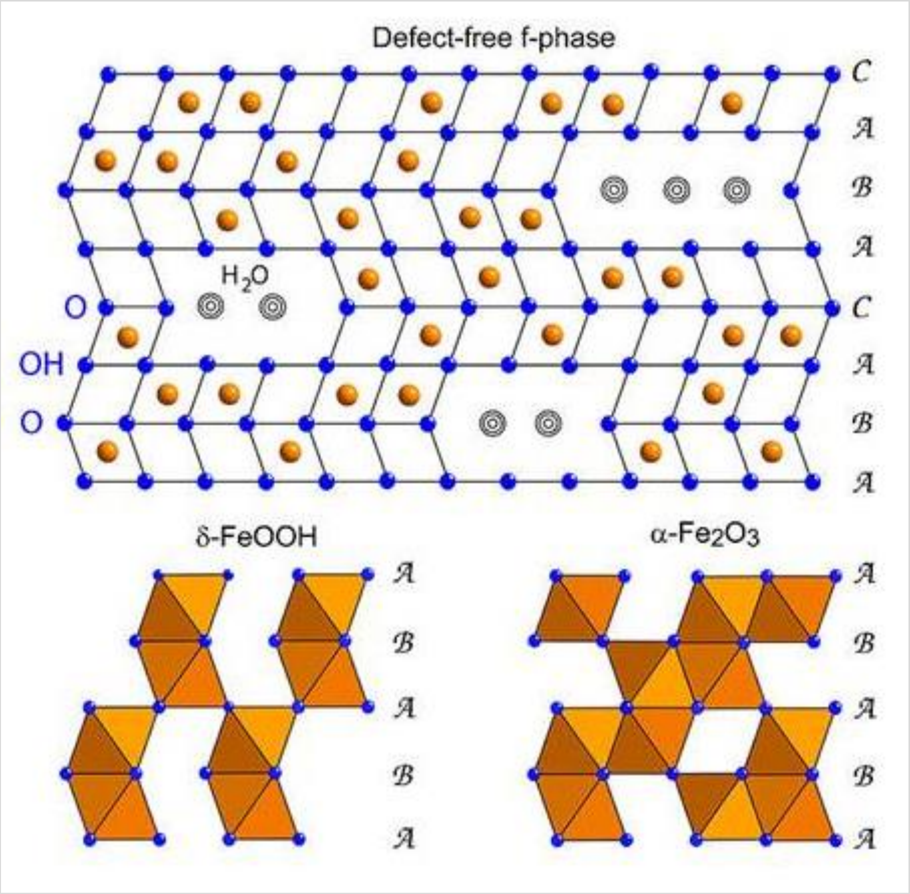

Figure 2.5: FHYD standard multiphase. Projection along [$1\bar{1}0$] vector (after Manceau, 2011).

2.3.2 Michel model

Michel *et al.*, 2007c, recently proposed a single phase model (referred as "akdalaite" model in this dissertation) from pair distribution function (PDF) derived from high energy synchrotron X-rays with the hexagonal space group *P6₃mc* (N° 186) with lattice parameters a = ~5.95 Å and c = ~9.06 Å F.M. Michel, 2007. The structure is isostructural to the mineral akdalaite ($Al_{10}O_{14}(OH)_2$) with a new FHYD chemical formula $Fe_{10}O_{14}(OH)_2$ (Michel *et al.*, 2007c). It shares the same anionic stacking as the Drits model i.e. double hexagonal ABAC. The ideal structure is closely related to the Baker-Figgis δ-Keggin cluster consisting of three types of iron occupying three distinct symmetry sites (Fe1, Fe2, and Fe3) (Michel *et al.*, 2007c). The structure consists of 13 Fe atoms and 40 oxygen atoms and the central Fe3 in tetrahedral site is connected by μ4-oxo bridges to 12 peripheral Fe atoms in octahedral sites arranged in edge-sharing groups of three as shown in Figure 2.6 (Michel *et al.*, 2007c).

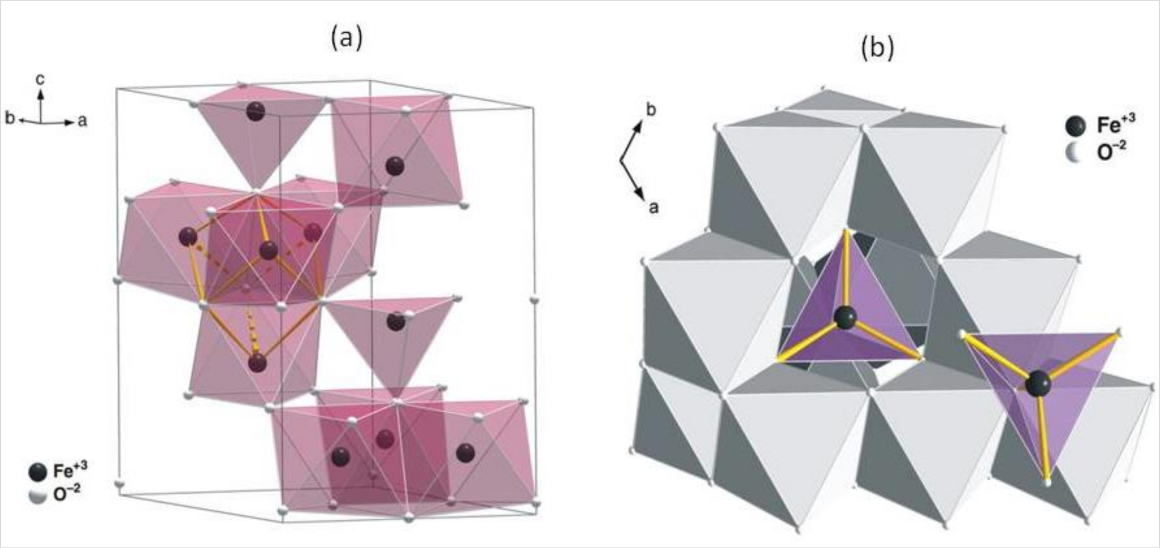

Figure 2.6: FHYD Michel's model. Polyhedra representation of the (a) Ferrihyhydrite hexagonal unit cell, (b) Ideal FHYD structure viewed along the c-axis (from Michel *et al.,* 2007c).

A clear visualization of the basic structural motif (δ-Keggin moiety) of the FHYD "akdalaite" model as proposed by Michel *et al.*, 2007c, as given by Hiemstra, 2013, and Pinney *et al.*, 2009, is depicted in Figure 2.7. The Fe1 and Fe2 irons are both octahedrally coordinated but occupying a different Wyckoff symmetry with slightly differing Fe-O geometries and the central Fe3 is tetrehedrally coordinated as shown in Figure 2.7. Each oxygen ion in the tetrahedron is linked to three edge-shared Fe octahedral. The Fe1 sites arranged itself in an edge-sharing layers separated by a mixed layer of Fe2 and Fe3 sites. There are four oxygen types (O1, O2, O3, and O4) with O1 binding a proton Pinney *et al.*, 2009. In its ideal form the structure suggests the presence of 20% iron in tetrahedral sites (Fe3) and 80% iron octahedral sites (Fe1 and Fe2). According to Michel *et al.*, 2007c, for disordered FHYD there are vacancies in both Fe3 and Fe2 sites while Fe1 is fully occupied. A particle size-dependent occupancy was observed on both Fe2 and Fe3 sites: both sites showed a decrease in occupancy with decreasing particle size while completely filled Fe1 sites do not show any size-dependent changes (Michel *et al.*, 2007c).

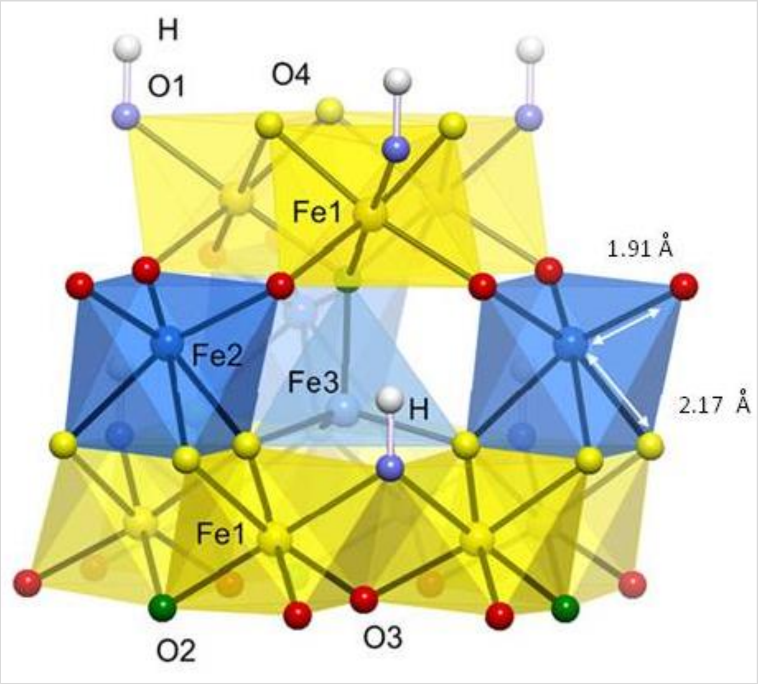

Figure 2.7: Structural motif δ-Keggin moiety of FHYD (Hiemstra, 2013).

The akdalaite model proposed by Michel *et al.*, 2007c, has been criticized by several groups e.g. (Rancourt and Meunier, 2008; Manceau, 2009; Manceau, 2011). It was pointed out that the model is periodic defect-free and for that reason it failed to reproduce XRD data and is also inconsistent with EELS, XANES and Mössbauer spectroscopy (MS) results (Manceau, 2011). Secondly, the ideal chemical formula $Fe_{10}O_{14}(OH)_2$ is anomalously H-poor for a hydrous oxyhydroxide formed at the surface of the earth. Its mass density including Fe vacancies is 4.90 g/cm^3 and is significantly higher than the experimental value of 3.96 g/cm^3 (Manceau, 2011). The model also somehow violates Pauling's 2nd rule (Pauling, 1929) because some ^{IV}Fe-O distances are equal or larger than the ^{VI}Fe-O distances, and it contains 20% tetravalent octahedral iron $^{VI}Fe^{4+}$, 20% divalent tetrahedral iron ($^{IV}Fe^{+2}$) (Rancourt and Meunier, 2008; Manceau, 2009).

Furthermore, high energy X-rays PDF analysis of three FHYD samples with different scattering domain sizes (FHYD = 2 nm, FHYD = 3 nm, and FHYD = 6 nm) by Michel *et al.*, 2007c, directly contradicts previous results by the same author (Michel *et al.*, 2007b). In the first paper (Michel *et al.*, 2007b), in agreement with Drits *et al.*, 1993, it was reported that there were no structural differences in the three FHYD samples and the difference in diffraction patterns is only due to their different coherent scattering domains. Subsequently the initial model was revised (Michel *et al.*, 2007c) and three different unit-cell parameters and atomic coordinates proposed for the three samples.

A further revision the ‘akdalaite’ model for FHYD was proposed after criticism by Rancourt and Meunier, 2008, and Manceau, 2009, validating the use of periodic model for nanomaterial and encompassing for very few unit cells by aging FHYD2 in the presence of adsorbed citrate at 175 °C for 14 h. The new revised akdalaite-like structural model (referred to as ‘ferrifh’ model) brought forward the ordered FiM phase of FHYD2 as an intermediate phase in the transformation of FHYD2 to α-Fe_2O_3 (Michel *et al.*, 2010). The akdalaite and ferrifh models share however the same akdailate polyhedra structure; they only differ in the positions of the Fe and O atoms in the unit cell. During refinement of Fe site occupancy in the fitting of experimental PDFs it was indicated that cation sites in the FHYD are only fully occupied at aging times $\geq$ 8 h (Michel *et al.*, 2010). This simply means that all the cation sites are fully occupied on the ordered FHYD form but not in the disordered FHYD.

In the “ferrifh” model it was suggested that in its pristine disordered form Fe2 and Fe3 sites had vacancies occupancy of between 45-50% while Fe1 had full cationic occupancy; the ordered form has full cationic occupancy for Fe1, Fe2 and Fe3 (Michel *et al.*, 2010). That is, in the ordered ferrifh FHYD structure all the cation sites are fully occupied while the disordered FHYD structure has between 45-50% vacancies on Fe2 and Fe3 sites. The differences in sites occupancy translate in density differences, which amount to 4.85-4.9 g/cm^3 for the ordered phase and 4.0-4.3 g/cm^3 for the disordered phase (Michel *et al.*, 2010). The density of disordered FHYD is consistent with the experimental and calculated density of FHYD 3.96 and 4.15 ± 0.1 g/cm^3, respectively. The ferrifh model also addressed the issues of the Fe-O distances and the violation of Pauling’s 2nd rule.

Manceau, 2010, and Manceau, 2011, in his critical evaluation of the ‘ferrifh’ model suggested that ferrifh is similar to hydromaghemite. According to Manceau, 2011, the ferrifh model was derived from γ-Fe_2O_3, a compound whose XRD pattern can be fitted with a mixture of FHYD6, α-Fe_2O_3, FHYD2, and low tetrahedral γ-Fe_2O_3. Barrón *et al.*, 2012, also questioned the validity of the ferrifh model and contended that "ferrifh" and "hydromaghemite" could be two terms that designate the same phase, which has a strong FiM behavior and >3% water loss between 383 and 623 K.

Other shortcomings of the ferrifh model include the violation of Pauling's 3rd distortion rule (Pauling, 1929) and the presence of short Fe-Fe distances of close to 2.907 Å across the long shared edges (see Figure 2.8) (Manceau, 2011). According to Pauling's 3rd rule (Pauling, 1929) the anionic structure with shared edges is less stable than the one with corner sharing. This results from the drastic increase in Coulombic interaction between cations enhanced by the shorter cation distances in edge shared polyhedra (Manceau, 2010; Manceau, 2011).

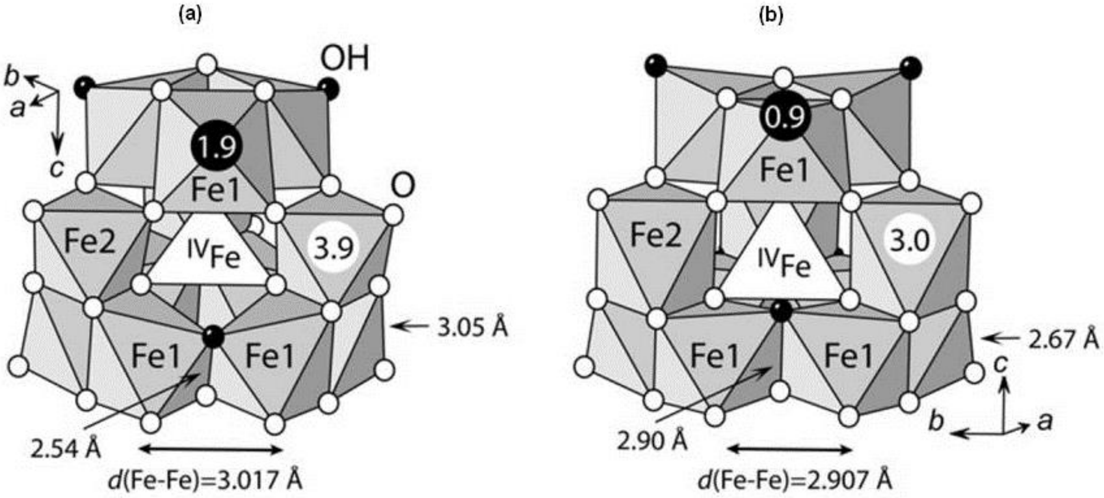

Figure 2.8: Comparison of the akdalaite and ferrifh models (a) akdalaite, (b) "ferrifh" (from Manceau, 2011).

The ferrifh model (Figure 2.8 (b)) consists of 75 % Fe octahedra (Fe1) which has shared edge lengths that are considerably longer than the unshared edge lengths, *d*(O1-O3 = 2.90 Å) and *d*(O2-O3 = 2.67 Å), respectively (Manceau, 2010; Manceau, 2011). Manceau's main argument was that this is a direct violation of the Pauling distortion rule (3rd rule) and as such the "ferrifh" model should not be considered correct. He further made a point that in a stable oxide the Coulombic repulsion between cations is shielded by O^{2-} by shortening the shared edges and lengthening the unshared edges. The example of α-FeOOH was used which showed long unshared edge lengths (2.90-3.02 Å) and short shared edge lengths (2.69-2.68 Å) (Manceau, 2010). There was no violation of the Pauling's 3rd rule in akadalaite model (Figure 2.8 (a)) since the shared edges have shorter lengths (2.54 Å) compared to the unshared edges (3.05 Å).

To summarize, there exists obvious disagreements between the two models used to describe the structure of FHYD. This calls for further experimental investigations to be carried on the topic, particularly to test for the presence or absence of tetrahedrally coordinated Fe^{3+}. Experimental results on the structure of FHYD2 and FHYD 6 are discussed in chapter 5.

2.4 Ferrihydrite surface structural models

2.4.1 Manceau model

As mentioned, FHYD, a typical nanocrystalline material, possesses a high surface-to-volume ratio, such surface effects play a crucial role in the chemistry of the material. For this reason, geometric models describing its surface structure have been extensively investigated. Based on bond-valence theory, Manceau and Gates, 1997, proposed a structure of the surface Fe octahedra in FHYD built-up from Drits model (in which Manceau is a co-author). Similar to the Drits model, the bulk Fe atoms in Manceau's surface structure model for FHYD are octahedrally coordinated to bridging oxo (O) and hydroxo (OH) ligands and the surface Fe atoms are also octahedrally coordinated but to H_2O ligands (Figure 2.9).

The structure of surface Fe sites in FHYD was built mainly on valence charge balance considerations (Manceau and Gates, 1997). In FHYD, Fe atoms can be coordinated to O, OH, and H_2O (Russell, 1979; Stanjek and Weidler, 1992; Zhao *et al.*, 1993). Zhao *et al.*, 1993, estimated that about 35% Fe atoms are located at the surface. Considering all three types of ligands that can be bonded to Fe atoms, the H_2O ligands can only be singly-coordinated to Fe and oxygen can be bonded to several Fe atoms when valence charge balance is taken into account (Manceau and Gates, 1997). Accordingly, H_2O ligands can only be coordinated to surface Fe atoms. As a result, bulk Fe atoms will be predominately coordinated to O and OH ligands and surface atoms coordinated to OH and H_2O groups (Manceau and Gates, 1997).

Surface $(OH)_I$ and $(H_2O)_I$ ligands are singly-coordinated to Fe and the external second shell water molecules $(H_2O)_{II}$ attach to these surface ligands by O_I-H$\cdots$$O_{II}$ bonds (H-bonds) (Manceau and Gates, 1997). The $(H_2O)_{II}$ molecules form strong and weak bonds with the surface $(H_2O)_I$ ligands (see Figure 2.9). A strong bond ($(H_2O)_{II}^{strong}$) is formed when a single $(H_2O)_{II}$ group interacts with a single O_I-H and the OI-H•••O_{II} H-bonds makes an angle of about 180 ° creating a trigonal orientation. In some other cases a single $(H_2O)_{II}$ can be simultaneously attached to two different surface O_I-H creating weak bond ($(H_2O)_{II}^{weak}$) bond that forms small O_I-H$\cdots$$O_{II}$ angle.

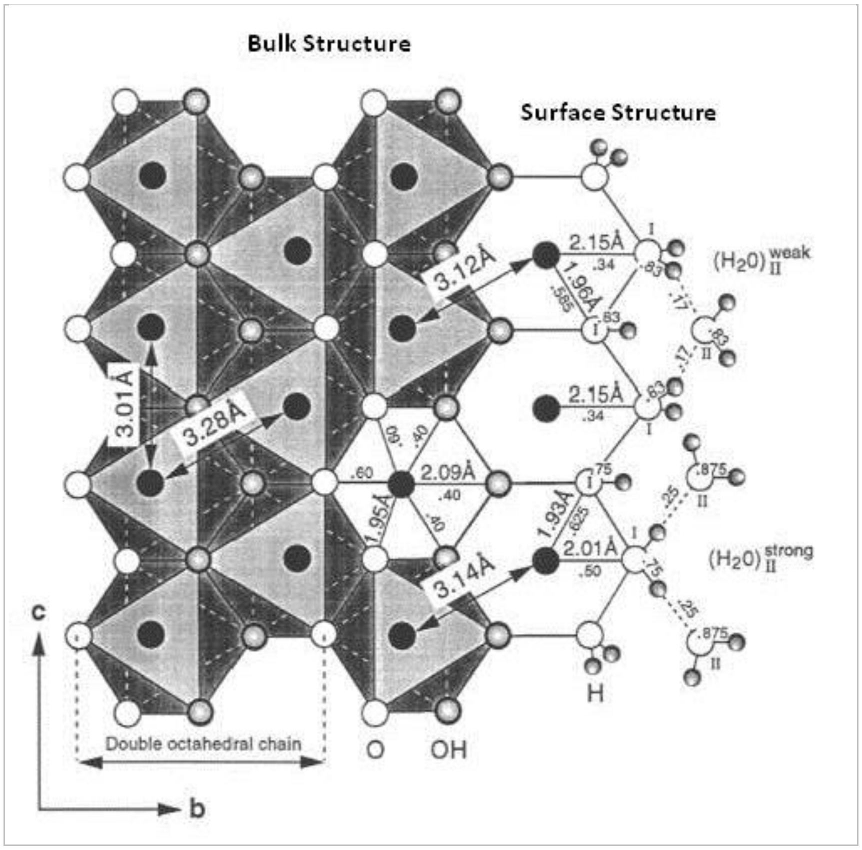

Figure 2.9: Surface structural model for FHYD after (Manceau and Gates, 1997).

This surface model for FHYD structure is supported by earlier work on the structural OH groups in FHYD (Russell, 1979). Using IR spectra Russell found that the amount of structural OH in FHYD was about half of the amount in akaganeite (β-FeOOH) and made a suggestion that the surface OH groups in FHYD were more easily accessible than the bulk OH groups. The surface structure proposed by Manceau and Gates, 1997, clearly shows how exposed the surface OH groups are and H-D exchange is expected to be more rapidly at the surface OH groups than the bulk OH groups as observed by Russell, 1979. It is obvious that the surface structure is predominately of OH groups, and this suggests that it is possible to largely dehydrate FHYD without collapsing its bulk structure. This has been experimentally observed by Stanjek and Weidler, 1992, who dehydrated FHYD without any transformation to crystalline phase. The authors derived a formula of $Fe_{1.75}O_{2.26}(OH)_{0.74}$ with a low OH/Fe ratio of 0.42. It has also been recently shown that FHYD can be dehydrated to a very low OH/Fe ratio of 0.2 without changing its core mineral structure (Xu *et al.*, 2011).

2.4.2 Hiemstra model

Another surface structural model for FHYD has been developed by Hiemstra and van Riemsdijk, 2009. Consistent with the Drits model, the FHYD bulk structure was described by the authors as having an average composition close to FeOOH, with a mass density of ~ 4.5 g/cm^3. The authors also formulated a multi-site surface complexation (MUSIC) model for FHYD and the model suggests that the reactivity of FHYD is dominated by single-coordinated surface groups. These single-coordinated surface groups may form the edges of exposed octahedral and provide the sites for the binding of foreign ions such as uranyl and arsenite through the formation of bidentate inner sphere complexes. The other single-coordinated surface groups, present at a single corner of the two adjacent Fe octahedra, may form the sites of double-corner bidentate complexes, which can adsorb other ions such as carbonate and phosphate (Hiemstra and van Riemsdijk, 2009).

2.4.3 Hiemstra surface depletion (SD) model

A recent paper on the structure of the controversial nanocrystalline FHYD has been published by Hiemstra, 2013. The observation by Xu *et al.*, 2011 that FHYD2 can be largely dehydrated to a composition of $Fe_{10}O_{14}(OH)_2$ (OH/Fe= 0.2) without collapsing its mineral structure was taken into account. The question that was raised is how a highly defective mineral core like FHYD can be dehydrated and still maintain its structure. This prompted Hiemstra, 2013, to revisit the surface and core structure of FHYD. The hypothesis was that the polyhedral coordination chemistry of the surface differs fundamentally from the core (Hiemstra, 2013). Supporting evidence of this hypothesis can be found in the work by Zhao *et al.*, 1993. Using both XANES and EXAFS pre-edge features it was observed that differences exist between bond length distances and coordination chemistry of iron sites closest to the surface and iron sites in the bulk of FHYD particles (Zhao *et al.*, 1993).

Hiemstra, 2013, developed a quantitative surface depletion (SD) model to describe the surface structure and composition of FHYD derived from the Michel model. Figure 2.10 shows a structure of surface depleted FHYD2 particle (d ≈ 2.5 nm). The structure is built by horizontal layers of Fe1 sites (yellow) and in between successive Fe1 sheets is a mixed layer of Fe2 (dark blue) and Fe3 (light blue). On building up the SD model it was first proposed that the Fe3 polyhedron was only stable in the mineral core and depleted from the surface due to the poor fitting of the Fe(III) in a tetrahedron. Furthermore, the lower stability for the Fe2 at the surface was suggested by Michel's PDF analysis (Michel *et al.*, 2007c) which showed a large depletion of Fe2 sites. As suggested by Hiemstra, 2013, less stability of the Fe2 sites maybe due to its strong asymmetry in its coordination sphere caused by the three short and three long Fe-O bonds in the Fe2 octahedra (see Figure 2.10). A bond length difference of ~ 0.24 Å and 0.36 Å has been reported in Fe2 sites for FHYD2 and FHYD6, respectively. The most stable Fe1 octahedra only have a small bond length difference of ≤ 0.08 Å between the long and short Fe-O bonds (Hiemstra, 2013).

The SD model was created by constructing a series of depleted particles of different sizes using the Crystal Maker program, with the highly depleted Fe2 and Fe3 sites eliminated at the surfaces for reasons discussed above. Consequently, the SD model was built with only the Fe1 polyhedra having single-coordinated surface groups. Previous work (Poulson *et al.*, 2005) have shown that the Fe isotope exchange between hexaquo Fe (III) and a 3 nm FHYD is limited by number of available surface Fe sites in FHYD. A maximum isotopic Fe exchange of 26±5 % was obtained between a 3nm FHYD and hexaquo Fe (III) within a period of 11 days and remained constant over a ~3 months period. This observation suggests that only about 26±5 % Fe sites are available in a ~ 3nm FHYD particle. From the SD model with only Fe1 sites having singly-coordinated surface groups, a total of 25 % labile Fe were calculated for a ~3 nm particle. This good agreement between experimental results and calculated labile Fe validates the SD model.

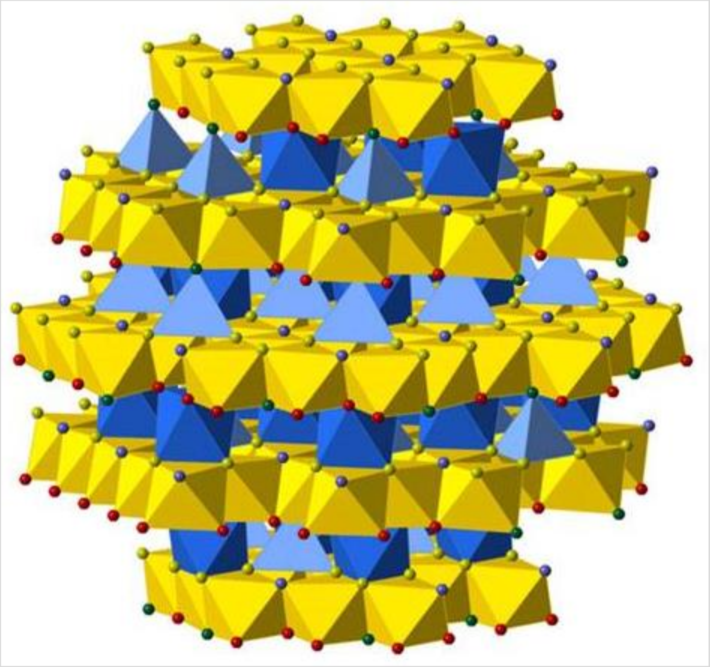

Figure 2.10: Structure of surface-depleted FHYD2 particle (Hiemstra, 2013).

2.5 Experimental observations

2.5.1 X-ray diffraction

As alluded to earlier, ferrihydrite is a poorly ordered hydrous ferric oxide with a characteristic of XRD patterns of two to six broad lines, hence the "n-line FHYD" standard terminology was adopted to describe the different types of the mineral e.g. 2-line FHYD, with n being the number of XRD lines (Jambor and Dutrizac, 1998). The well crystallized FHYD6 shows six diffuse lines with corresponding d-spacings of 0.15 (doublet), 0.17, 0.20, 0.22-0.23, and 0.25 nm (Janney *et al.*, 2000b; Janney *et al.*, 2001), and its XRD pattern can be indexed with a hexagonal unit cell with $a = 0.508\,nm$ and $c = 0.94\,nm$ (Drits *et al.*, 1993; Jambor and Dutrizac, 1998). The sixth line on the FHYD6 XRD pattern can only be realized by treating the barely resolved doublet at about ~ 0.15 nm as separate peaks (Janney *et al.*, 2001). The less crystalline FHYD2 shows only two broad peaks at 0.15 and 0.25-0.26 nm (Janney *et al.*, 2000a; Janney *et al.*, 2000b).

2.5.2 Electron microscopy techniques

Transmission electron microscopy work on FHYD has been previously reported e.g. (Eggleton and Fitzpatrick, 1988; Zhao *et al.*, 1994a; Janney *et al.*, 2000a; Janney *et al.*, 2000b; Janney *et al.*, 2001; Pan *et al.*, 2006; Pan *et al.*, 2010). Eggleton and Fitzpatrick, 1988, reported crystallite sizes in the range ~2-6 nm for FHYD6 and ~2-3 nm for FHYD2. The *d*-spacings obtained from selected area electron diffraction (SAED) were found to be in good agreement with the *d*-spacings calculated from XRD. A more comprehensive work on the structure of FHYD using HR-TEM and nanodifraction pattern has been carried out by Janney group (Janney *et al.*, 2000a; Janney *et al.*, 2000b; Janney *et al.*, 2001). Their single crystal nanodiffraction work confirms all three components suggested by the multiphase Drits model. The feroxyhite-like structure was however described as “double chain structure” by Janney *et al.*, 2000a but in principle the two structural components are the same (Manceau, 2009).

One of the interesting questions that can be investigated using TEM related techniques such as electron energy loss spectroscopy (EELS) is the presence or absence of tetrahedral coordinated Fe^{3+} in the structure of FHYD. The first few FHYD EELS results on the Fe^{3+} coordination environment using reference compounds were reported (Pan *et al.*, 2006; Pan, 2007; Pan *et al.*, 2009; Pan *et al.*, 2010). The authors used EELS to evaluate the effects of electron beam induced damage in FHYD; they observed the migration of Fe^{3+} from octahedral to tetrahedral sites and the reduction of ferric iron to ferrous iron. Using nonlinear least squares (NLLS) fitting methods, Pan *et al.*, 2006; Pan, 2007; Pan *et al.*, 2009; Pan *et al.*, 2010, incorporated standard reference materials to model the Fe $L_{2,3}$ edge of FHYD and estimate the percentage of Fe^{3+} in octahedral and tetrahedral coordination. From linear extrapolation estimate to very low electron dose down to 1 electron/nm^2, the authors suggested that all the Fe^{3+} iron in pristine FHYD occupy octahedral sites. It was stated that the exact intrinsic structure of the nanocrystalline FHYD still remains unclear since their extrapolation extended to very low electron dose (1 electron/nm^2) that is not practically possible to achieve (Pan *et al.*, 2010). In fact, fitting the spectrum recorded at the lowest possible dose achieved by the authors (3×10^4

electron/nm^2), without extrapolation, yielded a significant amount (25 ±5 %) of iron in tetrahedral coordination (Pan *et al.*, 2010).

2.5.3 Neutron diffraction

The structure of synthetic FHYD has been previously investigated by few independent neutron diffraction studies (Seehra *et al.*, 2000; Jansen *et al.*, 2002; Harrington *et al.*, 2011). Jansen *et al.*, 2002, examined the structure of non-deuterated FHYD6 to determine only the oxygen and iron frameworks. The comparatively small contribution of hydrogen to the coherently scattered Bragg diffraction peaks (due to the large incoherent scattering length of hydrogen) makes it impossible to determine specific hydrogen arrangements in non-deuterated samples for neutron scattering. Rietveld refinement analysis of neutron data described the structure of FHYD as a mixture of two phases i.e. defect-free and defective phases as proposed on the Drits model (section 2.3.1). However, the ultradispersed nano hematite phase was not detected in this work (Jansen *et al.*, 2002). The *d*-phase with the trigonal space group $P\bar{3}1$c has a double hexagonal ABACA stacking, while the *f*-phase has alternating ABA and ACA stacking with the space group *P*3 (Figure 2.11).

A temperature dependent peak at $2\theta \cong 14^{\circ}$ indexed as (002) according to the hexagonal structure was observed in the temperature-dependent neutron data (see Fig. 1in Jansen *et al.*, 2002). The (002) peak was determined to be of magnetic nature, it contributed to the coherent magnetic scattering superimposed in the Bragg diffraction pattern. The magnetic structure of FHYD revealed an ordered AFM state below Néel temperature $T_N = 300 \pm 20$ K as extrapolated from the magnetic peak (002).

Seehra *et al.*, 2000, carried out neutron scattering and magnetic properties study of deuterated FHYD2 (FeOOD.nD$_2$O) nano-sized particles. In agreement with Jansen *et al.*, 2002, an AFM ordering for FeOOD particles below $T_N = 350$ K was observed (Seehra *et al.*, 2000). Comparisons of neutron and XRD diffraction data showed that there was an extra peak in the neutron data at $Q = 1.3\ \text{Å}^{-1}$, where Q is the momentum transfer function $Q = \frac{4\pi \sin\theta}{\lambda}$. Similarly to Jansen *et al.*, 2002, the peak was determined to be predominately of magnetic nature and was indexed as (002) reflection. A temperature variation investigation of the peak from 10-450 K showed a temperature dependence of the intensity of the peak. A decrease in intensity of the peak with increasing temperature was observed up to $T \cong 350$ K above which it became temperature independent. The magnetic transition from an AFM to a paramagnetic (PM) state of the core FHYD2 was estimated to $T_N = 350$ K .

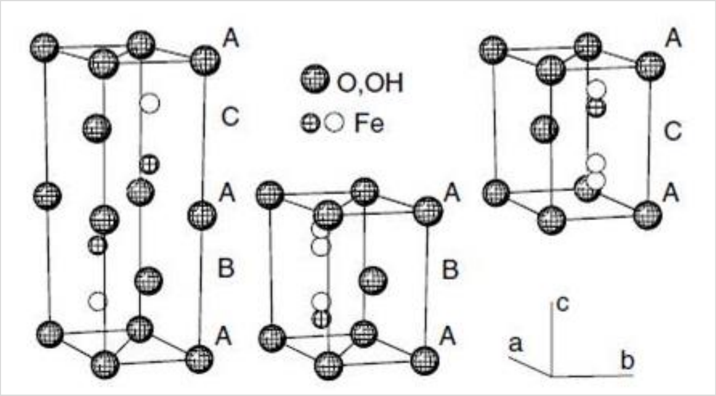

Figure 2.11: The structure of FHYD from Rietveld analysis of neutron data (from Jansen *et al.*, 2002).

Neutron scattering study was also performed by Harrington *et al.*, 2011, on deuterated FHYD2 and its structure was examined using pair distribution function (PDF). The advantage of using PDF analysis is that it is the Fourier transform of the total scattering (Bragg + diffuse) diffraction pattern. A first attempt to fit the PDF data was performed using the Drits model (section 2.3.1) and each of the three phases was refined separately. The abundant *f*-phase when fitted returned an R_w vaue of 50 %. The ultra-dispersed hematite showed a very poor fit to the experimental PDF returning an R_w value of 79 %. All three phases with a constrained ratio of 6:3:1 (*f*-phase: *d*-phase: hematite) as proposed by Drits were simultaneously refined against the experimental PDF data. Surprisingly, the refinement yielded a poor fit (R_w =55 %) worse than the *f*-phase alone. The model proposed by Michel (see section 2.3.2) was also tested against the neutron PDF experimental data. Good agreement was found between the experimental and calculated PDF. The authors concluded that this good agreement indicates that the Michel's model is in large part correct and it can be used as a starting point for any further experimental and theoretical studies (Harrington *et al.*, 2011).

2.5.4 EXAFS/XANES

Eggleton and Fitzpatrick, 1988, used X-ray absorption spectra to investigate the coordination environment of Fe^{3+} in FHYD and proposed that FHYD structure should contain 35% T_d $Fe^{3+}$and 65% O_h Fe^{3+}. From their XAS study they found a $^{IV}Fe^{3+}/^{VI}$ Fe^{3+}ratio similar to that of γ-Fe_2O_3. However, the presence of T_d Fe^{3+} in FHYD was ruled out by subsequent XANES study (Manceau *et al.*, 1990). As pointed out by Manceau *et al.*, 1990, the poor quality of the spectra presented by Eggleton and Fitzpatrick, 1988, should not allow conclusive findings. The low resolution (25 eV half-width) could not permit the resolution of spectral features of ca. 2 eV width. Synchrotron based K-edge XANES spectroscopy revealed that both the structure and intensities of normalized pre-edge FHYD spectra was close to that of α-FeOOH (O_h Fe^{3+}) and different from γ-Fe_2O_3 (T_d $Fe^{3+}$and O_h Fe^{3+}) (Manceau *et al.*, 1990), ruling out the presence of T_d Fe^{3+} in FHYD structure. The presence of T_d Fe^{3+} was also ruled out by Manceau and Drits, 1993, using EXAFS spectroscopy data.

A study of the coordination environment of Fe^{3+} in FHYD carried out using XAFS pre-edge features revealed the presence of 20-30 % tetrahedral sites (Zhao *et al.*, 1994a). Based on shape and intensity of the K-edge pre-edge resulting from the 1s→3d formally forbidden dipole transitions ($\Delta l \neq 1$), the authors observed that the pre-edge features (see Fig. 4 in Zhao *et al.*, 1994a) of FHYD resemble that of Fe_3O_4 and are clearly distinct from that of α-FeOOH. The pre-edge features of α-FeOOH were clearly resolved showing two peaks due to crystal field effect while pre-edge features of FHYD showed a single broad peak similar to magnetite (Zhao *et al.*, 1994a). The single peak pre-edge features of FHYD were fitted with two peaks, the percentage of Fe^{3+} in T_d coordination was estimated from the peaks areas (Zhao *et al.*, 1994a).

It is known that the crystal field effect in ligands coordination causes a lifting of the degeneracy of the *d*-orbitals in transition metals (Douglas *et al.*, 1994). The *d*-orbital splits into low energy t_{2g} and high energy e_g orbitals in octahedral crystals and split into t_2 and e levels in tetrahedral crystals (Douglas *et al.*, 1994). The crystal field effect dictates that the Fe_3O_4 (33 % tetrahedral iron and 67 % octahedral iron) pre-edge should have four peaks corresponding to the splitting of the t_{2g} and e_g levels of the octahedral Fe^{3+} and t_2 and e levels of the tetrahedral Fe^{3+}. Instead, a single broad peak was observed (Zhao *et al.*, 1994a). The limited energy resolution at the Fe K-edge (~ 1 eV) was pointed out as the reason for the observed single broad peak in Fe_3O_4. The e and t_2 levels are very close in energy and they appear as a single peak (Zhao *et al.*, 1994a). The XAFS pre-edge data contradicted previous XANES results by the same author (Zhao *et al.*, 1993). The XANES spectra of FHYD were found to be similar to those of octahedrally coordinated Fe^{3+} e.g. α-FeOOH. It was suggested that tetrahedral coordination in FHYD is predominately at the FHYD surface (Zhao *et al.*, 1994a). This interpretation was however challenged by Manceau and Gates, 1997, according to whom the changes in the pre-edge peak intensities were due to distortions of the surface Fe octahedra as a result of dehydration.

As mentioned, the presence of T_d Fe^{3+} in Michel's model has been disputed by Manceau, 2011 arguing that the results by Michel were over fit and that the Drits model could account for EXAFS results without including T_d Fe^{3+}. Carta *et al.*, 2009, using the same technique (EXAFS) estimated a 4 % presence of tetrahedral coordination in FHYD structure. Most recent study (Maillot *et al.*, 2011) using high quality EXAFS data recorded at cryogenic temperatures revealed the presence of T_d Fe^{3+} in FHYD in support of Michel's model. Based on analysis of mean Fe-O distances in the first coordination shell of iron using the Landweber iteration method, the authors obtained a mean Fe-O of (1.97±0.01 Å) for FHYD. This value was found to be close to that of γ-Fe_2O_3 (1.96±0.01 Å) but significantly shorter than those of octahedrally coordinated Fe^{3+} model compounds i.e. α-Fe_2O_3 (2.01±0.01 Å), α-FeOOH (2.01±0.01 Å) and akaganeite (γ-FeOOH) (2.00±0.01 Å). The short Fe-O distance in FHYD compared to the other model compounds with only O_h Fe^{3+} lead to the conclusion that there is a significant amount of tetrahedrally coordinated Fe^{3+} in FHYD ranging between 20±5 % to 30±5 %. A combined fitting of EXAFS and XANES Fe K-edge study of FHYD also yielded a tetrahedral Fe^{3+}content of about 15±5 % (Mikkuta, 2011).

In another study, Peak and Reiger, 2012a, using X-ray absorption spectroscopy Fe $L_{2,3}$-edge instead of the extensively used K-edge, also revealed a substantial amount of T_d Fe^{3+} in

FHYD. Unlike the main K-edge which shows 1s→np transitions, the $L_{2,3}$ exhibit structural features resulting from the 2p → 3d transitions. It was concluded that FHYD contains a substantial amount (30-40 %) tetrahedral coordinated Fe^{3+}.

Another recent study on the Fe^{3+} coordination environment by Guyodo *et al.*, 2012, using synchrotron X-ray magnetic circular dichroïsm (XMCD) suggested the presence of 20-30% T_d Fe^{3+} in the structure of FHYD, which favors Michel's model. XMCD spectra were derived from the difference of two X-ray absorption spectra (XAS) acquired with both left and right circularly polarized X-rays in the presence of a magnetic field. Due to its high sensitivity to site occupancy XMCD has found renew interest in coordination chemistry. Guyodo *et al.*, 2012, measured the XAS for XMCD at the Fe K and $L_{2,3}$ -edges for FHYD6 using γ-Fe_2O_3 as a reference standard. They observed that at the K-edge, the XMCD spectra of the FHYD6 were similar to that of γ-Fe_2O_3 reported in previous studies (Carvallo *et al.*, 2010; Sikora *et al.*, 2010), which originate mainly from T_d Fe^{3+} sites with very little effects from octahedral Fe^{3+}. The similarities of the Fe L_3 edge of the FHYD6 and γ-Fe_2O_3 was taken as evidence for the presence of tetrahedral coordinated Fe^{3+} (Guyodo *et al.*, 2012). Multiplet theoretical calculations (Brice-Profeta *et al.*, 2005) indicated that the positive peak is due to T_d Fe^{3+} and the two peaks originate from O_h Fe^{3+}. Guyodo *et al.*, 2012, applied the Ligand Field Multiplet model (Thole *et al.*, 1985) to calculate the percentage of tetrahedral and octahedral contributions in the XMCD spectra for FHYD6 and γ-Fe_2O_3. They obtained 37.5 ± 3 % of tetrahedral Fe^{3+} for γ-Fe_2O_3 and up to 28 ± 3 % T_d Fe^{3+} for FHYD6. This result is consistent with earlier observations (Eggleton and Fitzpatrick, 1988; Maillot *et al.*, 2011; Peak and Reiger, 2012a).

2.5.5 Mössbauer spectroscopy

The presence and/or absence of tetrahedrally coordinated Fe^{3+} in the bulk and at the surface of FHYD has also been extensively studied by Mössbauer spectroscopy (MS) (Murad and Schwertmann, 1980; Murad, 1988; Cardile, 1988a; Pankhurst and Pollard, 1992; Pollard *et al.*, 1992; Zhao *et al.*, 1994a; Murad, 1996). At room temperature the MS spectra of FHYD usually show broad paramagnetic doublets while the MS spectra recorded at 4.2 K usually consist of magnetically resolved sextets (Murad and Schwertmann, 1980; Murad, 1996; Jambor and Dutrizac, 1998). The doublet is a result of the presence of SPM crystallites causing fast relaxation of the spins (MØrup, 1983; Murad, 1996). At Low temperature, below blocking temperature (T_B), the detrimental effects of the thermal energy are offset and the magnetic nature of materials fully revealed.

Low temperatures MS spectra of FHYD have been previously fitted with a number of sextets (Murad and Schwertmann, 1980). The authors emphasized that results from such fitting should not be taken as a proof that Fe^{3+} is necessary present in a number of discrete sites, rather, it could indicate a distribution of magnetic hyperfine field (B_{hf}) which results from the different types and arrangement of neighbouring ions (i.e. O, OH, H_2O) for the interior and surface Fe^{3+} ions. Zhao *et al.*, 1994a, pointed out that the nucleus of the surface iron ion normally has smaller B_{hf} compared to the interior iron ions. For this reason, MS spectra of FHYD are often fitted with distributions of the hyperfine parameters, i.e. the room temperature spectra with distributions of the quadrupole splitting (ΔE_Q) and the low temperatures (below T_B) with distributions of B_{hf}.

Murad, 1988, ascribed the two distributions of B_{hf} of the MS spectra recorded at 4.2 K to both O_h Fe^{3+} and T_d Fe^{3+} in FHYD structure. According to this author, part of the asymmetry of the room temperature MS spectra was a result of tetrahedral coordination. However, subsequent work by Bigham *et al.*, 1994, identified the same material as a new iron(III) oxyhydroxysulfate rather than the "well-crystallized FHYD". Cardile, 1988a, attempts to fit the room temperature MS spectra of FHYD with a number of doublets failed to yield conclusive results about T_d Fe^{3+} in FHYD. Two different models were used, the first model consisted of three doublets in octahedral sites and second model consisted of one doublet in tetrahedral site and two doublets in octahedral sites. Surprisingly, both models yielded similar results hence it was concluded that Mössbauer spectroscopy cannot differentiate between T_d Fe^{3+} and O_h Fe^{3+}, nor can it demonstrate conclusively that T_d Fe^{3+} is present in FHYD (Cardile, 1988a).

A uniaxial anisotropy mean field model which incorporates both AFM and FiM into simple two-sublattice formalism was used to fit the MS spectra recorded at 4.2 K in applied magnetic fields of 0, 3, 6, and 9 T (Pankhurst and Pollard, 1992). The MS spectra of both FHYD2 and FHYD6 displayed very symmetric absorption lines. It was observed that as the applied field was increased the MS spectra of FHYD2 split into two sextets while the MS spectra of FHYD6 became rather broad with no splitting (Pankhurst and Pollard, 1992). The FHYD2 and FHYD6 spectra were therefore fitted with two sextets and one sextet, respectively. For the FHYD2, the two sextets had the same isomer shift (δ = 0.48 (2) mm/s) but slightly different quadrupole splitting (ΔE_Q = 0.04(4) and -0.01(4) mm/s). The average magnetic hyperfine fields amounted to B_{hf} = 49.7 (1) and 48.4(1) T, respectively. As the two ΔE_Q values are equal within experimental uncertainties, it was concluded that they represent one type of crystallographic Fe environment (Pankhurst and Pollard, 1992). The sextet of FHYD6 had hyperfine parameters δ = 0.48 (2) mm/s, ΔE_Q = 0.11(4) mm/s, and B_{hf} = 49.0(1) T. Pankhurst and Pollard, 1992, argued that if T_d Fe^{3+} was present it should give δ and ΔE_Q values that were different from that of O_h Fe^{3+} rather than similar values. The fact that there was no asymmetry in the zero-field and applied magnetic field MS spectra were taken as further proof that there was no T_d Fe^{3+} contribution in the structure of FHYD. For FHYD6 the spectra were fitted with an AFM model while a better fit for FHYD2 was achieved by using a FiM model. On the basis of these results, the authors concluded that the FHYD2 and FHYD6 differ in their magnetic structures.

The above interpretation of the Mössbauer spectra by Pankhurst and Pollard, 1992, was disputed by Zhao *et al.*, 1994a., particularly the claim that the MS spectra of FHYD6 did not split as the magnetic field was applied. Zhao *et al.*, 1994a, noted that in applied magnetic field the spectra of FHYD6 did split albeit with rather poor resolution as compared to that of FHYD2. The use of symmetry of the spectra to prove the absence of 4-fold coordinated Fe^{3+} by Pankhurst and Pollard, 1992, was also questioned. It was noted that the MS spectra of bulk Fe_3O_4 and γ-Fe_2O_3 exhibit asymmetric absorption lines in zero-field and these lines becomes more asymmetric when an external magnetic field is applied (Zhao *et al.*, 1994a). This is so because the δ and ΔE_Q values of T_d Fe^{3+} are significantly different from that of O_h Fe^{3+}. Zhao *et al.*, 1994a contended that symmetry observed by Pankhurst and Pollard, 1992, on the spectra of FHYD2 and FHYD6 was due to small particle size effect as observed for Fe_3O_4 and γ-Fe_2O_3 fine particles. Zhao *et al.*, 1994a, concluded that the presence of T_d coordination in FHYD could not be ruled out if small particle size effect is taken into account.

2.5.6 Thermogravimetric –Differential Thermal Analysis (TG-DTA)

Another major discrepancy between Drits and Michel models lies in the amount of structural water present in the FHYD structure. It is generally accepted that the DTA curves of pure synthetic FHYD give a low-temperature endotherm attributed to the expulsion of surface adsorbed water and a moderately strong exothermic event at 573-673 K marking the conversion to hematite after removal of structural OH/H_2O (Towe and Bradley, 1967).

Figure 2.12 shows the DTA curves of pure FHYD2 and FHYD6 reported by Eggleton and Fitzpatrick, 1988 which features two well-defined exothermic peaks. The first exotherm at 623 K was interpreted by these authors as the growth of an intermediate FiM γ-Fe_2O_3 phase as evident from their XRD pattern, and the second exotherm around 755 K marked the conversion of the γ-Fe_2O_3 to α-Fe_2O_3. However, no intermediate cubic phase was reported during FHYD transformation to α-Fe_2O_3 in DTA experiments by Campbell *et al.*, 1997, even when two exothermic peaks were present. The formation of the cubic (Fe_3O_4/γ-Fe_2O_3) intermediate phase was only observed during heating in the presence of organics.

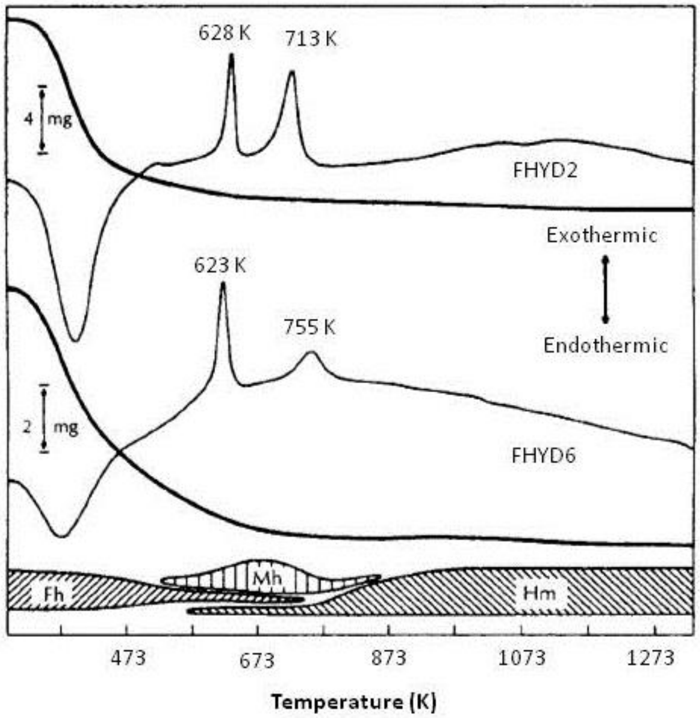

Figure 2.12: DTA curves and TG curves of synthetic FHYD2 and FHYD6 (after Eggleton and Fitzpatrick, 1988).

A study of structural water in FHYD by Xu *et al.*, 2011, using TG-DSC also suggested a one-step transformation process (FHYD→ α-Fe_2O_3). FHYD2 transformed to α-Fe_2O_3 at 688 K without the formation of a cubic intermediate phase as confirmed by their *in situ* temperature resolved XRD and PDF data. This findings by Xu *et al.*, 2011, also indicated that FHYD contains very little structural OH with an estimated OH/Fe molar ratio of as low as 0.18 ± 0.01. This result supports Michel's akdalaite structural model (Michel *et al.*, 2007c) for FHYD that has an OH/Fe ratio of 0.2 as opposed to an average OH/Fe ratio of 1.0 obtained for Drits model. However, the claim that FHYD contains very little structural water was disputed by Manceau, 2011, stating that there is no mineral at the surface of the earth that is hydrated but contains as little structural hydroxyl and water.

2.6 Reduction of iron oxides under hydrogen

2.6.1 TPR experiments

This section reviews the reduction mechanisms of iron oxides under hydrogen atmosphere as described in the literature. The reduction of a metal (M) oxide under hydrogen atmosphere can be summarized according to the following reaction (Bowa Chansongo, 2009)

$$\mathrm{M_xO_y + yH_2 \rightarrow yH_2O + M_x} \qquad 2.1$$

The transformation of iron oxides under reducing atmospheres is one of the most studied topics due to their industrial interests. Extensive work on reduction of iron oxides has been performed mainly on both supported and unsupported α-Fe_2O_3 catalysts using temperature programmed reduction (TPR) technique (Sastri *et al.*, 1982; Bukur *et al.*, 1995a; Bukur *et al.*, 1995b; Bukur *et al.*, 1995c; Manteanu *et al.*, 1997; Manteanu *et al.*, 1999; Jin and Datye, 2000; Lin *et al.*, 2003; Manteanu *et al.*, 2003; Venugopal *et al.*, 2003; Venugopal and Scurrell, 2004; Jozwiak *et al.*, 2007; Pourghahramani and Forssberg, 2007; Messi *et al.*, 2008; Williams and Carter, 2009; Zieliński *et al.*, 2010). However, despite considerable attention given to the reduction mechanism of α-Fe_2O_3 there is still differing opinions about the reaction pathways. Sastri *et al.*, 1982 studied the reducibility of pure α-Fe_2O_3 doped with foreign metal oxides. They have found that the reduction of pure α-Fe_2O_3 to metallic iron (α-Fe) proceeds by a consecutive two-step reduction mechanism via Fe_3O_4 according to Eqs.2.2-2.3.

$$3Fe_2O_3 + H_2 \rightarrow 2Fe_3O_4 + H_2O \tag{2.2}$$

$$Fe_3O_4 + 4H_2 \rightarrow 3Fe + 4H_2O \tag{2.3}$$

TPR studies on small size α-Fe_2O_3 particles (Wimmers *et al.*, 1986) were also consistent with the two-step reduction mechanism. Their TPR profiles consisted of two reduction peaks that were assigned to the reduction of α-Fe_2O_3 to Fe via Fe_3O_4. The two-step reduction mechanism of α-Fe_2O_3 was further supported by others studies (Manteanu *et al.*, 1997; Manteanu *et al.*, 1999; Manteanu *et al.*, 2003).

However, the reduction of α-Fe_2O_3 appears to be more complicated than the simple two-step reduction pathway. Independent work by different groups (Pinna, 1998; Venugopal *et al.*, 2003; Venugopal and Scurrell, 2004; Jozwiak *et al.*, 2007) suggested a three-step reduction mechanism (Eqs. 2.4-2.6) according to the Bell's diagram (Figure 2.13).

$$3Fe_2O_3 + H_2 \rightarrow 2Fe_3O_4 + H_2O \tag{2.4}$$

$$Fe_3O_4 + H_2 \rightarrow 3FeO + H_2O \tag{2.5}$$

$$FeO + H_2 \rightarrow Fe + H_2O \tag{2.6}$$

It is widely accepted that in the Fe-H-O system the FeO phase only appears at temperatures above 570 ˚C because it is thermodynamically unstable below this temperature. However, it is also possible to form FeO as an intermediate even at temperatures below 570 ˚C in the course of α-Fe_2O_3 reduction under irreversible thermodynamics conditions as shown by Bell's diagram in Figure 2.13 (Pineau *et al.*, 2006).

A most recent paper (Zieliński *et al.*, 2010) on the reduction of α-Fe_2O_3 under hydrogen focused on the influence of experimental parameters on the TPR profiles. By considering all the experimental parameters (heating rate, hydrogen concentration, and sample mass) that affects the TPR profiles, the authors observed a crucial thermodynamics parameter (equilibrium constant $k = \frac{X_{H_2O}}{X_{H_2}}$) of the reaction that is affected by these experimental parameters. The three-step reduction mechanism was thermodynamically possible at X_{H_2O}/X_{H_2}ratio over 0.35 (see Figure 2.14) and the reaction proceeds in two-steps at X_{H_2O}/X_{H_2}ratio less below 0.35.

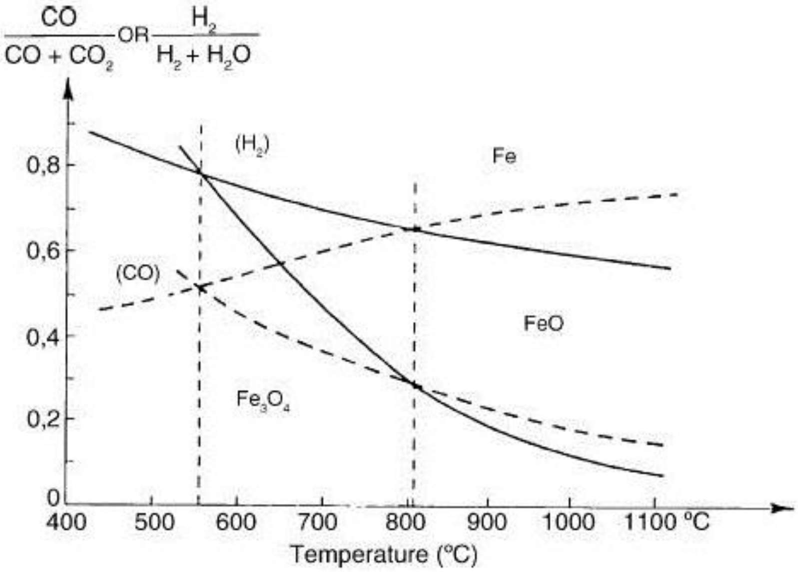

Figure 2.13: Bell's diagram for the Fe-C-O and Fe-H-O system at 1 atm (from Pineau *et al.*, 2006).

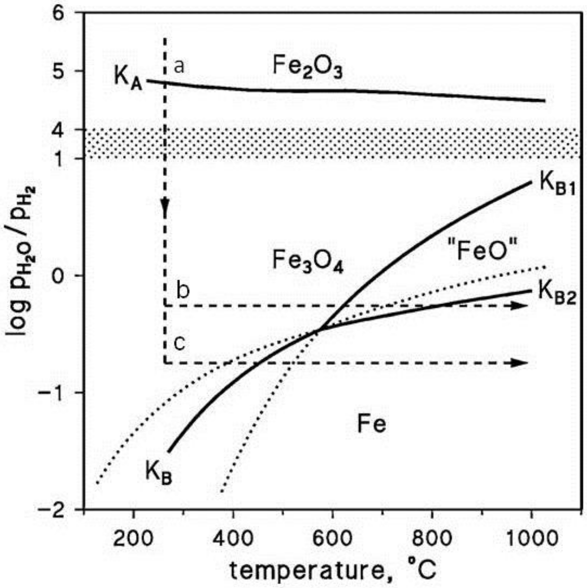

Figure 2.14: Iron-iron oxide phase diagram in H_2O/H_2 atmosphere (Zieliński *et al.*, 2010).

Their results also revealed that a one-step (α-Fe_2O_3 → α-Fe) reduction process is possible at extremely low X_{H_2O}/X_{H_2} ratio. The calculated equilibrium constants (K_A, K_B, K_{B1} and K_{B2}) in Figure 2.14 allows to predict the reduction route of α-Fe_2O_3 in TPR. These constants represent the following reactions (Zieliński *et al.*, 2010):

$$K_A = \frac{X_{H_2O}}{X_{H_2}}; \mathrm{Fe_2O_3} \rightarrow \mathrm{Fe_3O_4} \tag{2.7}$$

$$K_B = \frac{X_{H_2O}}{X_{H_2}}; \mathrm{Fe_3O_4} \rightarrow \mathrm{Fe} \tag{2.8}$$

$$K_{B1} = \frac{X_{H_2O}}{X_{H_2}}; \mathrm{Fe_3O_4} \rightarrow \mathrm{FeO} \tag{2.9}$$

$$K_{B2} = \frac{X_{H_2O}}{X_{H_2}}; \mathrm{FeO} \rightarrow \mathrm{Fe} \tag{2.10}$$

It can be seen from Figure 2.14 that the α-Fe_2O_3 → Fe_3O_4 reduction (marked by the line 'a') is thermodynamically possible even at high X_{H_2O}/X_{H_2}ratio, while the reduction Fe_3O_4 → α-Fe (marked 'c') can only occur at sufficiently low X_{H_2O}/X_{H_2} ratio, below 0.35. At X_{H_2O}/X_{H_2}ratio above 0.35 two-step reduction (Fe_3O_4 → FeO → α-Fe) is suggested (reaction marked 'b').

From the results presented above, it is obvious that the pathway of the reduction of Fe(III) oxides (e.g. hematite) depends on the TPR conditions. The obvious difference between the proposed two-step (α-Fe_2O_3 → Fe_3O_4 → α-Fe) and three-step (α-Fe_2O_3 → Fe_3O_4 → FeO → α-Fe) reactions is the presence or absence of the wüstite phase in the two mechanisms. Temperatures above 570 ˚C strongly favour the three-step mechanism since wüstite is stable at these temperatures, while the two-step mechanism is common below 570 ˚C. However, there are other experimentally factors such as the equilibrium constant ($K = X_{H_2O}/X_{H_2}$) that determines the reduction pathway of iron oxides.

2.6.2 X-ray diffraction studies

The use of X-ray diffraction methods in the study of reduction/activation of iron oxides are demonstrated by many examples. Shroff *et al.*, 1995 used XRD to identify iron oxides phases formed after reducing α-Fe_2O_3 catalyst in H_2 and after CO and syngas activation. Jozwiak *et al.*, 2007 reported the reduction behaviour of iron oxides using a combination of H_2-TPR and *in situ* XRD. However, none of these studies explicitly used the *in situ* XRD method to investigate the reduction mechanism of FHYDs nanoparticles. We present here a complete set of *in situ* XRD data obtained during thermally-induced reduction of FHYDs samples in hydrogen.

2.6.3 Mössbauer spectroscopy studies

MS has played a vital role in the characterization of iron based FTS process (Bibicu and Frunza, 2006). MS, a technique which is based on the recoilless emission and resonant absorption of nuclear γ-ray is interpreted using the three parameters (isomer shift, quadrupole splitting, and magnetic hyperfine splitting) originating from the interaction of the nucleus with its environment (see Chapter 3 for details). The MS hyperfine interaction parameters are generally specific for each iron phase (Goldanskii and Herber, 1968; Long, 1984; Bødker *et al.*, 1992; Long and Grandjean, 1993; Maddock, 1997). As a result, the technique is useful in identifying different iron species in catalyst after activation with high accuracy. In some other cases, X-ray diffraction methods fails to distinguish between two iron compounds with similar XRD features and a common example is the inverse spinel types Fe_3O_4 and γ-Fe_2O_3. The capabilities of MS to distinguish the different iron oxides can be used to overcome this XRD shortfall because MS gives unique hyperfine parameters for each iron phase. Lyubutin *et al.*, 2009 used MS to prove that Fe_3O_4 was the type of spinel present in their reduction experiments.

MS studies on the reduction, activation, and carburization behaviour of iron oxides based FTS and water-gas-shift (WGS) catalysts are well documented in literature e.g. Niemantsverdriet and Delgas, 1999 described the successes of *in situ* MS in catalysis. Bødker *et al.*, 1992 reported the study of carbon-supported iron catalysts using *in situ* MS at cryogenic temperatures and they have demonstrated that application of external magnetic fields improves the resolution of the MS spectra, and hence the information obtained. Pérez-Alonso *et al.*, 2008 successfully employed MS to study cerium containing iron catalysts for FT synthesis. They found that presence of cerium oxide in their samples stabilized the metastable FeO phase and lowered the reduction rate of the catalyst. Gavaría *et al.*, 2007 successfully demonstrated the capabilities of MS to monitor the reduction behaviour of α-Fe_2O_3 to Fe_3O_4 and it was easily observed that the six lines spectrum of α-Fe_2O_3 evolved with time to two distinct six-lines sub-spectra typical of Fe_3O_4 corresponding to *A*-sites (Fe^{3+}) and *B*-sites (Fe^{2+},Fe^{3+}) of the spinel structure. MS methods have been previously used in the investigation of the preparation of nanocrystalline iron by reducing synthetic and natural FHYD2 nanoparticles in H_2 (Schneeweiss *et al.*, 2008; Schneeweiss *et al.*, 2010; Schneeweiss *et al.*, 2011).

Chapter 3

Experimental techniques

3.1 Introduction

This chapter presents the theoretical aspects of the techniques used in this study. It is structured as follows. Theoretical and instrumental aspects of transmission electron microscopy are introduced in section 3.2 followed by electron energy loss spectroscopy in section 3.3. Section 3.4 review the basics of Mössbauer spectroscopy and section 3.5 the basics of magnetism and magnetic measurements. A brief introduction to the principles of X-ray diffraction is given in section 3.6 followed by a brief overview of Raman spectroscopy in section 3.7. The chapter ends by a review of the theoretical and instrumental aspects of the Temperature Programmed Reduction (TPR) in section 3.8. The experimental conditions (parameters) used in this study can be found in the experimental section of each relevant chapter (chapters 4-6) of the thesis.

3.2 Transmission electron microscopy (TEM)

3.2.1 General overview

The study of the structure of materials with very small crystallites requires techniques that allow imaging at the atomic scale. Because of its high spatial resolution HR-TEM provides greatly improved understanding of the correlation between the atomic structure of materials and their chemical and physical properties (Buseck *et al.*, 1992).

For structural characterization of the nano-sized FHYD three different transmission electron microscopes were used. TEM studies were performed on the JEOL JEM-2100 with a conventional LaB_6 gun, and the newly developed aberration-corrected Schottky-FEG JEOL JEM-ARM200F, and the cold-FEG Zeiss SESAM (Figure 3.1). The three microscopes offer different capabilities e.g. the SESAM because it is a cold-FEG and it is monochromated offer a high spectral resolution useful for EELS experiments.

Most recent advanced microscopes such as JEOL JEM-2100 and JEOL JEM-ARM200F allows the combination of HR-TEM, NANO-BEAM, STEM, HAADF-STEM, EELS, EF-TEM and EDS in one instrument. However, for the EELS work of this study a high spectral resolution was needed to resolve fine structures in the Fe L-edge of FHYD samples. As a result a cold-FEG and monochromated high spectral resolution SESAM microscope was used for the EELS experiments.

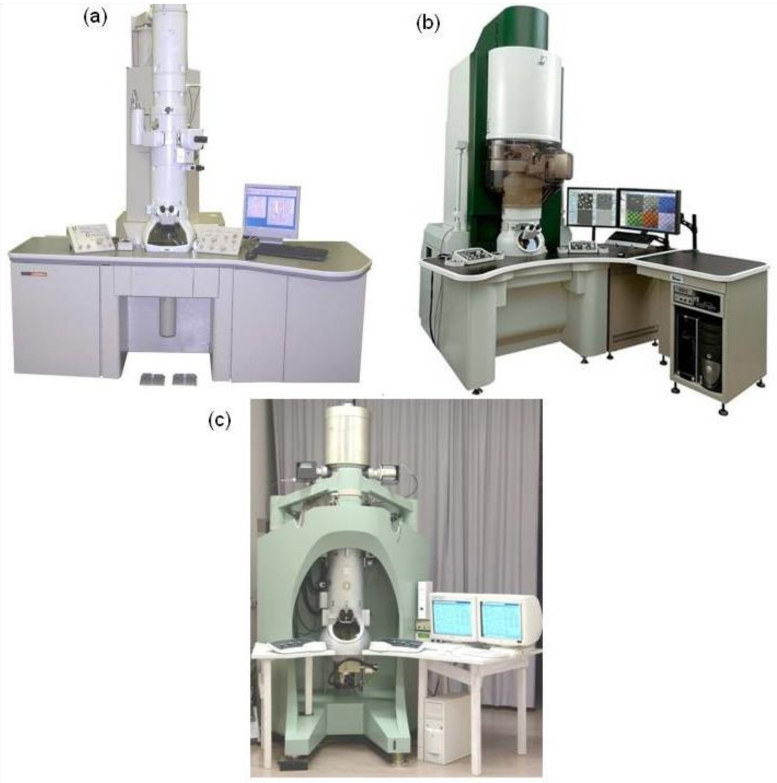

Figure 3.1: Three different TEM microscopes used in this study (a) LaB_6 JEOL JEM-2100, (b) Schottky-FEG JEOL JEM-ARM200F, and (c) Cold-FEG Zeiss SESAM.

Over the past years, the technique of diffraction based on electrons has been a valuable tool for providing crystallographic information of materials (Williams and Carter, 1996; Williams and Carter, 2009). Diffraction as a wave phenomenon is well developed and documented for X-rays and visible light. It was de Broglie's hypothesis in 1927 which predicted that particles should also behave as waves that gave birth to electron diffraction. The extreme short wavelength (≈ 2 pm), strong atomic scattering, and the ability to examine tiny volumes of matter (≈10 nm^3) gives electron diffraction advantages over other diffraction methods such as X-rays and neutron (Bendersky and Gayle, 2001). Electron diffraction can be understood using the reciprocal lattice and Ewald sphere concepts.

3.2.2 The reciprocal lattice and Ewald sphere

The reciprocal lattice is a geometrical mathematical construction that helps to understand diffraction by giving the experimentalist a pictorial representation of diffraction. The reciprocal lattice is a $3D$ array of points each point located a distance $1/d_{hkl}$ from the lattice origin represents sets of parallel (hkl) atomic planes. In real space any translational vector of the lattice, $\vec{r}_n$, can be defined by the equation (Williams and Carter, 1996; Reimer, 1997; Williams and Carter, 2009):

$$\vec{r}_n = n_1\vec{a}_1 + n_2\vec{a}_2 + n_3\vec{a}_3 \qquad 3.1$$

where n_1, n_2, n_3, are all integers and the vectors $\vec{a}_1$, $\vec{a}_2$, and $\vec{a}_3$are unit-cell translations in real space. Any reciprocal vector, $\vec{g}_{hkl}$ normal to crystal lattice plane with Miller indices hkl can be defined in a similar way to the lattice vector in real space

$$\vec{g}_{hkl} = h\vec{a}_1^* + k\vec{a}_2^* + l\vec{a}_3^* \qquad 3.2$$

and the magnitude of the reciprocal vector is $|\vec{g}_{hkl}| = 1/d_{hkl}$where d_{hkl} is the distance between parallel planes in the crystal. The translation lattice vectors in real space $\vec{a}_i$ and the reciprocal lattice vectors $\vec{a}_j^*$ have this relation

$$\vec{a}_i \cdot \vec{a}_j^* = \begin{cases} 0 \; if \; i \neq j \\ 1 \; if \; i = j \end{cases} \; (i, j \; = 1,2,3) \qquad 3.3$$

The Ewald sphere known as the sphere of reflection is a sphere of radius $1/\lambda$ used to determine whether diffraction will occur within a crystal lattice. Figure 3.2 shows the Ewald sphere in a reciprocal lattice. From the origin of the reciprocal lattice O a vector $-\vec{\mathrm{K}}_\mathrm{I}$ is drawn and at its endpoint C a sphere of radius $1/\lambda$ is constructed. $\vec{\mathrm{K}}_{\mathrm{D}}$ is a vector representing possible scattered wave and it can be any vector beginning at C and ends at the surface of the sphere. The vector $\vec{\mathrm{g}} = \vec{\mathrm{K}}_{\mathrm{D}} - \vec{\mathrm{K}}_{\mathrm{I}}$ and whenever the surface of the sphere intersects a reciprocal lattice point the Bragg condition is satisfied and diffraction occurs. The Ewald sphere can intersect with a reciprocal lattice rod (relrod) even when it misses the actual reciprocal lattice point and diffraction will occur (Williams and Carter, 2009).

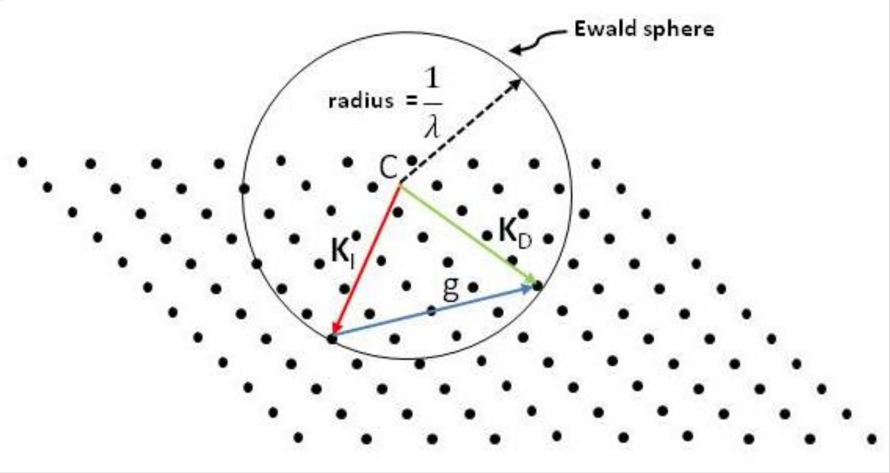

Figure 3.2: The Ewald sphere of a reflection intersecting an array of reciprocal-lattice points (from Williams and Carter, 2009).

Laue zones: in the previous section it is discussed that the intersection of the Ewald sphere with the reciprocal lattice point results in a diffraction spot. The reciprocal points can be at 90° to the incident beam or at large angles. When the Ewald sphere intersects reciprocal lattice points that are normal to the incident beam a zero-order Laue zone (ZOLZ) is formed (see Figure 3.3 (b)). The next planes of reciprocal lattice points parallel to the ZOLZ towards C, produces first-order (FOLZ), second-order (SOLZ), and higher-order Laue zone (HOLZ) (Williams and Carter, 1996; Reimer, 1997; Williams and Carter, 2009).

Mathematically, the Laue zones can be constructed by taking the dot product of the translation vector of the crystal ($\vec{r}_n$) and the reciprocal lattice vector ($\vec{g}_{hkl}$) (Williams and Carter, 1996; Reimer, 1997; Williams and Carter, 2009)

$$\vec{r}_n \cdot \vec{g}_{hkl} = n_1 h + n_2 k + n_3 l = N \qquad 3.4$$

where N is an integer. Diffraction patterns that come from the plane where $N = 0$ are termed zero-order Laue zone (ZOLZ). Eq. 3.4 tells us that for $N = 0$, all the ($\vec{g}_{hkl}$) for a given value of ($\vec{r}_n$) lie in a plane through the origin of the reciprocal lattice and are normal to a common direction called the zone axis ($\vec{r}_n$) . Figure 3.3 (a) shows a family of three planes that have the zone axis [$n_1n_2n_3$] as a common line of intersection. The FOLZ, SOLZ are obtained for $N = 1, 2,$ respectively. And all zones higher than that are called higher-order Laue zone (HOLZ) (Williams and Carter, 1996; Reimer, 1997; Williams and Carter, 2009).

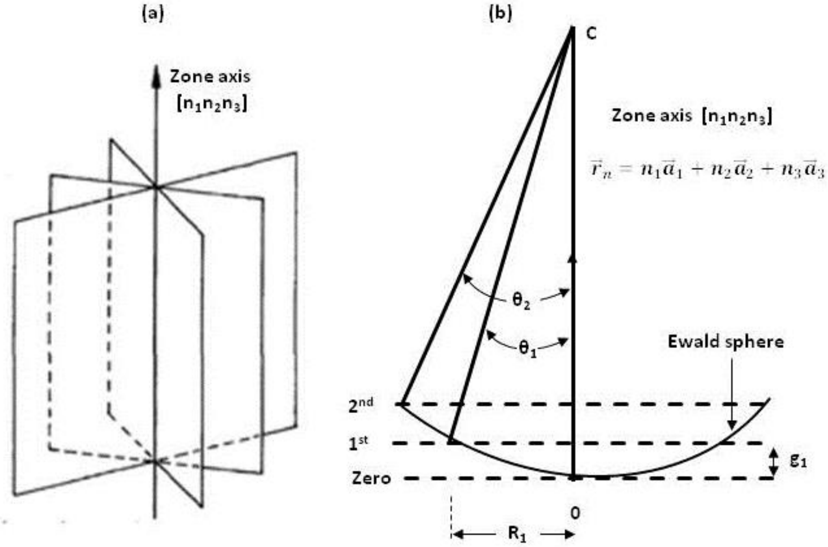

Figure 3.3: Lattice planes (*hkl*) with a common zone axis [$n_1n_2n_3$], (b) the Ewald sphere intercepts showing positions of zero-order and higher order Laue zones (after Reimer, 1997).

In an observed experimental diffraction pattern, the distance (R) between transmitted (000) and diffracted spots is related to the interplanar spacing, d_{hkl}, of hkl planes in the crystal and the electron wavelength λ by the following expression (Williams and Carter, 1996; Williams and Carter, 2009):

$$R = \frac{\lambda L}{d_{hkl}} \tag{3.5}$$

where L is the camera length (distance between the sample and the screen) and the term λL is called the camera constant (see Figure 3.4). By meassuring R, the distance between planes atoms, d_{hkl}, can be obtained from Eq. 3.5.

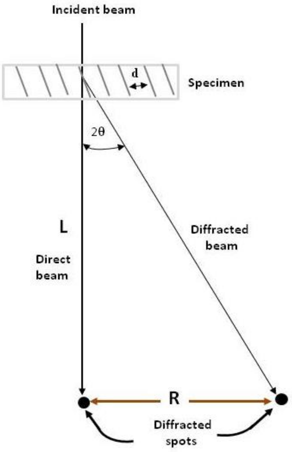

Figure 3.4: **Geometry of formation of diffraction pattern.**

The electron diffraction theory described above can be easily visualized in Figure 3.4. The incident electron beam pass through a specimen with hkl diffraction planes separated by interplanar spacing d. Part of the incident electron pass through the specimen un-diffracted while part of the beam gets diffracted at some distance R from the primary beam. It can be seen that Eq. 3.5 can be derived from the geometry of Figure 3.4 and and the interplanar spacing, d.

3.2.3 TEM imaging

3.2.3.1 TEM basics

A TEM uses a series of electromagnetic lenses to manipulate the electron trajectory to form small electron probe and enlarged image of the specimen. Electromagnetic lenses focuses electrons by concentrated magnetic fields generated by currents flowing through annular coils between soft-iron pole pieces (Buseck *et al.*, 1992). The TEM consist mainly of three sets of lenses (Williams and Carter, 1996; Tonejc, 1999; Williams and Carter, 2009): (1) the condenser lens which forms part of the illumination system and its role is to bring focused electron beam into the specimen, (2) the objective lens which is at the heart of the instrument is situated below the specimen stage and its role is to bring scattered and transmitted beam into focus and forms the first image of the specimen, (3) the first image and diffraction pattern produced by the objective lens is then magnified and projected into the viewing screen by a set of magnifying lens and projector lens (Figure 3.5).

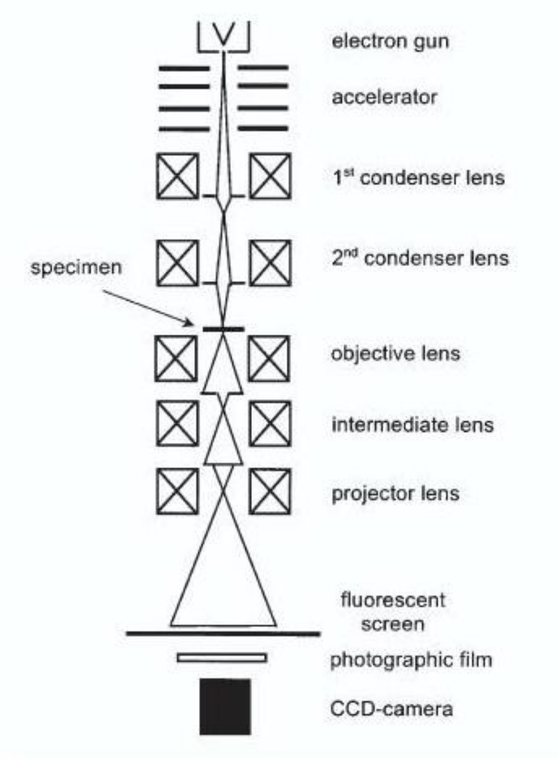

Figure 3.5: TEM column showing the electron ray path TEM lenses (from Karkik, 2001).

An important factor in the imaging system is the wavelength of electrons which determines the angular range of the scattering from the specimen (Buseck *et al.*, 1992). The wavelength of electrons depends on the accelerating voltage and is given by (Williams and Carter, 2009):

$$\lambda = \frac{h}{\sqrt{2m_e eV}} \tag{3.6}$$

where h is the Planck's constant, e is the elementary charge, m_e is the electron mass, and V is the accelerating voltage. The high voltage of the accelerating potential in the electron microscope causes the electron to travel a fraction of the speed of light and therefore the mass and effective voltage should include relativistic effects. The electron wavelength with relativistic effects taken into account becomes (Williams and Carter, 2009):

$$\lambda = \frac{h}{\sqrt{2m_e eV\left(1 + \frac{eV}{2m_e c^2}\right)}} \tag{3.7}$$

where c is the speed of light. The electron beam from the electron gun is focused into the thin specimen by the condenser lenses and after interaction with the specimen it gets scattered. The scattered radiation is brought back into focus by the objective lenses and image is produced and magnified by the projector lenses (Buseck *et al.*, 1992).

3.2.3.2 TEM modes of operation

Image Contrast

In order to understanding imaging in TEM it is important to first understand and discuss the two important mechanisms producing image contrast. Contrast (C) is defined quantitatively as the difference in intensity in two adjacent areas in an image (Williams and Carter, 2009):

$$\mathrm{C} = \frac{(\mathrm{I2} - \mathrm{I1})}{\mathrm{I1}} = \frac{\Delta \mathrm{I}}{\mathrm{I}} \tag{3.8}$$

This image contrast arises when the incident electron wave changes both its amplitude and its phase as it traverses the specimen. Usually in a TEM a distinction is made between the amplitude and phase contrast. Amplitude contrast is briefly described below and phase contrast will be covered under high resolution imaging because it forms basis of high resolution TEM.

Amplitude contrast: conventional TEM uses this type of contrast for image formation. Amplitude contrast is produced as a result of loss of electrons from the incident beam. There are two forms of amplitude contrasts i.e. mass-thickness contrast and diffraction contrast. Mass thickness contrast arises from exclusion of some of imaging electrons from the beam as a result of being scattered at large angles. As electrons penetrate the specimen they are elastically scattered off axis by nuclear interactions and each imaging electron interact independently with the atoms in the specimen. High Z-regions in the specimen will scatter more electrons because the cross section for elastic scattering is a function of Z.

Another mechanism giving rise to mass-thickness contrast is the difference in the thickness of the sample; thicker regions are expected to scatter more electrons than thinner regions because there will be more elastic scattering since the mean-free path remains fixed. Usually mass-thickness contrast is used in imaging noncrystalline and biological materials where diffraction contrast does not exist (Williams and Carter, 2009).

Diffraction pattern (DP) and image formation

The underlying idea of electron microscopy is to use electrons to form images of the specimen. Unscattered, elastically scattered, and inelastically scattered electrons form the basis of TEM imaging. After an interaction of the electron beam with the crystallographic structure of the specimen the uniform electron intensity in the incident beam is transformed into a nonuniform intensity in the exit electron wave and this creates image contrast in TEM as shown in Figure 3.6.

In the image formation process, a plane wave illuminates the specimen and gets diffracted and transmitted through the specimen. The parallel transmitted wave is brought into focus at the back focal plane of the objective lens (Figure 3.6). The formation of an image is mathematically described by two successive Fourier-transformations (Buseck *et al.*, 1992). The specimen is illuminated with plane parallel waves and the objective lens produces a Fourier transform $\tilde{\psi}(\vec{q})$ of the specimen function $\psi(\vec{r})$ at the back focal plane to produce a DP (Buseck *et al.*, 1992; Karkik, 2001). The function, $\tilde{\psi}(\vec{q})$, at the back focal plane is then Fourier transformed to produce a magnified and inverted image ($\psi(\vec{r}')$) of the specimen wavefunction ($\psi(\vec{r})$) at the image plane (Buseck *et al.*, 1992; Karkik, 2001). There are several mechanisms of image formation in a TEM and that is the subject of the following subsections.

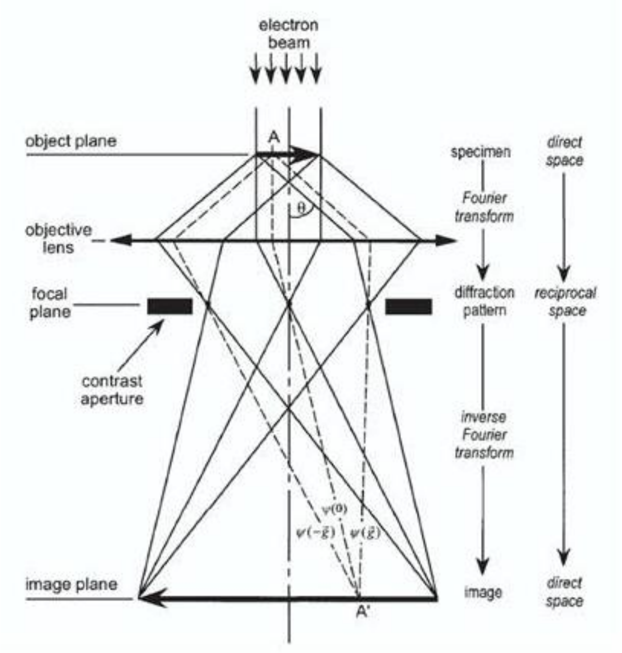

Figure 3.6: Schematic diagram showing the formation of DP and image in a TEM (Karkik, 2001).

Conventional dark and bright field imaging

Diffraction contrast: Bragg- diffracted beams are used to create diffraction contrast in the TEM. The objective aperture below the specimen is used to select which beam can be used to form the image. In cases where diffracted beams are intercepted by the objective aperture and only the transmitted beam is allowed to pass through a bright field (BF) image is created (Figure 3.7 (a)) (Williams and Carter, 2009).

When the objective aperture at the back focal plane is positioned to pass only the diffracted beam, a dark-field (DF) image is formed (Figure 3.7 (b)). There are two methods in which a DF image can be formed. In the first method (Figure 3.7 (b)), the objective aperture is displaced to block the direct beam travelling on the optical axis path. On the other hand, the objective aperture is not moved but the incident beam is tilted off-axis instead (Figure 3.7 (c)). This operation is called the centered Dark-Field operation because the diffracted beam collected at the center of the axis path.

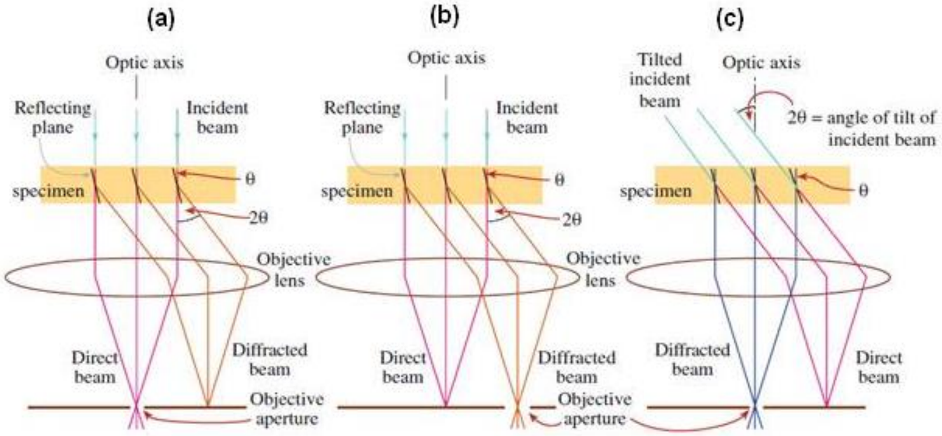

Figure 3.7: TEM imaging modes (a) BF, (b) off-axis DF, and (c) centered DF (Williams and Carter, 2009).

High resolution imaging

Phase contrast: Besides using amplitude contrast to form images, phase shift can be used to form images and this technique is used in high-resolution imaging. Very thin TEM specimens are approximated as phase objects for high energy fast electrons (Buseck *et al.*, 1992). The electron wave suffers phase changes as it traverses through the specimen. Phase contrasts arise from interference between unscattered and scattered electron beams (Buseck *et al.*, 1992; Williams and Carter, 1996; Williams and Carter, 2009). Unlike diffraction contrast where one beam can be selected to form images phase contrast requires the selection of more than one beam collected at the objective aperture to form the image. The process of high resolution TEM imaging is well outlined in a well presented book by Buseck *et al.*, 1992 and an interested reader can find this book worthy reading.

STEM imaging

Another method of forming an image in a TEM is to scan the beam across the without changing its direction. STEM imaging requires the beam to be scanned parallel to the optic axis so that it mimics the parallel beam in TEM mode even though it is scanning. Although STEM imaging can be performed in a TEM by switching between TEM and STEM modes, there are also dedicated STEM instruments. Similarly, to a TEM mode operation, there are several image modes operation in STEM imaging. In STEM imaging, electron detectors are used in exactly similar way apertures are used in static-beam TEM for image formation (Williams and Carter, 1996; Williams and Carter, 2009). Figure 3.8 shows several image modes that are possible with STEM.

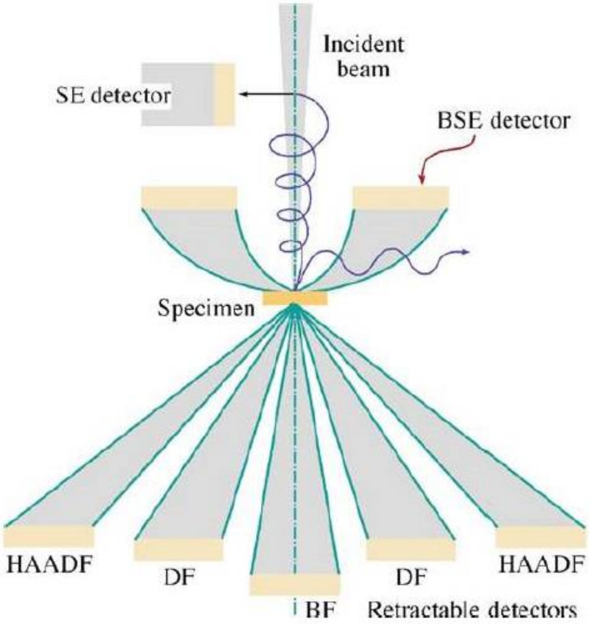

Figure 3.8: Different imaging mechanisms in STEM (Williams and Carter, 2009).

A BF image can be formed in STEM mode operation by inserting a BF electron detector onto the axis path of the microscope (Figure 3.8). This detector will intercept the un-diffracted electron beam wherever the electron beam is scanning on the sample and thus form a direct-beam signal. Such signal travel gets amplified through the computer amplification system as it travels from the detector to the computer display where a BF image is formed. Several factors such as defocus, specimen thickness, diffraction contrast affects STEM imaging.

In STEM mode operation, DF images are also formed from diffracted or scattered electrons. The DF image is formed from integration of the low-angle ($\sim 10 - 50\, mrad$) scattered electron intensity. An electron detector which surrounds (hence the name annular DF detector) the BF detector is used to collect all the scattered electrons around the BF detector. The advantage of using STEM ADF imaging is that the images show high contrast and less noise compared to convectional DF TEM images (Williams and Carter, 1996; Williams and Carter, 2009).

Another type of detector that can be used to form images in STEM mode is the high-angle ADF (HAADF). We have noticed the normal ADF detector only picks electrons scattered around small angles and these contains Bragg diffracted electrons. The HAADF detector (Figure 3.8) collects electrons scattered at high angles ($> 50\, mrad$) (Williams and Carter, 1996; Williams and Carter, 2009). The main advantage of using the HAADF detector is that it effectively avoids the Bragg effects and diffraction contrast affecting the image. This is because the HAADF detector mainly collects electrons subjected to Rutherford scattering (incoherent, elastic electrons from atomic nuclei).

3.3 Electron Energy Loss Spectroscopy (EELS)

3.3.1 Introduction

EELS has became a standard tool in identifying and quantifying elements present in a material (Egerton, 2003; Egerton, 2005a; Egerton and Malac, 2005b; Egerton, 2011). It has also proved to give useful information on the coordination and oxidation state of metal oxides (Garvie and Buseck, 1998; van Aken *et al.*, 1998; van Aken and Liebscher, 2002; Pan *et al.*, 2006; Pan *et al.*, 2009; Pan *et al.*, 2010; Egerton, 2011). The analysis of the energy distribution of the initially monoenergetic electrons after interaction with the specimen forms the basis of the EEL spectroscopy (Egerton and Malac, 2005b; Egerton, 2011). In a TEM column, incident electrons interact with constituent atoms through the Coulombic electrostatic forces and get scattered. Depending on the energy loss of the incident electrons after interaction with the specimen, two types of scattering events can occur i.e. elastic and inelastic scattering.

Elastically scattered electrons are these electrons that lose zero or negligible amount of energy. These electrons make main contribution to electron diffraction and image contrast in TEM. Although elastically scattered electrons are not primary part of the EELS technique, they are relevant for the following reasons (Egerton, 2011):

1. Elastic scattering modifies the angular distribution of the inelastically scattered electrons since both types of interaction processes occur within the sample.
2. Elastic scattering can change the probability of localized inelastic scattering by redistributing the electron flux (current density) within each unit cell of a crystalline material.
3. The ratio of elastic and inelastic scattering can provide an estimate of the local atomic number or chemical composition of the specimen.

In inelastic scattering part of the kinetic energy of the incident energy is transferred to the electrons or atoms of the specimen through Coulombic interaction with the nucleus and/or atomic electrons. These electrons which lose energy by exciting atomic electrons from core states are the basis of the EELS technique and this chapter will concentrate on processes by which electrons are inelastically scattered. Covered in this chapter is the theory on electron scattering that includes the Born approximation, the differential cross-section, dipole selection rule. The features of the EELS spectra and the instrumentation of the technique will be discussed under separate sections of the chapter.

3.3.2 Inelastic scattering of electrons

3.3.2.1 Born approximation for electrons

Electron scattering process is treated as wave phenomenon with the electron wavefunction satisfying the Schrödinger wave equation. Consequently, it is convenient to describe the primary electrons as electron waves in developing scattering formalism. The Schrödinger wave equation takes the form (Fultz and Howe, 2002):

$$(\nabla^2 + k_0^2)\, \psi(\vec{r}) = U(\vec{r})\, \psi(\vec{r}) \qquad 3.9$$

where $k_0^2 \equiv \frac{2m_e E}{\hbar^2}$, $U(\vec{r}) \equiv \frac{2mV(\vec{r})}{\hbar^2}$, and m_e and $\vec{r}$ are defined as the mass of the electron and its coordinates in the atom, respectively.

The differential form of the Schrödinger equation is transformed to the appropriate integral form for scattering problems using the Green's function, $G(\vec{r}, \vec{r}')$ (Fultz and Howe, 2002). The function provides response at $\vec{r}$ for a point scatter at $\vec{r}'$.

$$(\nabla^2 + k_0^2)\, G(\vec{r}, \vec{r}') = \delta(\vec{r}') \qquad 3.10$$

The scattered function, $\psi_n(\vec{r})$, is then obtained by integrating

$$\psi_n(\vec{r}) = \int U(\vec{r}')\, \psi(\vec{r}')\; G(\vec{r}, \vec{r}')\, d^3\vec{r}' \qquad 3.11$$

In order to obtain an explicit solution to the integral Eq. 3.11, an approximation is required. The first-order Born approximation is usually used. This approximation assumes that the wave is undiminished and is scattered only once, and as such this assumption can only be valid when the scattering is weak (Fultz and Howe, 2002).

The incident electron before scattering and the scattered wave within the first Born approximation should take the plane wave form as follows

$$\Phi_0 = \exp\left(2\pi i \vec{k}_0 \cdot \vec{r}\right) \qquad 3.12$$

$$\Phi_n = \exp\left(2\pi i \vec{k} \cdot \vec{r}'\right) \qquad 3.13$$

where $\vec{k}_0$ and $\vec{k}$ is the wave vector of the incident and scattered electron, respectively; $\vec{r}$ and $\vec{r}'$ is the vector coordinate of the incident and scattered electron, respectively (see Figure 3.9)**.** The total wavefunction of the system of the plane incident and scattered waves is the product of the atomic states and plane waves states (Reimer, 1997):

$$\psi_0 = a_0(\vec{r}_j)\exp(2\pi i\vec{k}_0 \cdot \vec{r}_i) \tag{3.14}$$

$$\psi_n = a_n(\vec{r}_j)\exp(2\pi i\vec{k} \cdot \vec{r}_i) \tag{3.15}$$

where $a_0(\vec{r}_i)$ and $a_n(\vec{r}_j)$ are the atomic wave functions; $\vec{r}_i$ and $\vec{r}_j$ are the coordinates of the incident and atomic electrons, respectively.

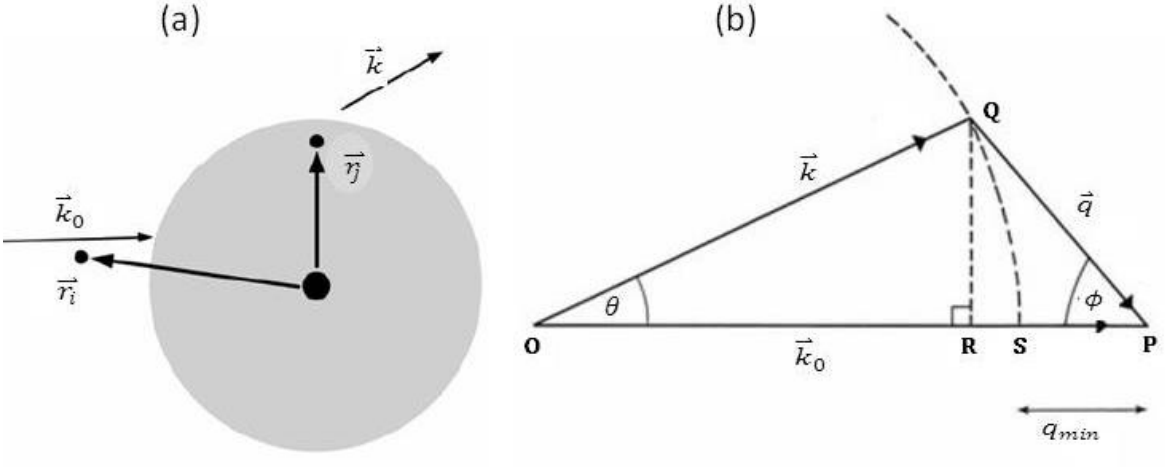

Figure 3.9: Schematic showing wavevectors and position vectors for electron scattering (after (a) Miao, 2007 and (b) Egerton, 2011).

3.3.2.2 Relativistic kinetics of scattering

Since the relationship between the magnitude q of the scattering vector depends both on the scattering angle θ and energy loss, it is therefore necessary to consider both the conservation of momentum and energy to the collision when deriving the relationship between q and θ (Egerton, 2011). The low of conservation of energy dictates that

$$W - \Delta E = W' \tag{3.16}$$

Where W' is the total energy of the scattered electron, and it can be recalled that ΔE is the energy supplied to the atom, and W is the total energy of the incident electron (kinetic energy E_0 + rest energy $m_e c^2$) given by the Einstein equation:

$$W = \gamma m_e c^2 \tag{3.17}$$

and by using the relativistic energy-momentum relation $[W^2 - (pc)^2 = (m_e c^2)^2]$ (see Taylor and Wheeler, 1992) one obtains

$$W = \sqrt{(m_e c^2)^2 + (pc)^2} = \sqrt{(m_e c^2)^2 + \hbar^2 k_0^2 c^2} \tag{3.18}$$

where $p = \gamma m_e v = \hbar k_0$ is the incident momentum and Eq. 3.16 becomes

$$W - \Delta E = W' = \sqrt{(m_e c^2)^2 + \hbar^2 k^2 c^2} \tag{3.19}$$

where ΔE is being the energy loss, k is the wave number of the scattered electron and its value can be worked out by substituting W from Eq.3.18 in Eq. 3.19. It is important to note that the resulting equation (Eq.3.20) relates the change in magnitude of the fast-electron wave vector to the energy loss (Egerton, 2011)

$$\begin{aligned} k^2 &= k_0^2 - 2\Delta E \left[\frac{m_e^2}{\hbar^4} + \frac{k_0^2}{(\hbar c)^2}\right]^{1/2} + \frac{\Delta E^2}{(\hbar c)^2} \\ &= k_0^2 - 2\gamma m_e \Delta E/\hbar^2 + \Delta E^2/(\hbar c)^2 \end{aligned} \tag{3.20}$$

It is generally convenient for numerical calculations to convert each wave number to a dimensionless quantity by multiplying it by the Bohr radius a_b and by making use of the equality $R a_b^2 = \hbar^2/2m_e$ (R being the Ryberg energy), Eq. 3.20 can becomes

$$(k a_b)^2 = (k_0 a_b)^2 - (\Delta E/R)[\gamma - \Delta E/(2 m_e c^2)] \tag{3.21}$$

For most inelastic collisions, the ΔE^2 term in Eq. 3.21 is found to be insignificant and the value of $(k_0 a_b)^2$ is obtained from the kinetic energy E_0 of the incident electron as follows

$$(k_0 a_b)^2 = (\Delta E/R)(1 + E_0/2m_e c^2) = (T/R)(1 - 2T/m_e c^2) \qquad 3.22$$

where $T = m_e v^2/2$ is an "effective" incident energy.

As mentioned above, the conservation of momentum should also be taken into consideration when deriving the relationship between q and θ for an inelastic event. This can be simply achieved by applying the cosine rule in the vector triangle (see Figure 3.9 (b))

$$q^2 = k_0^2 + k^2 - 2k_0 k \cos\theta \qquad 3.23$$

and taking the derivative of Eq.3.22 at constant ΔE and E_0 gives

$$d(q)^2 = 2k_0 k \sin\theta \, d\theta = (k_0 k/\pi) d\Omega \qquad 3.24$$

The value of $(qa_b)^2$ can then be obtained by substituting Eq. 3.21 into Eq. 3.23

$$(qa_b)^2 = \frac{2T\gamma^2}{R}\left[1 - \left(1 - \frac{\Delta E}{\gamma T} + \frac{\Delta E^2}{2\gamma^2 T m_e c^2}\right)^{1/2} \cos\theta\right] - \frac{\Delta E}{R} + \frac{\Delta E^2}{2Rm_e c^2} \qquad 3.25$$

In principle Eq. 3.25 can be used to compute qa_b for any given value of θ. However, high-precision arithmetic is required when computing qa_b for small θ using this procedure since the terms inside the brackets in Eq. 3.25 involves subtracting almost identical numbers. As shown in Figure 3.9 (b), the value of $\theta = 0$ corresponds to $q = q_{min} = k_0 - k$, and the binomial expansion of the square root in Eq. 3.25 indicates that the terms up to the second order in ΔE cancel and Eq. 3.25 can be reduced to

$$(qa_b)^2_{min} \approx \Delta E^2/4RT + \Delta E^3/(8\gamma^3 RT^2) \qquad 3.26$$

It turns out that only the ΔE^2 term is of significance in Eq. 3.26 for $\gamma^{-3}\Delta E/T \ll 1$ (which basically to all collisions) and the equation can takes this form

$$q_{min} \approx k_0 \theta_{\Delta E} \qquad 3.27$$

where $\theta_{\Delta E} = \Delta E/(2\gamma T) = \Delta E/(\gamma m_e v^2)$ is the characteristic inelastic scattering angle.

3.3.2.3 The differential cross-section

The most important quantity in scattering theory is the differential cross-section ${d\sigma}/_{d\Omega}$, which represents the probability of an incident electron to be scattered (per unit solid angle Ω) by a given atom (Egerton, 2011). From a classical (particle) point of view, the electrons travel on hyperbolic trajectories due to attractive Coulombic force around the nucleus (+Ze) as depicted in Figure 3.10. If there was no Coulombic interaction between the electron and the nucleus, the electron would travel straight and pass the nucleus with a distance a between them defined as the impact parameter. The scattering angle θ is determined by the impact parameter a, with θ decreasing as a increases because of weaker electrostatic attraction at distances further away from the nucleus.

Figure 3.10 shows that electrons that pass through an element area of $d\sigma$ of the incident beam is scattered into a cone of solid angle $d\Omega$. The ratio of the element area ($d\sigma$) to the solid angle ($d\Omega$) gives the quantity called differential cross-section. This quantity describes the angular distribution of the scattered electrons.

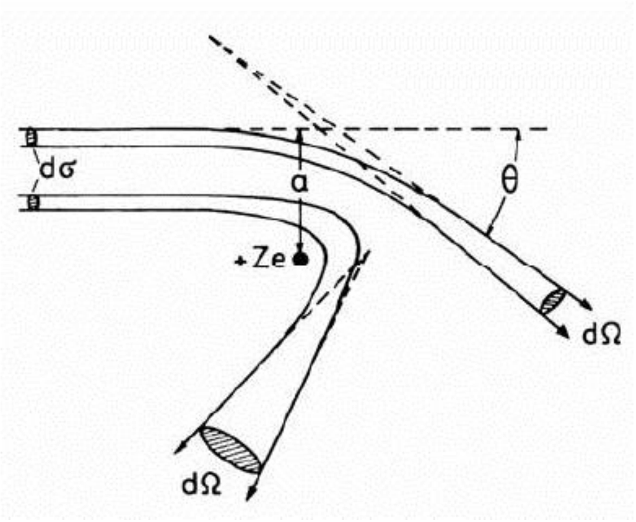

Figure 3.10: Illustration of the differential cross-section $d\sigma/d\Omega$ (from Reimer, 1997).

For inelastic scattering, the differential cross-section can be calculated from quantum mechanical scattering theory using the golden rule (Reimer, 1997):

$$\frac{d\sigma_{0n}}{d\Omega} = \frac{4\pi^2 m^2}{h^4}\frac{k}{k_0}\,|\langle\psi_n|\,V(\vec{r}_i,\vec{r}_j)|\psi_0\rangle\,|^2 \qquad 3.28$$

where $\psi_0$and ψ_n are the products of the incident and scattered waves with wave vectors $\vec{k}_0$ and $\vec{k}$, respectively, m is the electron rest mass, h is the Planck's constant, and $V(\vec{r}_i,\vec{r}_j)$ is the perturbing Hamiltonian (Coulomb interaction potential) which takes the form (Reimer, 1997; Miao, 2007):

$$V(\vec{r}_i,\vec{r}_j) = -\frac{e^2 Z}{4\pi\epsilon_0 r_i} + \sum_{j=1}^{Z}\frac{e^2}{4\pi\epsilon_0|\vec{r}_i-\vec{r}_j|} \qquad 3.29$$

The first term in Eq. 3.29 represents interaction between the incident electron and the nucleus and the repulsive Coulombic interaction between incident and atomic electrons is represented by the second term. The symbol Z denotes the atomic number of the atom, e is the elementary charge, and ϵ_0 is the permittivity of free space.

The differential cross-section can be obtained by substituting Eqs. 3.14, 3.15, and 3.29 into Eq. 3.28, and obtain

$$\frac{d\sigma_{0n}}{d\Omega} = \frac{4\pi^2 m^2}{h^4}\,\frac{k}{k_0}\left|\langle\Phi_n\left|-\frac{e^2 Z}{4\pi\varepsilon_0 r_i}\right|\Phi_0\rangle\langle a_n|a_0\rangle + \langle a_n\Phi_n\left|\sum_{j=1}^{Z}\frac{e^2}{4\pi\varepsilon_0\left|\vec{r}_i-\vec{r}_j\right|}\right|a_0\Phi_0\rangle\right|^2 \tag{3.30}$$

The orthogonality of the atomic wave functions ($\langle a_n|a_0\rangle = \delta_{n0}$) makes Eq. 3.30 to become less complicated since the first term cancels out. The differential cross-section becomes the subject of the second term only

$$\langle a_n\Phi_n\left|\sum_{j=1}^{Z}\frac{e^2}{4\pi\varepsilon_0\left|\vec{r}_i-\vec{r}_j\right|}\right|a_0\Phi_0\rangle$$

$$= \iint \exp\left(-2\pi i\vec{k}\cdot\vec{r}_i\right) a_n^*\left(\sum_{j=1}^{Z}\frac{e^2}{4\pi\varepsilon_0\left|\vec{r}_i-\vec{r}_j\right|}\right)a_0 \exp\left(2\pi i\vec{k}_0\cdot\vec{r}_i\right) d^3\vec{r}_i d^3\vec{r}_j \tag{3.31}$$

By introducing the parameter $\vec{q} = 2\pi(\vec{k}-\vec{k}_0)$ with $\left|\vec{k}\right| \neq \left|\vec{k}_0\right|$ instead of equal magnitudes of $\vec{k}$ and $\vec{k}_0$ used for elastic scattering Reimer, 1997 and using the integral

$$\int \frac{\exp\left(-i\vec{q}\cdot\left(\vec{r}_i-\vec{r}_j\right)\right)}{\left|\vec{r}_i-\vec{r}_j\right|}d^3\vec{r}_i = \frac{4\pi}{q^2} \tag{3.32}$$

By making use of the parameter q and the integral (Eq. 3.32) we obtain the differential cross-section

$$\frac{d\sigma_{0n}}{d\Omega} = \frac{k}{k_0}\frac{4}{a_b^2 q^4}\left|\sum_{j=1}^{Z}\int a_n^* a_0 \exp\left(-i\vec{q}\cdot\vec{r}_j\right)d^3\vec{r}_j\right|^2 \tag{3.33}$$

where the physical constant a_b is the Bohr radius ($a_b = \frac{4\pi\varepsilon_0\hbar^2}{me^2}$). Because Eq. 3.33 now contains the electron mass (m_e) and some relativistic effects should be corrected for m, in doing so Eq. 3.33 becomes (Miao, 2007)

$$\frac{d\sigma_{0n}}{d\Omega} = \frac{k}{k_0}\frac{4\gamma^2}{a_b^2 q^4}\left|\sum_{j=1}^{Z}\int a_n^* a_0 \exp(-i\vec{q}\cdot\vec{r_j})d^3\vec{r_j}\right|^2 \tag{3.34}$$

here $\gamma^2 = (1 - v^2/c^2)^{-1}$ is the relativistic correction factor for mass, v and c, respectively, represents the speed of the incident electron and speed of light in vacuum. Eq. 3.34 can be written in a simplified form using a closely related quantity known as the generalized oscillator strength (GOS) defined as

$$f(q) = \frac{\Delta E}{R(a_b q)^2}\left|\sum_{j=1}^{Z}\int a_n^* a_0 \exp(-i\vec{q}\cdot\vec{r_j})d^3\vec{r_j}\right|^2 \tag{3.35}$$

where the Ryberg energy is defined as $R = \frac{me^4}{8\varepsilon_0^2 h^2}$, ΔE is the excitation energy that promotes atom from state $a_0$to a_n. When the GOS factor is introduced in Eq. 3.35, the differential cross-section takes the form

$$\frac{d\sigma_{0n}}{d\Omega} = \frac{k}{k_0}\frac{4\gamma^2 R}{q^2\Delta E}f(q) \tag{3.36}$$

3.3.2.4 Bethe theory

The key quantity in Bethe theory is the GOS factor which describes the response of an atom when a given energy and momentum are supplied by the fast moving incident electrons (Egerton, 2011). The differential cross-section outlined above (section 3.3.2.2) describes the transition between the electronic states 0 and n with a discrete energy loss Reimer, 1997. However, in cases such as ionizing transitions to a “continuum” of states the energy loss spectrum is continuous rather than discrete function of the energy loss (Egerton, 2011). As a result, it is more convenient to define a GOS per unit energy loss, $df(q,\Delta E)/d\Delta E$. Using the GOS per energy loss, the angular and energy dependence for inelastic scattering are then specified by a double-differential cross-section

$$\frac{d^2\sigma_{0n}}{d\Omega d\Delta E} = \frac{k}{k_0}\frac{4\gamma^2 R}{q^2\Delta E}\frac{df(q,\Delta E)}{d\Delta E} \tag{3.37}$$

However, it makes sense to relate the double-differential cross-section to the data which contain substantial amount of details arising from the bonding in the solids. This can be achieved by weighting Eq. 3.37 by the density of unoccupied states ($\rho(E_n)$) and we obtain

$$\frac{d^2\sigma_{0n}}{d\Omega d\Delta E} = \frac{4\gamma^2 R}{q^2\Delta E}\frac{df(q,\Delta E)}{d\Delta E}\rho(E_n) \qquad 3.38$$

where k/k_0 can be taken as unity since ΔE is very small compared to the incident electron's kinetic energy and k will always be very close to k_0.

Figure 3.11 shows the plot of $df(q,\Delta E)/d\Delta E$ as a function of ΔE and the scattering angle for K excitation of a carbon calculated using the hydrogenic model (Reimer, 1997; Fultz and Howe, 2002; Egerton, 2011). The plot gives the surface known as the Bethe surface. Each individual curve in the figure represents qualitatively the angular dependence of inner-shell scattering, since the double-differential cross-section (Eq.3.38) is proportional to $E^{-1}q^{-2}df(q,\Delta E)$, while q^2 increases with the square of the scattering angle (Reimer, 1997; Fultz and Howe, 2002; Egerton, 2011).

Shown in Figure 3.11 is that the intensity is concentrated in the Bethe ridge at higher scattering angles. This implies that a relatively large objective aperture is required to include this intensity in the EEL spectrum. However, a small aperture can be enough to collect most of the intensity at energies above the ionization energy, (ΔE_t). The GOS is zero below the ionization threshold (ΔE_t), and after that it jumps to a maximum and then decreases with increasing ΔE (see Figure 3.11).

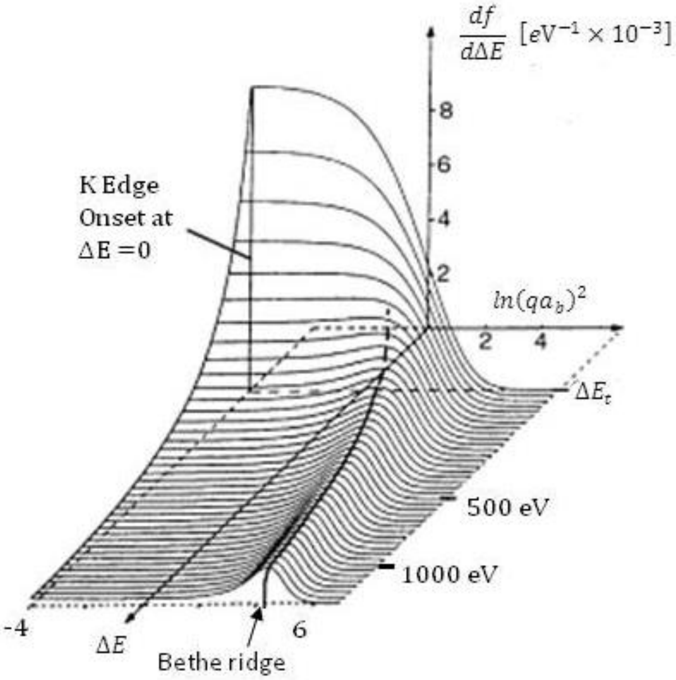

Figure 3.11: The Bethe surface for carbon K-edge (modified from Fultz and Howe, 2002).

3.3.2.5 Dipole selection rule

The probability of a transition between any two states in the event of an atom excitation during electron inelastic scattering is governed by optical dipole selection rule. This rule formally constrains the possible transitions between the two states in the system. In transition metals this dipole rule accounts for the prominence of $L_{3,2}$ edges ($2p \rightarrow 3d$) in the metals and their compounds (high density of d-states just above the Fermi level) (Egerton, 2011).

Eq. 3.27 shows that the momentum exchange can be approximated by $\hbar q_{min} \approx \hbar k_0 \theta_E = {}^{\Delta E}/_{v}$ while the momentum exchange upon the absorption of a photon energy ΔE is $\hbar q(photon) = {}^{\Delta E}/_{c}$ (Egerton, 2011). Taking the ratio of the momentum exchange one obtains

$$\frac{q_{min}}{q(photon)} \approx {}^{c}/_{v} \qquad 3.39$$

and this ratio is usually less than 2 for incident energies above 80 keV which is usually used in TEM. As such the change in Δl in the angular momentum quantum number between the initial and final states must be equal to ± 1 (Cornell and Schwertmann, 2003; Egerton, 2011), and this dipole selection rule applies approximately to the energy-loss spectrum. However, dipole forbidden transitions are sometimes observed when a large collection aperture is used. This behavior has been shown by lanthanum oxide showing sharp M_2 and M_3 peaks, representing $\Delta l = 2$ transitions from $3p$ level to high density of unfilled $4f$ states and a use of small collection angle (1.6 $mrad$) resulted in almost disappearance of these peaks (Egerton, 2011).

3.3.3 Features in EELS spectrum

3.3.3.1 The zero-loss spectrum

EEL spectroscopy measures the energy loss of incident electrons due to inelastic scattering by outer shell and inner shell electrons in the material (Reimer, 1997; Fultz and Howe, 2002; Egerton, 2011). However, elastic scattering occurs in the process giving rise to electrons that have lost negligible amounts energy and such electrons form the zero-loss peak in the EEL spectrum. Figure 3.12 shows an example of EELS spectra of a nickel oxide indicating the low loss (zero-loss and plasmon) and high energy loss region. The Zero-loss peak is due to electrons that are elastically scattered by the electrostatic field of the atomic nucleus. These electrons pass through the specimen without any noticeable loss of energy.

3.3.3.2 Plasmon excitations

The next small feature close to the zero-loss peak in the EELS spectrum arise from an inelastic event from electrons that have lost a small amount of energy due to plasmons excitations (Figure 3.12). when a fast-moving passes through a solid, the nearby electrons are displaced by Coulomb repulsion, thus creating a correlation hole that trails behind the electron (Egerton, 2009). In a case where the electron speed exceeds the Fermi velocity, the response of the atomic electrons becomes oscillatory and this results in regions of alternating positive and negative space charge along the trajectory of the electron in a process known as Plasmon wake

(Egerton, 2009). The periodicity of the Plasmon wake along the electron trajectory is given by $\lambda_w = {}^{v}/_{f_p}$ and f_p is the plasma frequency given by(Egerton, 2009)

$$2\pi f_p = \omega_p = \sqrt{\frac{ne^2}{\varepsilon_0 m}} \tag{3.40}$$

The backward attractive force of the positive correlation hole on the electron as it moves through the solid results in energy loss and this process that results in a creation of pseudoparticles known as plasmons, each carrying a quantum energy of (Egerton, 2009):

$$E_p = \left(\frac{h}{2\pi}\right)\omega_p = \left(\frac{h}{2\pi}\right)\sqrt{\frac{ne^2}{\varepsilon_0 m}} \tag{3.41}$$

where *h* is the Planck's constant, ε_0 is the permittivity of free space, *n* is the free-electron density, *e* and electron charge and m is the electron effective mass. This loss of energy by the incident electron gives rise to one or more prominent peaks in the EEL spectrum (see Plasmon peak in Figure 3.12).

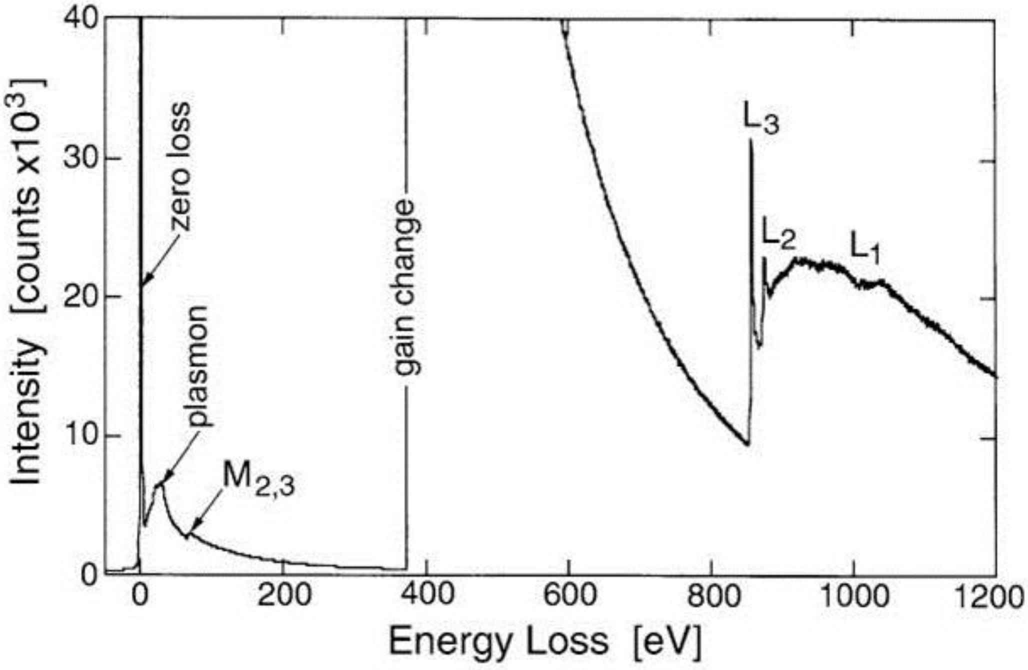

Figure 3.12: EELS spectrum of Ni metal showing zero loss, plasmons, and L-edge white lines (from Fultz and Howe, 2002).

3.3.3.3 Inner shell excitations

The most important feature for structural analysis in EELS is the inner shell excitations. The shapes of ionization edges exhibit considerable fine structure about the material due to molecular and/or solid state effects (Egerton, 2003; Egerton and Malac, 2005b; Egerton, 2011). Calculations from atomic theory indicate that K-edges has a triangular (sawtooth) shape while L, M, and high order edges can display rounded edges or sharply peaked edges (displaying so called white lines) as shown in Figure 3.12. This feature is caused by the excitations of core atomic electrons when high-energy electrons undergo inelastic scattering. The electron beam transfers sufficient amount of its energy to tightly bound core-shell electrons (K, L, M, N, etc, shells). The edge threshold occurs at the binding energies E_{k} of these shells. Since the shells (K, L, M, N, etc) correspond to the main principal quantum number $\mathrm{n} = 1,2,3,4,$ etc, respectively, the energy of these electrons in these shells has energies of the order of (Reimer, 1997)

$$E_n = -R\,(Z - \sigma_n)^2/n^2 \tag{3.42}$$

where R is the ionization energy and $Z - \sigma_n$ is the effective atomic number, decreased by screening.

From a quantum mechanics point of view, electrons from $\mathrm{n} = 1, 2, 3, 4,$ etc, energy levels may have *s*, *p*, *d*, *f*, and g states which correspond to the orbital quantum numbers $l = 0, 1, 2, 3, 4$ respectively (Reimer, 1997; Williams and Carter, 2009). There are $l = 0, 1, \ldots, n - 1$ possible values of the orbital quantum number resulting in quantized angular momentum $= \sqrt{l(l+1)\hbar}$. The electrons within these energy levels also have a spin quantum number described by $s = \pm\frac{1}{2}$ with angular momentum $= \sqrt{s(s+l)\hbar}$. The sum of the orbital quantum number (l) and the spin quantum number (s) results in the total quantum number $j = l \pm s$ with angular momentum $J = \sqrt{j(j+1)\hbar}$ (Reimer, 1997). Ionization edges in EELS are labelled according to the ionized subshell, e.g. K-edge (Figure 3.13). In the K-edge the electron is only in the 1s state and can only give rise to single K-edge.

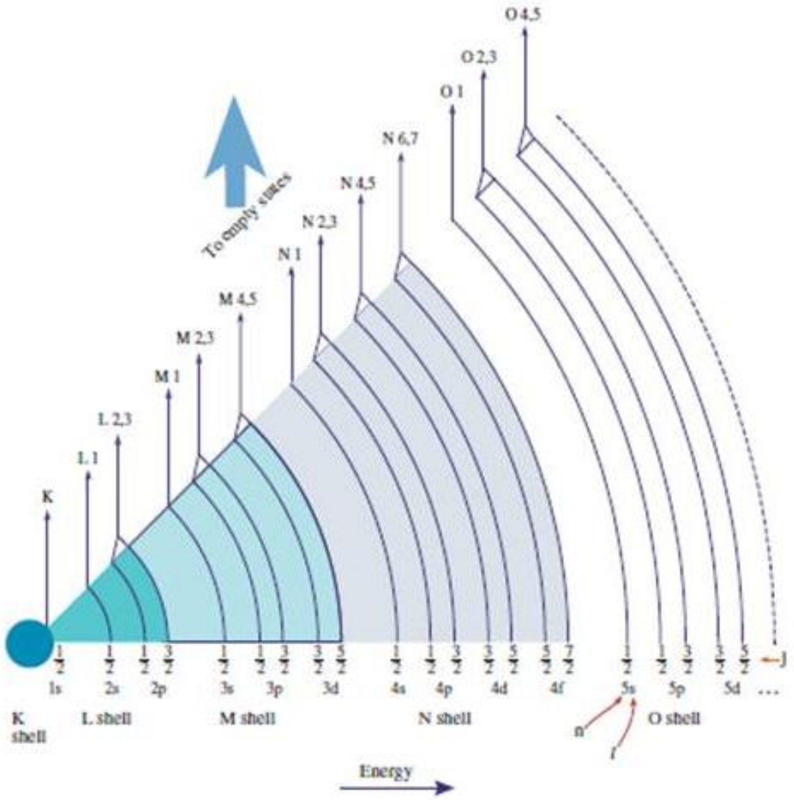

Figure 3.13: EELS edges nomenclature (Williams and Carter, 2009).

Unlike the K shell which only has only one energy level, the L shell has electrons in either 2s or 2p orbitals. The ejection of 2s electron gives an L_1 edge and while the ejection of an electron from a 2p orbital creates either an L_2 or L_3 edge. Splitting of the L shell into three subshells L_1, L_2, and L_3 is called spin orbit splitting (Williams and Carter, 1996; Fultz and Howe, 2002; Williams and Carter, 2009). Electrons in the core-shell cannot be excited to just any unoccupied state. The dipole-selection rule (described in section 1.2.4) states that the change Δl in the orbital quantum number between the initial and final states must be equal to ±1. From the dipole-selection rule the only permitted final state for the 2s electron in the L shell is the p state, and that gives a very weak ionization L_1 edge (Williams and Carter, 1996; Fultz and Howe, 2002; Williams and Carter, 2009). The dipole selection rule allows the excitation of 2p electrons to unoccupied 3d states. The same quantum rules apply to higher shells i.e. M, N, O, etc and their possible edges are shown in Figure 3.13.

3.3.3.4 EELS fine structure

Electron energy loss fine structures are observed in regions around core loss edge and they show distinct features that can be used to identify the local chemical environment of the specimen (Fultz and Howe, 2002). Fine structures around the ionization edge onset (within 30-50eV) are known as electron energy loss near-edge fine structure (ELNES). And oscillations from electron which escape from the atom instead of filling empty states is known as extended energy-loss fine structure (EXELFS). Only ELNES will be the subject of this discussion and interested reader about EXELFS can read about it elsewhere (Fultz and Howe, 2002; Williams and Carter, 2009). ELNES depends on the number and energy of density of unoccupied states (DOS) above the Fermi level of the excited atom (Fultz and Howe, 2002; Williams and Carter, 2009; Egerton, 2011).

Metals (like transition metals and rare-earth) with high densities of states at the Fermi have sharp features at their absorption edges. Such features are known as white lines and they arise from transitions into unoccupied d and f states. White lines are intense peaks in ionization edges occurring near the onset of $L_{3,2}$ edges of transition metals (Fultz and Howe, 2002; Williams and Carter, 2009; Egerton, 2011). As mentioned in previous paragraph the L_3 and L_2 lines correspond to electron transitions from $2\mathrm{p}_{3/2}$ and $2\mathrm{p}_{1/2}$ states to unfilled d states, respectively. The $(2j+1)$ degeneracy of the initial $2p_j$ $(j=\frac{1}{2},\frac{3}{2})$ states tells us that there are four $2\mathrm{p}_{3/2}$ electrons and two $2\mathrm{p}_{1/2}$ electrons, that gives a white line intensity ratio $(I(L_3)/I(L_2))$ of 2. However, Leapman and Grunes, 1980 reported high $(I(L_3)/I(L_2))$ ratios for some 3d transition metals. It is known that EELS white lines of first row transition metals contains a a wealth of information about the density of unoccupied states near the Fermi level and the chemical bonding of the metal. Density of unoccupied states can be quantitatively determined by integrating the intensities of white lines.

Another important effect observed in ELNES is the edge-onset shift known as chemical shift of an edge. Chemical shifts can be measured by EELS to an accuracy of at least 1 eV (Egerton, 2003; Egerton, 2011). The combination of both $(I(L_3)/I(L_2))$ ratio and chemical shifts can be used to get information about local atomic environment.

From ELNES structures elements in similar compounds or environment can be identified when reference spectra are available (Reimer, 1997). This means that even without the knowledge of DOS and Fermi surfaces, bond information can be determined by comparing observed experimental ELNES with standard specimens. The fingerprint method avoids comparing ELNES structures with theoretical calculated structures using band structure and DOS.

3.3.3.5 EELS instrumentation

Electron energy loss spectroscopy is a TEM fitted spectrometer which forms an energy-loss spectrum by measuring the changes in the energy distribution of an electron beam transmitted through a thin specimen (Egerton, 2003; Egerton, 2005a). The incident beam carries monoenergetic electrons which after interaction with the specimen emerge with an energy distribution that can be used to measure chemical and structural properties of the material (Egerton, 2003; Egerton and Malac, 2005b; Egerton, 2011). Electrons distinguished according to their kinetic energies (E_k = *Electron incident energy* (E_0) *– Energy loss in the specimen*) are drawn into the spectrometer (Egerton and Malac, 2005b). Only electrons scattered at small angles enters the EEL spectrometer and forms the EEL spectrum.

The most common and simplest form of EELS system is the post-column filter approach. In this method the electron spectrometer is mounted below the TEM viewing screen and at the heart of the filter lies the magnetic prism spectrometer (Figure 3.14). Other EELs systems are well-documented elsewhere for an interested reader (Egerton, 2003; Egerton, 2011).

In a uniform sector field ($\vec{B}$) from the magnetic prism Lorentz forces bend electrons of equal energies into curvatures of equal radius $R = {}^{mv}/_{eB}$ (where m = electron relativistic mass, v = speed of electron, and e = electronic charge) and drifts it to large angles (typically 90˚) (Reimer, 1997; Fultz and Howe, 2002; Egerton, 2011).

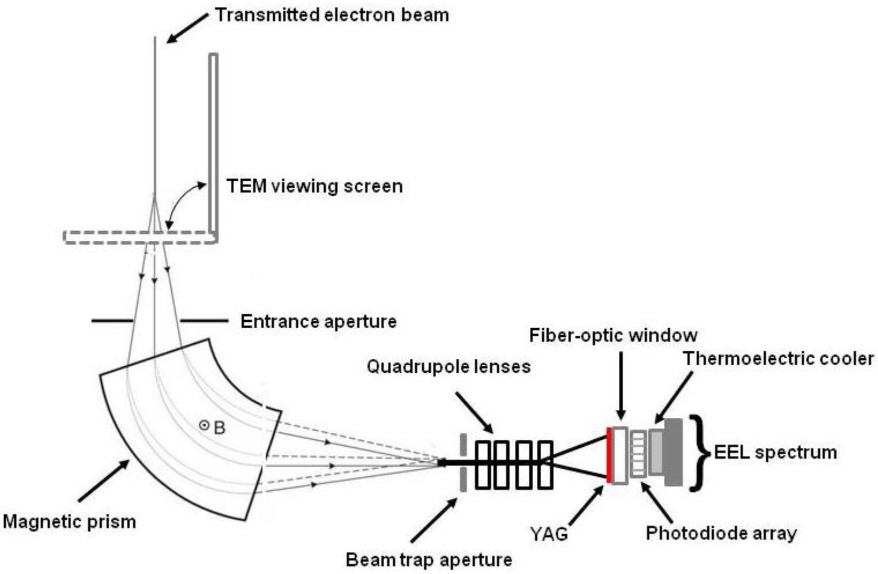

Figure 3.14: Post-column electron energy loss system. The magnetic prism disperses and focuses electron beam (slightly modified from Egerton, 2011).

The electron inside the magnetic sector field will also experience the Lorentz magnetic force (Egerton, 2003; Egerton and Malac, 2005b; Egerton, 2011):

$$\vec{F} = -e\vec{v} \times \vec{B} = Bev = \frac{mv^2}{R} \tag{3.43}$$

which provides the energy dispersion of electrons. The bending and dispersion actions by the magnetic prism resemble that of glass prism in the bending and dispersion of white light. However, in the case of the magnetic field prism on the electrons there is also a focusing action from the magnetic sector. Electrons are aligned according to their energies and an EEL spectrum is recorded by a photodiode array fiber optically coupled to a YAG scintillator (Figure 3.14).

3.4 Mössbauer Spectroscopy (MS)

3.4.1 Introduction

Mössbauer spectroscopy (MS) is a nuclear technique that involves the recoilless emission and resonant absorption of γ-rays by identical nuclei bound to solids (Wertheim, 1964; Goldanskii and Herber, 1968; May, 1971; Long, 1984; Long and Grandjean, 1993; Murad and Cashion, 2004; Dyar *et al.*, 2006). The technique based on Mössbauer effect was first investigated for the purpose of determining the coherence of phase of the scattered radiation. Nowadays MS is widely used in mineralogy and chemistry to provide a wide range of information on structural properties, valence state, bonding and site occupancies, magnetic properties, cation distribution and the coordination environment of iron.

3.4.2 The Mössbauer effect

Radioactive nuclides emit γ-rays when they undergo transitions from the excited nuclear states to the ground states during nuclear decays. The emitted γ-rays can be resonantly absorbed by identical nuclei which then undergo transitions from the ground states to excited nuclear states (Wertheim, 1964; Goldanskii and Herber, 1968; May, 1971; Long, 1984; Long and Grandjean, 1993; Murad and Cashion, 2004; Dyar *et al.*, 2006). During nuclear transitions an emitting nucleus (see Figure 3.15) gives off γ-rays with imparting momentum $\vec{p}_{\gamma}$. The law of momentum conservation dictates that the nucleus recoils with momentum $\vec{p}_{emitter} = -\vec{p}_{\gamma}$. The kinetic energy of recoil (E_R) is given by Eq. 3.44 (Dyar *et al.*, 2006).

$$E_R = \frac{(\vec{p}_{nucleus})^2}{2M_n} = \frac{\left(\vec{p}_{\gamma}\right)^2}{2M_n} = \frac{E_{\gamma}^2}{2M_n c^2} \qquad 3.44$$

where c is the speed of light, M_n is the mass of the nucleus, and E_{γ} is the energy of the gamma photon. The absorbing nucleus also experiences recoil, with $\vec{p}_{absorber} = +\vec{p}_{\gamma}$.

For γ-rays emitted by the source to be absorbed the resonance conditions must be fulfilled: the energy of the incident γ-rays must match the nuclear transition energy of the absorbing nucleus. This can be achieved only if the absorbing nucleus is identical to the emitting nucleus (May, 1971; Dyar *et al.*, 2006).

Due to recoils experienced during nuclear transitions resonant absorption does not occur for free nuclei, i.e. the energy of the incident γ-rays does not match with the nuclear transition energy of the absorber. This is so because for free nuclei the recoil energy of both the source and absorber are relatively large such that the spectral distributions of the emitter and absorber do not overlap (May, 1971; Dyar *et al.*, 2006).

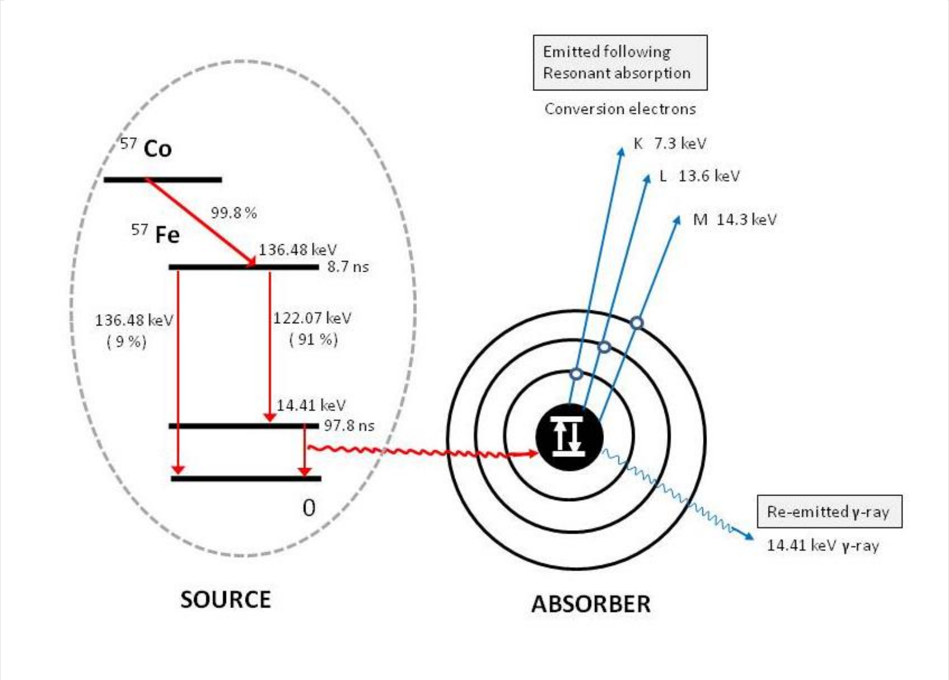

Figure 3.15: Nuclear decay scheme for ^{57}Co → ^{57}Fe (Modified from Dyar *et al.*, 2006).

In 1957 Rudolf L. Mössbauer found that when the nucleus is bound to a lattice the recoil energy can be neglected since the recoil energy is absorbed by the whole lattice rather than a single nucleus. In this case the mass of a nucleus M_n in Eq. 3.44 can be substituted for the mass of the whole solid (M) such that $E_R \approx 0$ for the solid since $M >> M_n$. That is, the emission and absorption occur virtually without any loss of energy by γ-rays. This is referred as the Mössbauer Effect (Wertheim, 1964; Goldanskii and Herber, 1968; May, 1971; Long, 1984; Long and Grandjean, 1993; Murad and Cashion, 2004; Dyar *et al.*, 2006). The MS technique based on this effect is used to measure very small changes in nuclear energy levels caused by interactions between the nucleus and its environment. Recoiless γ-rays have very narrow linewidths.

3.4.3 Mössbauer parameters

Very often, nuclei in the source and the absorber are in different chemical/physical environments. They do interact with their nearest neighbours through electric and/or magnetic interactions, commonly referred to as hyperfine interactions. These interactions produce different shift and/or splitting of the nuclear energy levels of the source and absorber since the local environments at the source and absorber are usually different. Much information about the valence state, coordination, the symmetry and the magnetic field at the Mössbauer nucleus can be obtained from Mössbauer parameters. The hyperfine interactions and the associated MS parameters are reviewed below.

3.4.3.1 Isomer shift (δ)

A nucleus carries a positive charge (protons) which interact (electric monopole interactions) with the surrounding electrons, mainly s-electrons. These interactions shift the nuclear energy levels of both the source and absorber. Due to the difference of their chemical environments the shift of the source and absorber are also different. As a result the centroid of the resonance spectrum shifts from the zero velocity as illustrated in Figure 3.16 (a). This is referred to as isomer shift, and is mathematically given by (Goldanskii and Herber, 1968; May, 1971; Long, 1984; Dyar *et al.*, 2006):

$$\delta = const\ [\ |\psi_s\ (0)|^2 - \ |\psi_a(0)|^2\ ]\ \frac{\Delta R}{R} \qquad 3.45$$

where $|\psi_s\ (0)|^2$ and $|\psi_a\ (0)|^2$ are the total electronic charge densities for the source and absorber, respectively, R is the average radius of the nucleus and ΔR represents the radius difference between the nuclear excited state and the nuclear ground state.

3.4.3.2 Quadrupole hyperfine splitting (Δ_{EQ})

All nuclei with nuclear spin quantum number, I, greater than half ($I > \frac{1}{2}$) possess nuclear quadrupole moments, Q (May, 1971; Neyens, 2003; Dyar *et al.*, 2006); it is a measure of the asymmetry of the nuclear charge distribution which gives rise to deviation of the nucleus from sphericity. The nuclear quadrupole moment can interact with an electric field gradient (EFG) at the nucleus (electric quadrupole interactions). The interaction between Q and EFG splits the excited nuclear energy level into ($I + \frac{1}{2}$) sublevels. For ^{57}Fe, the excited state ($I = 3/2$) splits into two sublevels (partial lifting of degeneracy) while the ground state ($I = 1/2$) does not split. This gives raises to two transition energies. Figure 3.16 (b) shows a graphic representation of quadrupole splitting (ΔE_Q), i.e. the distance between the two peaks. Mathematically the quadrupole splitting can be expressed as (May, 1971; Dyar *et al.*, 2006):

$$\Delta E_Q = \frac{1}{2}\, e^2 Q V_{zz} \left(1 + \frac{\eta^2}{3}\right)^{\frac{1}{2}} \tag{3.46}$$

where η is the asymmetry parameter and V_{zz} is the principal electric field gradient tensor. The asymmetric parameter η is given by (May, 1971; Dyar *et al.*, 2006):

$$\eta = \frac{|\, V_{xx} - V_{yy}|}{V_{zz}} \tag{3.47}$$

here V_{zz}, V_{yy}, V_{zz} denote the principal tensor components in order of decreasing modulus.

3.4.3.3 Hyperfine magnetic field ($\mathrm{B_{hf}}$)

All nuclei with a nuclear spin quantum number I > 0 possess magnetic dipole moments. The magnetic dipole moment of a nucleus with a spin I is given by $\mu = gI\mu_N$, with μ_N and g being the nuclear magneton and nuclear gyromagnetic ratio, respectively (May, 1971; Neyens, 2003; Dyar *et al.*, 2006). The interaction between the nuclear magnetic dipole moment μ and the magnetic field H at the nucleus (internally created by the surrounding electrons or externally applied) leads to a splitting of the nuclear energy levels into $2\mathrm{I}+1$ sublevels, i.e. a complete lifting of degeneracy through Zeeman effect. In the case of ^{57}Fe the excited state ($\mathrm{I}=3/2$) splits into four sublevels while the ground state ($\mathrm{I}=1/2$) splits into two sublevels. This gives rise to six transitions between the excited and ground states allowed by the selection rules ($\Delta M_I = 0, \pm 1$) as illustrated in Figure 3.16 (c). The Hamiltonian of the hyperfine magnetic interaction reads (Goldanskii and Herber, 1968; Long, 1984):

$$\mathrm{H_m} = -\mu\mathrm{H} = -\mathrm{g}\mu_\mathrm{N}\mathrm{IH} \qquad 3.48$$

and the energy eigenvalues are

$$\mathrm{E_n} = -\frac{\mu\mathrm{Hm_I}}{\mathrm{I}} = -\mathrm{g}\mu_\mathrm{N}\mathrm{m_I H} \quad (\mathrm{M_I} = \mathrm{I}, \mathrm{I}-1, \dots, -\mathrm{I}) \qquad 3.49$$

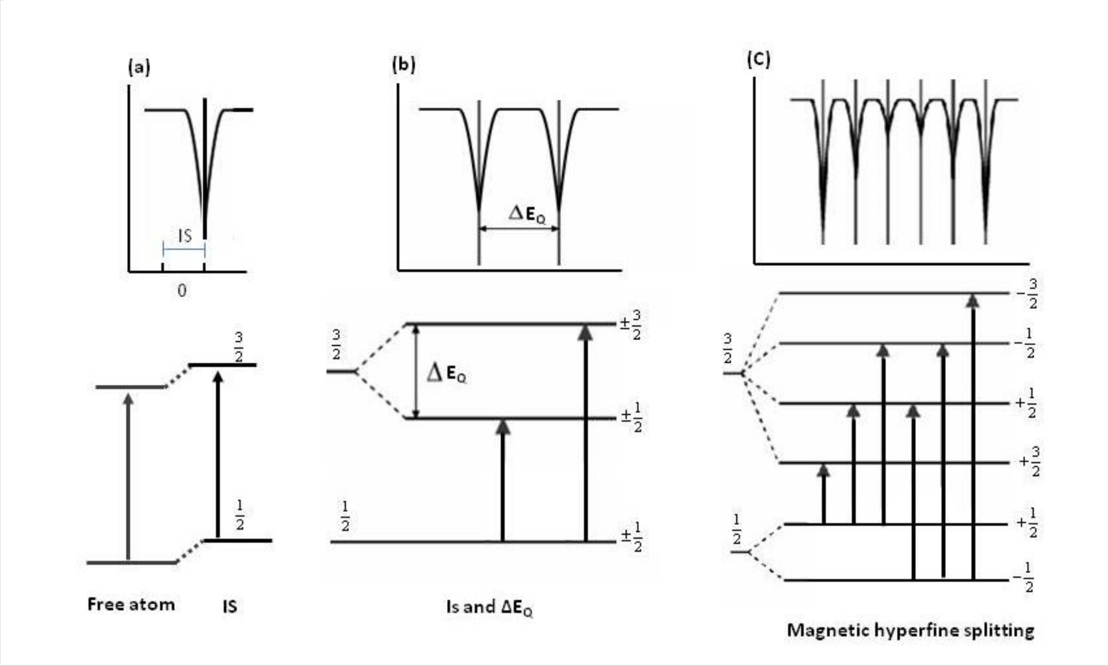

Figure 3.16: Schematic diagram showing hyperfine interactions. (a) Isomer shift, (b) Quadrupole splitting (doublet), and (c) Magnetic hyperfine splitting (sextet) (Dyar *et al.*, 2006).

As mentioned, by applying the magnetic dipole transition rule and assuming that the principal tensor component V_{zz} is zero, only six transitions are observed. The relative intensities of these sextets are given by $3{:}\,x{:}\,1{:}\,1{:}\,x{:}\,3$, where x is 2 if the sample is a random powder or unmagnetized foil, 4 if the γ-ray direction is normal to the magnetization and x is zero if the γ-ray direction is parallel to the magnetization direction (Long, 1984). Furthermore, the overall splitting of the spectrum is proportional to the magnetic field experienced by the nucleus and somehow proportional to the moment at the iron site. As a result, it is observed that above T_C or T_N the rapidly relaxing paramagnetic moments averages to zero, and only a paramagnetic doublet is observed (Figure 3.16 (b)). It has been established experimentally that below T_C and T_N the moments order and the nucleus experiences a static magnetization and magnetic hyperfine splitting is observed (Long, 1984).

The three MS hyperfine parameters, isomer shift, quadrupole splitting, and hyperfine magnetic field, can readily be determined from a MS spectrum. They act as fingerprints for phase identification as each species has a unique set of MS parameters. The areas under the absorption peaks of a MS spectrum give the relative contents of the associated phases. Other information obtained from the MS parameters includes the oxidation state, the spin state, the molecular symmetry and the nature of the magnetic interactions within the samples.

3.4.4 Mössbauer measurements

In a Mössbauer experiment the energy (monochromatic) of the incoming γ-rays is usually modified using the Doppler effect so as to account for (observe resonance) all the transition energies resulting from the shift and splitting of the energy levels (isomer shift, quadrupole splitting and magnetic splitting). To achieve this, the source is usually mounted on a transducer. The energy spectrum of the sample is scanned by varying the energy of the γ-rays (moving the source relative to the sample). The modified energy, E' , is given by the Doppler effect:

$$E' = E_\gamma \left(1 + \frac{v}{c}\right) \qquad 3.50$$

where v is the relative velocity, c is the speed of light, and E_γ is the γ-ray energy. The MS spectrometer consists in fact of two main parts: the driving system and the electronic system

(Figure 3.17). The driving system consists of a transducer, a driver and a digital function generator which has a main function to supply the signals needed by the transducer.

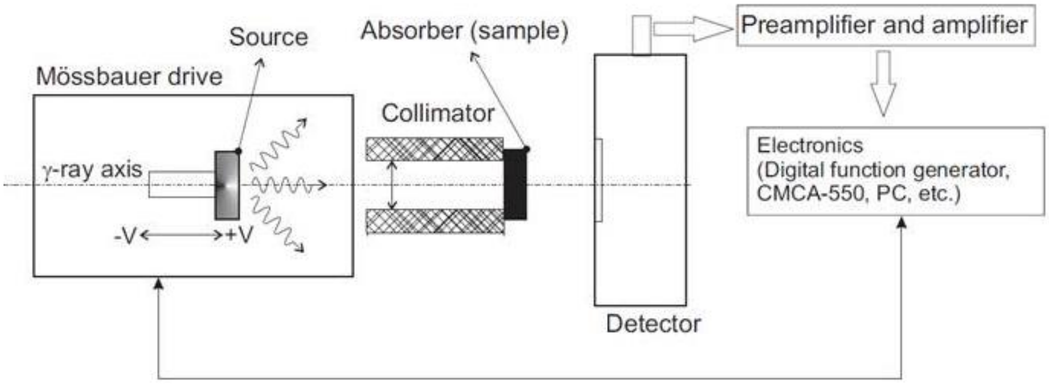

Figure 3.17: Schematic diagram of a transmission Mössbauer spectrometer setup (from Subramanian, 2010).

The electronic part consists of a detector, a preamplifier, an amplifier, a single channel analyser (to select the appropriate γ-rays energy), a data storage devise (multichannel analyser, MCA) and a computer for data display. The motion of the transducer is synchronised with the opening of the channels the multichannel analyser such that each velocity (energy) corresponds to only one channel of the MCA.

3.5 Magnetic properties measurements

3.5.1 Basics of magnetism

Magnetism originates mainly from the orbital motions of electrons about the nucleus and from spin motions of electrons. The magnetic dipole moment associated with the orbital motions amounts to (Buschow and de Boer, 2003; Orchard, 2007)

$$\vec{\mu}_L = -\frac{e}{2\,m_e}\vec{L} = -\frac{e}{2\,m_e}\hbar\vec{l} = -\mu_B\vec{l} \qquad 3.51$$

where $\vec{l}$ is the angular momentum of an electron and $\mu_B = e.\hbar/2\ m_e = 9.27 \times 10^{-24}$ J/T is the Bohr magneton. The absolute value of the orbital magnetic moment is

$$|\vec{\mu}_l| = \mu_B\sqrt{l(l+1)} \qquad 3.52$$

where l = 0, 1, 2, 3, …, n-1 is the orbital angular momentum quantum number and n the principal quantum number. The magnetic dipole moment associated with the spin is given by (Buschow and de Boer, 2003; Orchard, 2007)

$$\vec{\mu}_S = -g_e \frac{e}{2\ e_e}\vec{S} = -g_e \frac{e}{2\ m_e}\hbar\vec{l} = -g_e\mu_B\vec{s} \qquad 3.53$$

where $g_e = 2.002290716$ is the g-factor for a free electron and $\vec{s}$ the spin angular momentum. The total angular momentum is of an atom is (Buschow and de Boer, 2003; Orchard, 2007)

$$\vec{J} = \sum_i \left(\vec{l}_i + \vec{s}_i\right) = \vec{L} + \vec{S} \qquad 3.54$$

and the corresponding magnetic dipole moment is

$$\vec{\mu}_J = -\mu_B\left(\vec{L} + g_e\vec{S}\right) = -g\mu_B\vec{J} \qquad 3.55$$

where g is the Landé’s g-factor defined as

$$g = 1 + \frac{J\,(J+1) + S(S+1) - L(L+1)}{2J\,(J+1)} \qquad 3.56$$

The values of L, S and J for a free atom in the ground state are determined using Hund’s rules (Buschow and de Boer, 2003):

1. S takes the highest value (maximum) S allowed by the exclusion principle.
2. L takes the highest value possible consistent with the value of S (1st rule).
3. If the electron shells are less than half full, J = L – S; if the shells are more than half full, J = L + S.

The net magnetic moment of an atom, also called effective magnetic moment is (Buschow and de Boer, 2003; Orchard, 2007; Culity and Graham, 2009)

$$\mu_{eff} = g\mu_B\sqrt{J\,(J+1)} \qquad 3.57$$

For transition metals the magnetic properties arise mainly from d-orbitals. These d-orbitals are usually perturbed by ligand field splitting thus leading to a quenching (cancellation) of the orbital angular momentum (L) (Buschow and de Boer, 2003; Orchard, 2007; Culity and Graham, 2009). That is, the rotation of electrons about the nucleus is blocked (restricted) by the crystalline field such that L = 0 and the effective magnetic moment is

$$\mu_{eff} = \mu_S = g_e\mu_B\sqrt{S(S+1)} = 2\ \mu_B\sqrt{S(S+1)} \qquad 3.58$$

The 4f electrons are not affected by surrounding ligands (the electronic configuration $4f^n5s^25p^6$ put them too far inside compared to d-electrons in transitions metals) (Culity and Graham, 2009). Thus, the magnetic properties of Lanthanides are determined by their J-states and Eq. (3.56) applies to them.

Table **3.1** gives typical values of calculated (theoretical) and experimental magnetic dipole moments for selected transition elements (Buschow and de Boer, 2003).

Magnetism occurs in all materials but to different degrees. Depending on the existence or absence of a permanent atomic magnetic dipole moment a material can be classified as diamagnetic (Dia) if there is no permanent magnetic dipole moment at atomic level or paramagnetic (PM) if there is a permanent dipole magnetic moment at atomic level. Diamagnetism occurs in atoms with paired electrons such that such that the magnetic dipole moments of all electrons cancel out one another while atoms in PM materials have unpaired numbers of electrons on outer shells such that an atom has a net magnetic dipole moment. Applied magnetic fields induce magnetic dipole moments in Dia substances which are opposed to the applied field. In other words, atoms in Dia substances exhibit induced magnetic dipole moments only in applied magnetic field while atoms of PM materials have intrinsic magnetic dipole moments even in the absence of applied magnetic field.

Table 3.1: Theoretical (columns 8, 9 and 10) and experimental (labelled as M_{eff} in column 7) effective magnetic dipole moments for selected transition elements. The difference between the calculated and experimental M_{eff} is mainly due to orbital quenching (adapted from Buschow and de Boer, 2003).

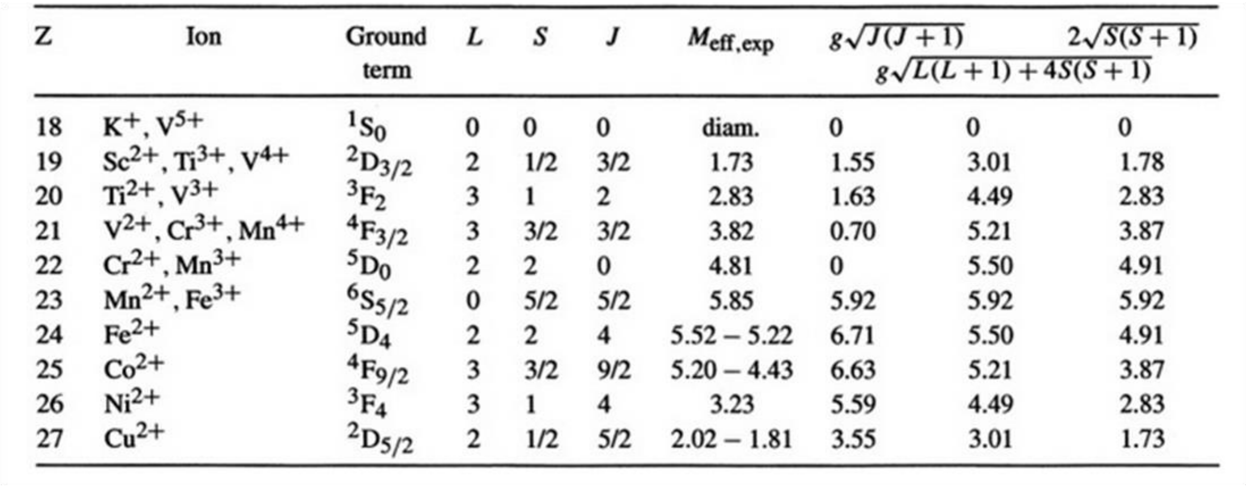

Z	Ion	Ground	L	S	J	$M_{\mathrm{eff,exp}}$	$g\sqrt{J(J+1)}$		$2\sqrt{S(S+1)}$
		term						$g\sqrt{L(L+1)+4S(S+1)}$	
18	K^+, V^{5+}	$^1S_0$	0	0	0	diam.	0	0	0
19	Sc^{2+}, Ti^{3+}, V^{4+}	$^2D_{3/2}$	2	1/2	3/2	1.73	1.55	3.01	1.78
20	Ti^{2+}, V^{3+}	$^3F_2$	3	1	2	2.83	1.63	4.49	2.83
21	V^{2+}, Cr^{3+}, Mn^{4+}	$^4F_{3/2}$	3	3/2	3/2	3.82	0.70	5.21	3.87
22	Cr^{2+}, Mn^{3+}	$^5D_0$	2	2	0	4.81	0	5.50	4.91
23	Mn^{2+}, Fe^{3+}	$^6S_{5/2}$	0	5/2	5/2	5.85	5.92	5.92	5.92
24	Fe^{2+}	$^5D_4$	2	2	4	5.52 – 5.22	6.71	5.50	4.91
25	Co^{2+}	$^4F_{9/2}$	3	3/2	9/2	5.20 – 4.43	6.63	5.21	3.87
26	Ni^{2+}	$^3F_4$	3	1	4	3.23	5.59	4.49	2.83
27	Cu^{2+}	$^2D_{5/2}$	2	1/2	5/2	2.02 – 1.81	3.55	3.01	1.73

Due mainly to peculiar features of their electronic structures magnetic dipole moments of adjacent atoms (or molecules) in PM materials may exhibit collectively strong short-range interactions, known as exchange interactions, in certain temperature ranges (Buschow and de Boer, 2003; Culity and Graham, 2009). Below certain critical temperatures these materials become ferromagnetic (FM), antiferromagnetic (AFM) or ferrimagnetic (FiM) (see also section 2.2.1). These magnetic orderings are also known as collective, cooperative or ordered forms of magnetism. The critical temperatures or magnetic transition temperatures are referred to as Curie temperature (T_C) for ferromagnetic and ferrimagnetic materials and Néel temperature (T_N) for antiferromagnetic materials as indicated in section 2.2.1.

3.5.2 Magnetic measurements

In magnetic measurements the responses of a material to an applied magnetic field (H) are measured in terms of:

- Volume magnetization[1] (M) defined as the total magnetic dipole moment per unit volume.

$$\vec{M} = \frac{\sum_{\text{atom}} \vec{\mu}}{\text{Volume}} \qquad 3.59$$

- Mass magnetization[2] (M or σ) defined as the total magnetic dipole moment per unit mass.

$$\vec{\sigma} = \frac{\sum_{\text{atom}} \vec{\mu}}{\text{Mass}} \qquad 3.60$$

For FM and FiM materials at sufficiently large applied magnetic field the magnetization reaches saturation when all the moments are aligned with the direction of the applied magnetic field. The saturation magnetization (M_S) which is an intrinsic property of a specific material is given by (Buschow and de Boer, 2003; Culity and Graham, 2009)

$$M_S = \frac{N_A g\, \mu_B}{2} = N_A\, g\, S \qquad 3.61$$

where $N_A = 6.022 \times 10^{23}$ mol^{-1} is the Avogadro number.

The response of a material to an applied magnetic field is also dependent of the medium in which it is placed. The overall response, taking into account the intrinsic material response (magnetization, M) and the influence of the medium is expressed in terms of the magnetic induction[3] (B) also referred to as magnetic flux density. B is the actual magnetic field inside a material; it is usually larger than the applied magnetic field (H), except for diamagnetic materials that are expelled by a magnetic field. The responsiveness of a material to an applied magnetic field is measured by the magnetic susceptibility (χ) which measures the ease with which the material can be magnetized in an applied field (Buschow and de Boer, 2003; Orchard, 2007; Culity and Graham, 2009),

$$\chi = \frac{\vec{M}}{\vec{H}} \qquad 3.62$$

---

[1] The units of volume magnetization are emu/cm^3 (in cgs) and A/m (in SI). The cgs unit of volume magnetization expressed as $4\pi M$ is Gauss (G).

[2] The units of mass magnetization are emu/g and emu/mol (in cgs), A.m^2/kg (in SI).

[3] The units of magnetic induction are Gauss (G) (in cgs) and Tesla (T) or Weber per square meter (Wb/m^2) (in SI).

Although χ is dimensionless, it is often conveniently expressed as mass susceptibility[4] (χ) defined as a ratio of the mass magnetization to the applied magnetic field ($\chi = \sigma/\mathrm{H}$), volume susceptibility[5] (κ) defined as a ratio of the volume susceptibility to the applied magnetic field ($\kappa = \mathrm{M}/\mathrm{H}$) or molar susceptibility[6] (χ_{mol}) defined as

$$\chi_{\mathrm{mol}} = \chi \, . \, \mathrm{MM} \qquad 3.63$$

where χ is the mass susceptibility and MM stands for molar mass. Volume and mass magnetic susceptibility are related, i.e.

$$\kappa = \rho \, . \, \chi \qquad 3.64$$

where ρ is the density.

The ability of a material to be magnetized in response to an applied magnetic field in a specific medium is referred to as magnetic permeability[7] (Buschow and de Boer, 2003; Culity and Graham, 2009),

$$\mu = \frac{\vec{\mathrm{B}}}{\vec{\mathrm{H}}} \qquad 3.65$$

The overall magnetic induction inside a magnetized material reads (Buschow and de Boer, 2003; Culity and Graham, 2009)

$$\vec{\mathrm{B}} = \mu_0\left(\vec{\mathrm{H}} + \vec{\mathrm{M}}\right) = \mu_0\left(\vec{\mathrm{H}} + \chi\vec{\mathrm{H}}\right) \qquad 3.66$$

where $\mu_0 = 4\pi \ 10^{-7}$ N.A^{-2} is the magnetic permeability of vacuum. Magnetic permeability can be expressed in terms of magnetic susceptibility as

$$\mu = \mu_0(1 + \chi) \qquad 3.67$$

The magnetic susceptibility of Dia materials is temperature independent while that of PM materials varies linearly as a function of temperature and obeys the Curie law (Culity and Graham, 2009)

---

[4] The units of mass magnetic susceptibility are emu/g or cm^3/g (in cgs) and m^3/kg (in SI).

[5] Volume magnetic susceptibility is in fact dimensionless in both cgs and SI. However, it is often expressed in emu/cm^3 or emu/g (in cgs) and m^3/kg (in SI).

[6] The units of molar magnetic susceptibility are emu/mol or cm^3/g (in cgs) and m^3/kg (in SI).

[7] Magnetic permeability is dimensionless in both cgs and SI.

$$\chi = \frac{C}{T} \qquad 3.68$$

where C is a constant known as the Curie constant. Both the diamagnetism and paramagnetism are referred to as linear forms of magnetism while collective forms of magnetism (FM, FiM and AFM) are referred to as non-linear magnetism, i.e. below T_C and T_N FM, FiM and AFM materials have non-linear responses to applied magnetic fields. For these materials the temperature dependence of the magnetic susceptibility obeys a more general law, known as Curie-Weiss law (Buschow and de Boer, 2003; Culity and Graham, 2009),

$$\chi = \frac{C}{T - \theta} \qquad 3.69$$

where θ is the Weiss constant; $\theta = 0$ for an ideal PM material, $\theta > 0$ indicate the presence of FM interactions and $\theta < 0$ indicate AFM interactions. Figure 3.18 shows the temperature dependence of the magnetization (σ_s) and reciprocal magnetic susceptibility ($1/\chi$) for Dia, PM, FM, FiM and AFM meterials. The constant C relates the magnetic susceptibility to the effective magnetic moment, i.e. (Buschow and de Boer, 2003; Culity and Graham, 2009)

$$C_m = \frac{N_A\, \mu_{eff}^2}{3\, k_B} \qquad 3.70$$

giving,

$$\mu_{eff} = \sqrt{\frac{3\, k_B\, C_m}{N_A}} = 2.828\sqrt{C_m} \qquad 3.71$$

where C_m is the Curie constant corresponding to molar magnetic susceptibility (χ_m) and k_B the Boltzmann constant.

Superparamagnetism (SPM) is a peculiar magnetic ordering of materials exhibiting collective magnetism (FM, FiM and AFM) which make them to exhibit a paramagnetic behavior at temperatures below T_C or T_N and above a critical temperature known as blocking temperature, T_B (see also section 2.2.1). It is caused by the thermal energy (k_BT) which becomes strong enough to spontaneously destroy the collective ordering of an assembly of FM, FiM and AFM nanoparticles and induces a spontaneous reversal of the directions of the magnetization when the crystallite size is small enough, below a certain threshold diameter (dependent on the nature of the materials and the preparation conditions). The threshold diameter varies in the range 10-30 nm for most iron oxides.

The dynamic response of an assembly of nanoparticles depends on the measuring time (τ_m) of the experimental technique used. Typically $\tau_m \sim 100\ s$ for magnetometry (Goya *et al.*, 2003). For single-domain particles, the time required to reverse the directions of the magnetic moments (relaxation time) over the anisotropy energy barrier ($E_a = KV$) is described by the Néel-Brown equation (Bødker *et al.*, 1994; Das *et al.*, 2010)

$$\tau = \tau_0 \exp\left({}^{KV}\!/_{k_B T}\right), \qquad 3.72$$

assuming non-interacting particles and uniaxial anisotropy. In Eq.3.72, K is the anisotropy constant, V the volume, T the absolute temperature, k_B the Boltzmann's constant and τ_0 is an attempt time typically in the range 10^{-12} – 10^{-9} s. Considering $\tau_0 \approx 10^{-9}$ s and $\tau_m \sim 100\ s$ Eq. 3.72 can be rearranged as (Carta *et al.*, 2009)

$$KV = \ln\left({}^{\tau_m}\!/_{\tau_0}\right) k_B T \ \approx 25\ k_B T \qquad 3.73$$

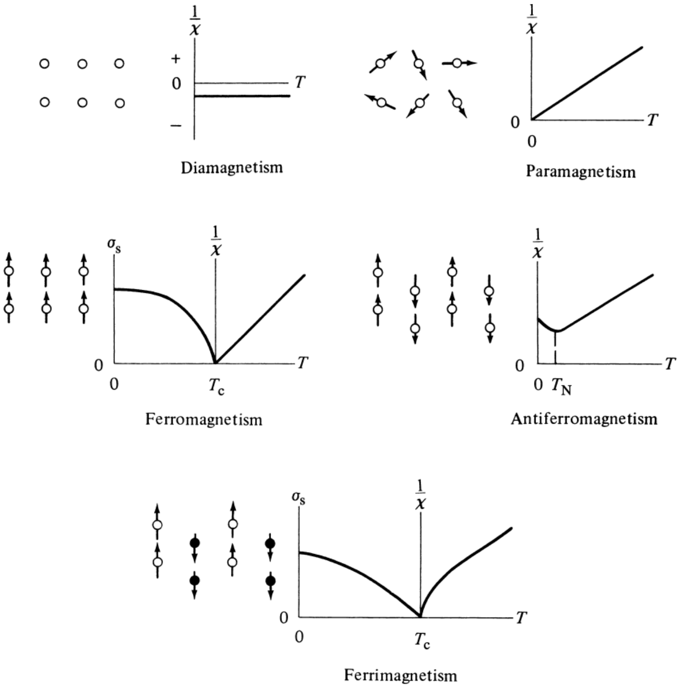

Figure 3.18. Temperature dependence of the magnetization (σ_s) and the reciprocal magnetic susceptibility ($1/\chi$) for Dia, PM, FM, AFM and FiM materials (extracted from Culity and Graham, 2009).

3.5.3 Magnetic measurements techniques

The magnetic moment in a sample can be measured by the force (Gouy method, Faraday balance), torque or induction techniques. In conventional inductive magnetometers the sample moves relative to a set of pickup coils, either by one-shot extraction or by vibration while the voltage induced by the moving magnetic moment of the sample in the coils is measured (Culity and Graham, 2009). That is, the voltage induced in the pickup coils is proportional to the magnetic moment in the sample.

In a vibrating sample magnetometer (VSM) the sample moves (by vibration) inside a set of pick up coils and the voltage induced by the moving magnetic moment of the sample in the coils is measured (Buschow and de Boer, 2003; Culity and Graham, 2009). The sample is attached to one end of a nonmagnetic rod, the other end of which is fixed to a mechanical vibrator (a linear motor). The moving sample generates an oscillating magnetic field which induces an alternating electromotive force (emf) in the detection coils whose magnitude is proportional to the magnetic moment of the sample. The alternating emf is then amplified with a lock-in amplifier which is sensitive only to signals at the vibration frequency. The instrument must be calibrated with a specimen of known magnetic moment having the same size, shape and permeability as the sample to be measured (Culity and Graham, 2009).

A more sensitive inductive technique uses a set of superconducting pickup coils and a superconducting quantum interference devise (SQUID) to measure the current induced in the pickup coils. The magnetic moment measured is independent of the sample speed during extraction. A SQUID magnetometer is of such high sensitivity that in an operating instrument the magnetic field is held exactly constant by a superconducting shield. The sample is moved slowly through a superconducting pickup coil coupled to the SQUID while flux quanta are counted (Culity and Graham, 2009). A superconducting magnet is required for the SQUID to operate. A SQUID magnetometer can achieve sensitivity of up to 10^{-8} emu or 10^{-11} $A.m^2$, i.e. one to two orders of magnitude more sensitive than the VSM (Culity and Graham, 2009).

3.6 X-ray diffraction

3.6.1 Introduction

X-ray powder diffraction is a powerful technique for structure and phase determination of crystalline materials (Suryanarayana and Norton, 1998; Pecharsky and Zavalij, 2009). The technique relies on interaction of X-rays with the electronic structure of materials. X-rays are scattered by periodic lattices of the crystals and diffraction peaks are observed when the incident beam and diffracted beam interfered constructively. The reflection of X-ray by crystals planes was envisaged by Bragg according to this relationship which is today known as the Bragg law (Suryanarayana and Norton, 1998; Hammond, 2009; Pecharsky and Zavalij, 2009):

$$2d_{hkl} \, sin \, \theta = n\lambda \qquad 3.74$$

where d_{hkl} is the interplanar spacings, θ is the Bragg angle, n is an integer known as the order of reflection and λ is the wavelength of the incident X-rays. Detailed derivation and explanation of Bragg's law can be found elsewhere (Hammond, 2009). Briefly, a Bragg diffraction pattern will be produced when an incident wave front with parallel propagation vectors, which form an angle θ with the *hkl* planes of the crystal, will constructively interfere with the reflected wave front that forms the same angle θ with all planes if specular reflection (mirror-like) conditions are met as depicted in Figure 3.19.

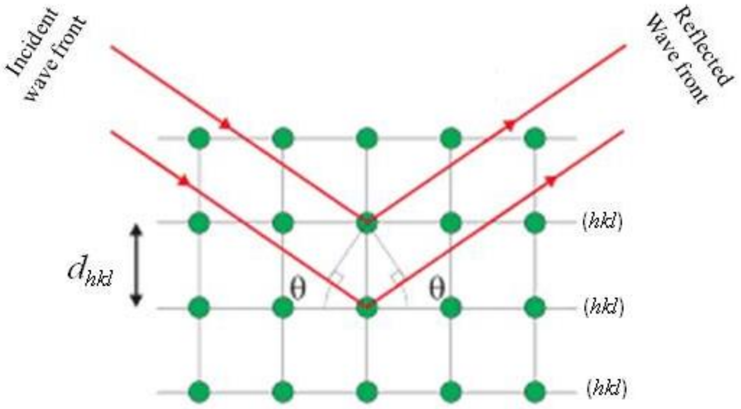

Figure 3.19: Geometrical illustration of Bragg's law (from Als-Nielsen and McMorrow, 2011).

The visual representation of the phenomenon of X-rays diffraction (XRD) by crystals by the Ewald sphere is the same as that of electron diffraction and it is covered in section 3.1 of the thesis. In a diffraction pattern X-ray intensities are recorded as a function of 2θ angle. By plotting the intensities and positions (2θ angles) of the resultant diffracted peaks of radiation produces a pattern, which is a distinctive feature of the material being studied (see section 1.2).

3.6.2 The powder diffraction pattern

The shape, peak and intensity of diffracted peaks are vital in the refinement of a diffraction pattern (Pecharsky and Zavalij, 2009). In this section, a brief discussion of their significance is presented.

3.6.2.1 Peak Shape

In a perfect crystal and perfect diffractometer, very sharp diffraction peaks will be observed. However, in reality there is no such thing as perfect crystal or perfect diffractometer. As a consequence, Bragg diffraction patterns will display peaks with widths resulting from the instrument and sample imperfections. The peak-shape-function (PSF) which is the convolution of the instrumental broadening (Ω) wavelength dispersion (Λ) specimen function (Ψ) and the background function (b) it can be represented as (Pecharsky and Zavalij, 2009):

$$PSF\ (\theta) = \ \Omega(\theta)\ \otimes \Lambda(\theta) \oplus \Psi(\theta) + \ b\ (\theta) \qquad 3.75$$

The peak shape of an XRD pattern is important in studying materials properties such as materials disorder and defects. The main contributors in Ψ are the stress and strain present in the specimen. In addition, variation in instrumental parameters such as axial divergence and nonideal specimen geometry causes peak asymmetry. The asymmetry in the XRD pattern is strongly dependant on the Bragg angle, as such it is prominently visible at low Bragg angles (2θ below $\sim 20° - 30°$) (Pecharsky and Zavalij, 2009). Particle or grain size also contributes in peak width. It can be determined from the following mathematical approximation known as the Scherrer equation (Pecharsky and Zavalij, 2009):

$$\tau = \frac{k\lambda}{\beta \cdot \cos\theta} \qquad 3.76$$

where τ is the mean particle size, β (in radians) is the line broadening at half maximum intensity (FWHM) after subtraction the instrumental broadening, θ is the Bragg angle, λ X-ray wavelength and k is the dimensionless shape factor constant.

3.6.2.2 Peak Position

Bragg peak position is a function of the unit cell dimensions and wavelength of the source radiation (Chester and Derouane, 2009; Pecharsky and Zavalij, 2009). However, measured Bragg peak positions are also influenced by geometric effects resulting from instrumental settings and sample displacement. Sample displacement is known to be the largest source of error in measured Bragg peak positions (Chester and Derouane, 2009; Pecharsky and Zavalij, 2009). Figure 3.20 illustrates the effect of sample displacement by distance s from the goniometer axis (small open circle in the center of the drawing) on the measured Bragg angle, θ_s (Pecharsky and Zavalij, 2009). Failure to properly position the sample surface on the focusing circle of the goniometer can result in a different measured θs and hence, peak displacement.

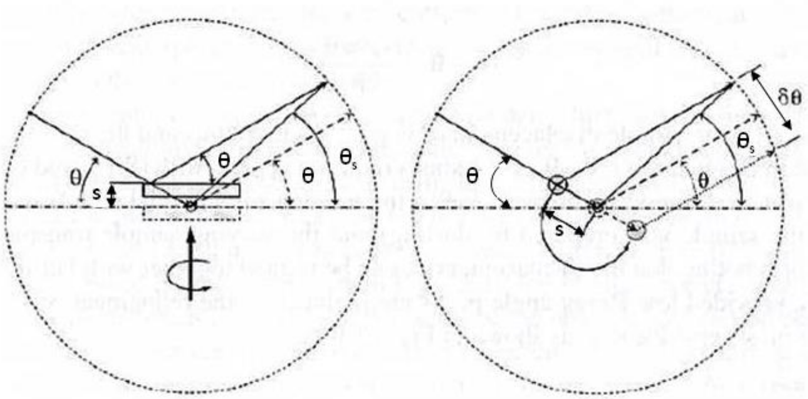

Figure 3.20: Effect of sample displacement from goniometer axis in the Bragg-Brentano geometry (left) and transmission geometry (right) adapted from Pecharsky and Zavalij, 2009.

Other factors from the specimen such as absorption and porosity affects the peak positions of the XRD (Pecharsky and Zavalij, 2009). The unit cell dimensions $(a, b, c, \alpha, \beta, \gamma)$

and the wavelength of the incident radiation are the two main factors that determine the Bragg angles, hence the peak position. Therefore the peak positions can be used to determine structural information of the specimen such as the unit cell if the Bragg angle and wavelength of the X-ray source is known.

3.6.2.3 Diffracted Peaks Intensity

XRD patterns consist of multiple peaks with varying intensities which are determined by the integral intensity, scale factor, multiplicity factor, Lorentz-Polarization factor, absorption factor, preferred orientation and extinction factor(see Pecharsky and Zavalij, 2009, for detailed discussion). Only the integral and Lorentz-Polarization factor are covered in this section. The intensity of a powder diffraction peaks is not only influenced by the structure factor of the material but also by the geometric factors resulting from the detection of the diffracted beam and polarization of the source. The integral intensity for a Bragg diffracted peak is given by (Chester and Derouane, 2009)

$$I\ (hkl) = KL_P(\theta)|F(hkl)|^2 \qquad 3.77$$

where K is a constant known as the scale factor which depends on the intensity and wavelength of the incident beam, sample/detector distance, unit cell volume, total volume of irradiated sample and the properties of electron for X-ray scattering. The factor L_P is the combined Lorentz and polarization factor at the diffraction angle for the *hkl* reflection and *F(hkl)* is the *hkl* reflection structure factor.

In X-ray Rietveld refinements, it is necessary to apply the Lorentz and polarization correction in the intensities of the XRD pattern. In practice Lorentz and polarization corrections are combined in one Lorentz-Polarization factor (Lp). The L_P factor combines two geometrical effects, one from the polarization of the radiation source and the Lorentz component which corrects for the detection of the diffracted radiation (Chester and Derouane, 2009; Pecharsky and Zavalij, 2009). The polarization factor expresses the reduction of intensity in the resulting XRD pattern and can be expressed as (Pecharsky and Zavalij, 2009)

$$P \propto \frac{1+\cos^2 2\theta}{2} \qquad 3.78$$

This factor arises from the fact that the incident radiation is partially polarized after scattering and possesses electric field component which lies in the plane perpendicular to the plane of the incident radiation and parallel to the plane of the reflected radiation (Kirkpatrick, 1927; Chester and Derouane, 2009). Eq.3.78 only applies to unpolarized X-rays but when a monochromator is employed it partially polarizes the X-ray beam and additional polarization correction terms are required (Chester and Derouane, 2009; Pecharsky and Zavalij, 2009). For an X-ray setup with monochromator, the polarization factor becomes

$$P \propto \frac{1-K+K\cdot\cos^2 2\theta\cdot\cos^2 2\theta_M}{2} \qquad 3.79$$

where $2\theta_M$ is the Bragg angle of the monochromator crystal and K is the fractional polarization of the beam. For unpolarized and unmonochromatized X-ray radiation, $K = 0.5$ and $\cos 2\theta_M = 1$, and for monochromatic radiation K should be experimentally refined.

The Lorentz factor takes into account two geometric considerations that has to do with the detection of the intensity scattered radiation (Pecharsky and Zavalij, 2009). Rotating a crystal causes various planes of the crystal to be in a satisfying reflection condition when irradiated with an X-ray beam (Buerger, 1940). However, these planes do not find themselves in these reflection conditions for the same amount of time. The time permitted for a plane to be at that reflection position is therefore proportional the total amount of X-rays for that particular reflection (Buerger, 1940). The first component arises from the fact that the contact time for different reciprocal lattice points with the Ewald's sphere is not constant (Chester and Derouane, 2009; Pecharsky and Zavalij, 2009). This is directly proportional to $1/\sin\theta$. The second component takes into consideration the geometric effects of the constant length of the receiving slit. For a constant specimen/receiving slit distance at any Bragg angle, the radius of the Debye ring is proportional to $\sin 2\theta$. The Lorentz factor which depends on both Bragg angle and diffraction geometry then becomes (Pecharsky and Zavalij, 2009)

$$\frac{1}{\cos\theta\sin^2\theta} \qquad 3.80$$

For unmonochromatized X-ray beam the combined Lorentz and polarization factors is thus expressed as

$$L_P = \frac{1 + \cos^2 2\theta}{\cos\theta \sin^2\theta} \tag{3.81}$$

And for monochromatized radiation the LP factor is given by:

$$L_P = \frac{1 + \cos^2 2\theta \cos^2 2\theta_M}{\cos\theta \sin^2\theta} \tag{3.82}$$

Details about the instruments and experimental conditions of the XRD measurements reported in this thesis are presented in Chapters 4 and 6 of the thesis.

3.7 Raman Spectroscopy

3.7.1 Introduction

Raman is a vibrational spectroscopy technique based on the analysis of inelastically scattered light (Raman and Kirishnan, 1928; Kuzmany, 1998). The technique uses inelastic scattering of electromagnetic radiation (usually laser light) by molecules to probe the structure of the molecule (Hanesch, 2009; Lin *et al.*, 2010). The monochromated laser light interacts with the vibrational modes in the crystal known as phonons and the energy of the scattered laser is shifted by the scattering (Hanesch, 2009). These energy shifts yield a Raman spectrum that is specific to each mineral under investigation because the phonons are specific for each material (Koningstein, 1972; Kuzmany, 1998; Weber and Merlin, 2000; Hanesch, 2009). Raman has been routinely used to study vibrational, rotational and other low frequency-modes to obtain information on molecular composition of matter and spectral fingerprinting in small amount of biological specimens even in liquid state (Lin *et al.*, 2010). The technique has also been used extensively in several studies to distinguish different iron oxides and oxyhydroxides present at the surfaces which present different magnetic properties (de Faria *et al.*, 1997; Hanesch, 2009).

3.7.2 The Raman Effect

The Raman effect was discovered by Raman and Kirishnan, 1928. They hypothesized that normal light should also be inelastically scattered by electrons in the same way as X-rays are inelastically scattered by electrons (Compton effect). The authors successfully used direct sunlight to prove their hypothesis. About sixty common liquids were studied, and the energy or wavelength of the sunlight changed after the sunlight light has participated in exciting the molecules into vibrational states (Raman and Kirishnan, 1928). This effect is known as the "Raman effect". In contrast to Raleigh scattering, Raman scattering is an inelastic scattering process which is usually generated by a monochromated laser light as illustrated in Figure 3.21.

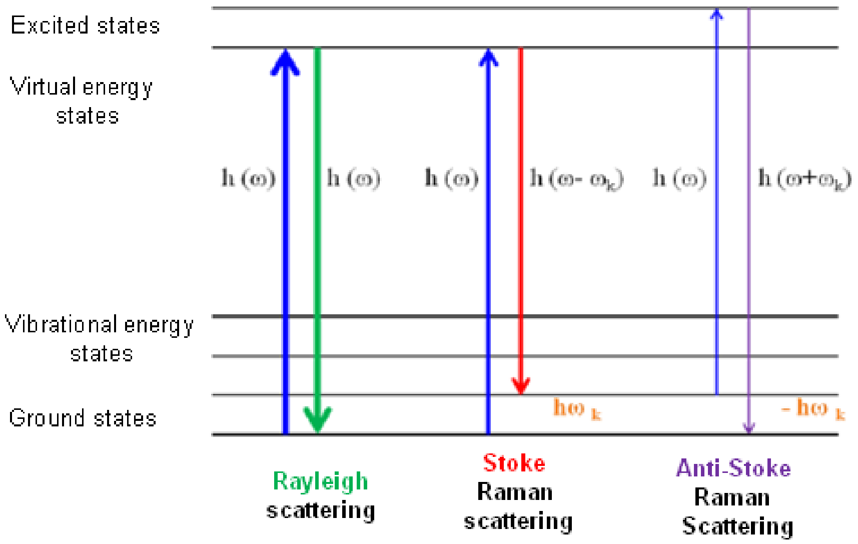

Figure 3.21:Energy level diagram showing states involved in Raman signal, (i) Rayleigh scattering, (ii) Stoke Raman and (iii) Anti-Stoke Raman (from Lin *et al.*, 2010).

During a scattering event, the laser photons may transfer their excitation energy to change the molecule from the ground state to a virtual state (Figure 3.21), and the excited molecule can return to a different vibrational or rotational after emitting a photon. The energy difference between the original and new state causes a frequency shift of the excited photon different from the excitation wavelength. When the excited molecule gets higher energy than that of before becoming excited, a down-shifted frequency is observed in a process termed as Stoke shift (Raman and Kirishnan, 1928; Koningstein, 1972; Kuzmany, 1998; Weber and Merlin, 2000; Lin *et al.*, 2010). In the case where the final vibrational state is less in energy than the initial state, the emitted gets an up-shifted frequency. This process is known as an anti-Stoke shift (Raman and Kirishnan, 1928; Koningstein, 1972; Kuzmany, 1998; Weber and Merlin, 2000; Lin *et al.*, 2010).

The change or shift in energy of the incident laser light after exciting molecules to vibration states forms basis of the Raman spectroscopy. This vibrational-reach information has become a commonly used tool in chemistry to study coordination complexes because of its specificity to the chemical bonds or symmetry of the molecules (Lin *et al.*, 2010).

3.8 Temperature Programmed Reduction (TPR)

3.8.1 Introduction

The temperature programmed reduction technique is a characterization method in which gas-solid chemical reactions are monitored by analyzing the gas composition of the reactor outlet, while the temperature is linearly increased (Kanervo, 2003). This technique was first proposed by Robertson *et al.*, 1975. And comprehensive reviews of the theory of this technique have been previously published e.g. (Jones and McNicol, 1986; Bhatia *et al.*, 1990).

The essence of the TPR technique is the reduction of a solid by a gas (usually H_2) while the temperature of the system is programmed to increase in a linear relation during the course of the TPR run. In the case of a reduction event, the concentration of the gas changes and this change which is monitored downstream of the reactor forms the basis of the TPR analysis. Depicted in Figure 3.22 is a typical reduction profile after a TPR run showing a series of peaks each representing a distinct reduction event.

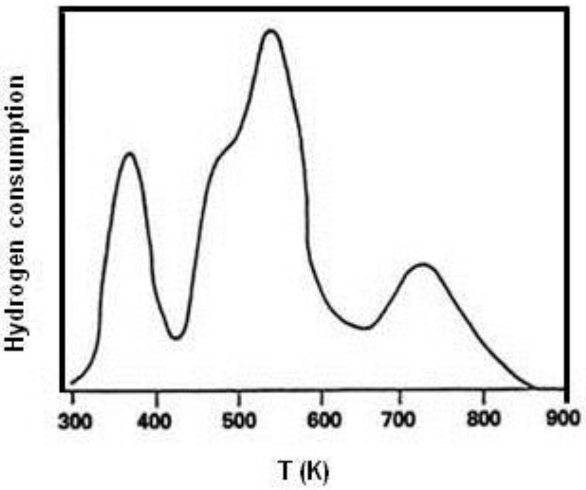

Figure 3.22: A typical TPR profile (from Jones and McNicol, 1986).

The position of the peak is determined by the chemical nature and environment of the chemical component present in the solid sample. The area under the peak corresponds to the amount of H_2 consumed during that reduction event. Quantitative analysis of the H_2 consumed can be used to determine the reduction pathways of the reducible species.

Usually supported iron catalysts for Fischer-Tropsch synthesis has to undergo pre-thermal treatments (Bukur *et al.*, 1995a; Bukur *et al.*, 1995b; Bukur *et al.*, 1995c). These studies have shown that pre-treatment conditions have significant effect on subsequent catalytic activity, reactivity, and stability. Pre-thermal treatments studies include hydrogen reduction, carbon monoxide activation, and syngas (mixture of CO and H_2). The TPR method is a useful technique developed to study the reduction process of metal catalysts (Pinna, 1998).

3.8.2 The TPR process

The TPR process can best be illustrated by Figure 3.23. In a TPR experiment a known amount reducing gas mixture **A** (usually 5% H_2/Ar or 10% H_2/Ar) is flown over the solid or catalyst inside the U-tube reactor **D** (Pinna, 1998). The heating rate and gas flow rate is controlled by the temperature programmer **C** and flow rate controller **B** respectively.

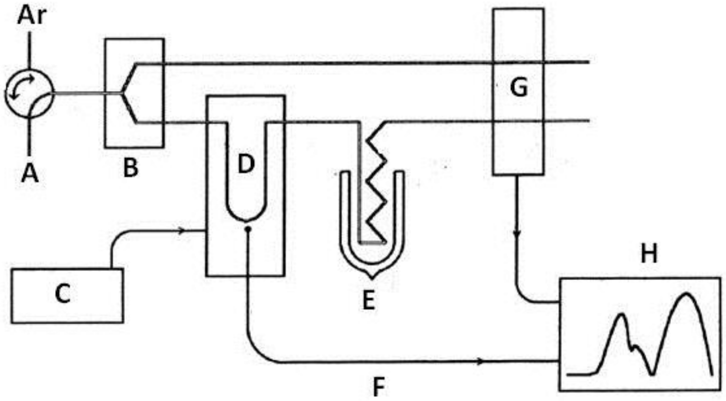

Figure 3.23: Schematic diagram of temperatured programmed reduction apparatus (from Manteanu *et al.*, 1999).

The temperature in the reactor is monitored by a thermocouple (**F** in Figure 3.23). During the course of a reaction in a TPR setup reduction will occur and certain amount of reducing gas will be consumed. The TPR process measures the variation of the outlet gas concentration by a thermal conductivity detector (TCD) (**G** in Figure 3.23**)**. A TPR profile (**H** in Figure 3.23) is obtained by recording the change in hydrogen concentration and temperature with time (Pinna, 1998). The cold trap (**E** in Figure 3.23**)** before the TCD detector is used to remove water formed during TPR runs.

3.8.3 TPR methods of evaluating kinetic parameters

Kinetic parameters (A, E_a, and $f(\alpha)$) sometimes referred as kinetic triplet are useful in thermally activated reactions in such that they provide opportunity for theoretical interpretation of experimental data (Vyazovkin, 2006). Here A is the pre-exponential linked to the vibrational frequency of the activated complex, E_a is the activation energy or the energy barrier and $f(\alpha)$ is the differential reaction kinetic model which is linked to the reaction mechanism (Wanjun and Donghua, 2005; Vyazovkin, 2006). Kinetics parameters can be determined by either employing the ‘modelistic’ or ‘model-free’ methods e.g. (Li and Tang, 1999; Pourghahramani and Forssberg, 2007). A single set of thermoanalytical data is enough to determine kinetic triplet in the case of model-fitting methods. The kinetic triplet (A, E_a, and $f(\alpha)$) using this method is determined simultaneously by fitting a single theoretical curve to the experimental curve (Li and Tang, 1999; Pourghahramani and Forssberg, 2007). The 'modelistic' method has received criticism for (1) assuming a reaction model $f(\alpha)$, (2) producing significantly different kinetic triplets that are both capable to reproduce the experimental curve, (3) employ a single heating rate which is always not enough to determine kinetic reactions. For this reasons the model-fitting method is making way for the recently favored model-free isoconversional methods.

Unlike modelistic methods, isoconversional methods measures kinetic triplet from several kinetic curves recorded at different heating rates. Model-free isoconversional methods allow the evaluation of the effective activation energy to be determined without assuming any form of the reaction model. In a heterogeneous reaction, a reaction which involves a solid and reducing/oxidizing gas mixture under both isothermal and non-isothermal conditions, the progress of the chemical reactions as a function of temperature T, and α, the extent of the reaction conversion is given by Eq. 3.83 (Kissinger, 1957; Chen *et al.*, 1993; Li and Tang, 1999; Manteanu *et al.*, 2003; Starink, 2003; Saha *et al.*, 2006; d'Arlas *et al.*, 2007; Pourghahramani and Forssberg, 2007; Boulkas and El Harfi, 2008):

$$\frac{d\alpha}{dt} = \beta\left(\frac{d\alpha}{dT}\right) = k(T)f(\alpha) = A\exp\left({-E_a}/{RT}\right)f(\alpha) \qquad 3.83$$

where $k(T)$ is the rate constant at temperature T and $k(T)$ takes the Arrhenius form, E_a is the activation energy, A is the Arrhenius pre-exponential factor, $f(\alpha)$ is function of the degree of conversion, R universal gas constant, and β is the heating rate (dT/dt).

Kissinger-Akahira-Sunose (KAS) method independently developed by Kissinger, 1957, and is based on the change in the peak maxima at different heating rates. The method assumes that the kinetic triplet (A, $f(\alpha)$, E_a) is independent of T, and also A and E are independent of α. The KAS method can be realized by rearranging Eq. 3.83 by means of integration by separation of variables to obtain the integral form ($g(\alpha)$) of the reaction model (Kissinger, 1957; d'Arlas *et al.*, 2007; Boulkas and El Harfi, 2008).

$$g(\alpha) = \int_0^{\alpha} \frac{d\alpha}{f(\alpha)} = \frac{A}{\beta} \int_0^{T_m} \exp\left({-E_a}/{RT} \right) dT \tag{3.84}$$

By letting $y \equiv \frac{E_a}{RT}$ Eq. 3.84 can be further simplified to

$$g(\alpha) = \int_0^{\alpha} \frac{d\alpha}{f(\alpha)} = \frac{AE_a}{\beta R} \int_y^{\infty} \frac{\exp(-y)}{y2} dy = \frac{AE_a}{\beta R} p(y) \tag{3.85}$$

where $p(y)$ is the famous temperature integral that has no analytical solution. Taking the natural logarithm in Eq. 3.85, the following expression is obtained.

$$ln\, g(\alpha) = ln \frac{AE_a}{R} - ln\, \beta + ln\, p(y) \tag{3.86}$$

and using the Coats-Redfern approximation of the temperature integral (d'Arlas *et al.*, 2007; Boulkas and El Harfi, 2008):

$$p(y) \cong \frac{exp(-y)}{y^2} \qquad (20 < y < 50) \tag{3.87}$$

Then Eq. 3.87 can be reduced to

$$ln\, \frac{\beta}{T_m^2} = ln\, \frac{AR}{E_a g(\alpha)} - \frac{E}{RT_m} \tag{3.88}$$

where T_m is the temperature at maximum conversion. Plots of $ln \frac{\beta}{T_m^2}$ versus $\frac{1}{T_m}$ at α =const for various heating rates should yield straight lines and E_a can be evaluated from the slope of these plots.

Ozawa-Flynn-Wall (OFW) method is an isoconversional integral method suggested by two independent workers (Ozawa, 1965 and Flynn and Wall, 1966) and is well documented in literature (d'Arlas *et al.*, 2007; Boulkas and El Harfi, 2008). The major difference in integral methods is the approximation of the temperature integral which is different for each method

(Starink, 2003). The procedure for deriving the OFW method is the same as in the KAS method except that the OFW method relies on the Doyles approximation (d'Arlas *et al.*, 2007; Boulkas and El Harfi, 2008).

$$ln\, p(y) = -5.331 - 1.052\, y \quad (20 < y < 60) \qquad 3.89$$

Inserting Eq. 3.89 in Eq. 3.86 and rearranging the OFW relation gives:

$$\ln \beta = \ln \frac{AE_a}{Rg(\alpha)} - 5.331 - 1.052 \frac{E_a}{RT_m} \qquad 3.90$$

For $\alpha = const,$ the activation energy can be evaluated from the slope (equaling$-1.052\ \frac{E_a}{R}$) of the plot of $\ln \beta$ versus $\frac{1}{T_m}$ (straight lines resulting from a set of different thermal experiments performed at different heating rates (β)).

The differential isoconversion method also known as Friedman method, in recognition of the work by Freidman (Friedman, 1963), is a method that evaluates the activation energy directly from the differential form of the reaction rate (Eq. 3.83) (d'Arlas *et al.*, 2007; Boulkas and El Harfi, 2008). Unlike, the integral methods described above the Friedman method avoid making any mathematical approximations. This method is derived by taking natural logarithms on both sides of Eq. 3.83 yielding (Starink, 2003; d'Arlas *et al.*, 2007; Boulkas and El Harfi, 2008):

$$ln\left(\beta\, \frac{d\alpha}{dT}\right) = -\frac{E_a}{RT} + ln\, A + ln\, f(\alpha) \qquad 3.91$$

At constant conversion (α=const), the plots of $ln\, \beta\ \frac{d\alpha}{dT}$ versus $\frac{1}{T}$ obtained at different heating rates should yield straight lines. The activation energy can be obtained from the slope of the straight lines which is given by$\frac{-E_a}{R}$. Here *T*, is the temperature taken at that particular constant conversion α for various heating rates of the experiments.

In this study, reaction mechanisms of pure 2- and 6-line FHYD and silica co-precipitated 2-line FHYD were studied using TPR analysis. Their kinetic triplets were obtained using isoconversional methods by Kissinger, Friedman, and Ozawa described by (Boulkas and El Harfi, 2008).

Chapter 4

Synthesis and Characterization of Ferrihydrite Nanoparticles

Abstract

Powder X-ray diffraction (XRD), transmission electron microscopy (TEM), Raman spectroscopy, Mössbauer spectroscopy (MS) and magnetic measurements on nanoparticles of FHYD2, FHYD6 and FHYD2/SiO_2 synthesised using rapid hydrolysis of Fe (III) are reported. FHYD2 and FHYD2/SiO_2 present two broad XRD peaks indicative of the poor crystallinity while FHYD6 features 6 peaks suggesting a relatively better crystallinity. TEM micrographs show globular nanoclusters with average crystallite sizes of 3.5, 4.0 and 6.0 nm for FHYD2/SiO_2, FHYD2 and FHYD6, respectively. Raman spectra suggest the same structural arrangements for the atoms in FHYD2 and FHYD6. Magnetization measurements reveal typical superparamagnetic (SPM) behavior above a blocking temperature (T_B) in the range 36 – 50 K and large anisotropy constants in the range K = $1.5 - 5.5 \times 10^5$ J/m^3. The crystallite size and surface atoms determine the magnetic properties of nanoparticles. Decreasing crystallite size (increasing fraction of surface atoms) results in decreasing T_B, increasing K and increasing the number of uncompensated surface spins which leads to increasing saturation magnetization (M_S) in the blocked state. MS measurements confirm the SPM nature of nanoparticles and point to the presence of a single Fe^{3+} phase in all three samples with high spin Fe^{3+} state. With increasing surface contributions atoms at the surface sense weaker exchange fields in the blocked state thus the hyperfine magnetic field (B_{hf}) decreases.

4.1 Introduction

The present chapter reports on attempts to synthesise 2-line FHYD (FHYD2) and 6-line FHYD (FHYD6) nanoparticles and 2-line FHYD nanoparticles deposited onto SiO_2 support

(FHYD2/SiO_2) from the hydrolysis of iron(III) nitrate nonahydrate ($Fe(NO_3)_3.9H_2O$) in water. It focuses on the characterisation of the nanoparticles thus prepared using XRD, TEM, Raman spectroscopy, MS and magnetic measurements. The phase composition and the effect of the crystallite size on the atomic structure and magnetic properties of the nanoparticles formed are discussed.

4.2 Experimental

4.2.1 Synthesis

Ferrihydrite formation mechanism

It was pointed out early that the most common way to synthesise iron oxydroxides in the laboratory is by using the hydrolysis of an acidic solution of Fe (III) salt solution (Sylva, 1972; Cornell *et al.*, 1989; Schwertmann and Cornell, 2000; Cornell and Schwertmann, 2003). The product formed and its crystallinity is determined by the rate of hydrolysis, pH, temperature, and nature of the anions present in the reaction. Figure 4.1 shows stability domain of some iron oxides formed by hydrolysis, with FHYD and hematite both shown to form at neutral pH. The first phase to precipitate during hydrolysis of Fe^{3+} is usually a disordered FHYD (Schwertmann and Cornell, 2000; Cornell and Schwertmann, 2003). A rapid hydrolysis at ambient temperatures and neutral pH produces a less crystalline form of FHYD with only two broad XRD peaks, hence the name 2-line ferrihydrite (FHYD2).

Figure 4.1 also shows the pH range where ferrihydrite precipitates (Manceau and Drits, 1993). At very low pH, exists the iron hexa-aqua-ion ($[Fe(H_2O)_6]^{3+}$) with a purple colour (Schwertmann and Cornell, 2000). This colour changes to orangish brown when the aquated Fe^{3+} ion is deprotonated to form hydroxo-aquo species e.g. $[Fe(H_2O)_5(OH)]^{2+}$ (Sylva, 1972). The orangish brown colour was the starting colour observed for Fe (III) solution during synthesis reported in this study. The dropwise addition of the KOH base further eliminated the protons from the central Fe cation to form mono- and binuclear species which interact further to form species of higher nuclearity (Sylva, 1972; Cornell and Schwertmann, 2003), an red brown iron oxyhydroxide precipitate, according to the reaction

$$[\mathrm{Fe(H_2O)_5(OH)}]^{2+}_{(aq)} + 2\mathrm{OH}^{-1}_{(aq)} \rightarrow \mathrm{Fe(H_2O)}_{3(s)} + 2\mathrm{H_2O}_{(l)} \qquad 4.1$$

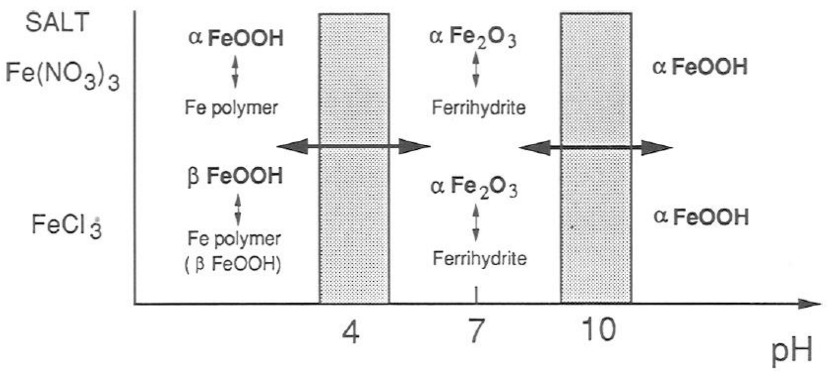

Figure 4.1: Stability domains of ferrihydrite and some iron oxides formed by hydrolysis of Fe (III) salts (adapted from Manceau and Drits, 1993).

The formation of well crystallized FHYD6 proceeds via iron (III) oxyhydroxynitrate intermediate (Schwertmann *et al.*, 1996). The nitrate compound which forms during rapid hydrolysis of $\mathrm{Fe(NO_3)_3}$ at elevated temperature (~ 80 °C) is given the general formula

$$\mathrm{FeO(OH)_{1-x}(NO_3)_x} \quad (0.2 < x < 0.3) \qquad 4.2$$

Its XRD pattern (see Fig.3, Schwertmann *et al.*, 1996) shows the poor crystalline nature of the compound consisting of only six broad XRD lines. Although the six XRD peaks are at similar positions with that of FHYD6, significant differences exist between the two XRD patterns. The same protocol as described by Schwertmann *et al.*, 1996, was followed to form the iron (III) oxyhydroxynitrate (a precursor for FHYD6 formation). Subsequent hydrolysis of the nitrate compound led to the formation of a more crystalline FHYD6. According to Schwertmann *et al.*, 1996, the tunnel structure of the iron (III) oxyhydroxynitrate breaks down and the nitrate is completely expelled from the structure as FHYD6 forms.

Synthesis procedures

FHYD2 nanoparticles were synthesized by rapid hydrolysis of $Fe(NO_3)_3.9H_2O$ in a water solution, a method previously reported (Schwertmann and Cornell, 2000). In this procedure, iron(III) nitrate nona-hydrate ($Fe(NO_3)_3.9H_2O$, 54.57 g) was added to distilled water (200 ml) to form a solution that was immediately titrated with a NaOH solution (~0.4 M solution), added drop wise, under vigorous stirring for 25 min until a final pH of ~6.6 was reached. The resulting precipitate was collected by filtration and washed repeatedly with distilled water for about 3 hours. The final FHYD2 product was then air dried overnight in a fume hood.

FHYD2/SiO_2 was synthesised by co-precipitation of FHYD2 and SiO_2. LUDOX HS-30 (Sigma-Aldrich) was used as source of silica and $Fe(NO_3)_3{\cdot}9H_2O$ as a source of Fe(III). The same protocol used to prepare FHYD2. However, after precipitation, a silica sol (LUDOX HS-30 supplied by Sigma-Aldrich) containing 30 wt% SiO_2 was added to the 2LFh precipitate. The FHYD2 precipitate and LUDOX mixture was thoroughly stirred for at least 15 minutes before filtering off the supernatant. The precipitate was dried overnight in a fume hood. The solid cake obtained after drying was finely crushed into a powder using a mortar and pestle.

FHYD6 nano-crystalline particles were prepared using a method described elsewhere (Carta *et al.*, 2009). Briefly, $Fe(NO_3)_3.9H_2O$ (54.57 g) was added to water (200 ml) and the resulting mixture heated to 75 ˚C for about 20 min. The solution was then cooled back to and kept at room temperature for 20 minutes before immersion in an ice bath for further 20 minutes, at which point it was titrated with sodium hydroxide (NaOH) solution (~0.4 M) until a pH of 7.2 was attained. A red brown precipitate was formed and it was filtered-off. The precipitate was continuously washed with distilled water for at least 3 hours followed by overnight drying in a fume hood. The sample was then readied for further analysis using different characterisation techniques.

4.2.2 Characterization techniques

X-ray diffraction

Powder X-ray diffractograms (XRD) were obtained using a Bruker D8 advanced diffractometer with Co Kα source ($\lambda = 1.79$ Å) operated at 35 kV and 40 mA. The scans were performed in the angular range 5 – 100° 2θ.

Transmission electron microscopy

Transmission electron microscopy (TEM) micrographs and selected area electron diffraction patterns (SAED) were recorded on a JEOL JEM-2100 operated at 200 kV. HAADF Scanning transmission microscopy (STEM) images were also obtained using the JEOL JEM-ARM-200F operated at 80 kV. Samples were prepared by grinding a small amount of FHYD powder with a mortar and pestle and ultrasonicating the powder in ethanol. A drop of the dispersed solution was placed on a holey carbon film supported by a copper grid.

Raman spectroscopy

Raman spectra were obtained from the samples by placing it on a microscope slide. Polarised data were collected for the region 100 – 4000 cm^{-1} with a Renishaw inVia Raman system, utilising the 785 nm line of a solid-state diode laser. The beam was focused with a Leica microscope using an x50 objective. Measurements were done for 10 seconds, scanned 50 times with a laser power at the sample of ~0.5 mW. Wire Version 3.2 software was used for data capturing and instrument control. The Raman band of pure Si was measured before data accumulation commenced for calibration purposes.

Mössbauer spectroscopy

Mössbauer spectroscopy (MS) measurements were performed at room temperature (300 K) and at 4.2 K using conventional acceleration constant spectrometers designed to operate in the absorption mode and equipped with ^{57}Co/Rh sources. Low temperature (LT) measurements were performed using the Spectromag SM4000-10 cryomagnet from Oxford Instruments designed to operate at variable temperatures (1.3 – 300 K) and applied magnetic fields up to 10 T. The MS spectra were analysed by means of a least squares program “Normos” that models them as a combination of quadruple doublets and sextets based on a Lorentzian line-shape profile. The individual absorption features were identified on the basis of their hyperfine parameters, i.e. the isomer shift (δ), quadrupole splitting (ΔE_Q) and magnetic hyperfine field

(B_{hf}) values. Metallic iron (α-Fe) was used to calibrate the velocity scale of the MS spectra, i.e. isomer shift values of all the species are reported relative to α-Fe.

Magnetic measurements

Magnetic measurements were performed using a Magnetic Property Measurement System (MPMS®) XL-7 SQUID magnetometer from Quantum Design, Inc. operating in the temperature range 2 – 400 K and capable of attaining magnetic field up to 70 kOe. The samples were first loaded at room temperature and then aligned (centred) in the middle of the magnetic field by means of a small applied magnetic field. Thereafter the samples were cooled in zero magnetic field up to the lowest temperature of the measurements, 2 K. Once the lowest temperature was attained, a small magnetic field (about 2 kOe) was applied and the temperature dependence of the magnetisation (M (T) curves) measured while heating up the samples from 2 to 380 K at a rate of 5 K/min. This is referred to as zero-field cooled (ZFC) mode. The samples were then cooled again at the same rate and in the same external magnetic field while recording M (T) data. This is referred to as field cooled (FC) mode. Measurements of the applied magnetic field dependence of the magnetisation (M (H) curves) were performed at fixed temperatures of 10, 100 and 300 K in applied magnetic field range – 50 kOe and + 50 kOe.

4.3 Results and discussions

4.3.1 Structural characterization

Figure 4.2 shows the X-ray diffractograms for the as synthesised samples FHYD2, FHYD2/SiO_2 and FHYD6. The diffractograms of FHYD2 (Figure 4.2 (b)) and FHYD2/SiO_2 (Figure 4.2 (c)) are quite similar and show two broad peaks at $2\theta = 41$ and $75°$ which correspond to interplanar distances of $d = 0.25$ and 0.15 nm, respectively. The broadening of the peaks is indicative of the poor crystallinity of the synthesised FHYD2 and FHYD2/SiO_2. For FHYD6, the pattern (Figure 4.2 (a)) consists of 6 peaks with interplanar distances of $d = 0.25, 0.23, 0.20, 0.17, 0.15$ nm thus suggesting a relatively better crystallinity as compared to FHYD2 and FHYD2/SiO_2. The patterns in Figure 4.2 are also similar to the ones previously reported for synthetic 2- and 6-line FHYD (Manceau and Drits, 1993; Jambor and Dutrizac, 1998; Janney *et al.*, 2001; Carta *et al.*, 2009). Note that the peaks for FHYD6 are usually counted 1 to 6 from low to high 2θ, the small shoulder just above *d* = 0.15 nm is taken as peak 5 (Janney *et al.*, 2001).

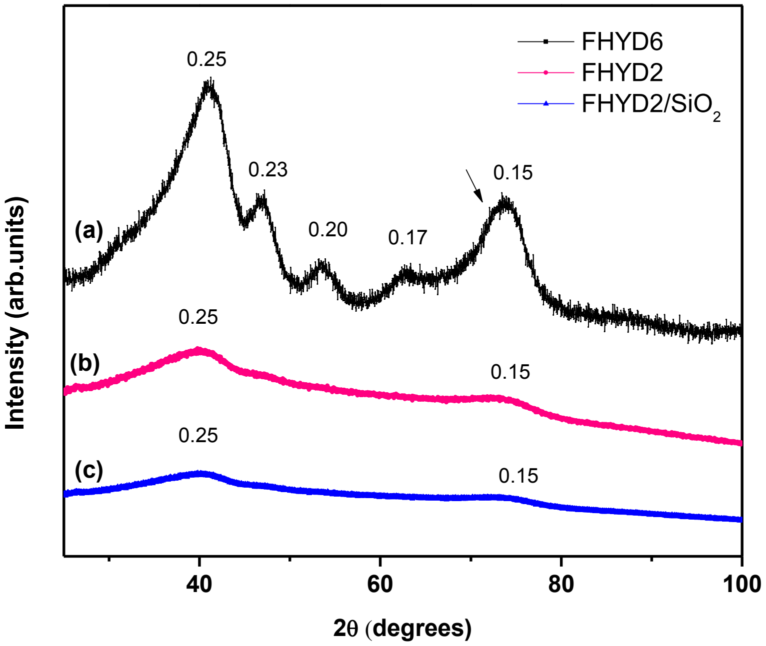

Figure 4.2: XRD patterns for synthetic (a) FHYD6, (b) FHYD2, and (c) FHYD2/SiO$_2$.

Figure 4.3 shows the bright field TEM micrographs and SAED patterns (inset) for FHYD2 which feature two diffractions rings with *d*-spacings of 0.15 and 0.25 nm similar to the ones obtained by X-Ray diffraction method. The BF image and electron diffraction pattern for the FHYD2/SiO$_2$ sample is similar to the pure FHYD2 (see Figure 4.4). This was expected since the SiO$_2$ was added to FHYD2 after precipitation.

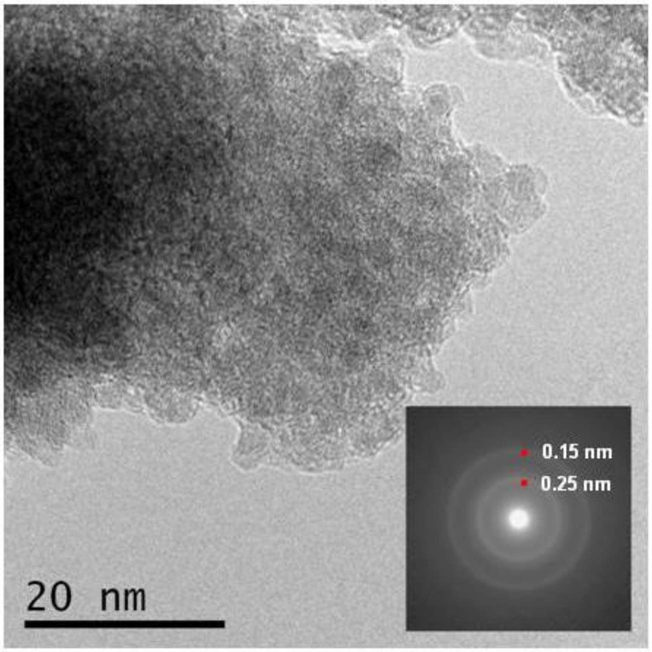

Figure 4.3: Bright field TEM image of FHYD2 and SAED pattern (inset).

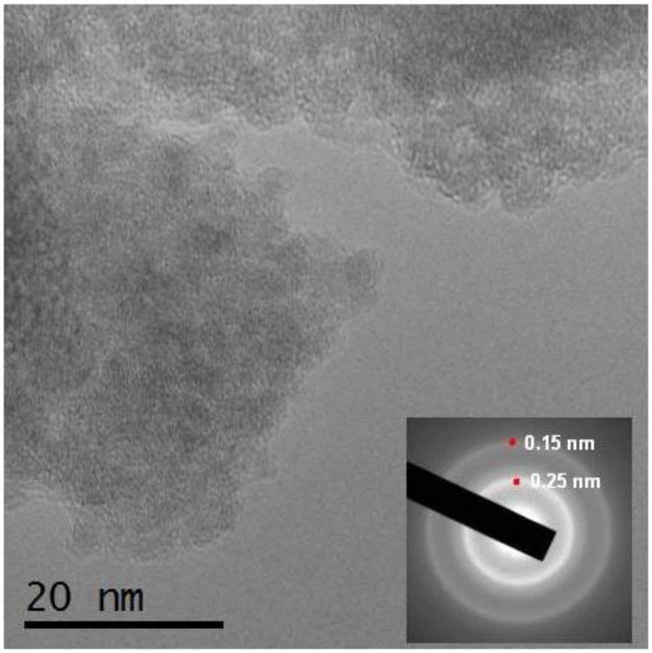

Figure 4.4: FHYD2/SiO$_2$ BF TEM image and SAED pattern (inset).

The SAED patterns for FHYD6 (insert in Figure 4.5) feature two bright and three very faint diffraction rings in between the bright rings. The measured *d*-spacings of 0.15, 0.17, 0.20, 0.23 and 0.25 nm are also equivalent to the *d*-spacings determined by powder XRD (Figure 4.2 (a)).

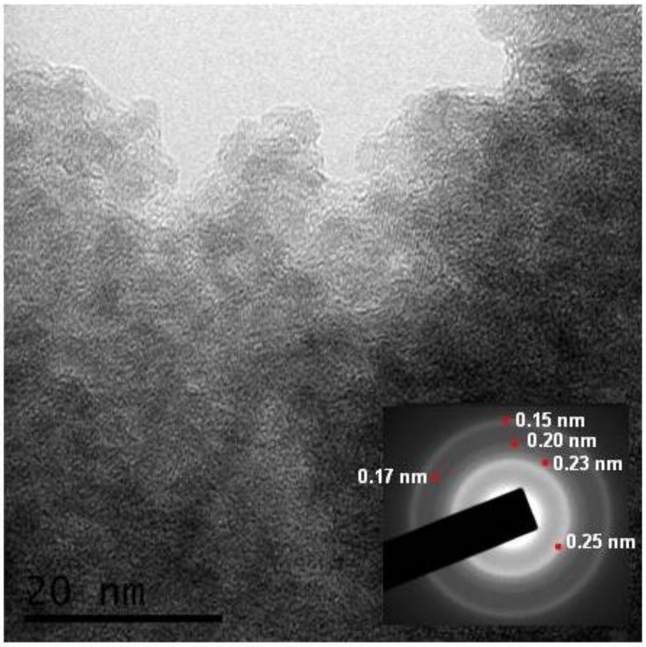

Figure 4.5: Bright field TEM micrograph of FHYD6 nanoparticles.

Figure 4.6 shows the crystallite size distributions obtained from scanning transmission microscopy (STEM) images (shown in Figure 4.6 (b)) for the synthesized FHYD2 particles. The nanoparticles appear to form typical globular nano-clusters which make them not clearly discernible. The size distribution data was fitted with a lognormal function according to the formula (Guyodo *et al.*, 2006):

$$f(d) = \frac{1}{\sqrt{2\pi\sigma d}} \exp\left[-\frac{\ln(d/d_0)^2}{2\sigma^2}\right] \qquad 4.3$$

where d_0 (average diameter = D_{av}) and σ represents the distribution peak position and standard deviation, respectively.

Crystal size distribution plots for FHYD2/SiO_2 are depicted in Figure 4.7. The average diameter (see Table 4.1) of the crystallites as obtained from STEM images by counting about 100 particles amounts to $D_{av} \approx 3.5$ nm for FHYD2/SiO_2. The distributions of the crystallite sizes are somewhat broader for FHYD6 as compared to FHYD2 and FHYD2/SiO_2 (Figure 4.8). The average particle size was determined by fitting the particle size distribution histogram with a lognormal function. The results are given in Table 4.1.

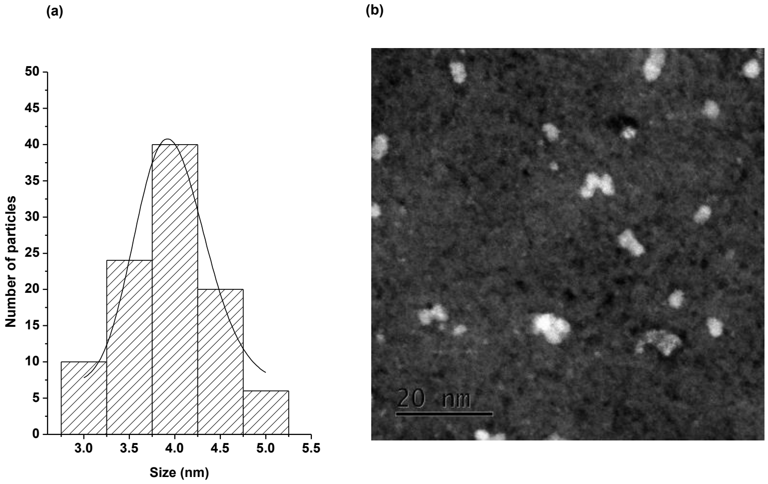

Figure 4.6: Crystallite size distribution for the FHYD2 sample: (a) Size distribution fitted with lognormal function, (b) The respective HAADF STEM micrograph.

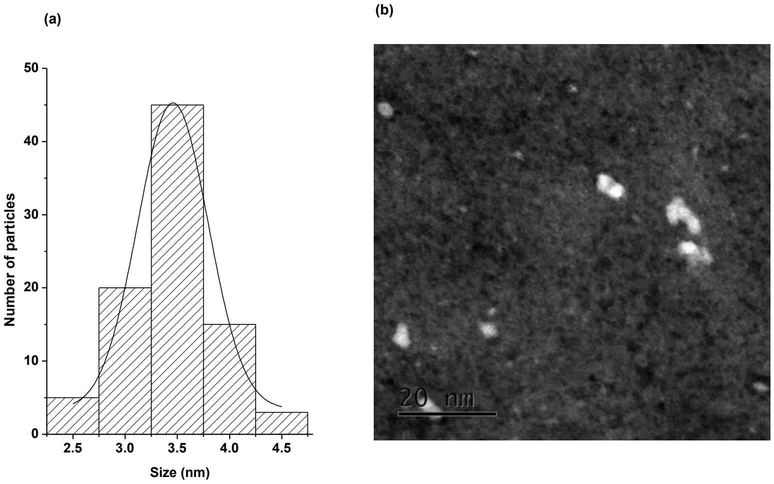

Figure 4.7: FHYD2/SiO_2 crystal size distribution (a) Histograms and (b) HAADF STEM image.

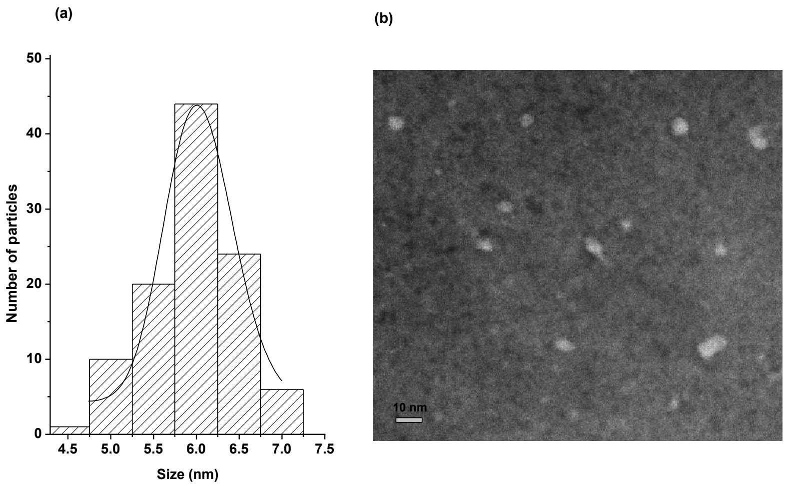

Figure 4.8: FHYD6 (a) Particle size distribution and (b) HAADF STEM image.

The Raman spectra of the synthesized FHYD2 and FHYD6 are shown in Figure 4.9. The two spectra are similar, suggesting the same structural arrangements of atoms. They are also similar to that of maghemite (γ-Fe_2O_3) spectra (Jacintho *et al.*, 2007) which also has Fe vacancy disorder like FHYD. Low laser power was used to avoid thermal degradation and XRD and TEM data appear to confirm the nature of the synthesized FHYD2 and FHYD6 as being 2- and 6-line FHYD, respectively. Three Raman spectral bands at 363, 505, and 716 cm^{-1} are also consistent with Raman features previously reported for synthetic FHYD (Mazzetti and Thistlethwale, 2002). The band 1362 cm^{-1} is probably due to two magnon scattering thought to originate from the same process as the band observed in hematite (Martin *et al.*, 1977). The sharp spike at 1046 cm^{-1} is due to NO_3^- since the nitrate ion usually present a strong feature at 1050 cm^{-1} (Martin *et al.*, 1977). The origin of NO_3^- anions can be traced to the $Fe(NO_3)_3.9H_2O$ precursor used during synthesis of FHYD2 and FHYD6. The presence of this anion is indicative of impure substance: no inference of coordination of this anion to Fe cation is made.

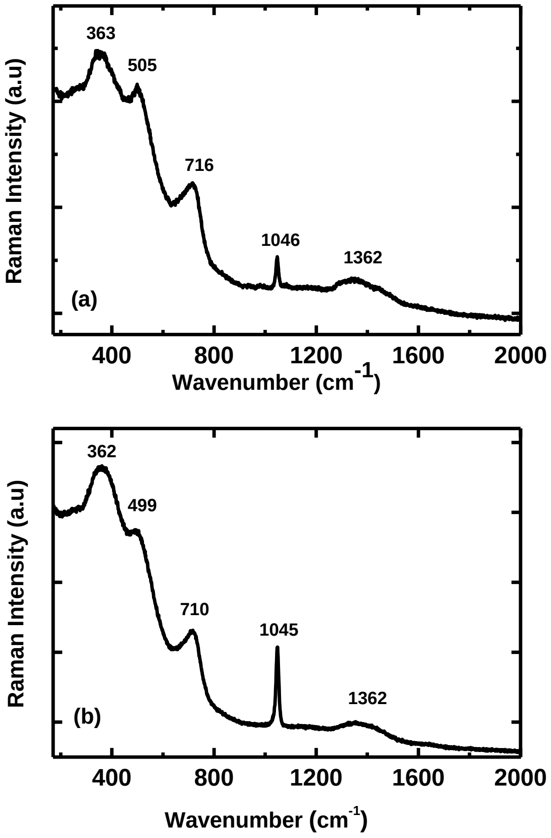

Figure 4.9: Raman spectra for (a) FHYD2 and (b) FHYD6.

Mazzetti and Thistlethwale, 2002, described the Raman spectra of 2- and 6-line FHYD as being both compatible and based on $Fe(O,OH)_6$ octahedra while other authors (Zhao *et al.*, 1993; Zhao *et al.*, 1994a) reported the presence of small amount of tetrahedrally coordinated Fe^{3+} (T_d) in FHYD. The coexistence of octahedrally and tetrahedrally coordinated Fe^{3+} in the structure of the sythesised FHYD2 and FHYD6 will be discussed in chapter 5 of this thesis.

To summarize, the above XRD, TEM and Raman results show that the synthesized FHYD2 have the same structure as 2-line FHYD while FHYD6 has the same structure as 6-line FHYD. It is well known that the nature and crystallinity of the product formed is determined by the rate of hydrolysis, pH, temperature and the nature of the anions present in the reaction (Cornell and Schwertmann, 2003). Hence, disordered and less crystalline FHYD, namely FHYD2 and FHYD2/SiO_2, characterized by two broad XRD reflections formed by rapid hydrolysis of Fe^{3+} at ambient temperatures and neutral pH. Note that the $Fe(NO_3)_3$ aqueous solution initially contains orangish yellow of mono- and binuclear species (see section 4.2.1). Hydrolysis with a base (NaOH) introduces OH^- ions and increases the OH:Fe ratio at which polymerization of the mono- and binuclear species develops (Cornell *et al.*, 1989; Cornell and Schwertmann, 2003). The OH:Fe ratio is increased by dropwise addition of the base and when it eventually reaches the ideal OH: Fe ~3 the poorly crystalline iron oxyhydroxide, FHYD2 and FHYD2/SiO_2, precipitates immediately. Note also that SiO_2 in FHYD2/SiO_2 contributes in stabilizing the small crystallites resulting in a relatively narrower distribution of crystallite size (see Table 4.1).

4.3.2 Magnetic characterization

The M (T) curves in ZFC and FC modes recorded in an applied magnetic field H = 2.0 kOe for the synthesised FHYD2, FHYD2/SiO_2 and FHYD6 are presented in Figure 4.10, they are typical of an assembly of superparamagnetic (SPM) nanoparticles. When individual SPM nanoparticles are cooled (to the lowest temperature of the measurements) in the absence of an applied magnetic field their magnetic moments become frozen but remain randomly aligned such that the resulting magnetisation should average to zero at 0 K (Duarte *et al.*, 2006). A magnetic field, H, is then applied and kept constant while heating up the sample (ZFC mode). The ordering energy associated with the magnetic field forces an alignment of the magnetic moments on H while the thermal energy (k_BT) in opposition causes their directions to fluctuate so as to force a random distribution of magnetic moments. M increases as long as the ordering energy remained higher than the thermal energy. Eventually M reaches a maximum when the two energies balance each other.

The temperature at the maximum magnetization is reached in ZFC mode is referred to as the blocking temperature (T_B) (Duarte *et al.*, 2006). Above T_B the thermal energy exceeds the ordering energy causing M to gradually decrease until the highest temperature of the measurements. When cooled under the same applied magnetic field (FC mode), the thermal energy decreases and thus M gradually increases, following almost the same path as in the ZFC mode until the vicinity of T_B. For all three synthesised samples full reversibility is not achieved in that M in ZFC mode and M in FC mode do not merge up to about 300 K implying that for each sample there is rather a distribution of $T_{B.}$ Below T_B the magnetic moments are blocked and almost all aligned on H and further cooling results only in a small increase of M.

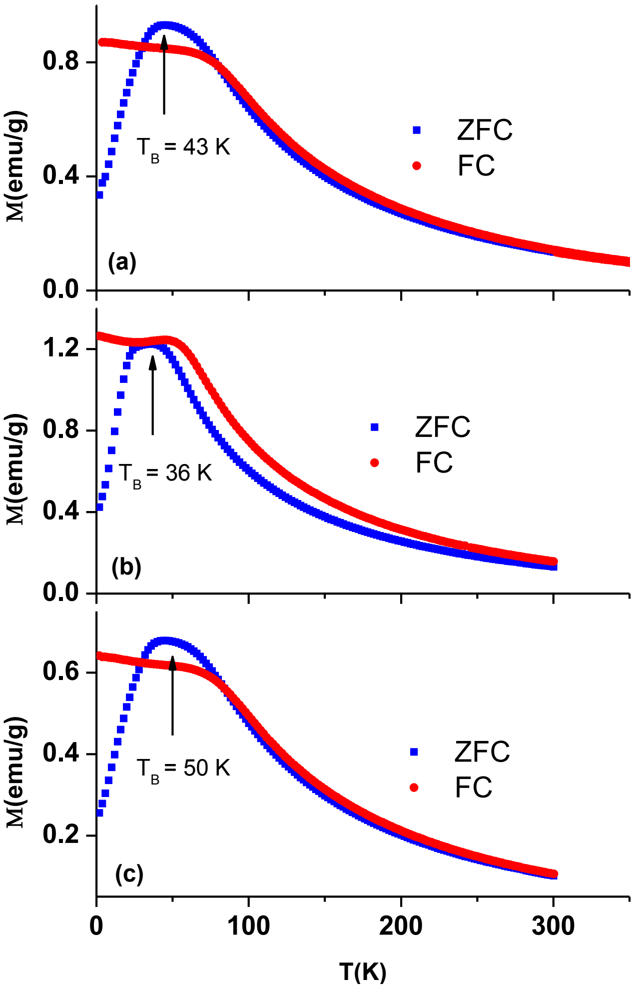

Figure 4.10: Temperature dependence of the magnetization in ZFC and FC modes for (a) FHYD2, (b) FHYD2/SiO$_2$, and (c) FHYD6. The blocking temperature, T_B, is obtained from the maximum in the M vs. T curve in ZFC mode.

The values of T_B obtained from M (T) curves in Figure 4.10 are given in Table 4.1. They amount to T_B = 43 K for FHYD2, T_B = 36 K for FHYD2/SiO$_2$ and T_B = 50 K for FHYD6. Interestingly, these values correlate well with average crystallite sizes D_{av} obtained from STEM images (also given in Table 4.1): T_B increases with increasing D_{av}.

The anisotropy constant (Table 4.1) of the synthesised FHYD2, FHYD2/SiO_2 and FHYD6 determined using Eq. 3.64 and T_B and D_{av} values amounts to $K = 5.5 \times 10^5$ J/m^3 for FHYD2/SiO_2, $K = 4.5 \times 10^5$ J/m^3 for FHYD2, and $K = 1.5 \times 10^5$ J/m^3 for FHYD6, assuming spherical shapes for the crystallites. These values are fairly consistent with $K = 3.12 \pm 10 \times 10^5$ J/m^3 reported for synthetic 6-line FHYD (Duarte *et al.*, 2006). They are almost one order of magnitude larger than $K = 2.40 \pm 10 \times 10^4$ J/m^3 reported for α-Fe_2O_3 with D_{av} = 5.9 nm (Bødker *et al.*, 2000), $K = 4.2 \pm 10 \times 10^4$ J/m^3 reported for γ-Fe_2O_3 with D_{av} = 5.1 nm (Komarida *et al.*, 2009) and $K = 3.11 \pm 10 \times 10^4$ J/m^3 found for Fe_3O_4 with D_{av} = 10 nm (Yoon, 2011).

Noteworthy, K increases with decreasing D_{av} as previously reported (Bødker *et al.*, 2000; Gilles *et al.*, 2000), probably due to the influence of surface anisotropy. It is well established that the average magnetic coordination number for nanomaterials is strongly reduced as finite size effects become pronounced (Kodama *et al.*, 1996; Kodama and Berkowitz, 1999a; Kodama, 1999b; Restropo *et al.*, 2004; Restropo *et al.*, 2006), and this affects their magnetic properties. The effective anisotropic energy of nanometer scale particle is governed by surface anisotropy. For example, Tronc *et al.*, 2000, reported surface anisotropy of $6 \times 10^{-2}\ \mathrm{erg/cm^2}$ for 3-10 nm maghemite particles. Gilmore *et al.*, 2005 reported the surface anisotropy contribution ($0.5 - 2 \times 10^{-2}\mathrm{erg/cm^2}$) of magnetite nanoparticles to the magnetocrystalline anisotropy constant. Surface anisotropy of $2.9 \times 10^{-2}\ \mathrm{erg/cm^2}$ magnetite particles gave rise to dramatic broadening of the total energy distribution Pérez *et al.*, 2008. For a 3.9 nm human chain ferritin particle a surface anisotropy constant of $6.5 \times 10^{-2}\mathrm{erg/cm^2}$ was reported (Cao *et al.*, 2010). As a result, relatively large K values in the synthesised FHYD2, FHYD2/SiO_2 and FHYD6 compared to bulk iron oxides could be due mainly to surface anisotropy.

Table 4.1:Blocking temperature, average crystallite size, hysteresis parameters and anisotropy constant for the synthesized FHYD2, FHYD2/SiO$_2$ and FHYD6.

Sample	$M_{S \text{ at } 10\text{ K}}$ (emu/g)	$M_{r \text{ at } 10\text{ K}}$ (emu/g)	M_r/M_S	H_C (kOe)	T_B (K)	$D_{av\ (TEM)}$ (nm)	K_{TB} (x 10^5 J/m^3)	K_χ (x 10^5 J/m^3)
FHYD2	17.3	1.1	0.06	1.10	44	4.0	4.5	4.0
FHYD2/SiO$_2$	19.9	0.9	0.04	0.91	36	3.5	5.5	5.9
FHYD6	14.6	1.0	0.07	1.05	50	6.0	1.5	1.7

Depicted in Figure 4.11 are the temperature dependence of the ac magnetic susceptibility (real part χ') at different fixed frequencies of 1, 10, 80, 500, and 1500 Hz for all three FHYD samples. All $\chi'(T)$ curves exhibit peaks at a temperature ($T_{max)}$ which increases with increasing frequency. This frequency dependence of T_{max} is typically of nanoparticles in SPM state as previously reported by other authors (Duarte *et al.*, 2006; Cao *et al.*, 2010).

The plot of $\ln\tau$ versus T_{max} (see insets in Figure 4.11) gives straight lines of slope equal to E_a/k (see Eq. 3.63). These give the activation energies in the range $E_a = 1.32 - 1.96 \times 10^{-20}\,J$ for all three samples. Using $E_a = K_{eff}V$ and the particle sizes (D_{av}) in Table 4.1, yielded anisotropy constants of 1.7, 4.0, and $5.9 \times 10^5\,J/m^3$ for FHYD6, FHYD2, and FHYD2/SiO$_2$, respectively. These values are comparable with anisotropy constants calculated from ZFC/FC measurements (see Table 4.1) and in good agreement with the value of $3.12 \times 10^5\,\mathrm{J/m^3}$ obtained for FHYD (Duarte *et al.*, 2006). It is probable that the relatively large magnetic anisotropy constants obtained for FHYD samples are due to surface anisotropy which becomes dominant for nanosized materials (Kodama *et al.*, 1996; Kodama and Berkowitz, 1999a; Kodama, 1999b; Restropo *et al.*, 2004; Restropo *et al.*, 2006).

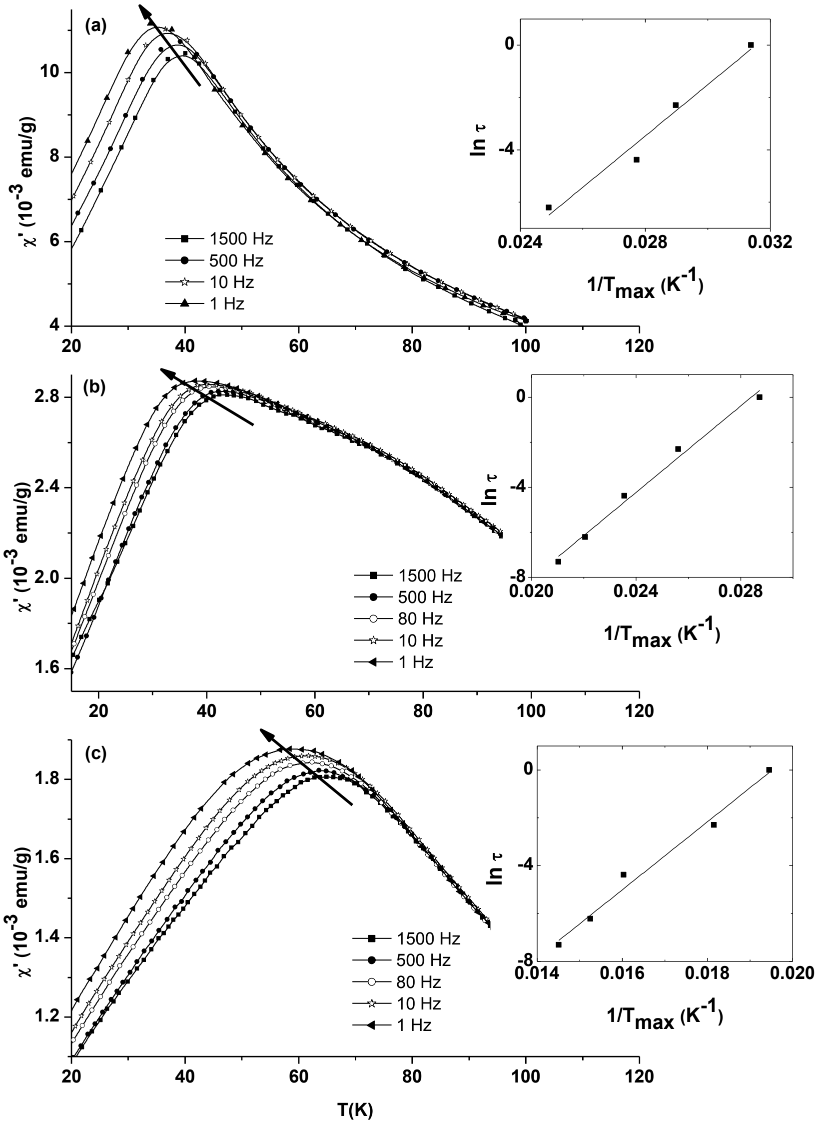

Figure 4.11: In-phase susceptibility (χ') of (a) FHYD2, (b) FHYD2/SiO$_2$, and (c) FHYD6 samples. The insets represents the corresponding Néel Arrhenius plots.

The temperature dependence of the magnetic susceptibility forFHYD2, FHYD2/SiO$_2$ and FHYD6 measured at a frequency of 80 Hz were used to determine the effective magnetic moment from the fit of the Curie-Weiss law to the experimental 1/χ' vs. T curves as shown on the insets in Figure 4.11 (the slopes of the linear parts, at high temperatures) using see Eqs. 3.60 and 3.62. These give μ_{eff} = 5.78 μ_B per atom for FHYD2 and μ_{eff} = 5.20 μ_B for FHYD6 which compare well with previously reported values μ_{eff} = 5.75 μ_B for 2-line FHYD and μ_{eff} = 5.17 μ_B

for 6-line FHYD (Eggleton and Fitzpatrick, 1988) as well as with the experimental value μ_{eff} = 5.85 μ_B and the theoretical value $\mu_{eff} = 2\sqrt{S\,(S+1)} =$ 5.92 μ_B expected Fe^{3+} (S = 5/2) (Buschow and de Boer, 2003).

According to the Néel model for antiferromagnetic nanoparticles, for a particle of size d, the number n of atoms per particle of magnetic moment μ_p and interatomic distance a is given by $n = (d/a)^3$ (Punnoose *et al.*, 2004), the number of uncompensated moments (at the surface) which contribute to the overall magnetic moments of the particle is given by $N_{un} = n^{1/2}$ (Seehra *et al.*, 2000; Punnoose *et al.*, 2004; Silva *et al.*, 2008). For Fe^{3+} cations in FHYD the interatomic distance is estimated to a ~ 3 Å (Seehra *et al.*, 2000; Punnoose *et al.*, 2004; Silva *et al.*, 2008) and the numbers of atoms per particle are estimated to 2370 for FHYD2 and 8000 for FHYD6 considering the average diameters d ≈ 40 and 60 Å, respectively (Table 4.1). Of these, the number of uncompensated moments per particle is estimated to N_{un} ~ 49 for FHYD2 and N_{un} ~ 89 for FHYD6 giving $\mu_p \approx$ 283 μ_B and $\mu_p \approx$ 465 μ_B, respectively. These values are fairly consistent with $\mu_p \approx$ 290 – 370 μ_B reported for FHYD of the average crystallite size in the range 4 – 5 nm (Seehra *et al.*, 2000; Punnoose *et al.*, 2004). The uncompensated spins are distributed throughout the entire volume of the nanoparticles; they are not necessarily concentrated at the surfaces.

Figure 4.12 shows for the three samples the M(H) curves measured at 10, 100 and 300 K in applied magnetic field range - 50 kOe – 50 kOe. At $T > T_B$, the M (H) curves (inserts in Figure 4.12) exhibit a sigmoidal shape at H→0, characteristic of AFM nanoparticles, the sigmoidal shape is more pronounced at 100 K though. This is consistent with the AFM nature of FHYD. Saturation is not attained even at the highest magnetic field of 50 kOe, there is also no coercivity and no remanence as expected for SPM nanoparticles.

Hysteresis loops appear at 10 K (blocked state) but there is no saturation until the highest field of 50 kOe. The hysteresis parameters at 10 K, i.e. the saturation magnetisation (M_S), the remanent magnetisation (M_r), the coercive field (H_c) and the remanence ratio (M_r/M_S) are given in Table 4.1. Note that M_S was determined from the Y-intercept of 1/H vs. M curves (extrapolation), i.e. highest value attained assuming H→∞. At 10 K, the synthesised FHYD2/SiO_2 has a slightly higher M_S (≈ 20 emu/g) as compared to FHYD2 (M_S ≈ 17 emu/g) and FHYD6 ($M_S \approx 15$ emu/g), i.e. M_S decreases with increasing crystallite size. This behaviour originates probably from the presence of uncompensated surface spins as proposed by Neél (LanXiang *et al.*, 2010). Hence, FHYD2/SiO$_2$ with the smallest crystallite size also has a high surface-to-volume ratio and more uncompensated surface spins, thus higher M_S. FHYD6 with the largest size possesses the smallest ratio and the smallest M_S. The two branches of the hysteresis loops at 10 K remain open up to relatively high fields ~ 30 kOe further confirming the presence of uncompensated moments at the surfaces (LanXiang *et al.*, 2010).

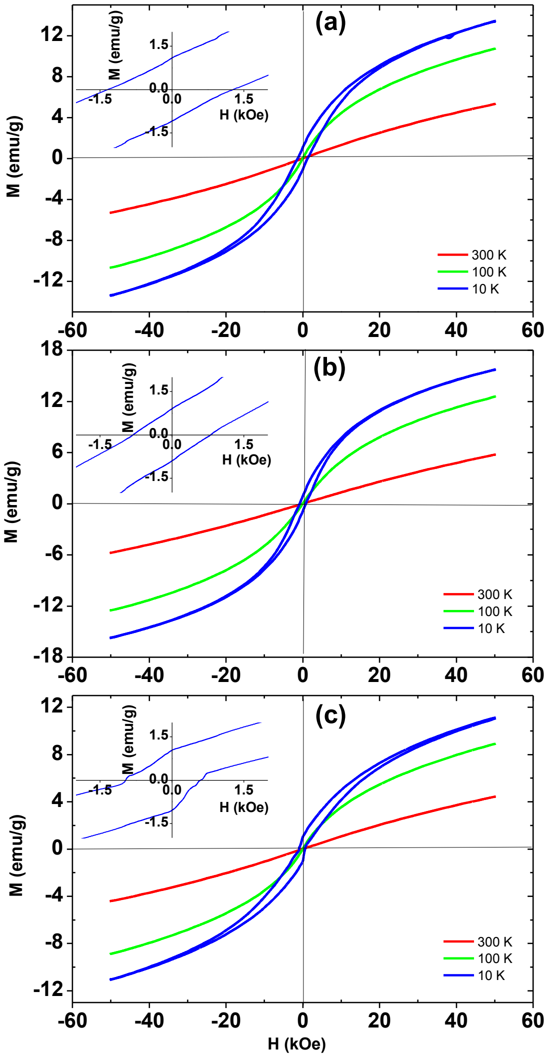

Figure 4.12: Applied magnetic field dependence of the magnetization recorded at 10 K for the synthesized samples: (a) FHYD2, (b) FHYD2/SiO$_2$, and (c) FHYD6. The inserts in (a) – (c) are enlarged scales highlighting the M_r and H_c values at 10 K.

The remanance ratio amounts to $M_r/M_S \approx 0.06$ for FHYD2, $M_r/M_S \approx 0.04$ for FHYD2/SiO_2 and $M_r/M_S \approx 0.07$ for FHYD6. These values are much smaller than $M_r/M_S \approx 0.5$ expected for non-interacting randomly oriented nanoparticles with uniaxial symmetry, they are also smaller that $M_r/M_S \approx 0.1$ expected for interacting particles (Goya *et al.*, 2003). This implies that at 10 K (blocked state) the nanoparticles strongly interact, probably through dipolar and/or exchange interactions. The hysteresis of FHYD6 at 10 K is asymmetric and constricted at low field ($H \rightarrow 0$) exhibiting a typical wasp-waisted shape. Such a behavior is presumably caused by a mixture of SPM and SD nanoparticles. This would imply that a fraction of nanoparticles in FHYD6 are unblocked at 10 K. Alternatively it could be due to a mixture of phases with distinct coercivity spectra (LanXiang *et al.*, 2010).

For the synthesized samples H_c at 10 K varies in a narrow range: H_c = 0.91 kOe for FHYD2/SiO_2, H_c = 1.10 kOe for FHYD2 and H_c = 1.05 kOe for FHYD6 (Table 4.1). These results suggest that in the blocked state the coercive force shows only a weak dependence on the size of the nanoparticles probably due to the competing influence of the strong coupling (dipolar and/or exchange) between the nanoparticles inferred to above from M_r/M_S ratios. The values of H_c obtained at 10 K for FHYD2, FHYD2/SiO_2 and FHYD6 are relatively close to $H_c \sim 1.13 – 1.23$ kOe reported at 5 K for FHYD nanoparticles synthesized using the reverse micelles method for which $K = 3.12 \times 10^5$ J/m^3 (Duarte *et al.*, 2006).

4.3.3 Mössbauer spectroscopy characterization

Figure 4.13 and Figure 4.14 show the MS spectra for the synthesised FHYD2, FHYD2/SiO_2 and FHYD6 recorded at 300 and 4.2 K, respectively. For all three samples the spectra at 300 K consist of quadrupole doublets fitted with distributions of the quadrupole splitting, ΔE_Q. Similarly, all the spectra recorded at 4.2 K consist of sextets fitted with distributions of the hyperfine magnetic field, B_{hf}. The hyperfine parameters thus obtained are given in Table 4.2. Note that the values ΔE_Q and B_{hf} reported in Table 4.2 are the distribution averages. This model was previously suggested by Murad, 1996, to take into account the defective nature of the structure of FHYD. It is believed that the distributions of ΔE_Q and B_{hf} probably result from the different types and arrangement of neighbouring ions (i.e. O, OH, H_2O)

for the interior and surface Fe^{3+} ions, with surface cations having smaller magnetic hyperfine fields compared to the bulk ones (Murad and Schwertmann, 1980; Zhao *et al.*, 1994a).

For all three samples, the hyperfine parameters δ = 0.35 mm/s, $\Delta E_Q \approx 0.68 - 0.71$ mm/s at 300 K (Table 4.2) are comparable and consistent with high spin Fe^{3+} species, their closeness suggests the existence of the same phase in all three samples. The presence of the quadrupole doublets denotes the SPM nature of the crystallites therein, caused by relatively fast relaxation of the spins due to small crystallite size (Murad and Schwertmann, 1980; MØrup, 1983; Guyodo *et al.*, 2006). In such cases B_{hf} average to zero and the corresponding MS spectrum consists of a paramagnetic-like doublet. This is consistent with average diameters ranging from 3.5 – 6.0 nm as obtained above from STEM data. In contrast, at 4.2 K (in the blocked state) magnetic interactions (Zeeman effect) split the nuclear spin levels of iron resulting in a six-line MS spectrum.

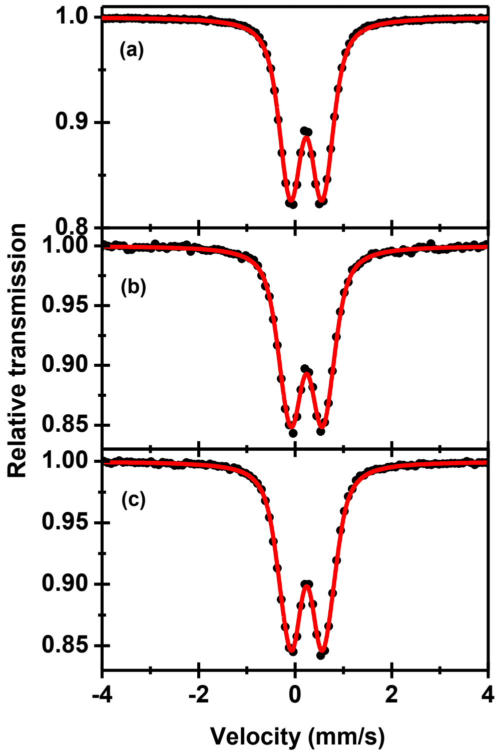

Figure 4.13: Mössbauer spectra recorded at 300 K for the synthesised samples (a) FHYD2, (b) FHYD2/SiO_2, and (c) FHYD6.

Since $\delta \approx 0.35$ mm/s at 300 K and $\delta \approx 0.48$ mm/s at 4.2 K are similar for all three samples the electronic environments for Fe^{3+} in all three samples should also be identical. Similar values of δ were also previously reported for FHYD at 4.2 K and ascribed to octahedrally coordinated Fe^{3+} species (Pankhurst and Pollard, 1992). The temperature induced increase in δ values from $\delta \approx 0.35$ mm/s at 300 K to $\delta \approx 0.48$ mm/s at 4.2 K is probably caused by the second order Doppler shift. The quadrupole splitting at 4.2 K remains in a narrow range ΔE_Q = -0.04 – -0.02 mm/s, it is also consistent with those found for the magnetically split MS spectra of FHYD (Childs and Johnston, 1980; Murad and Schwertmann, 1980; Long and Grandjean, 1993).

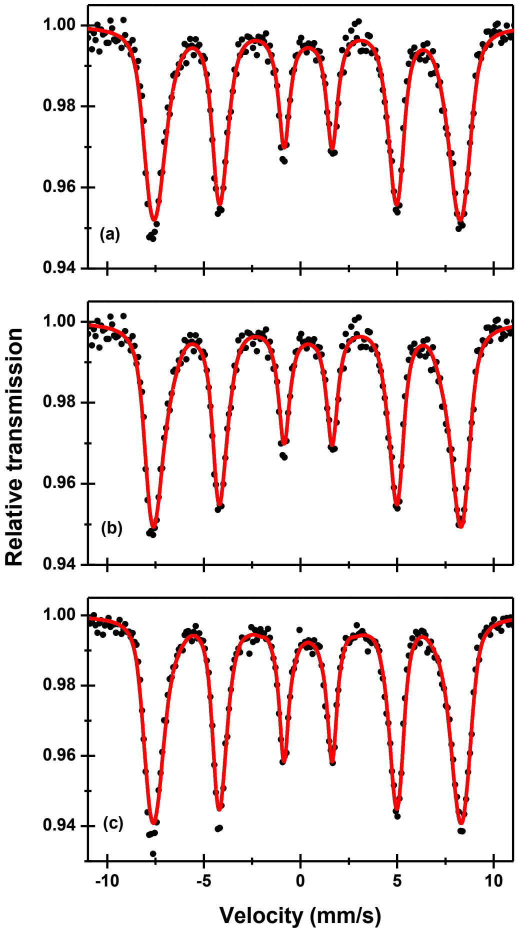

Figure 4.14: Mössbauer spectra recorded at 4.2 K for the synthesis samples: (a) FHYD2, (b) FHYD2/SiO_2, and (c) FHYD6.

All the sextets obtained at 4.2 K (Figure 4.14) have also similar $B_{hf} \approx 47.0 – 49.0$ T thus further pointing to the existence of a single phase. The above values are relatively smaller than $B_{hf} \approx 51$ T for α-FeOOH, $B_{hf} \approx 52$ T for γ-Fe_2O_3 and $B_{hf} \approx 53.5$ T for α-Fe_2O_3 at 4.2 K (Pankhurst and Pollard, 1992). They are rather in agreement with those previously reported for synthetic 2- and 6-line FHYD (Murad, 1996; Guyodo *et al.*, 2006). Interesting, for all the synthesised samples B_{hf} tends to slightly increase with increasing the average crystallite diameters, from $B_{hf} = 47.4$ T for FHYD2/SiO_2 ($D_{av} = 3.5$ nm), to $B_{hf} = 48.1$ T for FHYD2 ($D_{av} = 4.0$ nm) and $B_{hf} = 49.1$ T for FHYD6 ($D_{av} = 6.0$ nm). This points once again to relatively large surface effects of the smallest nanoparticles: as the surface contributions increase atoms at the surface experience weaker exchange fields, thus B_{hf} decreases.

Table 4.2: Mössbauer parameters of FHYD2, FHYD2/SiO$_2$ and FHYD6 recorded at 300 and 4.2 K fitted with distributions of hyperfine parameters.

Sample	300 K			4.2 K			
	δ (mm/s)	$\Delta E_Q{}^{*}$ (mm/s)	$W_\Delta{}^{**}$ (mm/s)	δ (mm/s)	ΔE_Q (mm/s)	$B_{hf}{}^{***}$ (T)	$W_B{}^{****}$ (T)
FHYD2	0.35	0.68	0.23	0.48	-0.03	48.1	7.9
FHYD2/SiO_2	0.35	0.69	0.27	0.49	-0.04	47.4	8.2
FHYD6	0.35	0.71	0.27	0.48	-0.02	49.1	7.4

(*): Average of the distribution of ΔE_Q.
(**): Width (standard deviation) of the distribution of ΔE_Q.
(***): Average of the distribution of B_{hf}.
(****): Width (standard deviation) of the distribution of B_{hf}.

The width (standard deviation) of the distribution of B_{hf} ranges from $W_B = 7.9$ T for FHYD2, to $W_B = 8.2$ T for FHYD2/SiO_2 and $W_B = 7.4$ T for FHYD6. These values are consistent with $W_B \approx 7.8$ T reported for a FHYD sample of poor crystallinity (Pankhurst and Pollard, 1992). Relatively large W_B is taken as an indication of relatively high anisotropy constants in all three samples. This corroborates the results of magnetic measurements discussed above. No Fe/SiO_2 species is observed from MS measurements suggesting that there is no strong interaction between Fe and SiO_2 support/binder in the synthesised FHYD2/SiO_2. However, it appears as though SiO_2 plays a significant role in restricting the distribution of the crystallite size to a narrow range as shown from STEM and magnetic measurements and, in this way, could be used to tune the magnetic properties of nanoparticles which are to a large extent size dependent.

4.4 Chapter Conclusions

Nanoparticles of 2- and 6-line FHYD as well as 2-line FHYD deposited on SiO_2 support were synthesised using rapid hydrolysis of $Fe(NO_3)_3.9H_2O$ solutions. The samples were characterised using powder XRD, TEM, Raman spectroscopy, Mössbauer spectroscopy and magnetic measurements. The X-ray diffractograms of FHYD2 and FHYD2/SiO_2 consist of two broad reflections indicative of the poor crystallinity of these samples while the difractogram of FHYD6 consists of 6 reflections suggesting a relatively better crystallinity than FHYD2 and FHYD2/SiO_2. The TEM micrographs feature typical globular nano-clusters with average crystallite size of 3.5, 4.0 and 6.0 nm for FHYD2/SiO_2, FHYD2 and FHYD6, respectively. The distribution of the crystallite sizes appear to be relatively broader for FHYD6 than for FHYD2 and FHYD2/SiO_2. SAED patterns feature *d*-spacings similar to the XRD data. The Raman spectra of FHYD2 and FHYD6 are similar suggesting the same structural arrangements for the atoms, they also feature patterns typical of FHYD. Disordered and less crystalline FHYD2 and FHYD2/SiO_2 formed by rapid hydrolysis of Fe^{3+} at ambient temperatures and neutral pH while a more crystalline FHYD6 formed by hydrolysis performed at 75°C.

M (T) curves reveal a typical SPM behaviour above blocking temperature T_B = 44, 50 and 36 K for FHYD2, FHYD6 and FHYD2/SiO_2, respectively. Below T_B the nanoparticles are in a blocked state with M increasing only slightly with decreasing T. The anisotropy constant was found to decrease with increasing crystallite size, amounting to $K = 5.5 \times 10^5$ J/m^3 for FHYD2/SiO_2, $K = 4.5 \times 10^5$ J/m^3 for FHYD2, $K = 1.5 \times 10^5$ J/m^3 for FHYD6. These values are consistent with $K = 3.12 \pm 10 \times 10^5$ J/m^3 reported for synthetic FHYD6 and also with $K = 0.4 - 6.1 \times 10^5$ J/m^3 reported for bulk FHYD.

M (H) measurements yield sigmoidal shape curves at T = 100 and 300 K (above T_B) without remanence, coercivity and saturation consistent with the SPM nature of FHYD. Hysteresis loops are obtained for all three samples in a blocked state (at 10 K) with that of FHYD6 exhibiting typical wasp-waisted shape indicating a mixture of SPM and SD nanoparticles. At 10 K the saturation magnetisation decreases with increasing crystallite size, from $M_S \approx 20$ emu/g for FHYD2/SiO_2 to $M_S \approx 17$ emu/g for FHYD2 and $M_S \approx 15$ emu/g for FHYD6, probably due to the presence of uncompensated surface spins. The remanence ratio $M_r/M_S \approx 0.06$ for all three samples are below $M_r/M_S \approx 0.1$ expected from interacting particles, implying that at 10 K (blocked state) the nanoparticles strongly interact. MS measurements confirm the SPM nature of nanoparticles in the three samples. These measurements at 4.2 K yield MS parameters typical of FHYD with Fe^{3+} in identical the electronic environments for all three samples.

This study underlines particularly the key influence of the crystallite size and surface atoms on the magnetic properties of nanoparticles. The fraction of surface atoms is known to increases with decreasing crystallite size. This results in increasing anisotropy constant due mainly to surface anisotropy, increasing the number of uncompensated surface spins which leads to increasing M_S in the blocked state. Further, with increasing surface contributions atoms at the surface sense weaker exchange fields in the blocked state thus the hyperfine magnetic field decreases. These observations are consistent with well known facts that in nanoparticles the crystallite size and geometry determine the extent and configuration of the magnetic domains.

Chapter 5

Ferrihydrite Structure: Evidence of T_d Coordinated Fe^{3+}

Abstract

In this chapter, EELS is used to probe the Fe L-edge of FHYD2 and FHYD6. Evidence of Fe^{3+} in Td coordination was found and the abundance of Fe^{3+} in T_d symmetry estimated from the NLLS fitting coefficients amounts to about 20 and 18% Fe^{3+} for FHYD2 and FHYD6, respectively. The MS spectra recorded in zero-field and in applied magnetic field were successfully fitted with a model accounting for iron atoms in three sites Fe1, Fe2 and Fe3 as per Michel's structural model for FHYD.

5.1 Introduction

As it has been extensively discussed in chapter 2, the structure of FHYD has been recently described by two competing models proposed by Drits *et al.*, 1993 and Michel *et al.*, 2007c. One of the main differences between the two models is about the presence (or absence) of T_d Fe^{3+} within the structure of FHYD. Attempts to address this issue are presented in this chapter based on explorations of the coordination environment of iron atoms in FHYD2 and FHYD6 nanoparticles using EELS and MS measurements. A high spectral resolution of better than 0.3 eV was used compared to the energy resolution of 0.8 eV used in the EELS work (Pan *et al.*, 2006; Pan, 2007; Pan *et al.*, 2009; Pan *et al.*, 2010).

5.2 Experimental

Electron energy loss spectroscopy

EELS measurements were performed at the Stuttgart Center for Electron Microscopy (sTEM) at the Max Planck Institute for Intelligent Systems using the Sub-Electron-Volt-Sub-Angstrom-Microscope (SESAM) transmission electron microscopy facility operating at 200 kV and equipped with a monochromator and in-column MANDOLINE imaging filter. Full description and capabilities of the SESAM microscope is reported elsewhere (van Aken *et al.*, 2007). EELS spectra obtained in image mode were acquired with an energy resolution of 0.2 – 0.3 eV, energy dispersion of 0.037 eV/channel and a collection angle of 3 mrad. Four different areas were investigated for each sample and for each area100 spectra were acquired using a time series script developed in-house for digital micrograph. The final pattern was obtained by aligning individual spectra and averaging in digital micrograph using a script.

The local electronic structure at the Fe atoms in FHYD was probed using the Fe $L_{3,2}$-edge which, as previously shown, is conventionally characterized by two intense sharp peaks termed "white lines". A method originally developed by Garvie and Buseck, 1998 and further developed by Pan group (Pan *et al.*, 2006; Pan, 2007; Pan *et al.*, 2009; Pan *et al.*, 2010) was adapted to determine the coordination environment of iron atoms using EELS reference spectra of iron oxides with well-known coordination chemistry. These included α-Fe_2O_3 (O_h Fe^{3+}), γ-Fe_2O_3 (62.5 % O_h Fe^{3+} and 37.5 % T_d Fe^{3+}), Fe_3O_4 (O_h Fe^{3+}/Fe^{2+} and T_d Fe^{3+}) and FeO (O_h Fe^{2+}). Prior to fitting, spectra were processed using Gatan's DM software (Gatan Microscopy Suite 2.11.1404.0). The energy scales were calibrated using reported energy values (Garvie and Buseck, 1998; van Aken *et al.*, 1998; van Aken and Liebscher, 2002). For Fe^{3+} bearing α-Fe_2O_3 and γ-Fe_2O_3 the main peak was set at 709.5 eV and for Fe^{2+} compound (FeO) it was set at 707.8 eV. For mixed valence compound Fe_3O_4 the maximum around the L_3 edge was centered at 708.9 eV. The spectra were then background stripped using power law model AE^{-r} (Egerton, 2011). To obtain single scattering distribution (SSD), plural scattering was removed by the Fourier-ratio deconvolution method (Egerton, 2011) using low-loss spectra taken at the same experimental conditions as the Fe $L_{2,3}$ edge.

A non-linear least square (NLLS) fitting routine performed within IGOR Pro (version 6.32A) software was used in this work. This software was preferred over MLLS/NLLS fitting performed in DM because it provides the user with options to constrain the fitting coefficients and accommodate small energy shift in edge positions. In all the procedures the fitting parameters were constrained in that the coefficients of each reference spectrum were set to be greater than zero and small energy shifts were allowed to occur (-0.3 to 0.3 eV) during fit iterations according to the approach used by Pan *et al.*, 2010. The goodness of the fit was measured by chi-squared (χ^2) defined as (Pan *et al.*, 2010):

$$\chi^2 = \sum_i \left(\frac{y - y_i}{\sigma_i}\right) \qquad 5.1$$

where y_i and y is the measured data value and fitted value for a given point, respectively and σ_i is the standard deviation estimate for y_i. The percentages of Fe^{3+} in tetrahedral and octahedral coordination were estimated from the weighting coefficients of the NLLS fitting procedures.

Mössbauer Spectroscopy

The MS experiments were performed using the Spectromag SM4000-10 cryomagnet described in section 4.2.2; the fitting procedures and MS parameters are also the same as described in this section. In addition, MS measurements were performed at 4.2 K in zero-field (ZFMS) and at 4.2 K in an external magnetic field (B_{app}) of 10 T applied parallel to the direction of γ-rays, referred to as in field Mössbauer spectroscopy (IFMS).

The internal hyperfine magnetic field (B_{hf}) obtained in ZFMS and the effective magnetic field (B_{eff}) measured in IFMS are related, i.e. (Murad and Cashion, 2004):

$$\vec{B}_{eff} = \vec{B}_{app} + \vec{B}_{hf} \qquad 5.2$$

The direction of $\vec{B}_{hf}$ is usually taken to be opposite that of the magnetisation ($\vec{M}$) and, in practice, the alignment of the spins is never perfect such that the relation between B_{eff} and B_{hf} is
(Helgason *et al.*, 2006)

$$B_{hf}^2 = B_{eff}^2 + B_{app}^2 - 2B_{eff}B_{app}\cos\theta \qquad 5.3$$

where θ is the angle between $\vec{B}_{app}$ and $\vec{M}$. For a magnetically split spectrum (sextet) an external magnetic field causes the effective magnetic field to increase or decrease and the intensities of the lines 2 and 5[8] of the MS spectra to vary depending on the magnetic ordering and direction of the applied field with respect to the direction of γ-rays.

5.3 Results and discussions

5.3.1 Electron energy loss spectroscopy (EELS)

In iron minerals, iron is mostly found in Fe^{2+} and Fe^{3+} oxidation states which is commonly coordinated octahedrally, and sometimes tetrahedral coordination is possible. The Fe $L_{3,2}$ edges of FHYD2 and FHYD6 as well as that of a certain number of reference compounds in Fe^{2+} and Fe^{3+} in octahedral (O_h) and tetrahedral (T_d) coordination are depicted in Figure 5.1. The standard compounds were selected to provide spectral reference for O_h and T_d coordinated Fe^{2+} and Fe^{3+} to be used to model the Fe L_3 edge for FHYD2 and FHYD6.

The $L_{3,2}$ edges of transition metals are characterized by sharp maxima known as "white lines" (Leapman and Grunes, 1980; Leapman *et al.*, 1982; Calvert *et al.*, 2005; Riedl *et al.*, 2006) as shown in Figure 5.1. All the fine structure features present in our EELS spectra were also identified in previous work (Chen *et al.*, 2009). Hematite shows a characteristic L_3 edge with a strong pre-peak at ~ 708.0 eV leading to the main L_3 peak at 709.5 eV. This strong L_3 splitting feature in α-Fe_2O_3 was attributed to the strong ligand-field splitting from O_h symmetry around the Fe^{3+} ion (Chen *et al.*, 2009). Maghemite also show features of a trivalent state iron with an L_3 pre-peak which is less intense compared to α-Fe_2O_3. It is known that the crystal field splitting is affected by factors such as the type of ligand and the geometry of the complex (Douglas *et al.*, 1994) and the ligands in γ-Fe_2O_3 are coordinated in O_h and T_d symmetry (Cornell and Schwertmann, 2003). The contribution of complexes coordinated in T_d geometry is less in the crystal field splitting compared to octahedral crystal fields due to fewer ligands in T_d symmetry. As a result, maghemite will not show a strong splitting compared to hematite.

---

[8] The lines of a magnetically split MS spectra are counted 1, 2, 3, 4, 5 and 6 from left to right with relative ratios 3:2:1:1:2:3 for randomly distributed particles in the absence of an applied magnetic field.

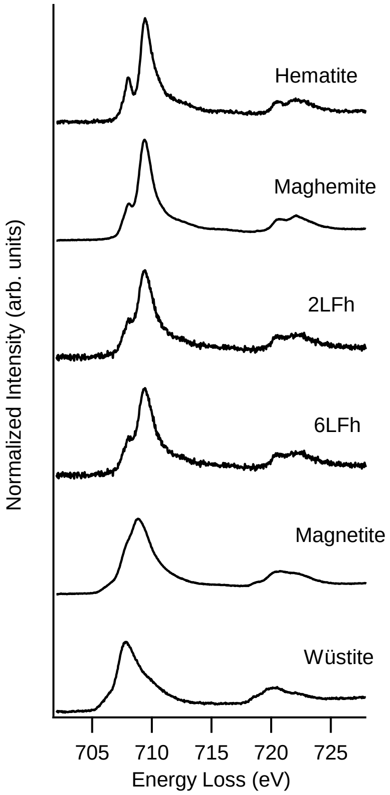

Figure 5.1: Fe L3,2 edge of FHYD2, FHYD6, and four reference spectra used in our fitting routine.

Magnetite shows the typical Fe $L_{3,2}$ edge of a mixed valence compound (van Aken and Liebscher, 2002; Chen *et al.*, 2009). The L_3 peak appears shapeless with no obvious split even with high resolution synchrotron experiments. This is due to the electron hopping between the Fe^{2+} and Fe^{3+} in the octahedral sublattice at room temperature (Chen *et al.*, 2009; Skomurski *et al.*, 2010). Fe^{2+} bearing compounds shows a ~ 2 eV chemical shift to lower energy with respect to the Fe^{3+} compounds (Chen *et al.*, 2009). This was observed in our experimental wüstite reference spectra as shown in Figure 5.1.

The Fe $L_{3,2}$ edges of FHYD2 and FHYD6 (Figure 5.1) show a significantly weaker splitting of the L_3 peak as compared to hematite, an indication of a weak crystal field around the iron. There are several factors that contribute to the weak ligand field in the FHYD molecular orbitals. Apart from oxygen ligands, there is a presence of weak-field ligands ((OH/H_2O) in FHYD which is expected to produce small crystal field splitting (Douglas *et al.*, 1994; Chen *et* *al.*, 2009). The poor crystalline nature of FHYD was also pointed out to contribute to the weak L_3 splitting (Chen *et al.*, 2009). In addition, ligands in T_d symmetry produce a small splitting and FHYD is believed to have some Fe^{3+} in T_d symmetry (Michel *et al.*, 2007c; Maillot *et al.*, 2011; Guyodo *et al.*, 2012; Peak and Reiger, 2012a) which is also a central subject of this investigation.

NLLS fitting approach using well characterized reference spectra were used to model the Fe L_3 edge of FHYD and the percentage of O_h and T_d Fe^{3+} were estimated from the weighting coefficients of each reference spectra (see Pan, 2007 for this procedure). Figure 5.2 (a) shows an NLLS fit of the FHYD L_3 edge obtained by fitting a model function consisting of three reference spectra and the relative proportions of the reference materials are also shown. The fitting was restricted to the Fe L_3 edge only (702 – 718 eV) in order to minimize errors populating from large fitting windows.

An accurate fit was obtained using a model function consisting of three reference spectra (γ-Fe_2O_3, αFe_2O_3, and FeO) as shown in Figure 5.2 (b). From the difference spectrum (experimental spectrum - model spectrum) it could clearly be seen that the model accurately explained experimental data. The high weighting coefficient of γ-Fe_2O_3 was taken as a strong indication of the presence of T_d Fe^{3+} in our FHYD2 sample. However, the presence of Fe^{2+} species (wüstite) in our fit posed challenges in the interpretation of our results. A fit without the wüstite reference (Figure 5.3) produced a rather poor fit with a mismatch on the pre-edge peak side. Three reference spectra that included either wüstite or magnetite as one of the references produced accurate fit to the experimental spectrum. The addition of Fe^{2+} species (either from FeO or Fe_3O_4) in the fitting routine was a requirement to produce a good match between experimental and calculated spectra.

The presence of Fe^{2+} in FHYD was reported to result from an electron beam damage process (Pan *et al.*, 2006; Pan, 2007; Pan *et al.*, 2009; Pan *et al.*, 2010). The authors termed the dose (10^8 electrons/nm^2) as a safe electron dose to prevent the reduction of Fe^{3+}. However, the contribution of the wüstite phase was reported in doses as low as 3×10^6 electrons/nm^2 by the same authors. In addition, Vaughan *et al.*, 2010 reported the presence of ferrous iron at lower electron fluencies (< 10^7 electrons/nm^2) than the dose deemed safe. They extrapolated the data back to zero fluence limit and estimated that only ~ 90 % of iron was in trivalent state and the remaining iron was in reduced ferrous state.

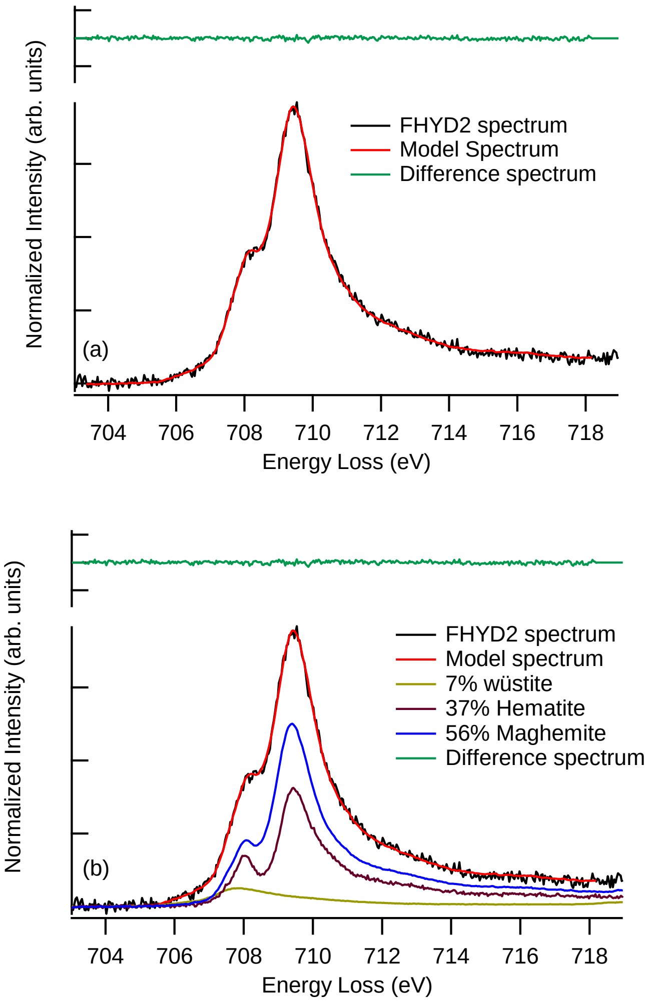

Figure 5.2: (a) The experimental FHYD2 spectrum (black), calculated fit curve (red), and (b) the reference spectra that produced the best fit. The difference spectrum is plotted on the same scale, however shifted vertically for clarification.

It is worth mentioning that it is puzzling that the fitting routine requires the contribution of Fe^{2+} species since precautionary measures were taken to avoid electron beam damage. Although the electron fluence used in this study was not measured, a set of 100 EELS spectra were taken in a time series fashion and then compared the first and last spectra to see if there were any changes between these spectra; no visible spectral changes were observed. The requirement to fit the experimental FHYD2 spectra with model function that consists of Fe^{2+} was a clear indication of the extreme sensitivity of the material under the electron beam. This observation challenges a previous report (Gloter *et al.*, 2004) which claims that natural FHYD contains a significant amount of Fe^{2+} species. The authors did not use other techniques to prove the existence of the ferrous iron in their sample. In fact Mössbauer spectroscopy results (Murad and Schwertmann, 1980) showed that iron in natural FHYD is present in Fe^{3+} oxidation state.

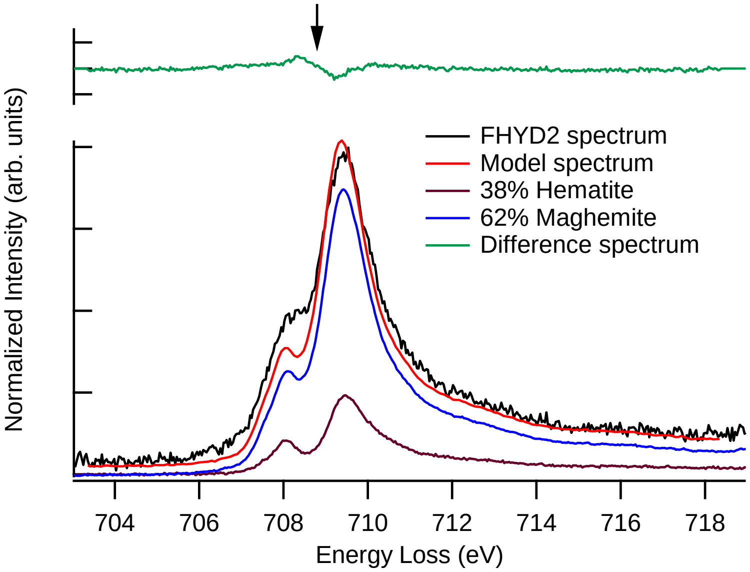

Figure 5.3: NLLS fit of FHYD2 showing the mismatch at the lower energy side of the main *L*3 peak as pointed by the arrow on difference spectrum which is shifted vertically for clarification.

The percentage of O_h and T_d Fe^{3+} coordination was estimated form the weighting coefficients of each reference spectra of the NLLS fitting routine. These weighting coefficients are specifically taken to represent the percentage of O_h and T_d coordination and not the volume fraction of each reference spectra. As noted by Pan *et al.*, 2006, "*Please note that the coefficients generated from the MLLS fitting are not taken to represent the volume percentage of each reference material present in FHYD6 and human liver ferritin cores, but are taken solely as estimates of the valence and local coordination of the iron in the material under investigation*". Table 5.1 summarizes the weighting coefficients and chi-squared (χ^2) values produced from the NLLS fitting of the FHYD2 spectra.

In this study NLLS fitting results suggest that a significant portion of Fe^{3+} in FHYD2 is in tetrahedral coordination. An amount of 20 ± 5 % Fe^{3+} was estimated to be four-fold coordinated. This supports earlier studies that suggested the presence of 20-30 % T_d Fe^{3+} in the structure of FHYD (Maillot *et al.*, 2011; Guyodo *et al.*, 2012; Peak and Reiger, 2012a). Peak and Reiger, 2012a estimated the relative percentages of O_h and T_d Fe^{3+} by fitting the experimental IPFY (inverse partial fluorescence yield) data of γ-Fe_2O_3 and FHYD2 with theoretical calculated data. A significant amount (30-40 %) of T_d Fe^{3+} in the FHYD2 structure was produced by the results of such fit. The similarities between the IPFYs of γ-Fe_2O_3 and FHYD2 provided further evidence of the presence T_d Fe^{3+} in FHYD2 (Peak and Reiger, 2012a). Iron $L_{3,2}$ XMCD (X-ray magnetic circular dichroïsm) measurements by Guyodo *et al.*, 2012, also suggested a concentration of 20-30 % tetrahedral sites in the structure of FHYD.

Table 5.1: Fitting coeficinets from FHYD2 NLLS fitting with and without the wüstite phase.

Fitting Coefficients ($\sum = 1$)			χ^2
α-Fe_2O_3	γ-Fe_2O_3	FeO	
0.38± 0.0082	0.62± 0.0232	-	2.53×10^{-5}
0.37± 0.0027	0.56± 0.0157	0.07± 0.0016	6.00×10^{-6}

Figure 5.4 shows the EELS spectra of FHYD6 fitted only with only Fe^{3+} references. The intensity of the calculated spectrum (from model function) was a bit lower than the experimental spectrum on the pre-edge peak (see mismatch on difference spectrum in Figure 5.4). An attempt to fit the experimental Fe L_3 edge of FHYD6 with a model function consisting of a combination of only Fe^{3+} reference spectra (α-Fe_2O_3 and γ-Fe_2O_3) produced unsatisfactory results especially on the L_3 pre-edge side. Similarly to FHYD2, a successful fit for FHYD6 was obtained by a model function consisting of linear combination of γ-Fe_2O_3, α-Fe_2O_3, and FeO reference materials.

Figure 5.5 shows an NLLS fit of the FHYD6 Fe L_3 spectrum and the corresponding relative percentages of each reference spectra. The NLLS fitting coefficients each reference spectra generated during the fitting procedure are shown in Fig. 5(b). The addition of small amount of Fe^{2+} species (either FeO or Fe_3O_4) produced a good match to the experimental L_3 edge of FHYD6 (see Figure 5.5 (b)). The improvement in the fit was determined by both the chi-squared (χ^2) value and visual inspection of the difference spectrum. The fitting coefficients and χ^2 values generated during the NLLS fitting procedure of the FHYD6 spectra are listed in Table 5.2.

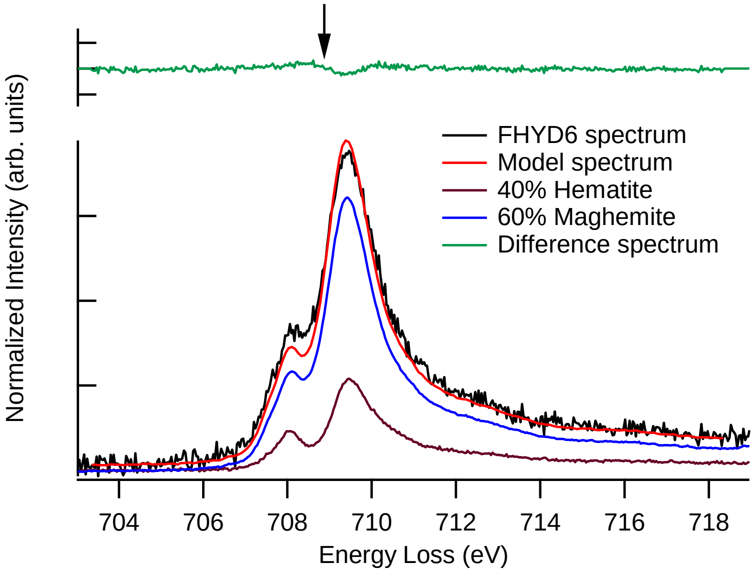

Figure 5.4: NLLS fit of FHYD6 showing the mismatch (clearly visible on the difference spectrum on the position of the arrow) at the lower energy side of the main *L*3 peak.

Table 5.2: Fitting coeficinets from FHYD6 NLLS fitting with and without the wüstite phase.

Fitting Coefficients ($\sum = 1$)			χ^2
α-Fe_2O_3	γ-Fe_2O_3	FeO	
0.40± 0.0071	0.60± 0.0170	-	1.56×10^{-5}
0.445± 0.0093	0.495± 0.0120	0.06± 0.0005	7.13×10^{-6}

The percentage of T_d Fe^{3+} was estimated from the γ-Fe_2O_3 spectra since α-Fe_2O_3 and FeO does not contain any tetrahedral Fe^{3+}. On the basis of the NLLS fitting, a significant amount (18 ± 5 %) of Fe^{3+} was estimated to be in T_d coordination for FHYD6. This amount is also comparable with previous reported values (Maillot *et al.*, 2011; Guyodo *et al.*, 2012; Peak and Reiger, 2012a).

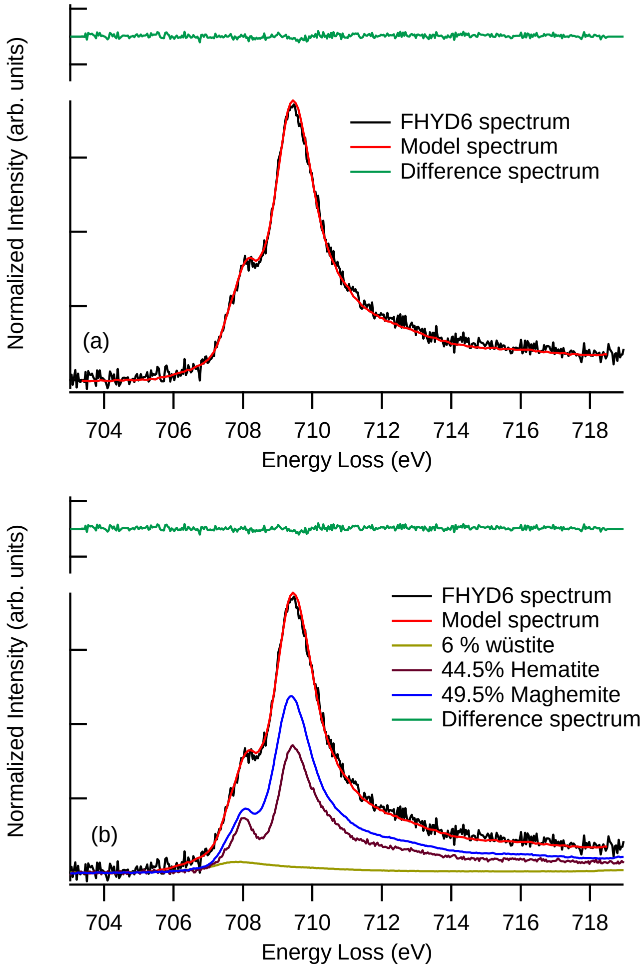

Figure 5.5: (a) The experimental Fe L_3 edge of FHYD6 (black), corresponding best fit curve (red), and (b) the relative proportions of the three reference compounds. The difference spectrum is plotted on the same scale, however shifted vertically for clarification.

5.3.2 Mössbauer Spectroscopy

Figure 5.6 (a) and (b) shows ZFMS[9] and IFMS spectra of FHYD2 recorded at 4.2 K in an applied magnetic field of 10 T. The corresponding ZFMS hyperfine parameters for the FHYD2 spectra are given in Table 5.3 together with the relative resonance absorption areas for each of the three Fe sites.

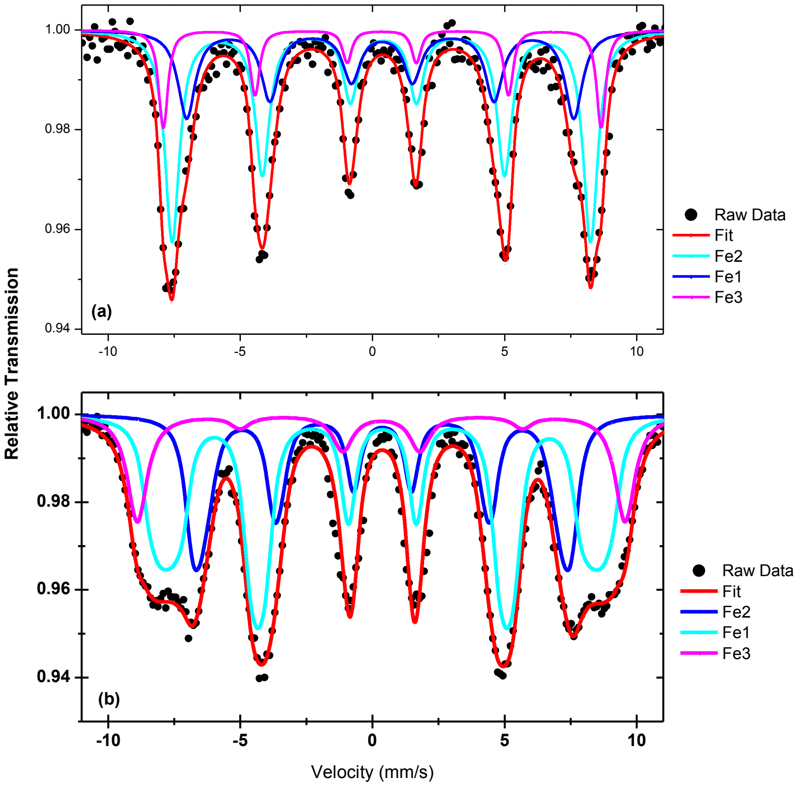

Figure 5.6: Mössbauer spectra of FHYD2 recorded at 4.2 K in (a) 0 T (b) 10 T applied parallel to the direction of γ-rays. Fe1, Fe2 and Fe3 correspond to the three types of Fe sites in FHYD structure.

ZFMS spectrum of FHYD2 yields three six-line sub-spectra (sextets) with parameters δ = 0.49 mm/s, ΔE_Q = -0.08 and B_{hf} = 49.1T; δ = 0.44 mm/s, ΔE_Q = -0.07 and B_{hf} = 45.4 T and; δ = 0.47 mm/s, ΔE_Q = 0.02 and B_{hf} = 51.4 T. These values are within the ranges $\delta \approx 0.45 - 0.50$

---

[9] Note that the ZFMS reported in Fig. 5.6 is exactly the same as in Fig.414 (a). The difference is that the ZFMS in Fig. 4.14 (a) was fitted with a model previously reported for FHYD to show that the synthesized phase was really FHYD2. And the ZFMS in Fig. 5.6 was fitted with a model used in this study.

mm/s, $\Delta E_Q \approx -0.10 - 0.06$ mm/s and $B_{hf} \approx 45.0 - 50.0$ T reported for FHYD at 4.2 K from ZFMS measurements (Childs and Johnston, 1980; Murad and Schwertmann, 1980; Murad and Weihenstephan, 1982; Madsen *et al.*, 1986; Maddock, 1997).

The hyperfine parameters obtained from IFMS spectra (Figure 5.6 (b)) for FHD2 amount to $\delta = 0.47$ mm/s, $\Delta E_Q = -0.04$ and $B_{eff} = 50.4$ T; $\delta = 0.48$ mm/s, $\Delta E_Q = -0.02$ and $B_{eff} = 43.2$ T and; $\delta = 0.45$ mm/s, $\Delta E_Q = 0.02$ and $B_{eff} = 57.2$ T. These values are summarized in Table 5.3 and they are in good agreement with literature reported values for FHYD (Childs and Johnston, 1980; Murad and Schwertmann, 1980; Murad and Weihenstephan, 1982; Madsen *et al.*, 1986; Maddock, 1997; Cornell and Schwertmann, 2003).

The coordination chemistry of Fe^{3+} of the FHYD with better crystallinity i.e. FHYD6 was also studied. Figure 5.7 (a) shows ZFMS[10] spectra of FHYD6 recorded at 4.2 K and Figure 5.7 (b) shows the corresponding IFMS spectra at 4.2 K in an applied magnetic field of 10 T. The ZFMS spectrum of FHYD6 gives three sextets with $\delta = 0.50$ mm/s, $\Delta E_Q = -0.05$ and $B_{hf} = 49.3$ T; $\delta = 0.43$ mm/s, $\Delta E_Q = -0.05$ and $B_{hf} = 45.8$ T and; $\delta = 0.50$ mm/s, $\Delta E_Q = 0.01$ and $B_{hf} = 51.6$ T. These values were also within the ranges $\delta \approx 0.45 - 0.50$ mm/s, $\Delta E_Q \approx -0.10 - 0.06$ mm/s and $B_{hf} \approx 45.0 - 50.0$ T reported for FHYD at 4.2 K from ZFMS measurements (Childs and Johnston, 1980; Murad and Schwertmann, 1980; Murad and Weihenstephan, 1982; Madsen *et al.*, 1986; Maddock, 1997).

---

[10] Note that the ZFMS for FHYD6 reported in Fig. 5.7 is exactly the same as in Fig.414 (c). The difference is that the ZFMS in Fig. 4.14 (c) was fitted with a model previously reported for FHYD to show that the synthesized phase was really FHYD6. And the ZFMS in Fig. 5.7 was fitted with a model used in this study.

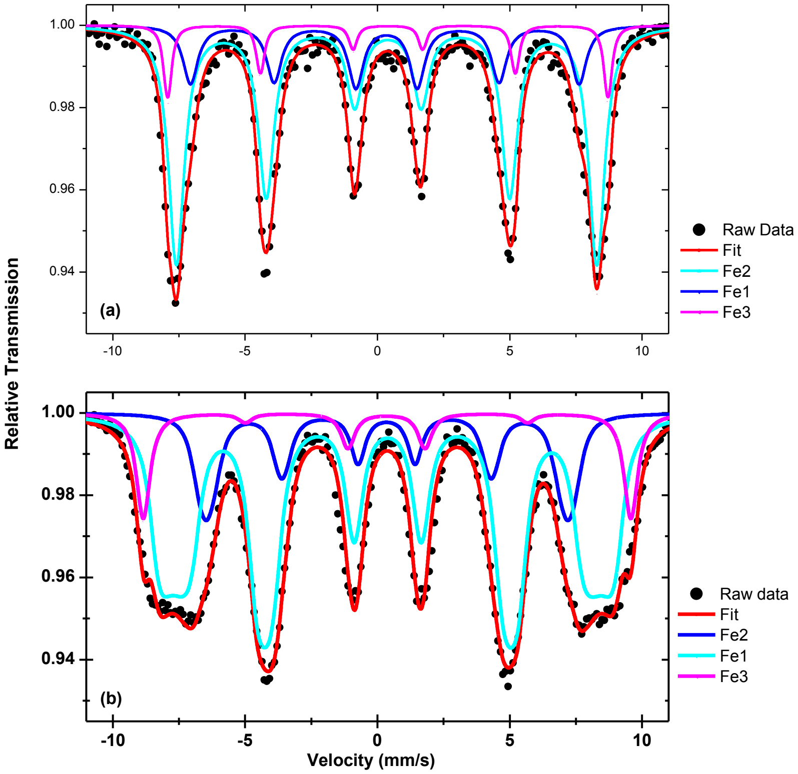

Figure 5.7: Mössbauer spectra of FHYD6 recorded at 4.2 K in (a) 0 T (b) 10 T applied parallel to the direction of γ-rays. Fe1, Fe2 and Fe3 correspond to the three types of Fe sites in FHYD structure.

From IFMS spectra of FHYD6 ones obtains δ = 0.48 mm/s, ΔE_Q = -0.04 mm/s and B_{eff} = 49.7 T; δ = 0.47 mm/s, ΔE_Q = -0.02 mm/s and B_{eff} = 42.3 T; δ = 0.47 mm/s, ΔE_Q = 0.02 mm/s and B_{eff} = 57.1 for FHYD6. These values are also consistent with $\delta \approx$ 0.44 – 0.50 mm/s, $\Delta E_Q \approx$ -0.08 – 0.04 mm/s and $B_{eff} \approx$ 43 – 57 T reported for FHYD from IFMS measurements (Childs and Johnston, 1980; Murad and Schwertmann, 1980; Murad and Weihenstephan, 1982; Madsen *et al.*, 1986; Maddock, 1997).

The MS results in Table 5.3 show that for both ZFMS and IFMS measurements the isomer shift varies in a narrow range $\delta \approx$ 0.43 – 0.50 mm/s, typical of Fe^{3+} species. The presence of divalent Fe species as inferred to from EELS analysis of FHYD2 and FHYD6 is therefore not supported by ZFMS and IFMS results. Previous Mössbauer spectroscopy results by Murad and Schwertmann, 1980, also showed that iron in natural FHYD is only present in Fe^{3+} oxidation state. The requirement to fit the EELS spectra of FHYD2 and FHYD6 with model function that consists of Fe^{2+} is therefore taken as an indication of the extreme sensitivity of the material under the electron beam. Noteworthy, the claim by Gloter *et al.*, 2004, that natural FHYD contains a significant amount of Fe^{2+} species was not supported by complementary techniques. The narrowness of the δ range observed here for FHYD2 and FHYD6 seems to imply that the electronic densities around Fe^{3+} nuclei are almost identical. Furthermore, the values of ΔE_Q are small and vary also in a narrow range 0.04 – -0.08 mm/s, which could indicate nearly cubic lattice site symmetry around the Fe^{3+} nuclei. However, ΔE_Q values in both ZFMS and IFMS for two of the three sextets are negative which imply that the corresponding nuclei are not perfectly spherical but rather slightly oblate as opposed to a slightly prolate shape for the sextet with positive ΔE_Q values (Murad and Cashion, 2004).

A comparison between ZFMS and IFMS data for FHYD6 and FHYD2 (Table 5.3) shows that for one of the sextets $B_{eff} \approx B_{hf} \approx 49$ T (and $\Delta E_Q < 0$) and the intensities of the lines 2 and 5 on the IFMS spectra increase as expected for antiferromagnetic (AFM) materials (Chen *et al.*, 2008). For the second sextet $B_{eff} \approx 43$ T (and $\Delta E_Q < 0$) is slightly smaller than $B_{hf} \approx 45$ T indicating that the spins tend to align antiparallel to B_{app} (i.e. B_{app} tend to subtract from B_{hf}) as usually observed on the octahedral sites of ferrimagnetic (FiM) materials (Chen *et al.*, 2008). However, contrary to what is expected for FiM materials the intensities of the lines 2 and 5 for IFMS spectra do not cancel out which might indicate that spin alignment is almost completely suppressed due to spin canting and/or to the presence of defects, vacancies and impurities (Linderoth *et al.*, 1994). For the third sextet $B_{eff} \approx 57$ T (and $\Delta E_Q > 0$) is much higher than $B_{hf} \approx 51$ T, i.e. B_{app} adds up to B_{hf}, the intensities of the lines 2 and 5 on IFMS spectra cancel out almost completely; similar behaviour is expected for Fe atoms on the tetrahedral sites of FIM materials (Chen *et al.*, 2008). The spin alignment is however also not perfect as indicated by the presence of small residual intensities for the lines 2 and 5.

Table 5.3: Mössbauer parameters of FHYD2, FHYD2/SiO$_2$ and FHYD6 obtained from the spectra recorded at 4.2 K with and without an applied magnetic field of 10 T parallel to the direction of γ-rays.

Sample	T (K)	B_{app} (T)	$^{\#}\delta$ (mm/s)	$^{\#}$ ΔE_Q (mm/s)	B_{hf}/B_{meas} (T)	▪A (%)	Fe sites
FHYD2	4.2	0	0.49	-0.08	49.1 ± 0.6*	53	Fe1 O_h
			0.44	-0.07	45.4 ± 0.2*	32	Fe2 O_h
			0.47	0.02	51.4 ± 0.2*	15	Fe3 T_d
	4.2	10	0.47	-0.04	50.4 ± 2.9**	54	Fe1 O_h
			0.48	-0.02	43.2 ± 1.7**	30	Fe2 O_h
			0.45	-0.04	57.2 ± 0.8**	16	Fe3 T_d
FHYD6	4.2	0	0.50	-0.05	49.3 ± 0.1*	67	Fe1 O_h
			0.43	-0.07	45.5 ± 0.1*	23	Fe2 O_h
			0.51	-0.00	51.6 ± 0.1*	10	Fe3 T_d
	4.2	10	0.48	-0.04	49.7 ± 3.1**	69	Fe1 O_h
			0.47	0.02	42.3 ± 1.6**	20	Fe2 O_h
			0.47	0.02	57.1 ± 0.6**	11	Fe3 T_d

(*): Hyperfine magnetic field, B_{hf}

(**): Effective magnetic field, B_{meas}, measured in an applied magnetic field of 10 T

Uncertainties: $^{\#}$ ± 0.02 mms^{-1}, ▪ ± 2%. The uncertainties on B_{meas} are the standard deviations of the distributions of B_{meas}.

The IFMS spectra of both FHYD2 and FHYD6 are successfully fitted with a model combining an AFM-like sub-lattice and two FiM-like sub-lattices both of which with a certain degree of imperfectly aligned magnetic moments due to spin canting and/or some degree of disorder. This model differs somehow from the two FIM sub-lattices for 2-line FYHD and a single AFM sub-lattice for 6-line FHYD proposed by Pankhurst and Pollard, 1992. It is however compatible with Michel's structural model for FHYD; in this scenario the three sextets apparent on the ZFMS and IFMS spectra of FHYD2 and FHYD6 correspond to the three different Fe sites Fe1, Fe2 and Fe3 of Michel's model. The two sextets with $B_{eff} \approx 49$ and $B_{eff} \approx 43$ T are ascribed to the octahedrally coordinated Fe1 and Fe2, respectively, while the sextet with $B_{eff} \approx 57$ T is ascribed to the tetrahedrally coordinated Fe3. Both ZFMS and IFMS results give relative abundances of approximately 53% for Fe1 (O_h), 31% for Fe2 (O_h) and 15% for Fe3 (T_d) for FHYD2; 67% for Fe1 (O_h), 23% for Fe2 (O_h) and 10% for Fe3 (T_d) for FHYD6. These values are fairly in agreement with the ideal values of 60, 20 and 20%, respectively, proposed by Michel, 2007a. However, additional analysis, particularly IFMS measurements with variable external magnetic field applied both parallel and normal to the direction of γ-rays, are needed to test the validity of this model.

Usually for Fe^{3+} increasing Fe-O bond length increases the isomer shift on the tetrahedral sites and increasing distortion either by increasing bond length or bond angle variation results in increasing quadrupole splitting (Cardile and Brown, 1988b). For FHYD2 and FHYD6 the electronic densities around Fe^{3+} nuclei are almost identical for Fe1, Fe2 and Fe3 as indicated by almost identical values of the isomer shift. The symmetry around iron nuclei on O_h sites Fe1 and Fe2 with absolute values $|\Delta E_Q| \approx 0.04 – 0.08$ mm/s could however be slightly more distorted than for the T_d sites Fe3 with $|\Delta E_Q| \approx 0.01 – 0.02$ mm/s probably due to slightly different Fe-O bond angle variation.

5.4 Chapter Conclusions

The structural properties of 2- and 6-line FHYD samples prepared by rapid hydrolysis of $Fe(NO_3)_3.9H_2O$ solutions are discussed. High resolution EELS results provide evidence for the presence of T_d Fe^{3+} in both FHYD2 and FHYD6 samples as proposed by the model of Michel and co-workers. However satisfactory better fits were obtained with the addition of Fe^{2+} species which is usually attributed electron beam damage during data acquisition. Even though there was no obvious evidence of such electron beam damage in our EELS spectra, the requirement to add Fe^{2+} species in our fitting procedure suggest that there was some electron beam induced reduction of ferric iron to ferrous state.

Both ZFMS and IFMS spectra were also successfully fitted to comply with the model proposed by Michel and co-workers, providing for Fe^{3+} cations in two slightly distorted octahedral sites Fe1 and Fe3 as well as on tetrahedral sites Fe3. The relative abundances obtained are from ZFMS and IFMS measurements were also fairly consistent with the relative amounts predicted by Michel’s model. Further analyses, particularly IFMS measurements with variable magnetic field applied both longitudinally and transversally to the direction of γ-rays, are needed to test the validity of the fitting model used in this study.

Chapter 6

Thermal Transformation and Reduction Behaviour of Synthetic Ferrihydrite Nanoparticles

Abstract

The thermal transformation of three FHYDs samples in high vacuum environment were investigated using magnetic measurements. FHYD2 and FHYD6 samples transformation to α-Fe_2O_3 started at relatively high temperatures (~ 580 K), the transformation was further delayed (up to T ~ 660 K) in the presence of SiO_2. The reduction of FHYD2, FHYD2/SiO_2, and FHYD6 in hydrogen atmosphere was investigated by temperature programmed reduction (TPR) technique, *in situ* X-ray diffraction, and *ex situ* room temperature Mössbauer spectroscopy. The reduction mechanism of the three forms of FHYD proceeded in three different ways. FHYD2 followed the widely accepted two-stage reduction process similar to that of hematite. The reduction of SiO_2 modified FHYD2 preceded in three steps involving magnetite and wüstite as intermediates. FHYD6 first thermally transformed to hematite which then reduced to Fe following the common two step reduction process.

6.1 Introduction

It is widely accepted that the dry heating of FHYD involves a one step transformation process to hematite (Cornell *et al.*, 1989; Cornell and Schwertmann, 2003). However, some other findings e.g. (Eggleton and Fitzpatrick, 1988) have suggested a two-step process that involves maghemite (γ-Fe_2O_3) as intermediate in the transformation of FHYD to hematite in an inert atmosphere. These authors obtained γ-Fe_2O_3 after heating FHYD6 at 580 K and the sample heated at 760 K fully transformed to α-Fe_2O_3. Stanjek and Weidler, 1992, investigated the dry heating of FHYD2 and FHYD6 samples and observed that the two forms of FHYD samples behaved differently upon heating. Hematite formed readily upon heating a FHYD6 sample at 500 or 600 K (Stanjek and Weidler, 1992). Recently, Xu *et al.*, 2011, investigated the dry thermal heating of FHYD2 to hematite and showed that the sample can be heavily dehydrated without any structural changes. The thermal transformation to α-Fe_2O_3 was only registered at 688 K.

Despite extensive research, the mechanism of FHYD transformation to the well crystalline hematite phase is still poorly understood. Experimental results suggest that α-Fe_2O_3 nucleates and grows within FHYD aggregates (Cornell *et al.*, 1989). This solid-state transformation is thought to be facilitated by the similar sharing of hexagonal close-packed anion sublattice between FHYD and α-Fe_2O_3. Stanjek and Weidler, 1992, proposed a transformation mechanism of FHYD to hematite that involves continuous of removal of structural OH from FHYD leading to reduction of average coordination number of oxygens and OH around iron and thus creating charge imbalance. When the concentration of defects reaches a critical value, structural rearrangements (e.g. face sharing) to α-Fe_2O_3 is initiated (Cornell *et al.*, 1989; Stanjek and Weidler, 1992; Cornell and Schwertmann, 2003).

In this study the solid state transformation of three FHYD samples to α-Fe_2O_3 in dry state conditions is investigated (see section 6.3.1). The magnetic measurements as a function of temperature and phase changes were monitored using Mössbauer spectroscopy. A considerable amount of work was done on the reduction behavior of various ferrihydrite nanoparticles in hydrogen atmosphere. Reduction pathways were investigated using H_2-TPR, Mössbauer spectroscopy, and in situ XRD.

6.2 Experimental

Magnetic measurements

The thermal transformation in high vacuum ($\sim 10^{-4}$ Torr) was performed using the vibrating sample magnetometer (VSM) option of the Quantum Design (QD) Physical Property Measurement System (PPMS®) magnetometer equipped with an oven operating in the temperature range 300 – 1000 K and applied magnetic field. The temperature dependence of the magnetisation was measured in a constant applied magnetic field of 0.5 kOe while heating the samples from 300 to 1000 K at a constant rate of 5 K/min and during cooling from 1000 to 300 K at the same rate.

Mössbauer experiments were performed at room temperature on samples that have undergone thermal transformation to specific temperature in the PPMS oven. The constant acceleration spectrometer described in section 4.2.2 was used. The fitting procedures were also the same as described in section 4.2.2.

Temperature programmed reduction

H_2-TPR measurements were carried out with the Micromeritics Autochem 2950 HP chemisorptions analyzer. Kinetics analysis for this work was done using the isoconversional methods approach which requires performing several experiments. Therefore, four different heating rates (β = 5, 10, 15, 20 ˚C/min) from room temperature to 850 ˚C were performed for all TPR measurements in this work. Heating was performed under 10% H_2/Ar reducing mixture with a flow rate maintained at 50 cm^3 STP/min. FHYD powder samples (~50-70 mg) were filled in a stainless steel U-tube for TPR experiments. A cold trap mixture to remove formed water during reduction was prepared by mixing isopropyl alcohol and dry ice in a Dewar flask. Before TPR measurements samples were vacuum dried at 80 ˚C and in the TPR instrument a drying step at 120 ˚C for 10 min was also carried out.

In-situ XRD

FHYD thermally induced reduction process under H_2 was monitored in an in-situ XRD setup (Figure 6.1). A newly designed in-situ capillary cell developed at the University of Cape Town with transmission geometry was used as a reaction chamber. The cell was mounted in a theta-theta configured Bruker Advance laboratory X-ray diffractometer equipped with a cobalt source (λ=0.178897 nm). Phase changes were monitored by a position sensitive detector (VÅNTEC-2000, Bruker AXS). In-situ measurements were taken over the scan range 30-103 °, step size of 0.0287907 °, and scan speed of 0.68sec/scan.

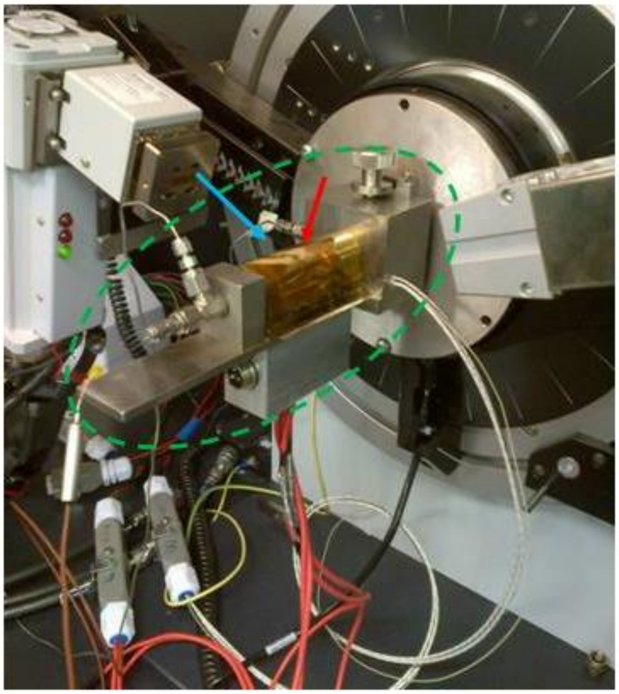

Figure 6.1: Capillary Cell (enclosed in green) mounted in a θ-θ configured Bruker diffractometer.

FHYD powders (~40 mg) were loaded in a borosilicate capillary with a 1 mm outer diameter and 0.02 mm wall thickness supplied by Capillary Tube Suppliers Ltd (UK). The reaction chamber was heated by two infrared heaters (Elstein, Germany) in series and the temperature was monitored via an internally mounted thermocouple. To minimize temperature gradients, the sample environment was enclosed with a specially designed aluminium shield with Kapton film window. Measurements were taken using a step-scan scanning mode from room temperature up to 450 °C at a step size of 50 °C and a ramp rate of 5 °C/min. All measurements were performed in pure H_2 at an average flow rate of ~1.6 ml/min.

Quantitative phase analysis of unknown phases after reduction was done using TOPAS 4.2, a Bruker software for profile and structure refinement based on Rietveld refinement. Good fits between experimental and calculated patterns were obtained using known structures of Hematite (α-Fe_2O_3), cubic unit cell of Magnetite (Fe_3O_4), and metallic body cantered cubic iron (α-Fe).

Mössbauer spectroscopy

Reduction experiments were carried out using a 316 stainless steel reactor coupled to a Mössbauer spectrometer and to a gas handling system. The reactor is designed to operate at high gaseous pressures of up to 15 bar and temperatures of up to 693 K. The main body of the reactor consists of an outer stainless steel chamber that is cooled with water during catalytic reactions. The temperature is regulated via a thermocouple in direct contact with the sample. The reactor is equipped with boron nitride (BN) windows transparent to γ-rays (i.e. BN has a low mass absorption coefficient, μ (0.87 and 16 cm^2/g) at 14.4 keV) mounted to the top and the bottom flanges.

All reduction reactions were conducted at 5 bar and at temperatures in the range 473 - 623 °C. Approximately 157 mg of the solid powder was loaded into the reactor. The reactor was then sealed and purged with argon (50 ml/min) for 10 minutes. The sample was then pressurised using argon gas to 5 bar and the temperature was increased steadily until the desired temperature was reached (after 2 hours). Hydrogen gas was then introduced into the system and the argon flow readjusted to get about 12% H_2/Ar mixture. A total flow of about 25 ml/min was maintained by means of a backflow regulator that enabled a constant set pressure for the duration of the experimentation of 16 h. After 16 h, the H_2 flow was terminated and the sample was allowed to cool back to room temperature within an hour. The reactor was then depressurised and Mössbauer spectra recorded at room temperature.

Mössbauer spectroscopy (MS) measurements were performed at room temperature (RT) using conventional acceleration constant spectrometers designed to operate in the absorption mode and equipped with 57Co/Rh sources. The MS spectra were analyzed by means of a least squares program “Normos” that models them as a combination of quadruple doublets and sextets based on a Lorentzian line-shape profile. The individual absorption features were then identified on the basis of their hyperfine parameters, i.e. the isomer shift (δ), quadrupole splitting (ΔE_Q) and magnetic hyperfine field (B_{hf}) values. The relative content of each phase was determined from the area (A) of the absorption peaks. Metallic iron (α-Fe) is used to calibrate the velocity scale of the MS spectra, i.e. the isomer shift values of all the species are reported relative to it.

6.3 Results and discussion

6.3.1 Thermal transformation of FHYD nanoparticles

Figure 6.2-Figure 6.4 show the temperature dependence of the magnetisation recorded on heating and cooling in the temperature range 300 – 1000 K and an applied magnetic field of 0.5 kOe under high vacuum (~10^{-4} Torr) for FHYD2, FHYD2/SiO_2 and FHYD6, respectively. The inserts in these Figures show the room temperature MS spectra collected after heating the samples to specific temperatures to monitor the phase transformations that might have occurred during heating. The corresponding MS parameters are given in Table 6.1.

It is recalled that at the start of the magnetisation measurements (T = 300 K) the nanoparticles in all three samples are in a SPM state with average crystallite diameters $D_{av} \approx 4.0$ nm for FHYD2, $D_{av} \approx 3.5$ nm for FHYD2/SiO_2 and $D_{av} \approx 6.0$ nm for FHYD6 (see TEM in Chapter 4). For FHYD2 (Figure 6.2), on heating at $300 \leq T \leq 1000$ K, the magnetization (M) first remains almost constant with increasing temperature up to approximately 580 K, thereafter it increases until reaching a broad maximum at T ~ 760 K. The increase occurs in two steps (see double sided arrows in Figure 6.2): the first and steeper increase occurs at T ~ 580 – 630 K, the second increase occurs at T ~ 630 – 780 K. Thereafter M decreases sharply with further increasing T up to approximately 850 K, after which it remains constant until the highest temperature of the measurements, 1000 K.

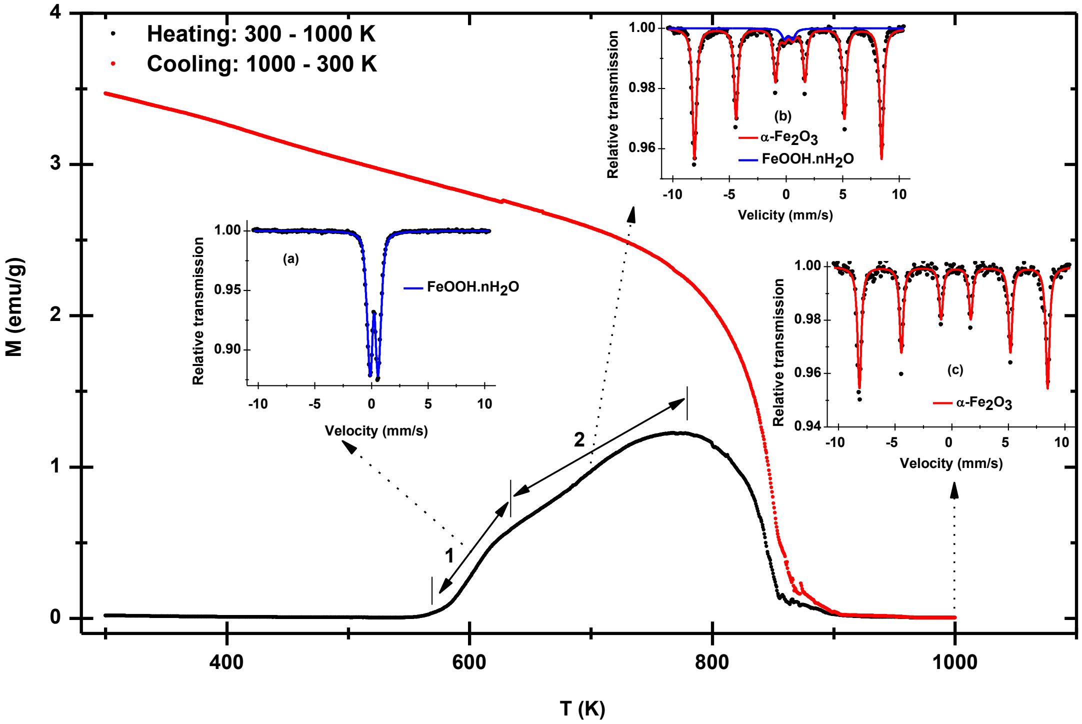

Figure 6.2: Temperature dependence of the magnetization of FHYD2 on heating and cooling in the temperature range 300 K ≤ T ≤ 1000 K under a uniform magnetic field H = 0.5 kOe and high vacuum (10^{-4} Torr). The inserts show the Mössbauer spectra of the same sample heated up to (a) 630 K, (b) 700 K and (c) 1000 K recorded at room temperature. The steps of the magnetization increase on heating are delimited by the double sided arrows.

For FHYD6 (Figure 6.3), M first decreases slightly with increasing T up to approximately 580 K as expected for SPM nanoparticles at temperatures above T_B. This is so because above T_B the thermal energy (k_BT) which causes the directions of the magnetic moments to fluctuate exceeds the magnetic ordering energy thus resulting in a gradual decrease of M. Above 580 K M increases with increasing T in two distinct steps: the first increase at T ~ 580 – 650 K is followed by a plateau at T ~ 650 – 710 K, the second and sharper increase occurs as from T ~ 710 K up to a peak at T ~ 850 K. Thereafter M decreases sharply until T ~ 920 K followed by a steady increase until T = 1000 K.

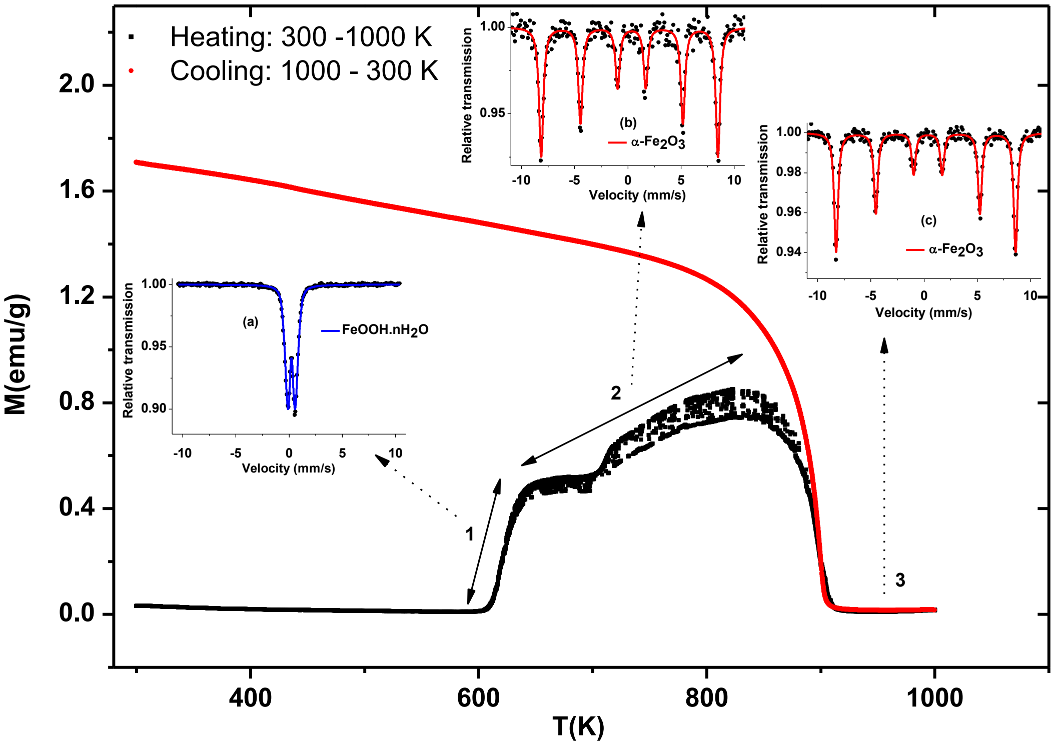

Figure 6.3: Temperature dependence of the magnetization of FHYD6 on heating and cooling in the temperature range 300 K ≤ T ≤ 1000 K under a uniform magnetic field H = 0.5 kOe and high vacuum (p ≈ 10^{-4} Torr). The inserts show the Mössbauer spectra of the same sample heated up to (a) 630 K, (b) 700 K and (c) 1000 K recorded at room temperature. The steps of the magnetization increase on heating are delimited by double sided arrows.

For FHYD2/SiO_2 (Figure 6.4), M also decreases first with increasing T but this trend extends up to T ~ 660 K, higher than T ~ 580 K for FHYD2 and FHYD6. Thereafter it increases sharply with increasing T up to T ~ 740 K and levels up at T ~ 740 – 880 K. Unlike the two-step increases observed for FHYD2 and FHYD6, M for FHYD2/SiO_2 increases in a single step at T ~ 660 – 740 K. At T ~ 900 K M decreases sharply up to T ~ 950 K, then it remains constant until T = 1000 K.

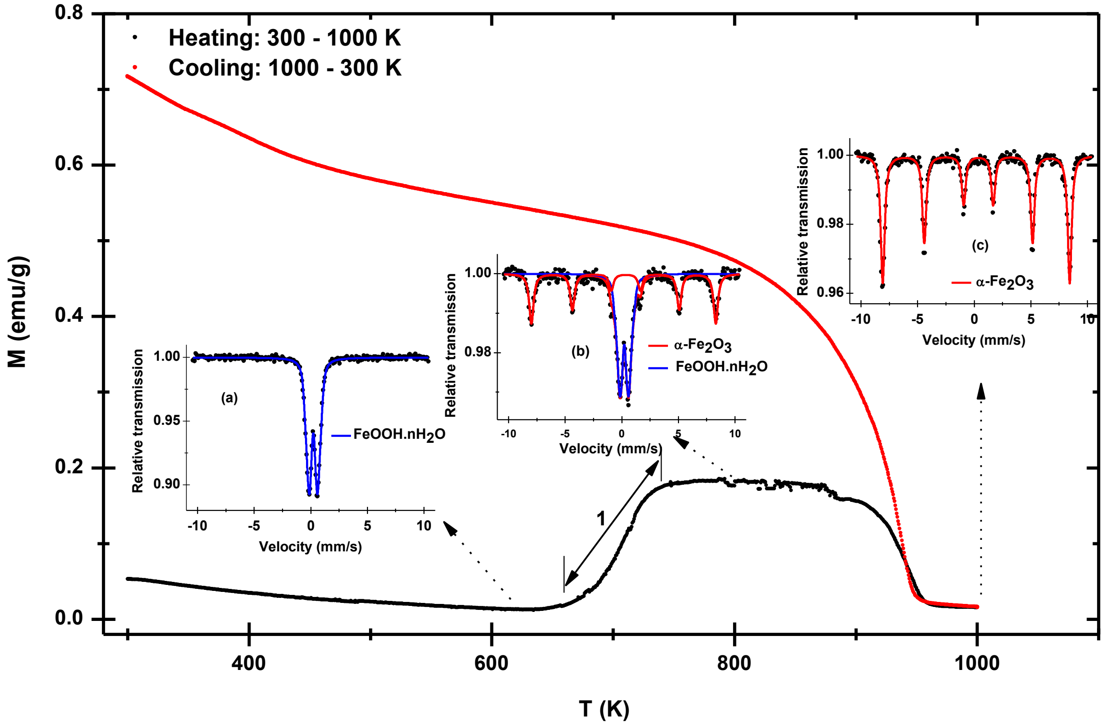

Figure 6.4: Temperature dependence of the magnetization of FHYD2/SiO_2 on heating and cooling in the temperature range 300 K ≤ T ≤ 1000 K under a uniform magnetic field H = 0.5 kOe and high vacuum ($p \approx 10^{-4}$ Torr). The inserts show the Mössbauer spectra of the same sample heated up to (a) 630 K, (b) 800 K and (c) 1000 K recorded at room temperature. The step of the magnetization increase on heating is delimited by the double sided arrow.

It is well known that FHYD is metastable and under favourable conditions it can transform to hematite (α-Fe_2O_3) or goethite (α-FeOOH) (Jambor and Dutrizac, 1998; Cornell and Schwertmann, 2003). The changes in the magnetization at T ≥ 580 K are taken as indications of phase transformations and magnetic transitions. For FHYD2 and FHYD6 such a phase transformation is initiated at T ~ 580 K, for FHYD2/SiO_2 it is initiated at T ~ 660 K. That is, the phase transformation occurs at a relatively high temperature for FHYD2/SiO_2 as compared to FHYD2 and FHYD6 probably due to the presence of SiO_2, i.e. SiO_2 tends to inhibit the transformation as previously reported (Karim, 1984; Glasauer *et al.*, 2000; Campbell *et al.*, 2002).

The sharp decreases in the magnetization at T ~ 800 – 850 K for FHYD2, T ~ 850 – 900 K for FHYD6 and T ~ 900- 950 K for FHYD2/SiO$_2$ are due to magnetic transitions of α-Fe$_2$O$_3$ from a weakly ferromagnetic (WFM) state to a paramagnetic (PM) state on heating. The M vs. T curves in (Figs. 6.2-6.4) yield a Curie temperature $T_C \approx 880$ K for FHYD2, $T_C \approx 950$ K for FHYD2/SiO$_2$ and $T_C \approx 920$ K for FHYD6. These values are all consistent with $T_C \approx 850 – 950$ K reported for α-Fe$_2$O$_3$ (Lin, 1959; Bødker *et al.*, 2000; Cornell and Schwertmann, 2003).

On cooling in an applied magnetic field H = 0.5 kOe, the magnetization for all three samples first remains constant up to their respective T_C, it then increases sharply with decreasing temperature until T ~ 800 K as α-Fe$_2$O$_3$ undergoes a magnetic phase transition from PM to WFM state. Thereafter M increases steadily until the lowest temperature of the measurements, 300 K. At temperatures below T ~ 800 K, M on cooling remains higher than M values on heating as the thermal energy (forcing a random distribution of the magnetic moments) decreases continuously while the magnetic ordering energy (associated with the magnetic forces and causing an alignment of magnetic moments on the applied magnetic field) remains constant. The presence of relatively larger crystallites on cooling than on heating also contributes to relatively higher values of M observed on cooling

The MS spectra of FHYD2, FHYD6 and FHYD2/SiO$_2$ heated up to 630 K during magnetization measurements (see insets (a) in Figure 6.2-Figure 6.4) were fitted with a quadrupole doublet of parameters $\delta \approx 0.35$ mm/s and $\Delta E_Q \approx 0.69$ mm/s (Table 6.1) characteristic of FHYD (Murad and Schwertmann, 1980; Murad, 1996; Cornell and Schwertmann, 2003). That is, the starting material still subsists in a SPM state at T ~ 630 K for all three samples. The occurrence of quadrupole doublets on the MS spectra of all three samples at 630 K indicate that the nanoparticles are still in a SPM state at this temperature.

For FHYD2 and FHYD6 the MS spectra recorded at room temperature after heating the samples up to 700 K (see insets (b) in Figure 6.2 and Figure 6.3, respectively) during magnetization measurements consist of six-lines (sextet) of parameters $\delta \approx 0.37$ mm/s, $\Delta E_Q \approx -0.20$ mm/s, $B_{hf} \approx 51.5$ T (Table 6.1) typical of α-Fe$_2$O$_3$ (Cornell and Schwertmann, 2003), i.e. FHYD is almost fully transformed to α-Fe$_2$O$_3$ at 700 K (traces (~ 5%) of FHYD is still present on the MS spectrum of FHYD2 though). In contrast, the MS spectrum of FHYD2/SiO$_2$ heated during magnetization measurements up to 800 K (see inset (b) in Figure 6.4) was fitted with a sextet typical of α-Fe_2O_3 superimposed to a quadrupole doublet ascribed to $FeOOH.nH_2O$ with relative abundances of approximately 43 and 57%, respectively. The sextets observed at 700 K for FHYD2 and FHYD6 and at 800 K for FHYD2/SiO_2 correspond to α-Fe_2O_3 with average crystallites size above ~15 nm (threshold diameter at which α-Fe_2O_3 becomes SPM (Kündig *et al.*, 1966)) while the doublets are the contributions from FHYD SPM crystallites, these SPM crystallites are predominant for FHYD2/SiO_2 at 800 K. This implies that the presence of SiO_2 hindered the thermal transformation to hematite to a certain extent.

Table 6.1 Room temperature MS parameters of FHYD2, FHYD2/SiO_2 and FHYD6 heated under vacuum during measurements of the temperature dependence of the magnetization to the temperatures of 630, 700, 800 and 100 K.

T (K)	Sample	$^{\#}\delta$ (mm/s)	$^{\#}\Delta E_Q$ (mm/s)	$^{\Phi}$ Bhf (T)	▪A (%)	Phase
630	FHYD2	0.33	0.62	-	100	SPM FHYD
	FHYD6	0.35	0.70	-	100	SPM FHYD
	FHYD2/SiO_2	0.36	0.69	-	100	SPM FHYD
700	FHYD2	0.34	0.68	-	5	SPM FHYD
		0.39	-0.20	51.3	95	α-Fe_2O_3
	FHYD6	0.38	-0.19	51.6	100	α-Fe_2O_3
800	FHYD2/SiO_2	0.34	0.61	-	43	SPM FHYD
		0.37	-0.22	50.51	75	α-Fe_2O_3
1000	FHYD2	0.40	-0.24	51.8	100	α-Fe_2O_3
	FHYD6	0.37	-0.21	51.6	100	α-Fe_2O_3
	FHYD2/SiO_2	0.39	-0.20	51.2	100	α-Fe_2O_3

Uncertainty: $^{\#}$ ± 0.02 mms^{-1}, $^{\Phi}$ ± 0.5 T, ▪ ± 2%

The room temperature MS spectra of all three samples recorded after heating the samples to 1000 K during magnetization measurements are all sextets with parameters characteristic of α-Fe_2O_3. This is expected as α-Fe_2O_3 is in a WFM state at all temperatures between $T_C \approx 850 – 950$ K and the Morin (structural) transition at $T_M \approx 270$ K (Lin, 1959; Bødker *et al.*, 2000; Cornell and Schwertmann, 2003).

It appears as if the phase transformation from FHYD to α-Fe_2O_3 is preceded by the loss of lattice water from the structure of FHYD and that it is also accompanied by an increase in the average crystallite size (sintering). In this scenario the first step of the increase in the magnetisation initiated at T ~ 580 K for FHYD2 and FHYD6 and at T ~ 660 K for FHYD2/SiO_2 corresponds probably to the loss of lattice water followed by sintering and structural changes which lead to the formation of α-Fe_2O_3. This process appears to have been completed just before T ~ 700 K for FHYD2 and FHYD6 while for FHYD2/SiO_2 it is still not completed at T = 800 K.

The second step of the magnetization increase observed for FHYD2 and FHYD6 on heating at T ~ 630 – 780 K and T ~ 710 – 850 K, respectively, probably correspond to further sintering. Such an increase in the magnetization is not observed for FHYD2/SiO_2. This could indicate that, in addition to inhibiting the transformation of FHYD to α-Fe_2O_3, SiO_2 also plays a role of preventing further sintering beyond a certain threshold crystallite diameter as was previously suggested (Hansen, 2006).

6.3.2 Reduction behavior of FHYD nanoparticles

6.3.2.1 Investigation of the reduction mechanisms through TPR

Heating rate influence on FHYD2 profiles in the range 5-20 ˚C/min is shown in Figure 6.5. Reduction peaks show a shift to higher temperatures as heating rate increases. Our TPR profiles look rather different from the FHYD TPR profiles obtained using the same method (Jozwiak *et al.*, 2007). The authors have used different experimental parameters from ours, 5%H_2-95% Ar gas mixture and 10%H_2-90% Ar was used in this work, a slow heating rate (1.07 ˚C/min compared to 5-20 ˚C/min), and a small sample size of 15 mg compared to 50 mg used in our experiments. It has been shown that TPR profiles strongly depend on a number experimental parameters (Wimmers *et al.*, 1986; Zieliński *et al.*, 2010). The variation of the H_2-TPR profile of α-Fe_2O_3 as a function of experimental parameters was investigated (Zieliński *et al.*, 2010). The authors demonstrated the effect of sample size, H_2 concentration of reducing gas mixture, and reaction rate on the TPR profiles of α-Fe_2O_3. Their study showed the strong effect of experimental parameters on the TPR of α-Fe_2O_3 and thus contributes to the diverse opinions on the reduction pathway reported on literature.

The TPR profiles in Figure 6.5 shows sharp reduction peak about 300 ˚C (depending on the heating rate *β*) with a shoulder (shown by an arrow) followed by a second broad reduction peak. The broadening of the second peak can be ascribed to a slow reduction process. These peaks based on quantitative analysis of H_2 consumed under the TPR peak were assigned to the two step reduction of FHYD2 to α-Fe via magnetite intermediate, $5Fe_2O_3{\cdot}9H_2O$/ $FeOOH{\cdot}0.4H_2O \rightarrow Fe_3O_4 \rightarrow$ α-Fe.

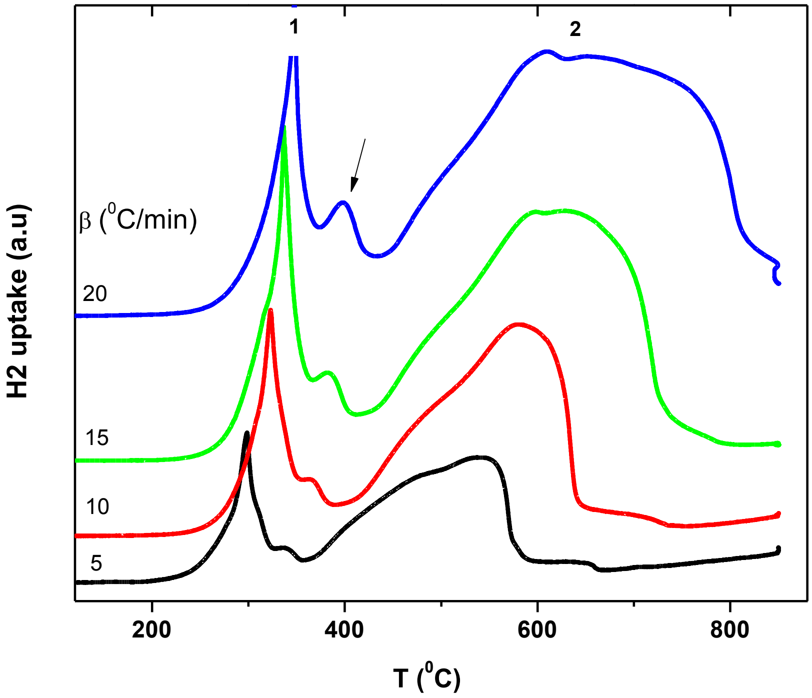

Figure 6.5: Heating rate influence on TPR profiles for FHYD2.

Quantitative analysis of hydrogen consumed under each reduction peak was performed in order to assign each reduction peak to certain reduction events. Table 6.2 lists experimental determined $n(H_2)/n(Fe)$ ratios for the first and second reduction peaks. The H_2 consumption for the first peak increased to a theoretical $n(H_2)/n(Fe)$ ratio (~ 0.17) of the reduction of $FeOOH{\cdot}0.4H_2O$ to Fe_3O_4. The second broad reduction peak has been assigned to the reduction of magnetite to α-Fe.

Table 6.2: Quantitative H_2 consumption for each TPR event for FHYD2.

β[‡‡‡]	Peak	n(H2)/n(Fe)	Assignment
5	1st	0.16	$FeOOH \cdot 0.4H_2O \rightarrow Fe_3O_4$
	2nd	1.33	$Fe_3O_4 \rightarrow Fe$
10	1st	0.19	$FeOOH \cdot 0.4H_2O \rightarrow Fe_3O_4$
	2nd	1.12	$Fe_3O_4 \rightarrow Fe$
15	1st	0.18	$FeOOH \cdot 0.4H_2O \rightarrow Fe_3O_4$
	2nd	1.04	$Fe_3O_4 \rightarrow Fe$
20	1st	0.19	$FeOOH \cdot 0.4H_2O \rightarrow Fe_3O_4$
	2nd	1.16	$Fe_3O_4 \rightarrow Fe$

In order to obtain information about kinetic parameters from TPR profiles kinetic analysis was performed by applying isoconversional methods of Kissinger, Ozawa, and Friedman (d'Arlas *et al.*, 2007). The activation energies for each reduction event can be simply obtained from the slope –E/R of the straight lines of the Kissinger plots (Figure 6.6). For the reduction of FHYD2 to Fe_3O_4 the activation energy of 74 kJ was obtained. This value is close to the reported activation energy of the reduction of α-Fe_2O_3 to Fe_3O_4 (Jozwiak *et al.*, 2007) and this might suggest the same reduction mechanism for both systems. The reduction of magnetite to α-Fe (peak 2) yielded a calculated value of 58 kJ which is in agreement with the 55 kJ obtained by Jozwiak *et al.*, 2007.

[‡‡‡] Heating rate dT/dt

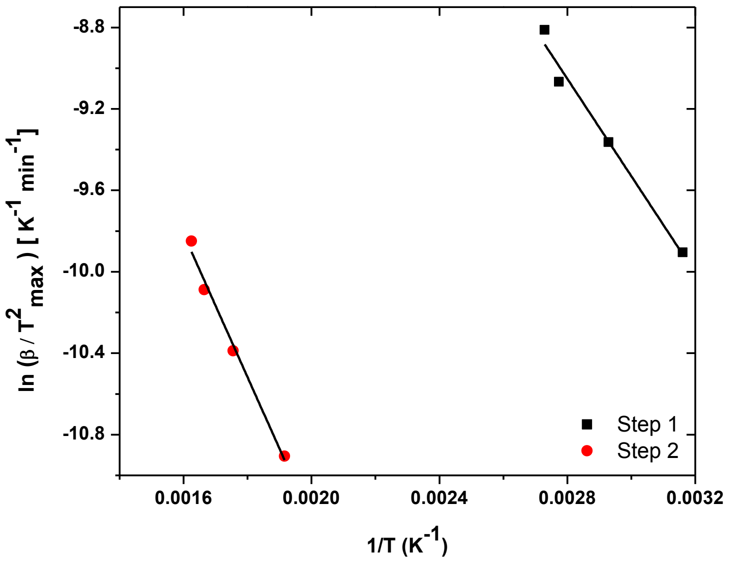

Figure 6.6: Kissinger method Arrhenius plots for the reduction of FHYD2.

The Ozawa integral method which is based on Doyle's approximation has been successful applied in kinetic analysis of thermally activated reactions (d'Arlas *et al.*, 2007). The activation energies using this method can be determined from a plot of ln β against 1/T (T being the temperature at constant conversion). Presented in Figure 6.7 are the Ozawa plots where activation energies can be calculated from their slopes –1.052E/R. The demarcation in the low 1/T and high 1/T side represents separate contributions from the first and second reduction peaks. The calculated average activation energies obtained from α = 0.1-0.2 conversions was 78 kJ and averaging the activation energies from high conversions (α = 0.3-0.7) yielded an activation energy value of 58 kJ. These values are consistent with the results obtained using the Kissinger method.

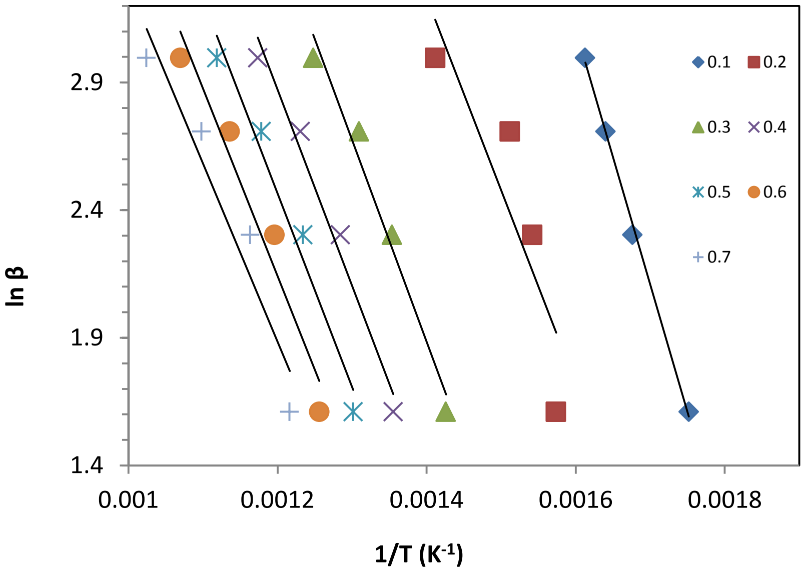

Figure 6.7: Ozawa plots for the reduction of FHYD2 in H_2.

H_2-TPR measurements were taken for silica (SiO_2) modified FHYD2 to investigate the role of SiO_2 promoter on the reducibility and reaction kinetics of FHYD2. Presented in Figure 6.8 is the H_2-TPR profiles of SiO_2 supported FHYD2 showing the influence of the heating rate on the profiles and peak positions. It can be clearly seen that in all TPR runs the reduction peaks show the normal shift to higher temperatures as the heating rate increases. A rather different and complex situation from that of pure FHYD2 was observed with the SiO_2 supported FHYD2. However, high heating rates still causes shifts in peak positions to higher temperatures. It is known that the presence of mixtures of iron oxides, promoters, and development of oxide-promoter interaction usually results in complex TPR profiles (Messi *et al.*, 2008).

H_2-TPR profiles of SiO_2 co-precipitated FHYD2 show three fairly well separated reduction peaks denoted by 1, 2, and 3 (see Figure 6.8). Similarly to the pure FHYD2, the first reduction peak had a shoulder (shown by an arrow in Figure 6.8). The first reduction event at about 300 ˚C was assigned to the reduction of FHYD2/SiO2 to Fe_3O_4 followed by the reduction of magnetite to metastable wüstite at reduction temperatures below 570 ˚C. It is known that metastable wüstite can be stabilized by oxidic support surface (MgO, SiO_2, Al_2O_3) (Jozwiak *et al.*, 2007). In this case SiO_2 was used as support for FHYD2 nanoparticles. The third reduction peak indicates the complete reduction of the stabilized nonstoichiometric wüstite phase to metallic iron. This three step reduction mechanism (FHYD2 → Fe_3O_4 → FeO →Fe) of silica co-precipitated FHYD2 to metallic iron was confirmed by quantitative analysis of H_2 consumption for each reduction peak (see Table 6.3).

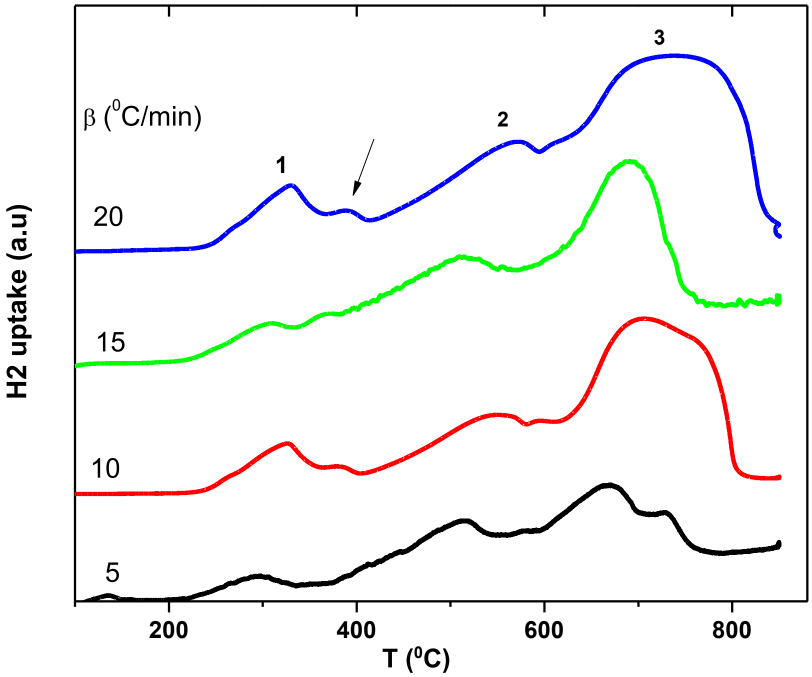

Figure 6.8: FHYD2/SiO_2 TPR profiles recorded at various heating rates.

Quantification of H_2 consumption of SiO_2 co-precipitated FHYD2 TPR profiles are summarised in Table 6.3. The calculated $n(H_2)/n(Fe)$ ratio of reduction peak 1 corresponded to the $n(H_2)/n(Fe)$ theoretical ratio (0.17) of the reduction of $5Fe_2O_3•9H_2O$ ($FeOOH·0.4H_2O$) to Fe_3O_4. The $n(H_2)/n(Fe)$ ratio of the second reduction peak increased to a theoretical value of the reduction of Fe_3O_4 to FeO. The quantification of H_2 consumption under the third reduction peak confirms the reduction of nonstoichiometric wüstite phase to metallic iron.

Table 6.3: Summary of H_2 consumed per mole of metal Fe for FHYD2/SiO_2.

β	Peak	n(H2)/n(Fe)	Assignment
5	1st	0.16	$FeOOH \cdot 0.4H_2O \rightarrow Fe_3O_4$
	2nd	0.38	$Fe_3O_4 \rightarrow FeO$
	3rd	0.92	$FeO \rightarrow Fe$
10	1st	0.14	$FeOOH \cdot 0.4H_2O \rightarrow Fe_3O_4$
	2nd	0.36	$Fe_3O_4 \rightarrow FeO$
	3rd	0.91	$FeO \rightarrow Fe$
15	1st	0.16	$FeOOH \cdot 0.4H_2O \rightarrow Fe_3O_4$
	2nd	0.35	$Fe_3O_4 \rightarrow FeO$
	3rd	0.99	$FeO \rightarrow Fe$
20	1st	0.17	$FeOOH \cdot 0.4H_2O \rightarrow Fe_3O_4$
	2nd	0.32	$Fe_3O_4 \rightarrow FeO$
	3rd	0.89	$FeO \rightarrow Fe$

The H_2-TPR data for SiO_2 co-precipitated FHYD2 data (Figure 6.8) were kinetically interpreted to determine the activation energies for each reduction step. Using the Kissinger method yielded straight Arrhenius plots (Figure 6.9) from which activation energies were calculated from the slope –E/R. For the first reduction peak activation energy of 73 kJ was obtained and this value was close to the activation energy of FHYD2 to Fe_3O_4. The reduction step of Fe_3O_4 to FeO (second reduction step) required a value of 53 kJ. An activation energy value of 100 kJ was calculated for the third peak which was assigned to the reduction of FeO to α-Fe. This value agrees well with the value reported in literature (Jozwiak *et al.*, 2007) for the same reduction step of wüstite to iron.

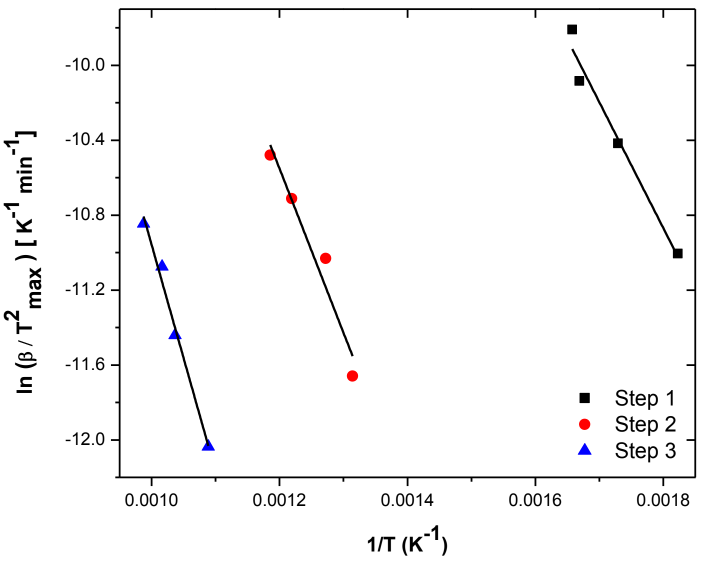

Figure 6.9: Arrhenius plots from the reduction of SiO_2 FHYD2.

Ozawa plots resulted from the reduction of FHYD2/SiO_2 data are shown in Figure 6.10. The plots show three distinct regions of straight lines that indicate the three step reduction process as it can be clearly seen in Figure 6.10. The left side of 1/T has denser region of straight lines followed by a less dense region the middle and only one straight line on the right side of 1/T. The separate peak obtained from a fixed conversion (α = 0.1) was assigned to the reduction of FHYD2/SiO_2 to Fe_3O_4 and it yielded activation energy of 76 kJ. The average activation energy of 55 kJ obtained from the middle region (α = 0.2-0.3) was typical of the conversion of Fe_3O_4 to FeO (Jozwiak *et al.*, 2007). The average activation energies obtained using the method developed by Ozawa are comparable to the energies obtained by the Kissinger method.

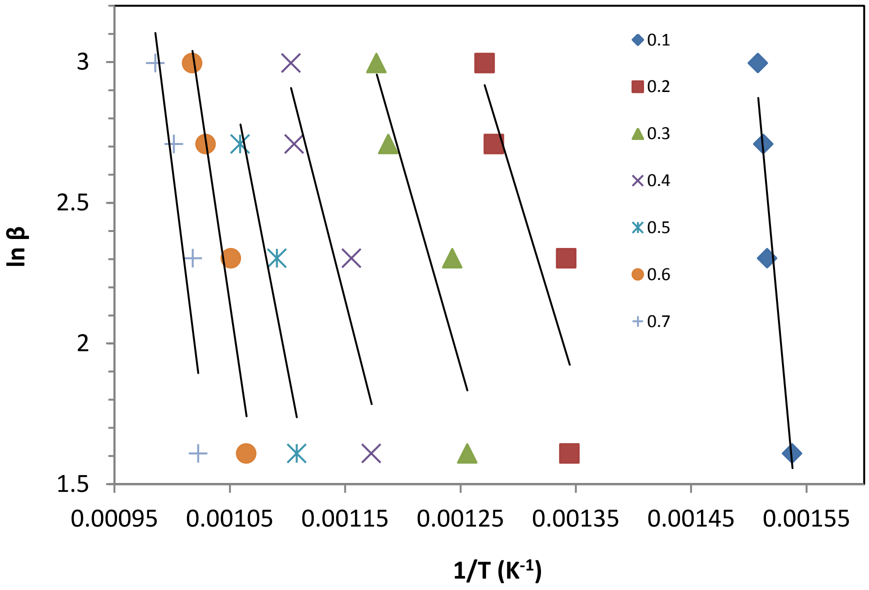

Figure 6.10: Ozawa plots for the reduction of silica FHYD2 in H_2.

The addition of silica is known to have some effects on the reduction of iron oxides (Arena *et al.*, 2005; Suo *et al.*, 2012,Dlamini *et al.*, 2002). It has been reported the addition of SiO_2 inhibits the reduction of iron oxides. This happens by the strong interaction of SiO_2 with neighbouring iron species that results in the formation of hardly reducible Fe-O-Si complexes (Arena *et al.*, 2005; Suo *et al.*, 2012). The addition of SiO_2 also influences the electronic structure of Fe atoms as revealed by XPS results (Suo *et al.*, 2012). The influence of SiO_2 on Fe atoms leads to electron-deficient state of all Fe species and as a result more core-level electron density of Fe nuclei takes part in Fe-O covalent bonds. Strengthen Fe-O bonds are formed and they become very difficult to cleave during reduction. Although the TPR method cannot be used to prove the existence of silicates phases, we have notice that complete reduction of the SiO_2 FHYD2 sample shifted to high temperatures (~ 650 – 800 °C) compared to the pure FHYD2 (550 – 700 °C) with these temperature range depending on the heating rate. This was a strong indication of the influence of SiO_2 on the reaction mechanism of FHYD2.

Another effect of the addition of SiO_2 on iron oxides reduction is the stabilization of unstable FeO phase (Wimmers *et al.*, 1986; Jozwiak *et al.*, 2007). This claim was supported by our TPR results which show the presence of the wüstite phase in our SiO_2 promoted FHYD2. The reduction pathway changed from two-step to three-step in the SiO_2 promoted FHYD sample.

The reducibility and reaction kinetics of FHYD6 under H_2 was studied and depicted in Figure 6.11 is the effect of heating rate on the H_2-TPR profiles of FHYD6 recorded in 10% H_2-90% Ar gas mixture. Reduction peaks maxima shift to higher temperatures as the heating rate is increased from 5 ˚C/min to 20 ˚C/min (see Figure 6.11). Before the first reduction peak at about 300 ˚C there is a noticeable feature at about 250 ˚C. That feature was predicted to probably arise from thermal transformation of FHYD6 to α-Fe_2O_3 due to removal of the OH groups or structural H_2O in the FHYD structure.

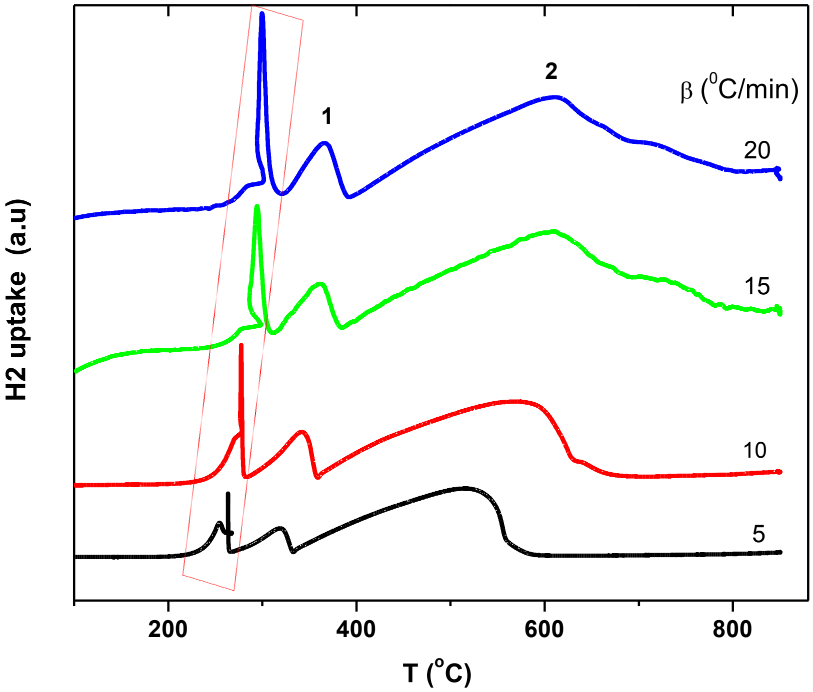

Figure 6.11: TPR profiles of FHYD6 at indicated various heating rates.

The typical TPR profiles of FHYD6 consist of three reaction events (one thermal event and two reduction peaks see Figure 6.11). All profiles show a spike in the temperature range ~ 220 – 250 °C (marked with dotted rectangle) which can be assigned to the thermal transformation of FHYD6 to hematite (α-Fe_2O_3). The existence of the α-Fe_2O_3 phase was confirmed by our Mössbauer spectroscopy and *in situ* XRD. A TPR run was interrupted in the temperatures just before 300 °C and the sample was passivated by plunging it in dry ice and room temperature Mössbauer spectra was recorded. The spectra showed a well developed magnetically splitted sextet which was fitted well with a sextet with magnetic hyperfine parameters corresponding to α-Fe_2O_3. The thermal transformation of FHYD6 first to α-Fe_2O_3 before reduction to Fe_3O_4 and α-Fe was also observed by in-situ XRD and in-situ Mössbauer spectroscopy.

To further support our argument that the first thermal event on the FHYD6 TPR profiles is a result of thermal transformation not reduction we have examined the temperature vs. time for the entire TPR run (Figure 6.12). It was observed that at exactly the temperature where the thermal event took place in the TPR, there was a change in the temperature in the system as clearly seen in Figure 6.12 (inset). This unexpected temperature change is a result of an exothermic reaction (according to (Eq.6.1)) associated with the formation of α-Fe_2O_3 following the removal of structural OH/H_2O groups and major structural rearrangement within FeOOH.nH_2O aggregates (Schwertmann and Murad, 1983; Cornell *et al.*, 1989; Stanjek and Weidler, 1992).

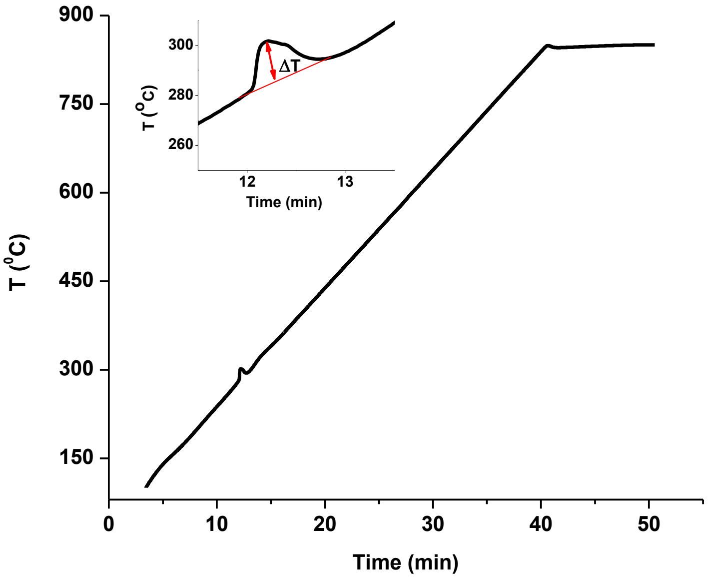

Figure 6.12: Temperature vs. time graph of the 20 °C/min TPR run of FHYD6.

A thermodynamics calculation suggests that the dehydration reaction of FHYD6 to α-Fe_2O_3 is spontaneous and releases a lot of heat. In a hydrogen atmosphere, both the structural OH and H_2O should be given off as water according to dehydration reaction of FHYD6. Under the influence of heat, the polymorphs of FeOOH and FHYD can be dehydrated to α-Fe_2O_3 (Cornell and Schwertmann, 2003).Using the widely accepted FHYD6 chemical formula, $5Fe_2O_3{\cdot}9H_2O$, which can also be written as $FeOOH{\cdot}nH_2O$ (n = 0.4) (Jambor and Dutrizac, 1998; Snow *et al.*, 2013), the dehydration reaction can be written similar to that of FeOOH (Cornell and Schwertmann, 2003) as,

$$2\mathrm{FeOOH}\cdot 0.4\mathrm{H_2O} \rightarrow \mathrm{Fe_2O_3} + 1.8\mathrm{H_2O} \tag{6.1}$$

This should be accompanied by a major structural rearrangement within $FeOOH.nH_2O$ aggregates (Schwertmann and Murad, 1983; Stanjek and Weidler, 1992) leading to the release of energy responsible for the DTA exotherms reported for ferrihydrite (Eggleton and Fitzpatrick, 1988; Xu *et al.*, 2011). Figure 6.12 also shows that during this transformation process a temperature change ΔT was recorded. The heat released when the 6lfh transforms to hematite is thought to contribute in the change of thermal conductivity of the H_2 gas. The change in the H_2 gas flow is recorded as a signal by thermal conductivity detector (TCD) in the TPR system. This signal is converted to H_2 consumed by the system even though it resulted from a process that did not involve any H_2 consumption.

After the thermal event explained above, our TPR profiles are similar to hematite profiles obtained by other workers (Manteanu *et al.*, 1997; Manteanu *et al.*, 1999; Lin *et al.*, 2003). The TPR profiles show two reduction peaks with H_2 consumption ratio of 1:8, a signature of hematite reduction to α-Fe via Fe_3O_4 intermediate. The total H_2 consumption (0.16 mol H_2/ mol Fe) of the first reduction peak at about above 300 °C (the exact position shift to higher temperature with increasing heating rate) corresponds to the theoretical H_2 consumption of reduction of α-Fe_2O_3 to Fe_3O_4.

Similarly to FHYD2 TPR profiles, the areas under each reduction peak for FHYD6 were integrated for quantitative determination of H_2 consumed for each reduction step and the results are presented in Table 6.4. The obtained n(H2)/n(Fe) ratio of the first reduction peak (peak 1) suggest the reduction path of α-Fe_2O_3 to Fe_3O_4 with a theoretical value of 0.17. The ratio of H_2 consumption for the second reduction process (peak 2) is assigned to the reduction of Fe_3O_4 to α-Fe phase.

Table 6.4: Ratio of moles of H_2 consumed per mole of Fe for FHYD6.

β	Peak	n(H2)/n(Fe)	Assignment
5	1st	0.14	$Fe_2O_3 \rightarrow Fe_3O_4$
	2nd	1.27	$Fe_3O_4 \rightarrow Fe$
10	1st	0.14	$Fe_2O_3 \rightarrow Fe_3O_4$
	2nd	1.02	$Fe_3O_4 \rightarrow Fe$
15	1st	0.15	$Fe_2O_3 \rightarrow Fe_3O_4$
	2nd	1.03	$Fe_3O_4 \rightarrow Fe$
20	1st	0.13	$Fe_2O_3 \rightarrow Fe_3O_4$
	2nd	1.00	$Fe_3O_4 \rightarrow Fe$

Arrhenius plots for FHYD6 TPR data in Figure 6.11 were obtained using the Kissinger method and are shown in Figure 6.13. The calculated activation energy for the reduction of hematite to magnetite (reduction step 1) was 77 kJ. For the second reduction peak (peak 2) which was assigned to the reduction of Fe_3O_4 to α-Fe activation energy of 60 kJ was obtained. The obtained activation energies are in good agreement with previous results (Jozwiak *et al.*, 2007)

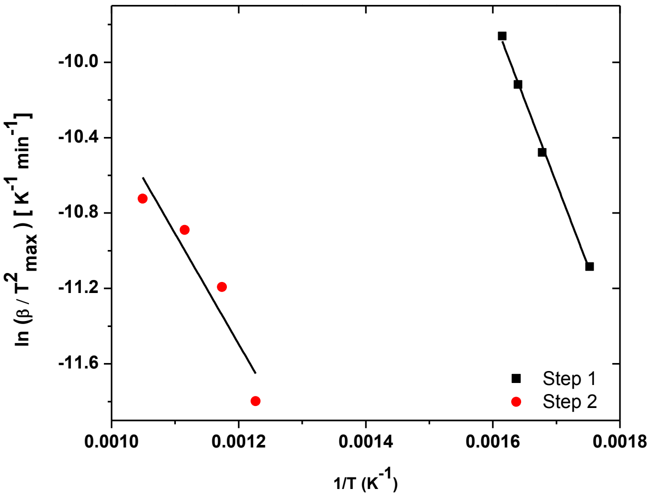

Figure 6.13: Kissinger plots from the reduction of FHYD6.

The Ozawa plots of FHYD6 at constant degree of conversion, α, up to 70 % are presented in Figure 6.14. The activation energies for the first and second reduction peaks in Figure 6.11 were obtained by averaging the activation energies of the clearly separated high and low dense regions of straight lines existing in the low 1/T and high 1/T of the plots (Figure 6.14) respectively. The values of the average activation energies obtained from these two different regions (α = 0.1-0.2 and 0.3-0.7) were comparable to the energies obtained by the Kissinger method which gives the average activation energy at T_{max}.

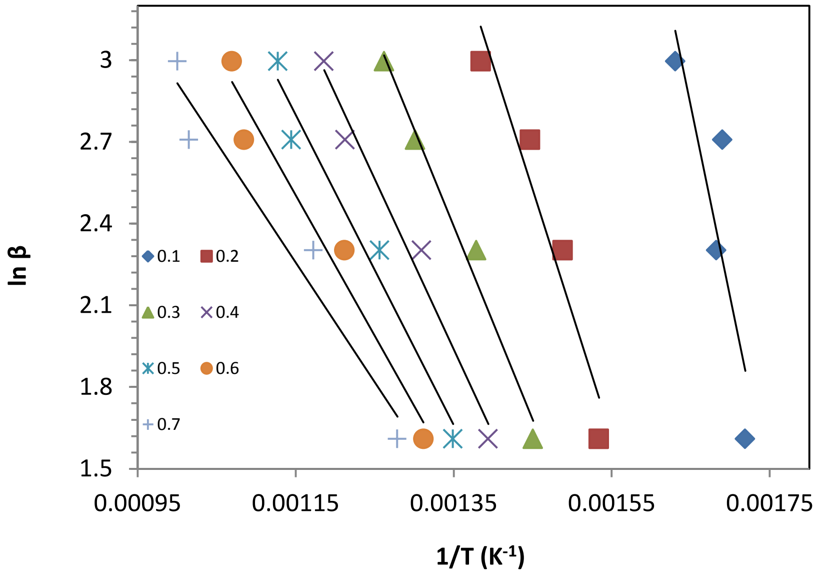

Figure 6.14: Ozawa plots for the reduction of FHYD6 in H_2.

6.3.2.2 Investigation of the reduction mechanisms through in-situ XRD

Figure 6.15 shows in-situ XRD patterns for pure FHYD2 from room temperature up to 450 °C at a step size of 50 °C. The unreduced FHYD2 shows two broad XRD peaks typically of 2-line FHYD. Up to temperatures about 200 °C, there were no structural changes observed in the pure FHYD2 as evidence form the two broad XRD peaks characteristic of nanocrystalline FHYD2 phase. The reduction of FHYD2 to Fe_3O_4 phase was observed at 250 °C, as shown by the formation of new diffraction peaks of a newly formed phase. These strong XRD reflections were identified as Fe_3O_4 phase according to PDF Card 00-019-0629. Additional reflections that matched with α-Fe (PDF Card 00-001-1262) started to emerge at 300 °C. Further heating up to 450 °C resulted in a complete disappearance of Fe_3O_4 phase and only metallic iron was present. The Fe_3O_4 and α-Fe phases were confirmed using phase identification capabilities of the EVA software. The XRD observations support our TPR findings that FHYD2 is reduced to α-Fe via Fe_3O_4 intermediate. Our findings are in good agreement with published results (Filip *et al.*, 2007; Schneeweiss *et al.*, 2008; Schneeweiss *et al.*, 2010; Schneeweiss *et al.*, 2011).

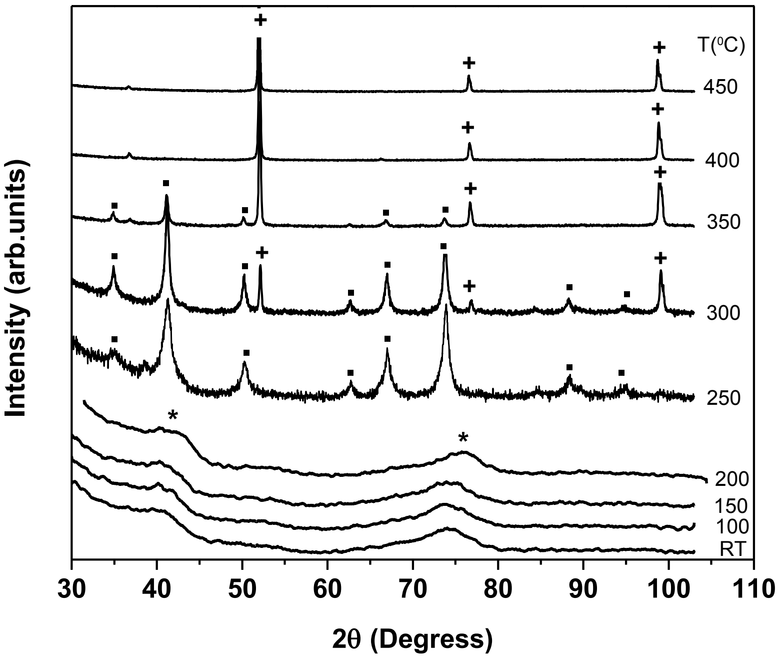

Figure 6.15: XRD patterns for FHYD2 sample reduced in H2 at temperatures up to 450 °C, where (*) FHYD2; (▪) Fe_3O_4; (+) α-Fe.

We have performed TG-DTA experiment to investigate the thermal behaviour of our FHYD2. TG-DTA measurements were carried out to get an idea of the temperature at which our FHYD2 sample thermally transforms to hematite due to dehydration. This gave us an idea whether it was possible for the sample to thermally transform to hematite before the actual reduction process. The TG-DTA curves for FHYD2 in Ar atmosphere are shown in Figure 6.16. Ideally, we would have performed this measurement in H_2 atmosphere to follow the dehydration and reduction processes simultaneously. However our H_2 system was inoperable during the thermal analysis experiments. A smooth weight loss totalling up to 24.2 % was observed on the sample in agreement with previous results (Eggleton and Fitzpatrick, 1988). The low temperature exothermic peak at 154 °C is normally attributed to the expulsion of loosely bound surface adsorbed water, while the endotherm at 425 °C indicates the conversion to α-Fe_2O_3 (Jambor and Dutrizac, 1998).

Thermal analysis curves for FHYD2 (Eggleton and Fitzpatrick, 1988) showed an unusually two-step conversion of FHYD2 to hematite via maghemite intermediate (see Chapter 2). This was experimentally observed by the appearance of two well separated exothermic peaks at 355 °C and 440 °C. The first exotherm was interpreted by the authors as a conversion of poorly crystallized maghemite to well crystallized one and the second exortherm was the conversion of maghemite to hematite. Our thermal analysis results indicate that the two-step dehydration of our FHYD2 sample is realized at ~ 425 °C in Ar atmosphere, which is much higher than the temperature (~250 °C) where reduction first occurred in the FHYD2 (Figure 6.15).

The experimental TG-DTA curve obtained in this study is very similar to the TG-DTA curves obtained by Xu *et al.*, 2011. They have observed that the weight loss below 300 °C was only due to expulsion of surface adsorbed water since their PDF data did not show any structural changes up to that temperature. Xu *et al.*, 2011, could not observed the maghemite intermediate phase (reported by Eggleton and Fitzpatrick, 1988) in the transformation of FHYD2 to hematite which took place at about 415 ±1 °C. If the dehydration process is not affected by the reaction atmosphere (Ar v/s H_2), one would expect a direct reduction of FHYD2 to magnetite at 250 °C since the thermal conversion to hematite occurs at a much higher temperature 425 °C.

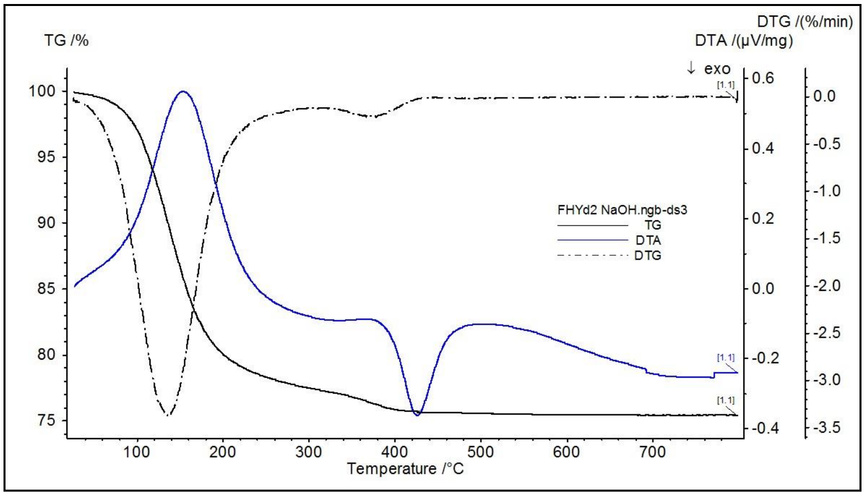

Figure 6.16: FHYD2 experimental TG-DTA curves.

Quantitative phase Rietveld refinements were performed using the TOPAS software, a successful Rietveld refinement was obtained for the 250 °C reduced sample using magnetite (Figure 6.17). The result indicates that the first step in the reduction of FHYD2 in H_2 atmosphere is the reduction to magnetite (FHYD2 → Fe_3O_4).

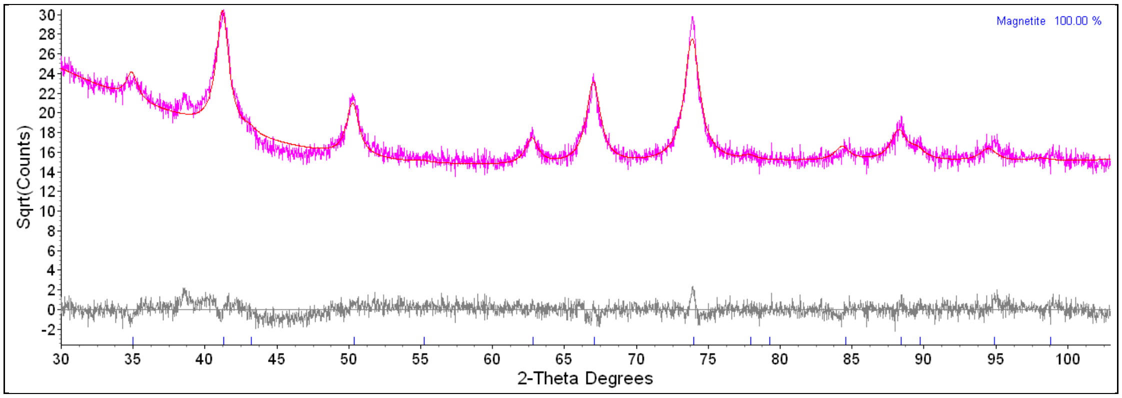

Figure 6.17: Experimental and calculated X-ray diffractograms of Fe_3O_4.

After the 300 °C, the magnetite was partially reduced to metallic iron (17.06 %) at 300 °C (see Figure 6.15) and a successful Rietveld refinement is shown in Figure 6.18.

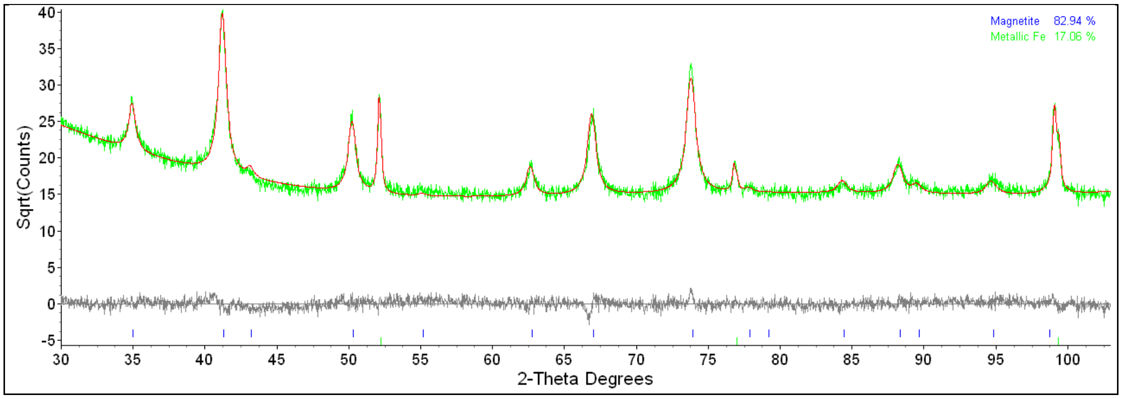

Figure 6.18: Experimental and simulated XRD diffractograms of FHYD2 sample reduced at 300 °C.

As the temperature was further increased to 350 °C, the α-Fe phase was increasing at the expense of the magnetite phase. The magnetite phase was fully reduced to α-Fe at 400 °C, as shown in the Rietveld refinement in Figure 6.19. The results suggest a two step reduction process for the reduction of FHYD2 to α-Fe via magnetite. This is in agreement with previous results where Wüstite (FeO) cannot be formed at temperatures below 570 ˚C (Wimmers *et al.*, 1986; Jozwiak *et al.*, 2007).

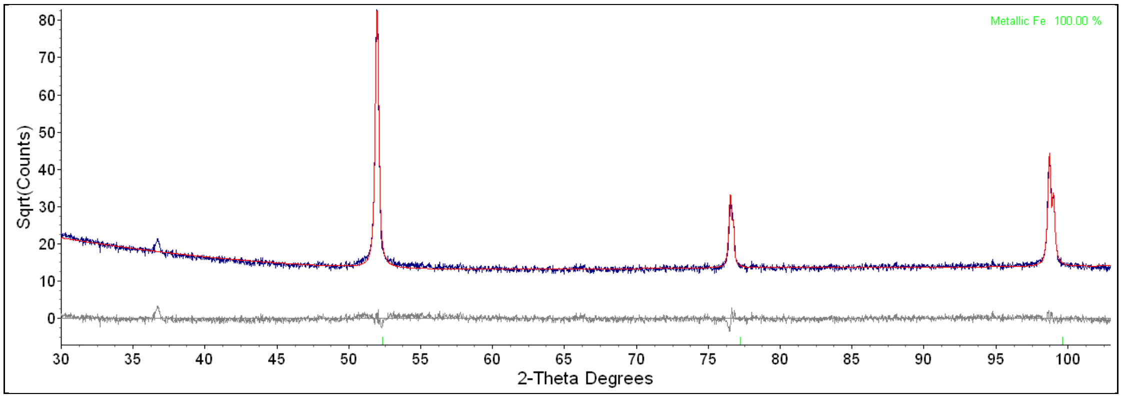

Figure 6.19: Experimental and theoretical X-ray patterns of α-Fe.

A summary of all the Reitveld refinement results for the reduction of pure FHYD2 under H_2 at temperatures up to 450 °C is displayed in Table 6.5.

Table 6.5: Rietveld refinement results for pure FHYD2.

Temperature (°C)	Phase	R_{wp} (%)	R_{Bragg} (%)	Phase composition (%)
250	Fe_3O_4	7.2	1.64	100
300	Fe_3O_4	6.65	1.33	82.94
	α-Fe		0.33	17.06
350	Fe_3O_4	7.03	1.96	19.47
	α-Fe		0.28	80.53
400	α-Fe	8.31	1.39	100
450	α-Fe	7.88	1.13	100

Where the figure of merits, R_{wp} and R_{Bragg} are the weighted profile residual and Bragg residual defined by (Pecharsky and Zavalij, 2009)

$$R_{wp} = \left[\frac{\sum_{i=0}^{n} wi\left(Y_i^{obs} - Y_i^{calc}\right)^2}{\sum_{i=0}^{n} wi\left(Y_i^{obs}\right)^2}\right]^{1/2} \times 100\% \tag{6.2}$$

$$R_{Bragg} = \frac{\sum_{j=1}^{m}\left|I_j^{obs} - I_j^{cacl}\right|}{\sum_{j=1}^{m} I_j^{obs}} \times 100\% \tag{6.3}$$

where the terms used in Eq.. 6.2 and 6.3 are defined as

- n is the total number of points measured in the powder diffraction pattern.
- Y_i^{obs} is the observed intensity of the *i*th data point.
- Y_i^{calc} is the calculated intensity of the *i*th data point.
- w_i is the weight of the *i*th data point, which is usually take as $w_i = 1/Y_i^{obs}$.
- m is the number of independent Bragg reflections.
- I_i^{obs} is the observed integrated intensity of the *j*th Bragg peak.
- I_j^{calc} is the calculated integrated intensity of the *j*th Bragg peak.

A similar investigation was carried on silica promoted FHYD nanoparticles (FHYD2/SiO_2) to study the role of SiO_2 on the reduction mechanism of FHYD2. It has long been long known that the role of silica is physical in nature i.e. it provides structural integrity in the catalyst by preventing sintering and thus providing catalyst large surface areas (Bukur *et al.*, 1990). However, a strong chemical interaction between the catalyst and support has been reported (Lund and Dumesic, 1981; Zhang *et al.*, 2006; Suo *et al.*, 2012). While these studies reported that the addition of silica might be beneficial, its addition is also find to inhibit the catalyst activity and reducibility due to the strong interaction between iron and silica. In this study we will only investigate the role of silica on the reduction of FHYD2 not its role in catalyst activity.

In-situ XRD powder diffraction patterns for SiO_2 co-precipitated FHYD2 obtained during H_2 reduction are presented in Figure 6.20. Similar to the pure FHYD2, the silica FHYD2 initially reduced to magnetite at 300 °C but it was not further reduced to α-Fe when the temperature was increased to 450 °C. This observation supports the suggestion of a strong catalyst-support interaction.

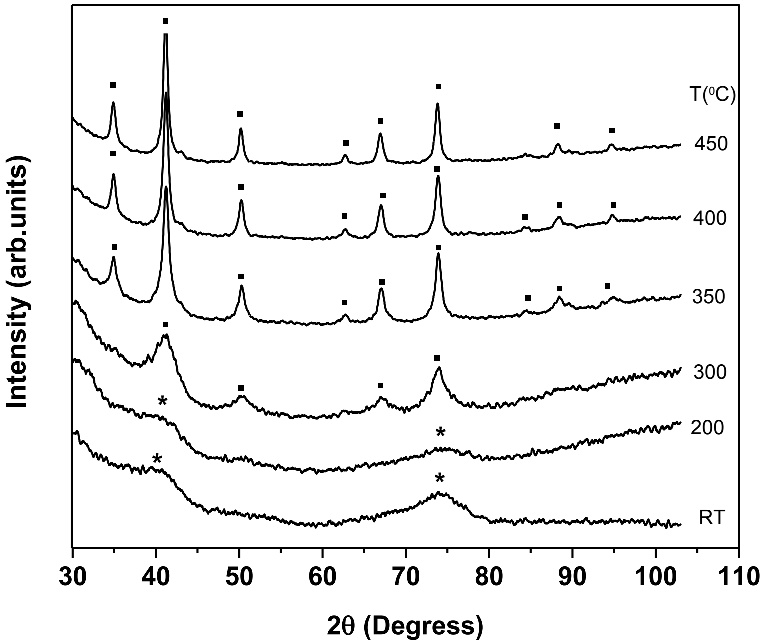

Figure 6.20: FHYD2/SiO$_2$ experimental X-ray diffractograms, where (*) FHYD2/SiO$_2$; (▪) Fe$_3$O$_4$.

For silica co-precipitated FHYD2 the first reduction step started to be observed at 300 °C (refer to Figure 6.20). The XRD pattern was refined and only magnetite gave a successful Rietveld refinement as shown in Figure 6.21.

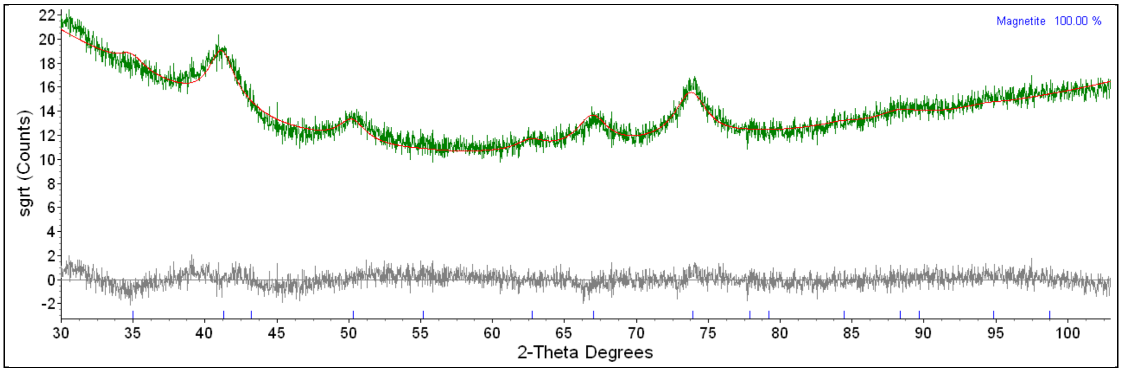

Figure 6.21: Obtained Reietveld refinement for FHYD2/SiO_2 reduced at 300 °C.

After 300 °C heat treatment, the XRD patterns for the reduced sample showed similar pattern. These patterns up to 450 °C were also successfully refined with magnetite phase only. Figure 6.22 shows the Rietveld refinement of the 450 °C reduced pattern.

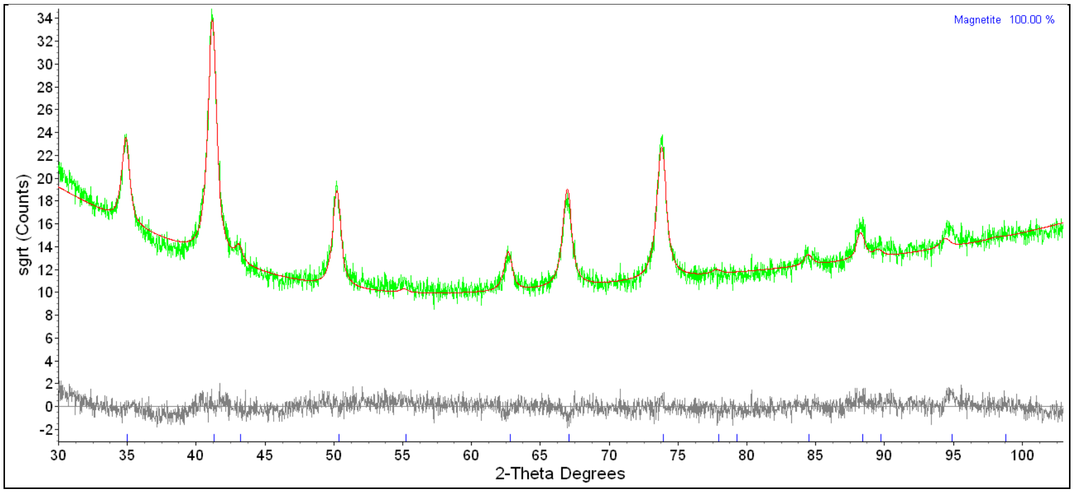

Figure 6.22: Calculated and experimental patterns for 450 °C reduced FHYD2/SiO_2 sample.

What was observed with the FHYD2/SiO_2 sample was that only the magnetite crystallites size were increasing with the increase in temperature with no further reduction to α-Fe as it was the case with pure FHYD2. TOPAS software (TOPAS V4.2) was used to perform Rietveld refinement using known Magnetite structure (PDF card 00-019-0629). The crystallite sizes reported in Figure 6.23 were obtained from such fittings.

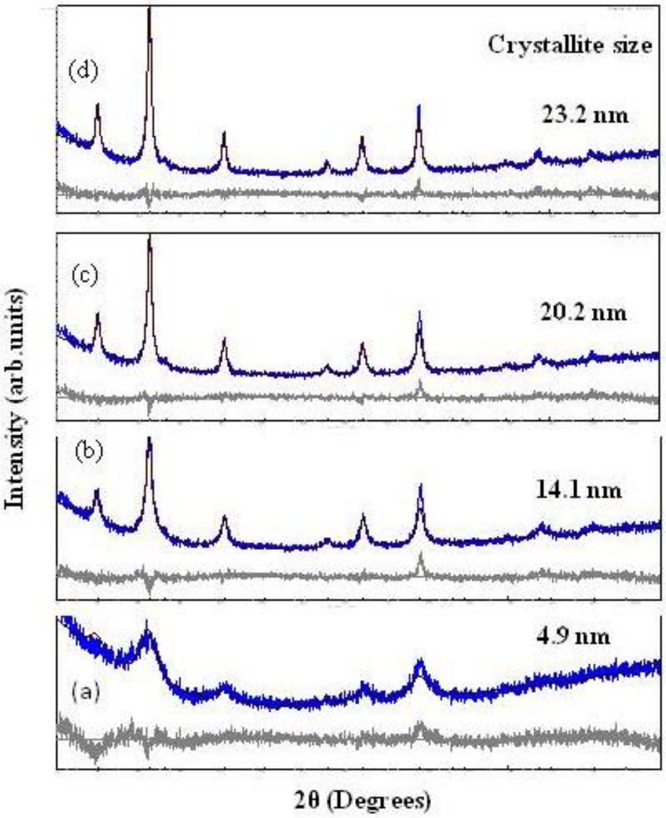

Figure 6.23: Reietveld refinements for FHYD2/SiO_2 sample reduced at (a) 300 °C, (b) 350 °C, (c) 400 °C, and (d) 450 °C. Blue is experimental data and black is the fit.

Pure FHYD6 sample was reduced in pure H_2 at temperatures up to 450 °C and the resulted XRD patterns are depicted in Figure 6.24. At temperatures as low as 200 °C phase changes were observed (Figure 6.24). The catalyst was observed to undergo thermal transformation and several reduction steps before it was eventually completely reduced to metallic iron at 450 °C. The thermally transformation and subsequent reduction was also observed with H_2-TPR.

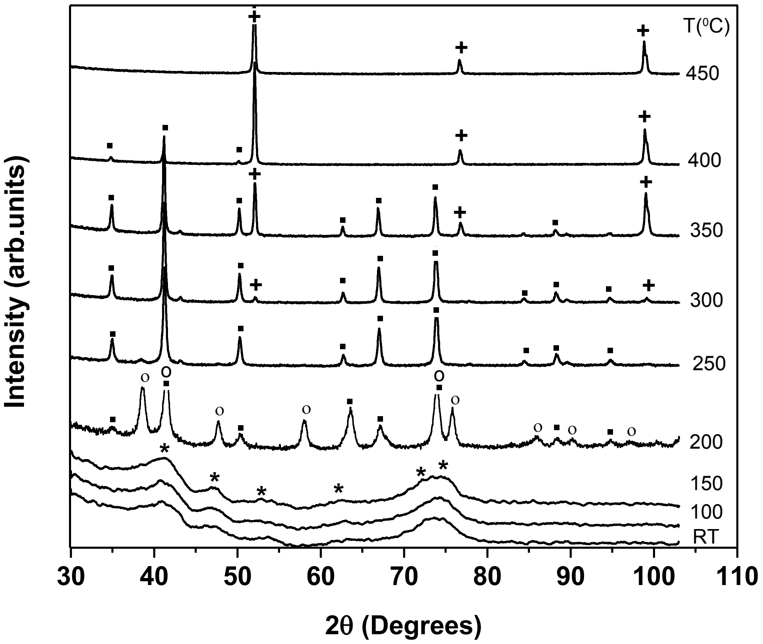

Figure 6.24: FHYD6 X-ray powder diffraction patterns, where (*) FHYD6; (○) α-Fe_2O_3; (▪) Fe_3O_4; (+) α-Fe.

Rietveld refinement was performed on the 200 °C reduced sample and agreement between calculated and experimental was obtained using hematite structure ($p\bar{3}c$) and magnetite as shown in Figure 6.25. It is believed that the preparation of our FHYD6 at elevated temperatures favoured the formation of hematite. It is also known that FHYD and α-FE_2O_3 forms at the same pH range. The formation mechanism of FHYD and other iron oxides by rapid hydrolysis Fe (III) salts is described in Chapter 4 section 4.2.1.

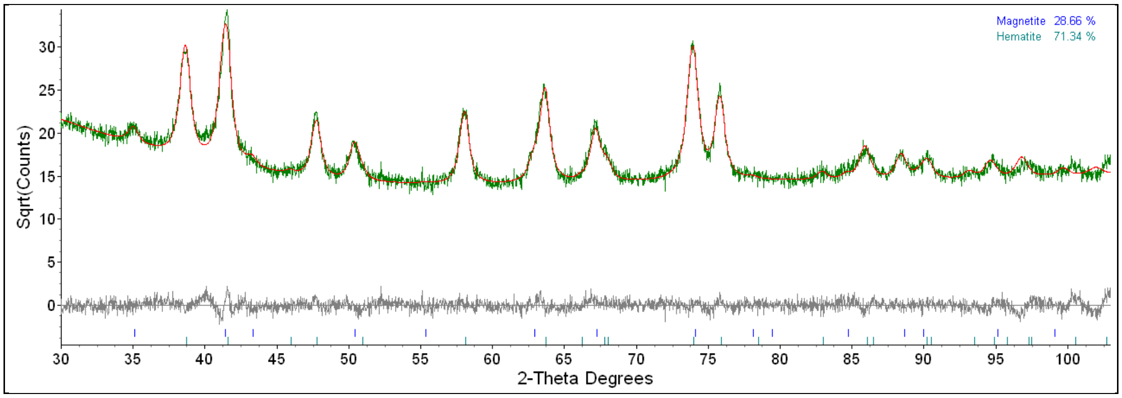

Figure 6.25: Experimental and calculated Rietveld refinement of a 200 °C reduced sample showing Fe_3O_4 and α-Fe_2O_3 contributions.

The contribution of the hematite phase at 200 °C in the refinement is clearly shown in Figure 6.26 below. A successful calculated XRD pattern estimated an amount of ~ 71 % total contribution of the α-Fe_2O_3 phase with a minor Fe_3O_4 phase (29 %).

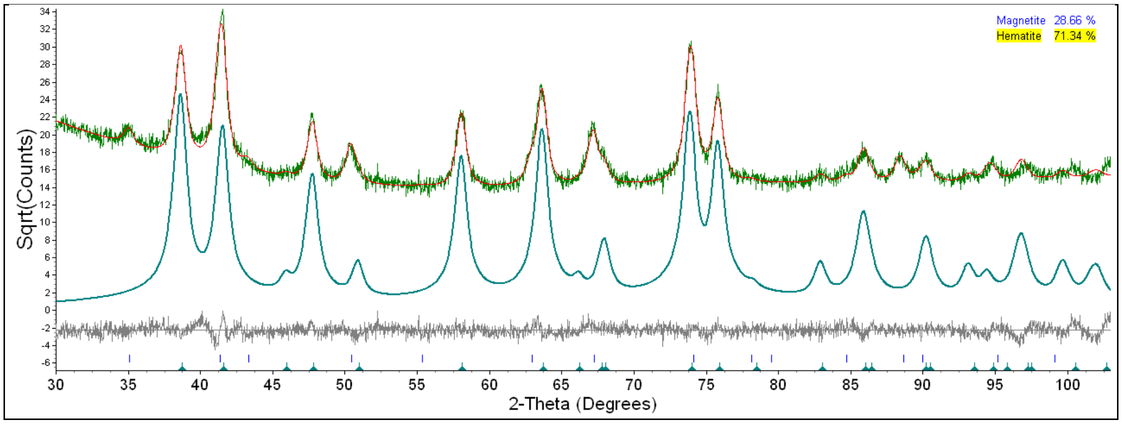

Figure 6.26: FHYD6 Rietveld refinement showing the hematite contribution for a sample at 200 °C.

The contribution of the α-Fe_2O_3 phase became less (4.21 %) in the *in situ* run of the FHYD6 sample at 250 °C, as the Rietveld refinement (Figure 6.27) recorded a high magnetite content of about 96 %. This was a reflection that the Fe_3O_4 phase was a reduction product of the hematite phase.

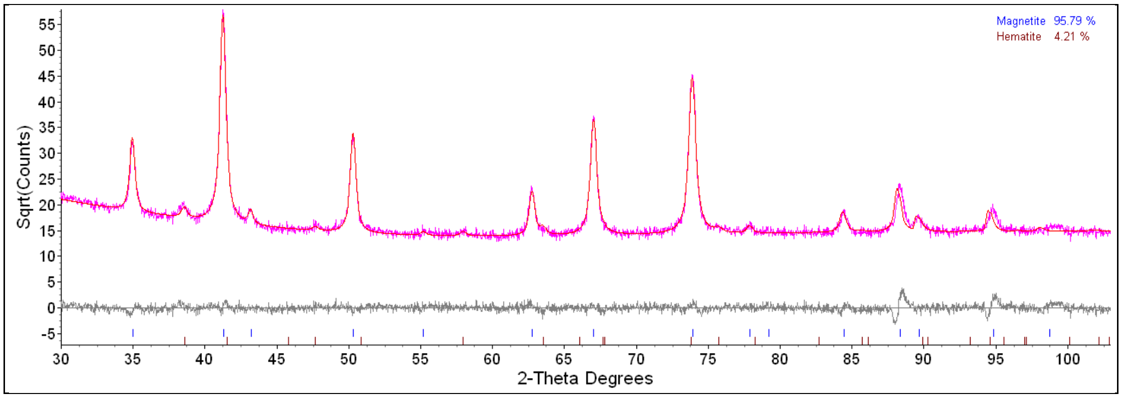

Figure 6.27: Experimental and theoretical XRD diffractograms for FHYD6 reduced at 250 °C.

It was observed that the XRD pattern in Figure 6.28 showed the appearance of α-Fe peaks together with magnetite at 300 °C. A Rietveld quantitative phase analysis indicates that about 57.98% of magnetite converted to metallic iron (Figure 6.28). No wüstite phase as an intermediate was observed during in-situ reduction of FHYD6 to α-Fe. It is known that wüstite it is an unstable phase below 570 °C (Wimmers *et al.*, 1986; Zhang *et al.*, 2006; Jozwiak *et al.*, 2007) and all our experiments were performed up to 450 °C.

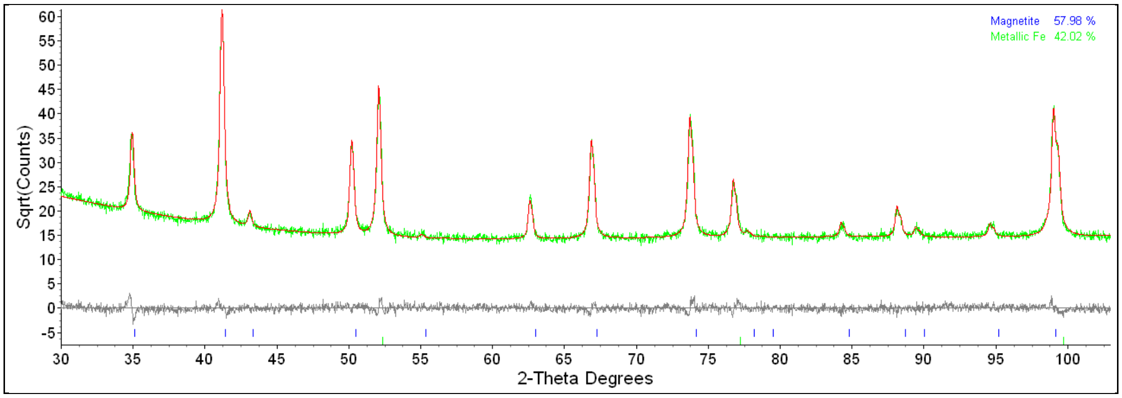

Figure 6.28: Rietveld refinement for FHYD6 reduced at 300 °C.

Only three α-Fe XRD peaks were observed at 450 °C indicating a complete reduction of FHYD6 to metallic iron (Figure 6.24). A successful Rietveld refinement for that pattern was obtained using only α-Fe phase as shown in Figure 6.29.

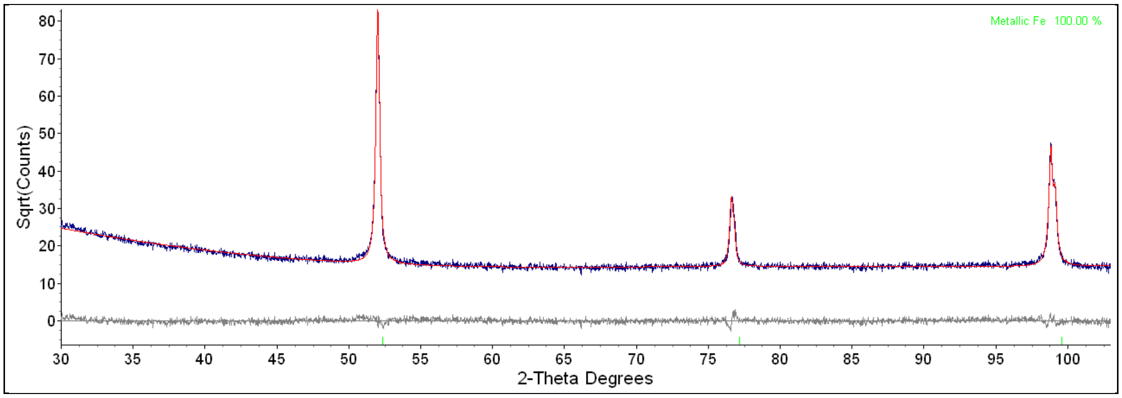

Figure 6.29: Experimental and calculated powder XRD patterns for FHYD6 reduced at 450 °C.

The type of iron oxides formed, R_{wp}, R_{Bragg} and phase composition values obtained from the reduction of FHYD6 sample are listed in Table 6.6.

Table 6.6: Summary of Rietveld refinement results for FHYD6.

Temperature (°C)	Phase	R_{wp} (%)	R_{Bragg} (%)	Phase composition (%)
200	α-Fe_2O_3	6.82	0.81	71.34
	Fe_3O_4		1.21	28.66
250	α-Fe_2O_3	7.46	2.25	4.21
	Fe_3O_4		1.33	95.75
300	Fe_3O_4	7.83	1.33	97.25
	α-Fe		2.02	2.75
350	Fe_3O_4	6.73	0.9	57.98
	α-Fe		0.47	42.02
400	Fe_3O_4	7.82	13.1	7.95
	α-Fe		0.28	92.05
450	α-Fe	6.82	0.36	100

6.3.2.3 Investigation of the reduction mechanisms through Mössbauer Spectroscopy

Transmission ^{57}Fe Mössbauer spectra of FHYD2 collected using ^{57}Co(Rh) source are presented in Figure 6.30. Reduction experiments were carried out in a Mössbauer *ex-situ* system under hydrogen flow for 16 h. FHYD2 was a precursor material in our reduction studies and the room temperature MS spectrum of untreated FHYD2 shows only a doublet of SPM Fe^{3+} ion (see chapter 4). Reducing the sample in H_2 at 200 ˚C converts the FHYD2 sample to Fe_3O_4 and α-Fe phases. The two phases were fitted with three Mössbauer sextets corresponding to the two distinct Fe sites in Fe_3O_4 i.e. tetrahedral *A*-sites and octahedral *B*-sites, the third sextet with δ = 0.011 mm/s and Bhf = 33.7 T (Table 6.7) was assigned to the α-Fe phase. There was still some evidence of unreduced FHYD2 as seen from the doublet contribution at the center of the 200 °C spectra.

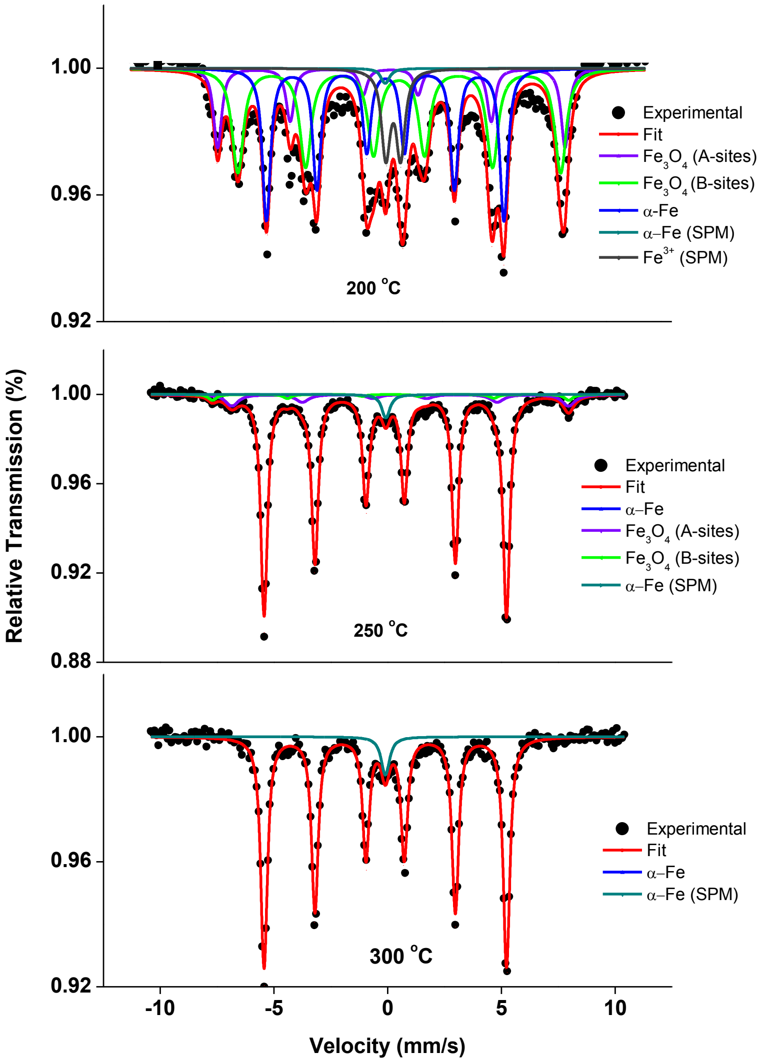

Figure 6.30: Mössbauer spectra of FHYD2 reduced at the temperatures indicated for 16 h.

After reduction at 250 °C, the spectrum indicated only the presence of Fe_3O_4 and α-Fe phases with a complete disappearance of the doublet representing the FHYD2 phase. The α-Fe phase was growing at the expense of the Fe_3O_4 phase as shown by the significant decrease in intensity of the Fe_3O_4 phase at 250°C. The emergence of a singlet at the center of the spectra was indicative of the formation of nano-sized Fe particles (Murad, 1996; Niemantsverdriet and Delgas, 1999). The formation of nanocrystalline iron by reducing synthetic and natural FHYDs in H_2 was also reported by other groups (Schneeweiss *et al.*, 2008; Schneeweiss *et al.*, 2010; Schneeweiss *et al.*, 2011).

Eventually, the contribution of the Fe_3O_4 phase completely disappeared at 300 °C with the spectra only showing a set of sextet and singlet corresponding to α-Fe and SPM α-Fe nanoparticles, respectively. The summary of all the hyperfine parameters obtained from the Mössbauer fittings of the reduced FHYD2 at different temperatures are presented in Table 6.7 below.

The origin of the doublet and singlet that we have observed in our spectra is well understood (Murad, 1996; Niemantsverdriet and Delgas, 1999). This superparamagnetic behaviour in nanoparticles arise purely from thermal effects and size of the particles. Due to their extremely small sizes, nanoparticles possesses high thermal excitations energies kT (where k is Boltzmann constant and T is the temperature) that are energetic enough to decouple the magnetization from the whole lattice. This is because when kT is greater than $KV,$ (where K is the anisotropy constant and V is the particle volume) the energy required to flip spins, the thermal fluctuations will begin to rapidly flip the spin directions and the nucleus will feel an average magnetization of zero and the spectrum start to resemble these of paramagnetic particles (Murad, 1996; Niemantsverdriet and Delgas, 1999).

Table 6.7: Values of hyperfine parameters for FHYD2 spectra recorded at room temperature.

T (˚C)	$^{\#}\delta$ (mm/s)	$^{\#}\Delta E_Q$ (mm/s)	$^{\Phi}$Bhf (T)	■ S (%)	Phase	Mössbauer Component
200	0.37	0.678	-	15.1	FHYD2	Doublet (Fe$^{3+)}$
	0.64	0.031	49.3	15.4	Fe_3O_4	Sextet [Fe^{3+}]
	0.27	0.009	45.8	31.3		Sextet (Fe^{3+}, Fe^{2+})
	0.01	-0.021	33.7	37.2	α-Fe	Sextet (Fe^{0})
	0.01	-	-	1.00		Singlet (Fe^{0})
250	0.66	0.002	48	2.5	Fe_3O_4	Sextet (Fe^{3+}]
	0.27	0.019	45.9	5.1		Sextet (Fe^{3+}, Fe^{2+})
	0.01	0.006	33.1	86.9	α-Fe	Sextet (Fe^{0})
	0.11	-	-	5.5		Singlet (Fe^{0})
300	0.01	0.008	33.1	95.6	α-Fe	Sextet (Fe^{0})
	0.014	-	-	4.4		Singlet (Fe^{0})

Uncertainty: $^{\#}$ ± 0.02 mms^{-1}, $^{\Phi}$ ± 0.5 T, ■ ± 2%

The MS spectra in Figure 6.30 shows that complete reduction of the FHYD2 sample to α-Fe was achieved at 300 °C after 16 h of heat treatment. We therefore performed time variation experiments at that temperature. The Mössbauer spectra of time variation experiments for FHYD2 at 300 °C are shown in Figure 6.31. The 2 h spectra clearly show the existence of Fe_3O_4 with a minor α-Fe phases. The spectra at 2, 4, and 8 h were all fitted with three sextets characteristic of Fe_3O_4 and α-Fe.

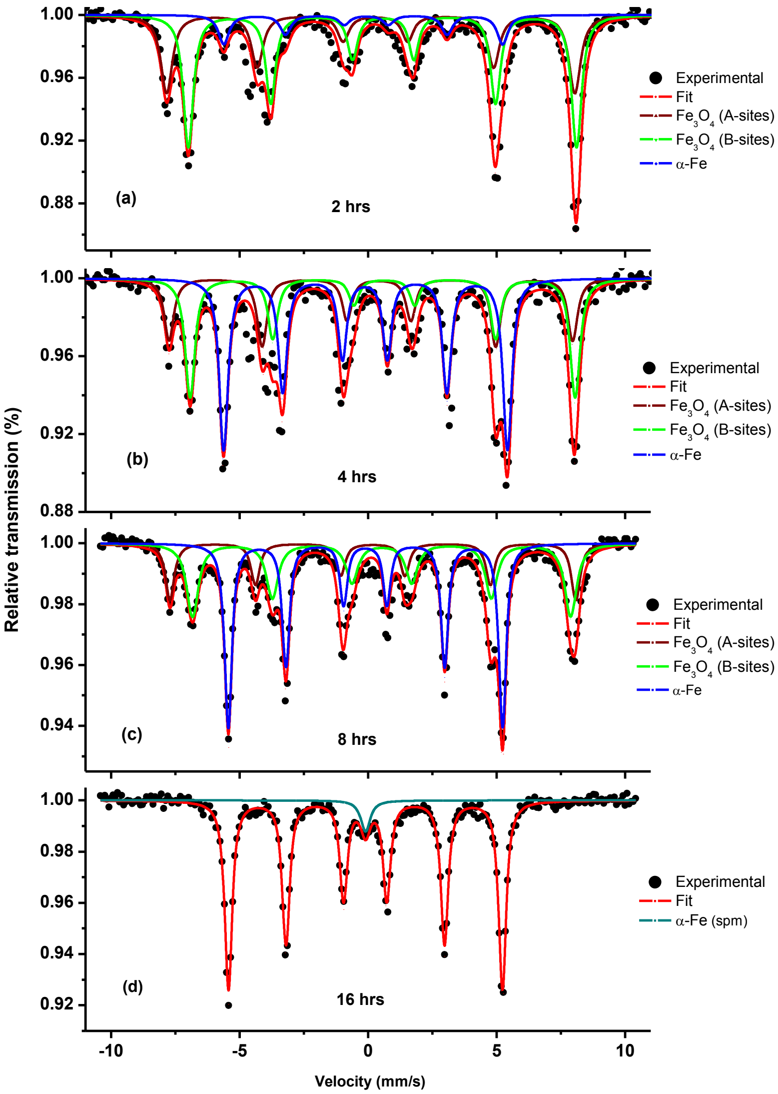

Figure 6.31: Time variation Mössbauer spectra of FHYD2 sample reduced at 300 °C for 2, 4, 8, and 16 h.

The Fe_3O_4 and α-Fe phases were still the only two crystalline phases recorded after 4 h of heating in H_2. However, the intensity of the α-Fe absorption lines significantly increased after 4 h reduction. This was an indication of the formation and growth of the α-Fe phase from the magnetite. The metallic Fe phase continued to grow as Fe_3O_4 was consumed during the 8 h reduction. All the spectra up to 8 h were fitted with two magnetite sextets (*A*-sites and *B*-sites) and one sextet for the α-Fe phase and the hyperfine interaction parameters from these fits are summarized in Table 6.8.

Table 6.8: Mössbauer parameters obtained from FHYD2 fits reduced at 300 °C at various reaction times of 2, 4, 8, and 16 h.

Reaction (h)	$^{\#}\delta$ (mm/s)	$^{\#}\Delta E_Q$ (mm/s)	$^{\Phi}$Bhf (T)	▪S (%)	Phase	Mössbauer Component
2	0.26	0	48.9	32	Fe_3O_4	Sextet [Fe^{3+}]
	0.68	0	45.8	63		Sextet (Fe^{3+}, Fe^{2+})
	0.01	0.007	33.3	5	α-Fe	Sextet (Fe^0)
4	0.36	0	49.0	15.8	Fe_3O_4	Sextet [Fe^{3+}]
	0.62	0	46.0	31.7		Sextet (Fe^{3+}, Fe^{2+})
	0.01	0.007	33.1	52.5	α-Fe	Sextet (Fe^0)
8	0.29	0	48.6	7.5	Fe_3O_4	Sextet [Fe^{3+}]
	0.58	0	44.9	15.6		Sextet (Fe^{3+}, Fe^{2+})
	0.01	0.007	33.4	77.3	α-Fe	Sextet (Fe^0)
16	0.01	0.008	33.1	95.6	α-Fe	Sextet (Fe^0)
	0.014	-	-	4.4		Singlet (Fe^0)

Uncertainty: $^{\#}$ ± 0.02 mms^{-1}, $^{\Phi}$ ± 0.5 T, ▪ ± 2%

The Mössbauer absorption spectra of FHYD2/SiO_2 recorded at various temperatures for reduction time of 16 h are shown in Figure 6.32. The Mössbauer spectra of the 200 °C heat treated sample shows three set of sextets and a doublet. The magnetic hyperfine fields (Bhf) of 49 and 45 T were in good agreement with the two sextets of Fe_3O_4 iron in distinct *A*-sites and *B*-sites, respectively. The doublet with an isomer shift of 1.321 mm/s has been attributed to the Fe^{2+} species due to the wüstite phase. The presence of the wüstite phase supports the H_2-TPR observations but however it contradicts the *in situ* XRD results. This could be the result of a lower sensitivity of the XRD technique to this phase due its small quantity as shown by the very small area of the Mössbauer resonance lines (S %) in Table 6.9.

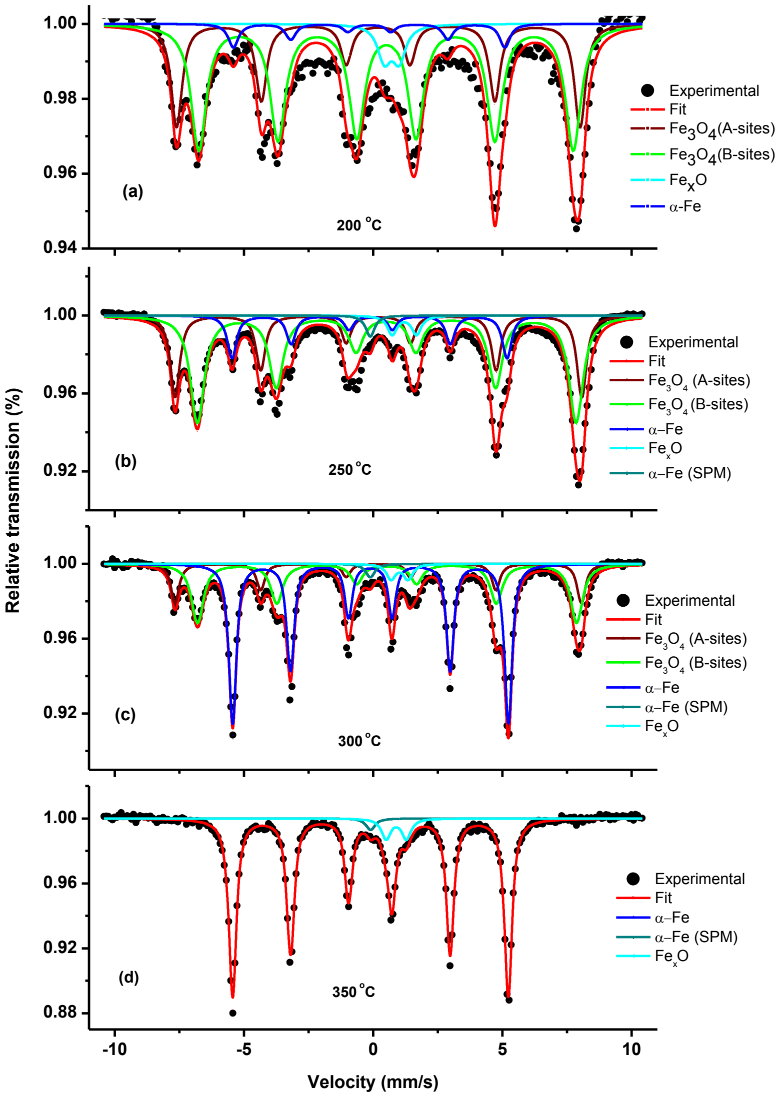

Figure 6.32: Mössbauer spectra recorded at 300 K for FHYD2/SiO_2 reduced at various temperatures.

The Mössbauer spectra recorded at 300 K showed that the amount of α-Fe phase increased from 7.5 % to 13.9 % after 200 and 250 °C heat treatments. The results demonstrate that the α-Fe phase was the reduction product of the Fe_3O_4 as this phase was growing at the expense of magnetite. This was clearly observed in the 300 °C reduced sample with the significant decrease in the intensity of the Fe_3O_4 absorption lines and sharp increase in the intensity of the sextet representing the α-Fe phase (see quantitative results in Table 6.9). There was a persistence of the wüstite phase (Fe^{2+} species) in all reduction temperatures (200 – 350

°C). This phase is known to be thermodynamically unstable below 570 °C but the presence of support materials like SiO_2 stabilizes the wüstite phase (Wimmers *et al.*, 1986; Jozwiak *et al.*, 2007). Because of the Fe^{2+} species from the wüstite phase, complete reduction of the FHYD2/SiO_2 to α-Fe was not realized at temperatures up to 350 °C. However, the dominant phase at 350 °C was the metallic iron in bulk and nano-size (SPM α-Fe) forms. The Mössbauer parameters obtained by fitting the experimental spectra with sub spectra consisting of Lorentzian-shaped lines are listed in Table 6.9.

Table 6.9: Values of hyperfine parameters from FHYD2/SiO_2 Mössbauer spectra.

T (˚C)	$^{\#}\delta$ (mm/s)	$^{\#}\Delta E_Q$ (mm/s)	$^{\Phi}$Bhf (T)	■ (S %)	Phase	Mössbauer Component
200	0.36	0	48.5	31.3	Fe_3O_4	Sextet [Fe^{3+}]
	0.66	0	45.3	60		Sextet (Fe^{3+}, Fe^{2+})
	0.99	0.90	-	1.2	FeO	Doublet (Fe^{2+})
	0.01	0.003	33.1	7.5	α-Fe	Sextet (Fe^0)
250	0.32	0.002	48.8	27.4	Fe_3O_4	Sextet [Fe^{3+}]
	0.62	0.029	45.5	53.8		Sextet (Fe^{3+}, Fe^{2+})
	0.94	1.321	-	1.7	FeO	Doublet (Fe^{2+})
	-0.01	-0.046	33.00	13.9	α-Fe	Sextet (Fe^0)
		-	-	3.2		Singlet (Fe^0)
300	0.31	-0.004	48.8	13.8	Fe_3O_4	Sextet (Fe^{3+}]
	0.64	0.018	45.5	30.8		Sextet (Fe^{3+}, Fe^{2+})
	0.65	1.135	-	3.0	FeO	Doublet (Fe^{2+})
	0.01	0.007	33.1	51.0	α-Fe	Sextet (Fe^0)
		-	-	1.3		Singlet (Fe^0)
350	1.01	0.785	-	5.7	FeO	Doublet (Fe^{2+})
	0.01	0.003	33.1	92.7	α-Fe	Sextet (Fe^0)
	0.01	-	-	1.6		Singlet (Fe^0)

Uncertainty: $^{\#}$ ± 0.02 mms^{-1}, $^{\Phi}$ ± 0.5 T, ■ ± 2%

The effect of reaction time on the reducibility of FHYD2/SiO_2 at 350 °C was investigated and the obtained experimental Mössbauer spectra are presented in Figure 6.33.

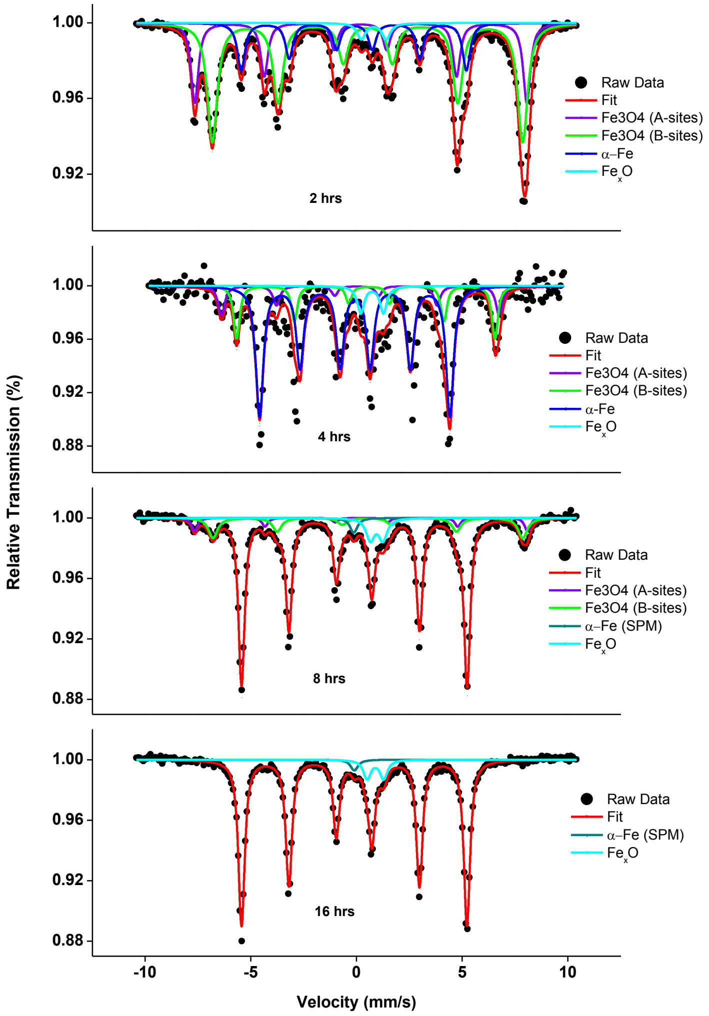

Figure 6.33: Mossbauer spectra of FHYD2/SiO_2 sample reduced at 350 °C for the indicated reaction times of 2, 4, 8, and 16 h.

The 2 h spectra consists of three magnetically ordered components characteristic of Fe_3O_4 and α-Fe phase, and a quadrupole doublet with a rather high isomer shift $\delta \approx 0.99$ mm/s at the central region of the spectra. The high value of δ is typical of Fe^{2+} species rather than SPM Fe^{3+} and it was attributed to the wüstite phase. An acceptable fit was obtained by fitting the spectra with three sextets (two from the *A*-sites and *B*-sites of Fe_3O_4 and one from α-Fe) and one doublet. The obtained results (Table 6.10) are in good agreement with values reported in literature (Cornell and Schwertmann, 2003; Lyubutin *et al.*, 2009).

There were no spectral changes between the 2 and 4 h heat treatments in terms of formation of additional phases. However, a significant increase in the intensity and area of the

Mössbauer resonance lines of the α-Fe phase was recorded after reducing the sample for 4 h. Similarly to the temperature variation experiments (Figure 6.32), the Fe^{2+} species (with average δ ≈ 1 mm/s) attributed to the wüstite phase appeared in all our reaction times considered in this investigation. From these observations it can be concluded that thermally reducing our SiO_2 precipitated FHYD2 sample at 350 °C for 16 h was not good enough to fully reduce it to α-Fe. The 8 and 16 h spectra also clearly show the presence of singlet due to the superparamagnetic behavior of metallic iron small particles (see Table 6.10).

Table 6.10: Hyperfine parameters for FHYD2/SiO_2 reduced at 350 °C for 2, 4, 8, and 16 h.

Reaction (h)	# δ (mm/s)	# ΔE_Q (mm/s)	ΦBhf (T)	■S (%)	Phase	Mössbauer Component
2	0.32	0	48.8	25.6	Fe_3O_4	Sextet [Fe^{3+}]
	0.67	0	44.9	50.3		Sextet (Fe^{3+}, Fe^{2+})
	1.00	0.990	-	3	FeO	Doublet (Fe^{2+})
	0.01	0.003	33.1	21.1	α-Fe	Sextet (Fe^0)
4	0.23	0.197	48.7	11.3	Fe_3O_4	Sextet [Fe^{3+}]
	0.74	-0.192	45.3	18.4		Sextet (Fe^{3+}, Fe^{2+})
	0.99	1.292		5.6	FeO	Doublet (Fe^{2+})
	0.03	-0.023	33.5	64.7	α-Fe	Sextet (Fe^0)
8	0.34	-0.018	48.9	5.4	Fe_3O_4	Sextet [Fe^{3+}]
	0.63	0.053	45.5	13.2		Sextet (Fe^{3+}, Fe^{2+})
	1.00	0.597	-	6.5	FeO	Doublet (Fe^{2+})
	0.01	0.007	33.1	73.0	α-Fe	Sextet (Fe^0)
	-0.13	-	-	2.0		Singlet (Fe^0)
16	1.00	0.785	-	5.7	FeO	Doublet (Fe^{2+})
	0.01	0.003	33.1	92.7	α-Fe	Sextet (Fe^0)
	0.01	-	-	1.6		Singlet (Fe^0)

Uncertainty: # ± 0.02 mms^{-1}, Φ ± 0.5 T, ■ ± 2%

Experimentally obtained Mössbauer spectra as a function of temperature for FHYD6 are presented in Figure 6.34. The 200 °C reduced sample shows spectra with the presence of two iron oxide phases, viz. α-Fe_2O_3 and Fe_3O_4. The fittings of these spectra were performed using three set of sextets corresponding to Fe_3O_4 *A*-sites (δ = 0.32 mm/s and Bhf = 48.9 T) and *B*-sites (δ= 0.63 mm/s and Bhf = 45.7 T) as well as one sextet with hyperfine parameters (δ= 0.38 mm/s and Bhf = 51.0 T) characteristic of hematite. These hyperfine parameters for α-Fe_2O_3 and Fe_3O_4 are in good agreement with previously reported values in literature (Cornell and Schwertmann, 2003; Lyubutin *et al.*, 2009). It has to be mentioned that a significant amount of the α-Fe_2O_3 phase was also recorded in our *in situ* XRD and H_2-TPR experiments of the same sample (see section 6.1 and 6.2).

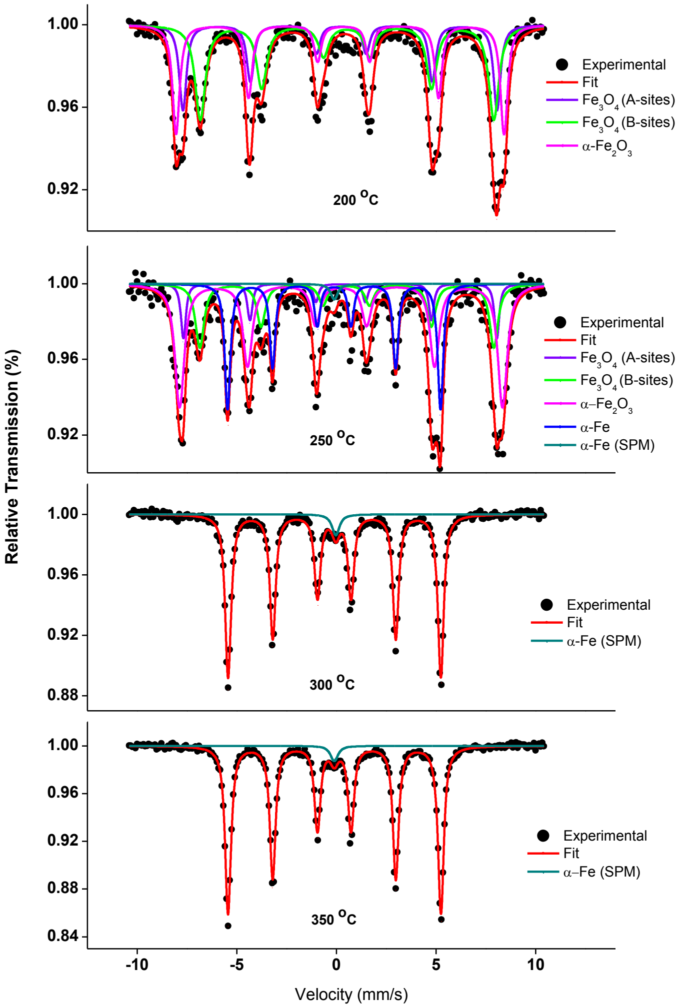

Figure 6.34: The Mössabuer spectra of FHYD6 reduced at different temperatures for 16 h.

A further reduction of the sample in H_2 at 250 °C converted some of the Fe_3O_4 phase to α-Fe with the α-Fe_2O_3 and Fe_3O_4 phases still present. The formation of the α-Fe phase at 250 °C was confirmed by the manifestation of an additional sextet with δ = mm/s and Bhf = 33.1 T and superparamagnetic (SPM) iron was also recorded. The hyperfine parameters obtained from fitting the spectra are listed in Table 6.11.

Metallic Fe was the only reduction product after the 300 and 350 °C heat treatment with the contribution of the α-Fe_2O_3 and Fe_3O_4 phases completely disappeared (see Figure 6.34). The spectra show a sextet and a singlet signifying bulk and nano-sized α-Fe particles, respectively (see Table 6.11). It can be noted that reducing the nanoparticles of FHYDs produces α-Fe nanoparticles. This method of producing iron nanoparticles by thermally reducing FHYD in H_2 was also reported (Schneeweiss *et al.*, 2008; Schneeweiss *et al.*, 2010; Schneeweiss *et al.*, 2011). It is evident from this results that our FHYD6 sample thermally transformed to α-Fe_2O_3 and the hematite phase reduction proceeded stepwise via the common two-step reduction process (α-Fe_2O_3 → Fe_3O_4 → Fe) (Sastri *et al.*, 1982; Wimmers *et al.*, 1986; Manteanu *et al.*, 1999; Jozwiak *et al.*, 2007; Pourghahramani and Forssberg, 2007).

Table 6.11: The hyperfine parameters obtained from the Mössbauer spectra of FHYD6 sample.

T (˚C)	# δ (mm/s)	# ΔE_Q (mm/s)	ΦBhf (T)	▪S (%)	Phase	Mössbauer Component
200	0.38	-0.173	51.0	32.8	α-Fe_2O_3	Sextet (Fe^{3+})
	0.32	-0.069	48.9	41.5	Fe_3O_4	Sextet [Fe^{3+}]
	0.63	0.016	45.7	25.7		Sextet (Fe^{3+}, Fe^{2+})
250	0.32	-0.062	51.3	15.4	α-Fe_2O_3	Sextet (Fe^{+3})
	0.33	-0.022	49.3	39	Fe_3O_4	Sextet [Fe^{3+}]
	0.61	0.014	45.7	18.9		Sextet (Fe^{3+}, Fe^{2+})
	-0.01	-0.001	33.1	26.7	α-Fe	Sextet (Fe^0)
300	0.01	0.010	33.1	96.6	α-Fe	Sextet (Fe^0)
	0.01	-	-	3.4		Singlet (Fe^0)
350	0.01	0.011	33.1	97.5	α-Fe	Sextet (Fe^0)
	0.002	-	-	2.5		Singlet (Fe^0)

Uncertainty: # ± 0.02 mms^{-1}, Φ ± 0.5 T, ▪ ± 2

Interconversions between FHYD and hematite

It was noted that in all our H_2 reduction experiments (H_2-TPR, *in situ* XRD, and Mössbauer spectroscopy) it was observed that FHYD6 first undergo a thermal transformation to hematite before the actual reduction process. This behaviour was not observed in the pure and SiO_2 precipitated FHYD2 samples and we took a closer look at the transformation of FHYD to hematite to elucidate the different behaviours of the FHYDs samples. It is widely accepted that the dry thermal transformation of FHYD to hematite involves internal dehydration/dehydroxylation and rearrangements of atoms within the aggregated structure towards the direction of hematite structure (Fischer and Schwertmann, 1975; Schwertmann and Murad, 1983; Cornell *et al.*, 1989; Cornell and Schwertmann, 2003). Experimental evidence reported in literature from Mössbauer spectroscopy, TEM, XRD, and neutron studies indicates that the α-Fe_2O_3 nucleates from within FHYD aggregates (Cornell *et al.*, 1989). It is believed that this solid state transformation of FHYD to α-Fe_2O_3 is facilitated because the two share the same hexagonal closed-packed (hcp) anionic stacking (Fischer and Schwertmann, 1975; Schwertmann and Murad, 1983; Cornell *et al.*, 1989; Cornell and Schwertmann, 2003).

We have observed that the thermal transformation from FHYD to hematite before the actual reduction process only happened in our FHYD6 sample. There are a number of reasons that can explain the “easy” thermal transformation of FHYD6 to α-Fe_2O_3 at low temperatures. It is known that FHYD and hematite forms in the same pH domain during the synthesis procedure (see Chapter 4 section 4.2.1). Unlike FHYD2, the FHYD6 nanoparticles were synthesized at elevated temperatures and these temperatures are known to favour hematite formation (Schwertmann and Cornell, 2000). It is high likely that our FHYD6 had some highly dispersed α-Fe_2O_3 phase which is in agreement with the Drits model of FHYD structure (Drits *et al.*, 1993). Another explanation may come from the same octahedra structure shared by FHYD6 and α-Fe_2O_3. Cornell and Schwertmann, 2003, reported that some of the face sharing between FeO_6 octahedra in α-Fe_2O_3 is also present in 6-line FHYD. The presence of face sharing in FHYD6 similar to α-Fe_2O_3 was thought to initiate the transformation (Stanjek and Weidler, 1992; Cornell and Schwertmann, 2003).

The Mössbauer spectra showing the reaction time evolution of the reduction of FHYD6 at 300 °C are depicted in Figure 6.35. The spectra after 2 h heat treatment clearly shows two magnetically split components whose Mössbauer hyperfine parameters (Table 6.12) corresponds to the two distinct Fe sites of the Fe_3O_4 phase i.e. T_d Fe^{3+} in *A*-sites and O_h Fe^{3+} + Fe^{2+} in *B*-sites. The area ratio S_A/S_B of the Mössbauer resonance lines was used to determine the stochiometry of Fe_3O_4 phase (Lyubutin *et al.*, 2009). The area ratio S_A/S_B from our results suggest the formation of stochiometric Fe_3O_4 phase (see Table 6.12).

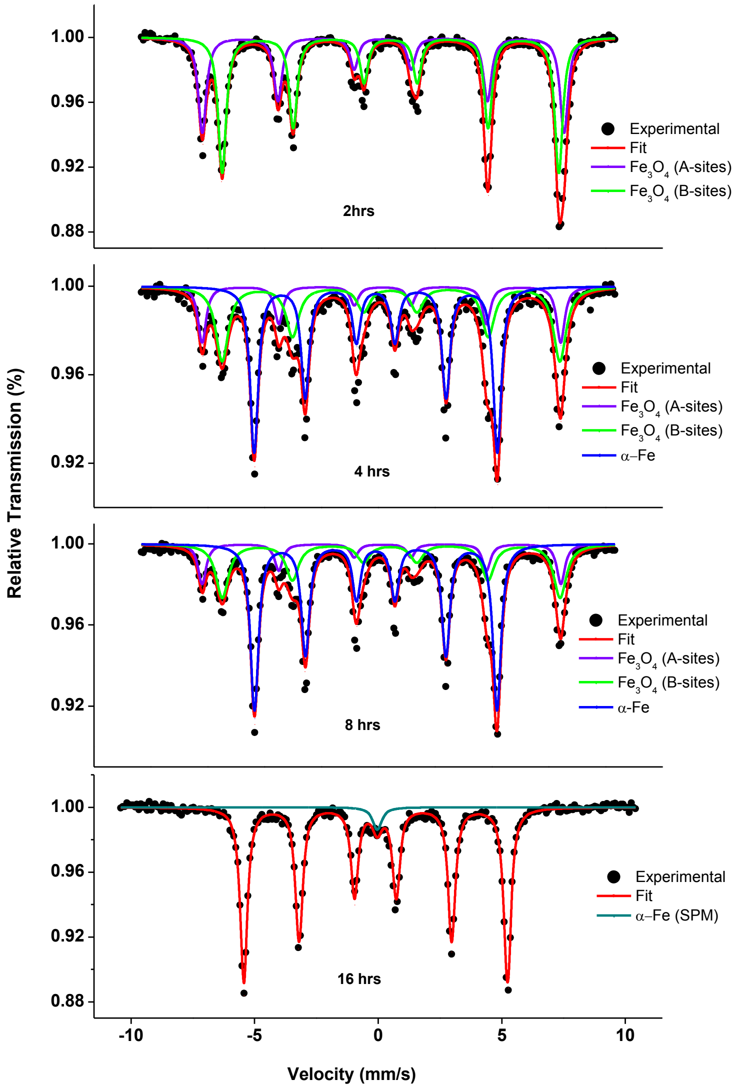

Figure 6.35: Room temperature Mössbauer spectra of FHYD6 reduced at 300 °C at different reaction times of 2, 4, 8 and 16 h.

The change of the reaction time to 4 h lead to the formation of α-Fe, as evidence by the additional sextet with $\delta = 0.01$ mm/s and Bhf = 33.1 T along with the Fe_3O_4 phase (Figure 6.35). A further increase in reaction time up to 8 h resulted in the growth of the α-Fe phase at the expense of the Fe_3O_4 phase with no additional phase formed. In agreement with results shown in Figure 6.34, complete reduction of the FHYD6 to α-Fe was achieved after 16 h of reduction time as shown in Figure 6.35. The Mössbauer hyperfine parameters obtained from analysis of the time variation spectra of the FHYD6 sample are summarized in Table 6.12.

Table 6.12: Mössbauer hyperfine parameters of the time varied FHYD6 sample reduced at 300 °C.

Reaction (h)	$^{\#}\delta$ (mm/s)	$^{\#}\Delta E_Q$ (mm/s)	$^{\Phi}$Bhf (T)	▪S (%)	Phase	Mössbauer Component
2	0.33	0.019	49.3	41.8	Fe_3O_4	Sextet [Fe^{3+}]
	0.66	-0.006	45.9	58		Sextet (Fe^{3+}, Fe^{2+})
4	0.23	0	48.7	29.2	Fe_3O_4	Sextet [Fe^{3+}]
	0.62	0	45.0	58.9		Sextet (Fe^{3+}, Fe^{2+})
	0.01	0.003	33.1	11.9	α-Fe	Sextet (Fe^0)
8	0.29	-0.048	48.9	13.8	Fe_3O_4	Sextet [Fe^{3+}]
	0.66	0.044	46.0	29.1		Sextet (Fe^{3+}, Fe^{2+})
	0.01	0.003	33.1	57.1	α-Fe	Sextet (Fe^0)
16	0.01	0.0100	33.1	96.6	α-Fe	Sextet (Fe^0)
	0.01	-	-	3.4		Singlet (Fe^0)

Uncertainty: $^{\#}$ ± 0.02 mms^{-1}, $^{\Phi}$ ± 0.5 T, ▪ ± 2%

6.4 Chapter conclusions

Precipitated FHYD nanoparticles were synthesized and their thermal transformation reduction mechanisms were successfully investigated under hydrogen atmosphere using magnetization measurements, TPR method, in-situ XRD, and in-situ Mössbauer spectroscopy.

Thermal transformations under vacuum and reduction mechanisms under hydrogen atmosphere of precipitated FHYD nanoparticles, namely FHYD2, FHYD2/SiO_2 and FHYD6, were investigated. The investigation methods included TPR, in-situ XRD, MS and magnetic measurements. For FHYD2 and FHYD6 the thermal transformation translates in two steps increase of the magnetisation. The first step starts at approximately 580 K with a loss of the lattice water and sintering, accompanied by structural changes and phase transformation from FHYD to α-Fe_2O_3 just below T ~ 700K. During the second step which starts at T ~ 700 K and extends to T ~ 780 – 850 K the increase in the magnetisation appears to be due mainly to crystallite size growth and probably to improved crystallinity. Further evidence for this emerges from the occurrence of well resolved magnetically (i.e. sextets) MS spectra for FHYD2 and FHYD6 when heated at $T \geq 700$ K confirming the presence of relatively large crystallites with average diameter above the threshold value $D_{av} \sim 10$ nm for most iron oxide nanoparticles.

For FHYD2/SiO_2 the magnetisation starts increasing at a relatively high temperature ~ 660 K as compared to 580 K for FHYD2 and FHYD6 and leads also to the formation of α-Fe_2O_3. The transformation is however incomplete in that residues of the FHYD in SPM state still persist at temperatures as high as 800 K, i.e. the presence of SiO_2 appears to inhibit the transformation. The magnetization values level up between T ~ 740 – 880 K which seems to point to no further sintering occurring with increasing temperature in this range, i.e. the presence of SiO_2 inhibits sintering at temperature above 740 K.

Magnetization measurements show that under vacuum the thermal dehydration/dehydroxylation of FHYD leading to the formation of α-Fe_2O_3 starts at relatively high temperatures (~ 580 K), it is further delayed (up to T ~ 660 K) in the presence of SiO_2. In contrast, thermal transformation in hydrogen atmosphere occurs at relatively lower temperature (~ 480 K) which seems to indicate that a gaseous environment facilitates the thermal dehydration/dehydroxylation process.

TPR hydrogen reduction measurements show different reduction mechanisms for all three samples studied. The FHYD2 showed a two-step reduction process to α-Fe, while the SiO_2 precipitated FHYD2 is completely reduced to α-Fe via Fe_3O_4 and FeO intermediates. The FeO phase was only detected on the SiO_2 precipitated FHYD2. Although we have not performed relevant experiments, our result supports previous reports that materials like SiO_2 stabilizes the FeO phase which is thermodynamically metastable below 570 ˚C.

The reducibility and reaction mechanisms of three FHYD systems (i.e. FHYD2, FHYD2/SiO_2, and FHYD6) were successfully studied with temperature programmed reduction. The three systems studied here showed completely different reduction paths. For FHYD2 with and without SiO_2 the general first reduction step is the reduction of FHYD to magnetite. After the Fe_3O_4 formation, the pure FHYD2 is directly reduced to α-Fe, while the SiO_2 containing FHYD2 is reduced to α-Fe via FeO. The FHYD6 sample showed two competing process i.e. thermal transformation and reduction. Due to thermal dehydration/dehydroxylation the structure of the FHYD6 collapsed to α-Fe_2O_3 and the usual reported two-step reduction of the α-Fe_2O_3 phase to α-Fe via Fe_3O_4 intermediate followed.

Reduction mechanisms of three forms of FHYD samples i.e. pure FHYD2, FHYD6, and SiO_2 co-precipitated FHYD2 under H_2 were successfully investigated using in-situ XRD. In pure H_2 atmosphere pure FHYD2 and FHYD6 were completely reduced to α-Fe. The presence of FeO was not observed with in-situ XRD however the sample with SiO_2 was not fully reduced to metallic Fe during the course of in-situ XRD experiments up to 450 °C.

Mössbauer spectroscopy was successfully used to characterize FHYDs samples after reducing in H_2 environment at different temperatures and different reducing times. With Mössbauer spectroscopy we were able to prove that the type of spinel phase observed in our *in situ* XRD experiments was indeed magnetite. The high sensitivity of this technique to Fe oxidation state enabled us to pick up Fe^{2+} species during FHYD2/SiO2 reductions, this divalent iron species was attributed to non-stochiometric wüstite phase (FeO). This phase was also predicted using quantitative analysis of H_2 consumed in our H_2-TPR but it was not detected in our *in situ* XRD reduction experiments.

In summary, the following reduction schemes in hydrogen atmosphere were proposed for the three FHYD samples investigated in our study according to

(i) FHYD2 $\rightarrow Fe_3O_4 \rightarrow$ α-Fe

(ii) FHYD2/$SiO_2 \rightarrow Fe_3O_4 \rightarrow$ FeO → α-Fe

(iii) FHYD6 → α-$Fe_2O_3 \rightarrow Fe_3O_4 \rightarrow$ α-Fe

The proposed reduction mechanisms were tested by H2-TPR, in situ XRD, and Mössbauer spectroscopy studies. It has to be mentioned that the transformation of FHYD6 to α-Fe_2O_3 was not a reduction process but purely a thermal event.

Chapter 7

Conclusions and Recommendations

The current chapter summarizes the key findings of the study and recommendations for future work. The significance and implications of the findings of this work in terms of the structure and reduction of FHYD will be discussed in this chapter.

7.1 Conclusions

Nanoparticles of 2- and 6-line FHYD as well as 2-line FHYD deposited onto SiO_2 support were synthesized using rapid hydrolysis of $Fe(NO_3)_3.9H_2O$ solutions. Their structural and magnetic properties and reduction mechanisms were characterized using variety of experimental techniques. The key findings of the study can be divided into two areas, i.e. the structural properties and reduction behavior of FHYD in H_2 atmosphere.

7.1.1 Structural and magnetic properties

The TEM micrographs of FHYD2, FHYD2/SiO_2 and FHYD6 feature typical globular nano-clusters with average crystallite size of 4.0, 3.5 and 6.0 nm, respectively. Disordered and less crystalline FHYD2 and FHYD2/SiO_2 form by rapid hydrolysis of Fe^{3+} at ambient temperatures and neutral pH while a more crystalline FHYD6 forms by hydrolysis performed at 348 K.

The temperature dependence of the magnetization reveal typical SPM behavior above blocking temperature T_B = 44, 36 and 50 K for FHYD2, FHYD2/SiO_2 and FHYD6, respectively. Below T_B the nanoparticles are in a blocked state with M increasing only slightly with decreasing T. The anisotropy constants are relatively high as compared to iron oxides amounting to $K = 4.5 \times 10^5$ J/m^3 for FHYD2, $K = 5.5 \times 10^5$ J/m^3 for FHYD2/SiO_2 and $K = 1.5 \times 10^5$ J/m^3 for FHYD6, i.e. K decreases with increasing crystallite size; the high values are mainly attributed to surface anisotropy. The effective magnetic moment $\mu_{eff} = 5.78\ \mu_B$ for FHYD2 and $\mu_{eff} = 5.20\ \mu_B$ for FHYD6 are consistent with previously reported values $\mu_{eff} = 5.75\ \mu_B$ for 2-line FHYD and $\mu_{eff} = 5.17\ \mu_B$ for 6-line FHYD as well as with the experimental value $\mu_{eff} = 5.85\ \mu_B$ and the theoretical value $\mu_{eff} = 5.92\ \mu_B$ expected Fe^{3+}. This study underlines particularly the key influence of the crystallite size and surface atoms on the magnetic properties of nanoparticles. The fraction of surface atoms increases with decreasing crystallite size. This results in increasing anisotropy constant due mainly to surface anisotropy, increasing the number of uncompensated surface spins which leads to increasing saturation magnetisation in the blocked state (below T_B). Further, with increasing surface contributions atoms at the surface sense weaker exchange fields in the blocked state thus the hyperfine magnetic field decreases. These observations are consistent with well-known facts that in nanoparticles the crystallite size and geometry determine the extent and configuration of the magnetic domains.

High spectral energy resolution (better than 0.3 eV) EELS experiments were performed on FHYD2, FHYD6 and iron oxides reference compounds with well-known coordination chemistry. The Fe *L*-edge of FHYD was modeled using the reference spectra and the percentage of T_d and O_h coordination was estimated from the fitting coefficients of the NLLS fitting routine. EELS study found evidence of the presence of Fe^{3+} in Td coordination in both FHYD2 and FHYD6 nanoparticles with abundances of 20 and 15%, respectively. MS spectra recorded at 4.2 K in zero-field and in an applied magnetic field of 10 T were successfully fitted with a model combining ferrimagnetic and antiferromagnetic ordering and Fe^{3+} atoms in Fe1, Fe2 and Fe3 sites. The relative abundance of T_d Fe^{3+} estimated from the resonance absorption lines of the Fe3 sites in the MS spectra amounts to 15% for FHYD2 and 10% for FHYD6, fairly consistent with the ideal value of 20%, respectively, proposed by Michel model.

7.1.2 Thermal transformation and reduction behaviour in H_2 atmosphere

Thermal transformations of FHYD nanoparticles synthesized to α-Fe_2O_3 under vacuum translated into a two-step increase of the magnetization, the corresponding to a loss of the lattice water and sintering accompanied by structural changes and phase transformation, the second step at relatively high temperatures is due mainly to crystallite size growth and improved crystallinity. The presence of SiO_2 tends to inhibit the transformation and sintering.

The mechanisms of the reduction of FHYD nanoparticles in H_2 were investigated using H_2-TPR, *in situ* XRD, and Mössbauer spectroscopy. The results obtained can be summarized as follows:

- The reduction of FHYD2 to α-Fe proceeds via a two-step mechanism via Fe_3O_4 intermediate phase, similar to the mechanism commonly known for the reduction of α-Fe_2O_3.
- The reduction pathway of FHYD2/SiO_2 to α-Fe proceeds via a three-step mechanism involving Fe_3O_4 and FeO intermediate phases. It is believed that the addition of the FeO intermediate phase is due to strong SiO_2 surface interactions that lead to the stabilization of the metastable wüstite phase even at temperatures below 843 K.
- FHYD6 undergoes first a thermal transformation to α-Fe_2O_3 prior to the reduction that comprises also two steps expected for the traditional reduction mechanism of α-Fe_2O_3.

7.2 Recommendations

The study of FHYD with electron beam techniques poses serious challenge due to the beam sensitivity of the material. Examples of electron beam damage in FHYD2 and FHYD6 are shown in Appendix A of this thesis. The use of low dose techniques and liquid nitrogen TEM cryo holders is highly recommended when investigating FHYD with electron beam related techniques to avoid beam damage.

The evidence of T_d Fe^{3+} in FHYD revealed by the MS and EELS study in this work is in support of several recent studies that advocate the presence of T_d coordination in the mineral. This challenges the structural model of FHYD proposed by Drits which contains 100 % Fe^{3+} in O_h coordination. Although the structural model proposed Michel contains some Fe^{3+} in T_d coordination (20 %), it is being disputed for its periodic nature. It has been argued that how can a highly disordered nanocrystalline material like FHYD be describe by a periodic model. Perhaps one should consider a hydrid model combining these two models. For example, it could be interesting to investigate a modified Drits model that incorporates Fe^{3+} in T_d coordination.

As mentioned, in MS spectra in applied magnetic field were fitted according to a model that accounts for iron atoms on Fe1, Fe2 and Fe3 sites. The validity of such model still needs to be tested, in particular with MS measurements in variable external magnetic field applied both parallel and normal to the direction of γ-rays.

During the reduction experiments in H_2 it was observed that there were two competing processes i.e. thermal transformation and reduction in one of the FHYD sample. It could be interesting and to use a complementary technique that can monitor the two processes. For example, TG/DTA experiments under H_2 flow can provide the capabilities to investigate thermal and reduction processes simultaneously.

References

Als-Nielsen, J. and McMorrow, D.: (2011) "Elements of Modern X-ray Physics", Wiley & Sons, Ltd, Chichester.

Arena, F., Gatti, G., Martra, G., Coluccia, S., Stievano, L., Spadaro, L., Famulari, P. and Parmaliana, A.: (2005) J.Catal., **231**, 365.

Bali, S., Bali, G., Eyring, E. M., Ernest, R. D. and Pugmire, R. J.: (2011) US Patent 12/857,385, Salt Lake City, UT.

Bali, S., Bali, G., Huggins, F. E., Seehra, M. S., Singh, V., Hancock, J. M., Harrison, R., Huffman, G. P., Pumire, R. J., Ernest, R. D. and Eyring, E. M.: (2012) Ind. Eng. Chem. Res. , **51**, 4515.

Barrón, V., Torrent, J. and Michel, F. M.: (2012) Am. Mineral., **97**, 253.

Bendersky, L. A. and Gayle, F. W.: (2001) J. Res.Natl.Stand.Technol., **106**, 997.

Bernal, J. D., Dasgupta, D. R. and Mackay, A. L.: (1959) Clay Miner. Bull., **4**, 15.

Bhatia, S., Beltrimini, I. and Do, D. D.: (1990) Catal. Today, **7**, 309.

Bibicu, I. and Frunza, L.: (2006) Romanian Rep. Phys., **58**, 427.

Bigham, J. M., Carlson, L. and Murad, E.: (1994) Mineral. Mag., **58**, 641.

Bødker, F., Hansen, M. F., Kock, C. B., Lefmann, K. and Mørup, S.: (2000) Phys. Rev. B, **61**, 6826.

Bødker, F., Mørup, S. and Linderoth, S.: (1994) Phys. Rev. Lett., **72**, 282.

Bødker, F., Mørup, S. and Niemantsverdriet, J. W.: (1992) Catal. Lett., **13**, 195.

Boulkas, A. and El Harfi, K.: (2008) Oil Shale, **25**, 426.

Bowa Chansongo, M. S. (2009). University of the Witwatersrand, MSc. Thesis.

Brice-Profeta, S., Arrio, M.-A., Tronc, E., Menguy, N., Letard, I. and Sainctavit, P.: (2005) J. Magn. Magn. Mater. , **288**, 354.

Buerger, M. J.: (1940) Proc. Natl. Acad. Sci. USA, **26**, 637.

Bukur, B. D., Lang, X., Mukesh, D., Zimmermann, W. H., Rosynek, M. P. and Li, C.: (1990) Ind. Eng. Chem. Res., **29**, 1588.

Bukur, D. B., Koranne, M., Lang, X., Rao, K. R. P. M. and Huffman, G. P.: (1995a) Appl. Catal. A: General, **126**, 85.

Bukur, D. B., Nowicki, L., Manne, R. K. and Lang, X.: (1995b) J. Catal., **155**, 366.

Bukur, D. B., Okabe, K., Rosynek, M. P., Li, C., Wang, D., Rao, K. R. P. M. and Huffman, G. P.: (1995c) J. Catal., **155**, 353.

Buschow, K. H. J. and de Boer, F. R.: (2003) "Physics of Magnetism and Magnetic Materials", Kluwer Academic Publishers, New York.

Buseck, P., Cowley, J. and Eyring, L., Eds.: (1992) "High-Resolution Transmission Electron Microscopy and Associated Techniques", Oxford University Press, INC, New York.

Calvert, C., Brown, A. and Brydson, R.: (2005) J. Electron Spectrosc. Relat. Phenom., **143**, 173.

Campbell, A. S., Schwertmann, U. and Campbell, P. A.: (1997) Clay Miner., **32**, 615.

Campbell, A. S., Schwertmann, U., Stanjek, H., Friedl, J., Kyek, A. and Campbell, P. A.: (2002) Longmuir, **18**, 7804.

Cao, C., Tian, L., Liu, Q., Liu, W., Chen, G. and Pan, Y.: (2010) J. Geophys. Res., **115**, B07103.

Cardile, C. M.: (1988a) Clay Clay Miner., **36**, 537.

Cardile, C. M. and Brown, I. W. M.: (1988b) Clay Miner., **23**, 13.

Carta, D., Casula, M. F., Corrias, A., Falqui, A., Navarrra, G. and Pinna, G.: (2009) Mater. Chem. Phys., **113**, 349.

Carvallo, C., Sainctavit, P., Arrio, M.-A., Guyodo, Y., Penn, R. L., Forsberg, B., Rogalev, A., Wilhelm, F. and Smekhova, A.: (2010) Geophys. Res. Lett. , **37**, L11306.

Chen, D., Gao, X. and Dollimore, D.: (1993) Thermochimica Acta, **215**, 109.

Chen, S.-H., Gloter, A., Zobelli, A., Wang, L., Chen, C.-H. and Coelliex, C.: (2009) Phys. Rev. B, **79**, 104103.

Chen, W., Mørup, S., Hansen, M. F., Bnet, T. and Peuker, U. A.: (2008) J. Magn. Magn. Mater., **320**, 2099.

Chester, A. W. and Derouane, E. G., Eds.: (2009) "Zeolite characterization and catalysis", Springer Science+Business Media, New York.

Childs, C. W. and Johnston, J. H.: (1980) Aust. J. Soil Res., **18**, 245.

Christensen, A. N., Jensen, T. R., Bahl, C. R. H. and DiMasi, E.: (2007) J. Solid State Chem., **180**, 1431.

Cornell, R. M., Giovanoli, R. and Schneider, W.: (1989) J. Chem. Tech. Biotechnol., **46**, 115.

Cornell, R. M. and Schwertmann, U.: (2003) "The iron oxides: Structure properties, reactions, occurrences, and uses", Wiley-VCH Verlag GmbH & CO, Weinheim.

Cowley, J. M., Janney, D. E., Gerkin, R. C. and Buseck, P. R.: (2000) J. Struct. Biol., **131**, 210.

Culity, B. D. and Graham, C. D.: (2009) "Introduction to Magnetic Materials", Willey Publishers, New Jersey.

d'Arlas, B. F., Rueda, L., Stefani, P. M., de la Caba, K., Mondregon, I. and Eceiza, A.: (2007) Thermochim. Acta, **459**, 94.

Da Casta, G. M., De Grave, E., Bowen, I. H., Vandenberghe, R. E. and De Bakker, P. M. A.: (1994) Clay Clay Miner., **42**, 628.

Das, R. K., Rawal, S., Norton, D. and Hebard, A. F.: (2010) J. Appl. Phys., **108**, 123920.

de Faria, D. L. A., Silva, S. V. and de Oliveira, M. T.: (1997) J. Raman Spectrosc., **28**, 873.

Dlamini, H., Motjope, T., Joorst, G., ter stege, G. and Mdlaleni, M.: (2002) Catal. Lett., **78**, 201.

Douglas, B., McDaniel, D. and Alexander, J.: (1994) "Concepts and Models of Inorganic Chemistry", John wiley & Sons, Inc., New York.

Drits, V. A., Sakharov, B. A., Salyn, A. L. and Manceau, A.: (1993) Clay Miner., **28**, 185.

Duarte, E. L., Itri, R., Lima Jr., E., Baptista, M. S., Berquó, T. S. and Goya, G. F.: (2006) Nanotechnol., **17**, 5549.

Dyar, M. D., Agresti, D. G., Schaefer, M. W., Grant, C. A. and Sklute, E. C.: (2006) Annu. Rev. Earth Planet. Sci., **34**, 83.

Egerton, R. F.: (2003) Micron, **34**, 127.

Egerton, R. F.: (2005a) "Physical Principles of Electron Microscopy", Springer Science + Bussness Media, Inc, New York.

Egerton, R. F.: (2009) Rep.prog.phys., **72**, 016502.

Egerton, R. F.: (2011) "Electron Energy-Loss Spectroscopy in the Electron Microscope", Springer Science + Business Media, LLC, New York.

Egerton, R. F. and Malac, M.: (2005b) J. Electron Spectrosc. Relat. Phenom., **143**, 43.

Eggleton, R. A. and Fitzpatrick, R. W.: (1988) Clay Clay Miner., **36**, 111.

F.M. Michel, L. E., S.M. Antao, P.L. Lee, P.J. Chupas, G. Liu, D.R. Strongin, M.A.A. Schoonen, B.L. Phillips, J.B. Parise (2007) Sci. Express, **316**, 1726.

Filip, J., Zboril, R., Schnheeweiss, O., Zeman, J., Cernik, M., Kvapil, P. and Otyepka, M.: (2007) Environ. Sci. Technol., **41**, 4367.

Fischer, W. R. and Schwertmann, U.: (1975) Clay Clay Miner., **23**, 33.

Flynn, J. H. and Wall, L. A.: (1966) J. Polym. Sci., **4**, 323.

Friedman, H. L.: (1963) J. Polym. Sci., Part C, **6**, 183.

Fultz, B. and Howe, J. M.: (2002) "Transmission Electron Microscopy and Diffractometry of Materials", Springer, New York.

Garvie, L. and Buseck, P. R.: (1998) Nature, **396**, 667.

Gavaría, J. P., Bohé, A., Pasquevich, A. and Pasquevich, D. M.: (2007) Physica B, **389**, 198.

Gilles, C., Bonville, P., Wong, K. K. W. and Mann, S.: (2000) Eur. Phys. J. B, **17**, 417.

Gilmore, K., Dzerda, Y. U., Klem, M. T., Allen, M., Douglas, T. and Ypung, M.: (2005) J. Appl. Phys., **97**, 10B301.

Glasauer, S. M., Hug, P., Weidler, P. G. and Gehring, A. U.: (2000) Clay Clay Miner., **48**, 51.

Gloter, A., Zbinden, M., Guyoto, F., Gaill, F. and Coelliex, C.: (2004) Earth and Planetary Sci. Lett., **222**, 947.

Goldanskii, V. I. and Herber, R. H., Eds.: (1968) "Chemical Applications of Mossbauer Spectroscopy", Academic Press INC, New York.

Goya, G. F., Berquó, T. S. and Fonseca, F. C.: (2003) J. Appl. Phys. , **94**, 3520.

Grau-Crespo, R., Al-Baitai, A. Y., Saadoune, I. and de Leeuw, N. H.: (2010) J. Phys. : Condns. Matter **22**, 255401.

Guyodo, Y., Banerjee, S. K., Penn, R. L. B., D., Berquo, T. S., Seda, T. and Solheid, P.: (2006) Phys. Earth Planet. In., **154**, 222.

Guyodo, Y., Sainctavit, P., Arrio, M., Carvallo, C., Penn, R. L., Erbs, J. J., Forsberg, B. S., Morin, G., Maillot, F., Lagrox, F., Bonville, P., Wilhelm, F. and Rogalev, A.: (2012) Geochem. Geophys. Geosyst., **13**, 1.

Hammond, C.: (2009) "The basics of crystallography and diffraction", Oxford University Press, Oxford.

Hanesch, M.: (2009) Geophys. J. Int., **177**, 941.

Hansen, T. W. (2006). University of New Mexico, PhD Thesis.

Harrington, R., Hausner, D. B., Xu, W., Bhandara, N., Michel, F. M., Brown Jr., G. E., Strongin, D. R. and Parise, J. B.: (2011) Environ. Sci. Technol, **45**, 9883.

Hausner, D. B., Bhadari, N., Pierre-Louis, A., Kubicki, J. D. and Strongin, D. R.: (2009) J. Colloid Interface Sci., **337**, 492.

Helgason, Ö., Rason, H. K. and MØrup, S.: (2006) J. Magn. Magn. Mater., **302**, 413.

Hiemstra, T.: (2013) Geochim. Cosmochim. Acta, **105**, 316.

Hiemstra, T. and van Riemsdijk, W. H.: (2009) Geochim. Cosmochim. Acta, **73**, 4423.

Hill, A. H., Jiao, F., Bruce, P. G., Harrison, A., Kockelmann, W. and Ritter, C.: (2008) Chem. Mater., **20**, 4891.

Jacintho, G. V. M., Corio, P. and Rubim, J. C.: (2007) J. Electroanal. Chem., **603**, 27.

Jambor, J. L. and Dutrizac, J. E.: (1998) Chem. Rev., **98**, 2549.

Janney, D. E., Cowley, J. M. and Buseck, P. R.: (2000a) Am. Mineral., **85**, 1180.

Janney, D. E., Cowley, J. M. and Buseck, P. R.: (2000b) Clay Clay Miner., **48**, 111.

Janney, D. E., Cowley, J. M. and Buseck, P. R.: (2001) Am. Mineral., **86**, 327.

Jansen, E., Kyek, A., Schäfer, W. and Schwertmann, U.: (2002) Appl. Phys. A, **74**, S1004.

Jeng, H.-T. and Guo, G. Y.: (2002) Phys. Rev. B, **65**, 094429.

Jin, Y. and Datye, A. K.: (2000) J. Catal., **196**, 8.

Jones, A. and McNicol, B.: (1986) "Temperature-Programmed Reduction for Solid Materials Characterization", Marcel Dekker Inc., New York.

Jozwiak, W. K., Kaczmarek, E., Maniecki, T. P., Ignaczak, W. and Maniukiewics, W.: (2007) Appl. Catal. A: General, **326**, 17.

Kanervo, J. (2003). Helsinki University of Technology, PhD Thesis.

Karim, Z.: (1984) Clays Clay Miner., **32**, 181.

Karkik, M.: (2001) Mater. Struct., **8**, 3.

Kilicoyne, S. H. and Cywinski, R.: (1995) J. Magn. Magn. Mater., **140-144**, 1466.

Kilicoyne, S. H., Mitchell, G. R. and Cywinski, R.: (1992) Physica B, **180-181**, 767.

Kirkpatrick, P.: (1927) Phys. Rev., **29**, 632.

Kissinger, H.: (1957) Anal. Chem., **29**, 1702.

Kodama, R. H.: (1999b) J. Magn. Magn. Mater., **200**, 359.

Kodama, R. H. and Berkowitz, A. E.: (1999a) Phys. Rev. B, **59**, 6321.

Kodama, R. H., Berkowitz, A. E., Mcniff Jr., E. J. and Foner, S.: (1996) Phys. Rev. Lett., **77**, 394.

Komarida, Y., Mito, M., Deguchi, H., Takagi, S., Millán, A., Silva, N. J. O. and Palacio, F.: (2009) Appl. Phys. Lett., **94**, 202503.

Koningstein, J. A.: (1972) "Introduction to the Theory of the Raman Effect", D.Reidel Publishing company, Dordrecht, Holland.

Kündig, W., Bömmel, H., Constabaris, G. and Lindquist, R. H.: (1966) Phys. Rev., **142**, 327.

Kuzmany, H.: (1998) "Solid-State Spectroscopy", Springer-Verlag, Berlin.

LanXiang, T., ChangQian, C., QingSong, L. and YongXin, P.: (2010) Geophys., **55**, 3174.

Leapman, R. D. and Grunes, L. A.: (1980) Phys. Rev. Lett., **45**, 397.

Leapman, R. D., Grunes, L. A. and Fejes, P. L.: (1982) Phys. Rev. B, **26**, 614.

Li, C. and Tang, T. B.: (1999) J. Mater. Sci., **34**, 3467.

Li, S., Krishnamoorthy, S., Li, A., Meitzner, G. D. and Iglesia, E.: (2002) J. Catal., **206**, 202.

Lin, C.-C., Kuo, M.-T. and Chang, H.-C.: (2010) J. Med. Biol. Eng., **30**, 343.

Lin, H., Chen, Y. and Li, C.: (2003) Thermochim. Acta, **400**, 61.

Lin, S. T.: (1959) Phys. Rev., **116**, 1447.

Linderoth, S., Hendriksen, P. V., Bødker, F., Wells, S., Davies, K., Charles, S. W. and Mørup, S.: (1994) J. Appl. Phys., **75**, 6583.

Lohitharn, N., Goodwin Jr., J. G. and Lotero, E.: (2008) J. Catal., **255**, 104.

Long, G. J., Ed.: (1984) "Mossbauer Spectroscopy Applied to Inorganic Chemistry", Plenum Press, New York.

Long, G. J. and Grandjean, F., Eds.: (1993) "Mössbauer Spectroscopy Applied to Magnetism and Materials Science", Plenum Press, New York.

Lund, C. R. F. and Dumesic, J. A.: (1981) J.Phys. Chem. , **85**, 3175.

Lyubutin, I. S., Lin, C. R., Korzhetskiy, Y. V., Dmitrieva, T. V. and Chiang, R. K.: (2009) J. Appl. Phys., **106**, 034311.

Maddock, A. G.: (1997) "Mössbauer Spectroscopy: Principles and Applications", Horwood Publishing, Chichester.

Madsen, M. B., MØrup, S. and Kock, C. J. W.: (1986) Hyperfine Interact., **27**, 329.

Maillot, F., Morin, G., Wang, Y., Bonnin, D., Ildefonse, P., Chaneac, C. and Calas, G.: (2011) J. Geochim. Cosmochim. Acta, **75**, 2708.

Makhlouf, S. and Parker, F. T.: (1997) Phys. Rev. B, **55**, R14717.

Manceau, A.: (2009) Clay Miner., **44**, 19.

Manceau, A.: (2010) Clay Miner., **45**, 225.

Manceau, A.: (2011) Am. Mineral., **96**, 521.

Manceau, A., Combes, J. M. and Calas, G.: (1990) Clays Clay Miner., **38**, 331.

Manceau, A. and Drits, V. A.: (1993) Clay Miner., **28**, 165.

Manceau, A. and Gates, W.: (1997) Clay Clay Miner., **45**, 448.

Manteanu, G., Budrugeac, P., Ilieva, L., Tabakova, T. and Andreeva, D.: (2003) J. Mater. Sci., **38**, 1995.

Manteanu, G., Ilieva, L. and Andreeva, D.: (1997) Thermochim. Acta, **291**, 171.

Manteanu, G., Ilieva, L. and Andreeva, D.: (1999) Thermochim. Acta, **329**, 157.

Martin, T. P., Merlin, R., Huffman, D. R. and Cardona, M.: (1977) Solid State Commun., **22**, 565.

May, L., Ed.: (1971) "An Introduction to Mossbauer Spectroscopy", Plenum Press, New York.

Mazzetti, L. and Thistlethwale, P. J.: (2002) J. Raman Spectrosc., **33**, 104.

Messi, C., Carniti, P. and Gervasini, A.: (2008) J. Therm. Anal. Calorim., **91**, 93.

Miao, S. (2007). Carlifonia Institute of Technology, PhD thesis.

Michel, F. (2007a). Stony Brook University, PhD Thesis.

Michel, F. M., BarrÓn, V., Torrent, J., Morales, M. P., Serna, C. J., Boily, J., Liu, Q., Ambrosini, A., Cismasu, A. C. and Brown Jr., G. E.: (2010) PNAS, **107**, 2787.

Michel, F. M., Ehm, L., Antao, S. M., Han, W. Q., Antao, S. M., Lee, P. L., Knorr, K., Eulert, H., Chupas, P. J., Liu, G., Strongin, D. R., Schoonen, M. A. A., Phillips, B. L. and Parise, J. B.: (2007b) Chem. Mater., **19**, 1489.

Michel, F. M., Ehm, L., Antao, S. M., Lee, P. L., Chupas, P. J., Liu, G., Strongin, D. R., Schoonen, M. A. A., Phillips, B. L. and Parise, J. B.: (2007c) Sci. Express, **316**, 1726.

Mikkuta, C.: (2011) Geochem. Cosmochiim. Acta, **75**, 5122.

Mohapatra, M. and Anand, S.: (2010) Int. J. Eng. Sci.Technol, **2**, 127.

MØrup, S.: (1983) J. Magn. Magn. Mater., **39**, 45.

Murad, E.: (1988) J. Magn. Magn. Mater., **74**, 153.

Murad, E.: (1996) Phys. Chem. Miner., **23**, 248.

Murad, E. and Cashion, J.: (2004) "Mössbauer spectroscopy of Enviromental Materials and their Industrial Utilization ", Kluwer Acadamic Press, Boston.

Murad, E. and Schwertmann, U.: (1980) Am. Mineral., **65**, 1044.

Murad, E. and Weihenstephan, F. N. J.: (1982) Miner. Mh., **H.2**, 45.

Neyens, G.: (2003) Rep. Prog. Phys., **66**, 633.

Niemantsverdriet, J. W. and Delgas, W. N.: (1999) Top. Catal., **8**, 133.

Orchard, A. F.: (2007) "Magnetochemistry", Oxford University Press, Oxford.

Ozawa, T.: (1965) Bull. Chem. Soc. Jpn., **28**, 1881.

Pan, Y. (2007). University of Leeds, PhD thesis.

Pan, Y., Brown, A., Brydson, R., Warley, A., Li, A. and Powell, J.: (2006) Micron, **37**, 403.

Pan, Y., Sader, K., Powell, J. J., Bletoch, A., Gass, M., Trinick, J., Warley, A., Li, A., Brydson, R. and Brown, A.: (2009) J. Struct. Biol., **166**, 22.

Pan, Y., Vaughan, G., Brydson, R., Bleloch, A., Gass, M., Sader, K. and Brown, A.: (2010) Ultramicroscopy, **110**, 1020.

Pankhurst, Q. A. and Pollard, R. J.: (1992) Clay Clay Miner., **40**, 268.

Pauling, L.: (1929) J. Am. Chem. Soc., **51**, 1010.

Peak, D. and Reiger, T.: (2012a) Environ. Sci. Technol. , **46**, 3163.

Pecharsky, V. K. and Zavalij, P. Y.: (2009) "Fundamentals of powder diffraction and structural characterization of materials", Springer Science+Business Media, LLC, New York.

Pérez-Alonso, F. J., Ojeda, M., Herranz, T., González-Carballo, J. M., Fierro, J. L. G., Bengoa, J. F. and Marchetti, S. G.: (2008) Open Mag. Reson. J. , **1**, 64.

Pérez, N., Guardia, P., Roca, A. G., Morales, M. P., Serna, C. J., Iglesias, O., Bartolomé, F., García, L. M., Batlle, X. and Labarta, A.: (2008) Nanotechnol., **19**, 475704.

Pineau, A., Kamari, N. and Gaballah, I.: (2006) Thermochim. Acta, **447**, 89.

Pinna, F.: (1998) Catal. Today, **41**, 129.

Pinney, N., Kubicki, J. D., Middlemiss, D. S., Grey, C. P. and Morgan, D.: (2009) Chem. Mater. , **21**, 5727.

Pollard, R. J., Cardile, C. M., Lewis, D. G. and Brown, L. J.: (1992) Clay Miner., **27**, 57.

Poulson, R. L., Johnson, C. M. and Beard, B. L.: (2005) Am. Mineral., **90**, 758.

Pourghahramani, P. and Forssberg, E.: (2007) Thermochim. Acta, **454**, 69.

Punnoose, A., Phanthavady, T., Seehra, M. S., Shah, N. and Huffman, P.: (2004) Phys. Rev.B, **69**, 054425.

Raman, C. V. and Kirishnan, K. S.: (1928) Nature, **121**, 501.

Rancourt, D. G. and Meunier, J. F.: (2008) Am. Mineral., **93**, 1412.

Reimer, L.: (1997) "Transmission Electron Microscopy", Springer, New York.

Restropo, J., Labaye, Y., Berger, L. and Greneche, J. M.: (2004) J. Magn. Magn. Mater., **272-276**, 681.

Restropo, J., Labaye, Y. and Greneche, J. M.: (2006) Physica B, **384**, 221.

Riedl, T., Gemming, T. and Wetzig, K.: (2006) Ultramicroscopy, **106**, 284.

Robertson, S. D., McNicol, B. D., de Baas, J. H. and Kloet, S. C.: (1975) J. Catal., **37**, 424.

Russell, J. D.: (1979) Clay Clay Miner., **14**, 109.

Saha, B., Maiti, A. K. and Ghoshal, A. K.: (2006) Thermochimica Acta, **444**, 46.

Sastri, M. V. C., Viswanath, R. P. and Viswanath, B.: (1982) Int. J. Hydrogen Energy, **7**, 951.

Schneeweiss, O., David, B., Žák, T., Filip, J., Tuček, J., Zbořil, R. and Mašláň, M.: (2010) Acta Phys. Pol., A, **118**, 749.

Schneeweiss, O., Filip, J., David, B., Zbořil, R. and Mašlán, M.: (2011) J. Nanopart. Res., **13**, 5677.

Schneeweiss, O., Grygar, T., David, B., Zboril, R., Filip, J. and Mashlan, M. (2008). AIP Confererence Proceedings

Schwertmann, U. and Cornell, R. M.: (2000) "Iron Oxides in the Laboratory", Wiley-VCH, New York.

Schwertmann, U., Friedl, J. and Pfab, G.: (1996) J. Solid State Chem., **126**, 336.

Schwertmann, U. and Murad, E.: (1983) Clay Clay Miner., **31**, 277.

Seehra, M. S., Babu, V. S. and Manivannan, A.: (2000) Phys. Rev. B, **61**, 3513.

Shroff, M. D., Kalakkad, D. S., Coulter, K. E., Kohler, S. D., Harrington, M. S., Jackson, N. B., Sault, A. G. and Datye, A. K.: (1995) J. Catal., **156**, 185.

Sikora, M., Juhin, A., Weng, T., Sainctavit, P., Detlefs, C., de Groot, F. and Glatzel, P.: (2010) Phys. Rev. Lett., **105**, 037205.

Silva, N. J. O., Amaral, V. S., Rodríguez-González, B., Liz-Marzán, L. M., Berquó, T. S., Banerjee, S. K., de zea Bermudez, V., Millan, A. and Palacio, F.: (2008) Phys. Rev. B, **77**, 134426.

Skomurski, F. N., Kerisit, S. and Rosso, K. M.: (2010) Geochim. Cosmochim. Acta, **74**, 4234.

Snow, C. L., Lilova, K. I., Radha, A. V., Shi, Q., Smith, S., Navrotsky, A., Boerio-Goates, J. and Woodfield, B. F.: (2013) J. Chem. Thermodyn., **58**, 307.

Stanjek, H. and Weidler, P. G.: (1992) Clay Miner., **27**, 397.

Starink, M. J.: (2003) Thermochim. Acta, **404**, 163.

Subramanian, R. (2010). universtät Stuttgart, PhD thesis.

Suo, H., Wang, S., Zhang, C., Xu, J., Wu, B., Yang, Y., Xiang, H. and Li, Y.: (2012) J. Catal., **286**, 111.

Suryanarayana, C. and Norton, M. G.: (1998) "X-ray diffraction: A practical approach", Plenum Press, New York.

Sylva, R. N.: (1972) Rev. Pure and Appl. Chem., **22**, 115.

Taylor, E. F. and Wheeler, J. A.: (1992) "Spacetime Physics", W.H. Freeman and Co., New York.

Thole, B. T., van der Laan, G., Fuggle, J. C., Sawatzky, G. A., Karnatak, R. C. and Esteva, J.-M.: (1985) Phys. Rev. B, **32**, 5107.

Tonejc, A.: (1999) Acta Chim. Slov., **46**, 435.

Towe, K. M. and Bradley, W. F.: (1967) J. Colloid. Interface Sci., **24**, 384.

Tronc, E., Ezzir, A., Cherkaoui, R., Chaneac, C., Nogues, M., Kachkachi, H., Fiorani, D., Testa, A. M., Greneche, J. M. and Jolivet, J. P.: (2000) J. Magn. Magn. Mater., **221**, 63.

van Aken, P. A., Koch, C. T., Sigle, W., Höschen, R., Rühle, M., Essers, E., Benner, G. and Matijevic, M.: (2007) Microsc. Microanal. , **13**, 862 CD.

van Aken, P. A., Liebscher, B. and Styrsa, V. J.: (1998) Phys.Chem. Miner., **25**, 323.

van Aken, P. A. and Liebscher, S.: (2002) Phys. Chem. Miner., **29**, 188.

Vatta, L. L., Sanderson, R. D. and Koch, K. R.: (2006) Pure Appli. Chem., **78**, 1793.

Vaughan, G., Brydson, R., Brown, A. and Sader, K.: (2010) J. Phys. : Conf. Series, **241**, 012051.

Venugopal, A., Aluha, J., Mogano, D. and Scurrell, M. S.: (2003) Appl. Catal., A: General, **245**, 149.

Venugopal, A. and Scurrell, M. S.: (2004) Appl. Catal., A: General, **258**, 241.

Vyazovkin, S.: (2006) J. Therm. Anal. Calorim., **83**, 45.

Wang, C., Baer, D. R., Amonette, J. E., Engelhard, M. H., Antony, J. and Qiang, Y.: (2009) J. AM. Chem. SOC., **131**, 8824.

Wanjun, T. and Donghua, C.: (2005) Thermochim. Acta, **433**, 72.

Weber, W. H. and Merlin, R., Eds.: (2000) "Raman Scattering in Materials Science", Springer-Verlag, Berlin.

Wertheim, G. K., Ed.: (1964) "Mossbauer Effect: Principles and Applications", Academic Press INC, New York.

Williams, D. B. and Carter, C. B.: (1996) "Transmission Electron Microscopy", Plenum Press, New York.

Williams, D. B. and Carter, C. B.: (2009) "Transmission Electron Microscopy", Springer Science+Bussness Media, LLC, New York.

Wimmers, O. J., Arnoldy, P. and Moulijn, J. A.: (1986) Phys. Chem, **90**, 1331.

Wright, J. P., Attfield, J. P. and Radaelli, P. G.: (2002) Phys. Rev. B, **66**, 214422.

Xu, W., Hausner, D. B., Harrington, R., Lee, P. L., Strongin, D. R. and Parise, J. B.: (2011) Am. Mineral., **96**, 513.

Yoon, S.: (2011) J. Korean Phys. Soc. , **59**, 3069.

Yu, J., Park, M. and Kim, J.: (2002) Geochem. J., **36**, 119.

Zboril, R., Mashlan, M. and Petridis, D.: (2002) Chem. Mater., **14**, 969.

Zhang, C. H., Wan, H. J., Yang, Y., Xiang, H. W. and Li, Y. W.: (2006) Catal. Commun., **7**, 733.

Zhao, J., Huggins, F. E., Feng, Z. and Huffman, G. P.: (1994a) Clay Clay Miner., **42**, 737.

Zhao, J., Huggins, F. E., Feng, Z., Lu, F., Shah, N. and Huffman, G. F.: (1993) J. Catal., **143**, 499.

Zieliński, J., Zglinicka, I., Znak, L. and Kaszkur, Z.: (2010) Appl. Catal. A: General, **381**, 191.

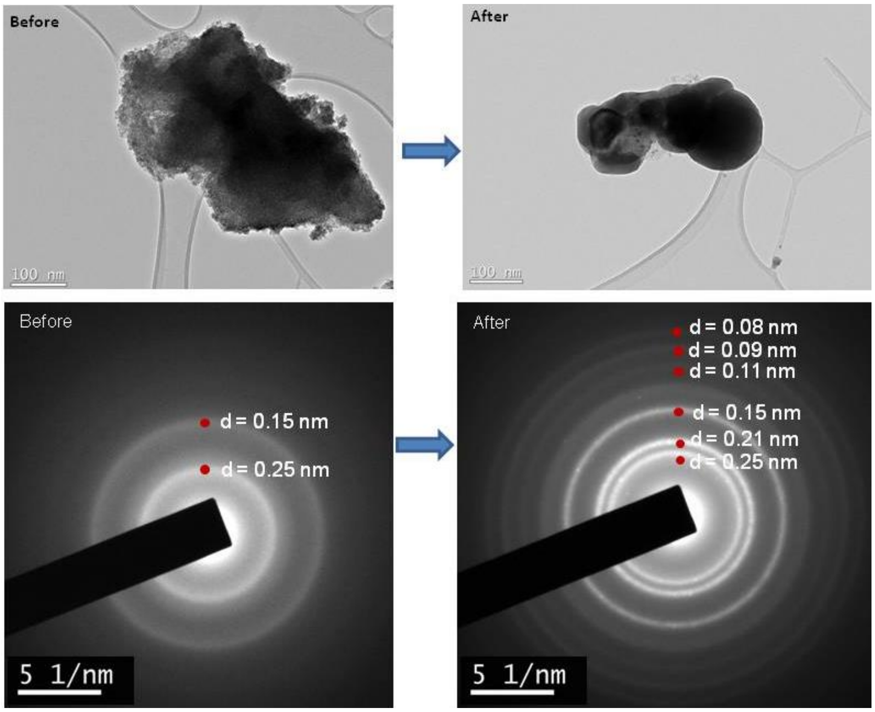

Figure A 0.1: FHYD2 electron beam phase transformation.

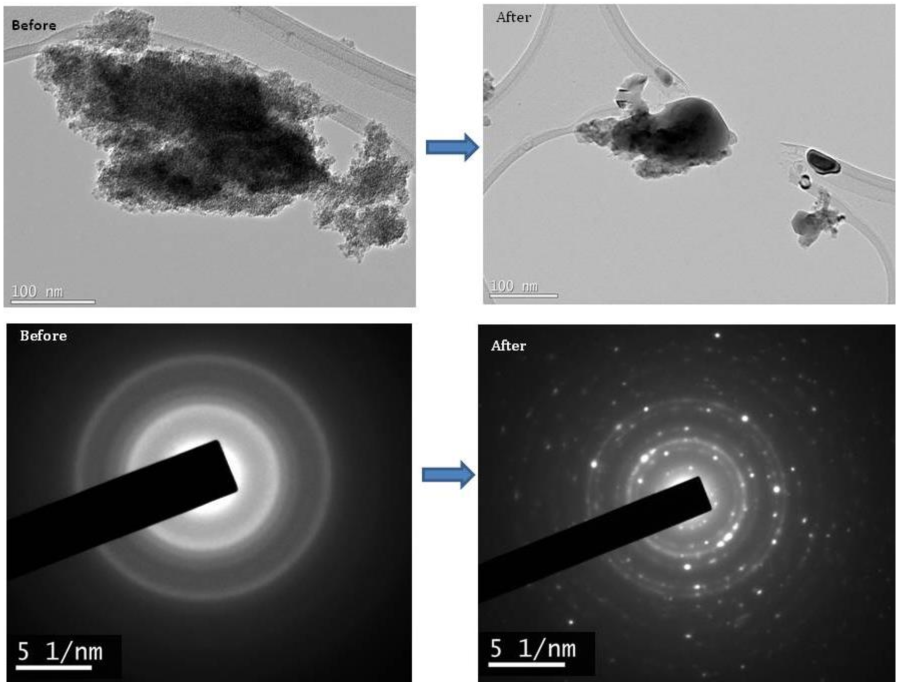

Figure A 0.2: FHYD6 electron beam phase transformation.

RESEARCH OUTPUTS

Publications

Synthesis and Characterization of 2- and 6-Line Ferrihydrite Nanoparticles

C.J. Masina[1], E.J. Olivier[1], C. Heiligers[1], J.H. Neethling[1], S. Manzini[2], A. Ferreira[2], W. Barnard[2], L. Lodya[2], E. du Plessis[2] and B.G. Anderson[2]
[1]Centre for HRTEM, Nelson Mandela Metropolitan University, PO Box 77000, Port Elizabeth, South Africa
[2]Sasol Technology, R&D, Materials Science, 1 Klasie Havenga Road, Sasolburg, South Africa

(To be Submitted)

Mechanism of Reduction in Hydrogen Atmosphere and Thermal Transformation of Synthetic Ferrihydrite Nanoparticles

C.J. Masina[1], J.H. Neethling[1], E. Ferg[2], S. Manzini[3], L. Lodya[3], P. Mohlala[3] and M.W. Ngobeni [3].
[1]Centre for HRTEM, Nelson Mandela Metropolitan University, PO Box 77000, Port Elizabeth, South Africa
[2]Department of Chemistry Nelson Mandela Metropolitan University, Port Elizabeth, South Africa
[3]Sasol Technology, R&D, 1 Klasie Havenga Road, Sasolburg, South Africa

(To be submitted in Applied Catalysis A : General or Thermochimicha Acta)

Structural and Magnetic Properties of Synthetic Ferrihydrite Nanoparticles

C.J. Masina[1], J.H. Neethling[1], E.J. Olivier[1], S. Manzini[2] and L. Lodya[2] .
[1]Centre for HRTEM, Nelson Mandela Metropolitan University, PO Box 77000, Port Elizabeth, South Africa
[2]Sasol Technology, R&D, 1 Klasie Havenga Road, Sasolburg, South Africa

(To be submitted)

Conferences attended

STRUCTURAL ANALYSIS OF SYNTHETIC 2-LINE FERRIHYDRITE

C.J. Masina[1], C. Heiligers[1], J.H. Neethling[1], B.G. Anderson[2] and E.J. Olivier[1]
[1] Centre for HRTEM, Nelson Mandela Metropolitan University, Port Elizabeth
[2]Sasol Technology R&D, Sasolburg

MSSA Conference October 2011, Pretoria, South Africa (Oral presentation)

AN ELECTRON ENERGY LOSS SPECTROSCOPIC STUDY OF SYNTHETIC 2-LINE FERRIHYDRITE

C.J. Masina[1], E.J. Olivier[1], J.H. Neethling[1] and B.G. Anderson[2]
[1] Centre for HRTEM, Nelson Mandela Metropolitan University, Port Elizabeth
[2]Materials Science Group, Sasol Technology R&D, Sasolburg

MSSA Conference December 2012, Cape Town, South Africa (Poster presentation)

Workshops attended

1. Pair Distribution Function (PDF) Analysis of diffraction data in real space. October 2011, ILL Grenoble, France.

2. Electron energy loss spectroscopy (EELS) course presented by Gatan. November 2012, NMMU, Port Elizabeth, South Africa.

3. Powder X-ray diffraction course (PXRD), November 2012, Wits University, Johannesburg, South Africa